

The hydraulic effect of  
**f a u l t**  
**z o n e s**  
in relation to deep  
hydro - geothermal  
energy exploration in  
the Upper Jurassic  
a q u i f e r  
of Southern Germany



---

Florian Konrad

Munich, 2022

---



# **The hydraulic effect of fault zones in relation to deep hydro-geothermal energy exploration in the Upper Jurassic aquifer of Southern Germany**

**Florian Markus Konrad**

Vollständiger Abdruck der von der *TUM School of Engineering and Design* der Technischen Universität München zur Erlangung des akademischen Grades eines

**Doktors der Ingenieurwissenschaften (Dr.-Ing.)**

genehmigten Dissertation.

Vorsitz: Priv.-Doz. Dr. rer. nat. habil. Arno Rein

Prüfer\*innen der Dissertation:

1. Prof. Dr. rer. nat. Florian Einsiedl
2. Prof. Dr.-Ing. Michael Manhart
3. Prof. Florian Wellmann, Ph.D.

Die Dissertation wurde am 25.01.2022 bei der Technischen Universität München eingereicht und durch die *TUM School of Engineering and Design* am 12.05.2022 angenommen.



## Abstract

Fault zones in the Upper Jurassic aquifer (UJA) of the North Alpine Foreland Basin are generally regions with possibly increased hydraulic properties. They are consequently often part of the geothermal exploration concepts in this area and a primary target for the drilling operation. However, data from this aquifer gathered in well tests shows that only four out of 44 successful wells exhibit hydraulic proof for the presence of such a fault zone in terms of a bi-/linear flow regime. Besides technical effects (e.g. errors in the reservoir pressure measurement, oscillations of production rates due to technical limitations, well properties), the contrast in hydraulic properties itself, between fault zone and surrounding host rock, can also prevent the detection of a fault zone in well test data. This means a certain threshold has to be surpassed until its effects become clearly visible. With this uncertainty in the detection of fault zones in pressure data goes along the question regarding their share in well productivity. Especially relevant is this question with a focus on hydraulically active fault zones that remain undetected in a well test (hydraulically hidden fault zones).

A simplified realistic numerical model was constructed and calibrated with pressure data from an exploration site south of Munich. In a first step, this model was used to observe the presence of linear and bilinear flow in dependence of the UJA parameter space. Sampling the possible hydraulic property combinations with the help of an HPC (high performance computing) cluster and automating the detection of the corresponding main flow type allowed to quantify the areas in parameter space where the fault zone-related flow regimes of interest are present. After more than 30,000 combinations between fault zone permeability, matrix permeability, fault zone storage, matrix storage and fault zone thickness were investigated, it was found that a bilinear flow could be observed for the first time in the parameter space of the UJA only if the matrix permeability was lower than  $2.0 \times 10^{-13} \text{ m}^2$ , and a linear flow for matrix permeability values was below  $6.0 \times 10^{-14} \text{ m}^2$ . Additionally, it was shown that fault zones, which have better hydraulic properties than the surrounding matrix, can indeed be hidden in well tests due to the parameter setting.

With this knowledge of flow regime transitions in the parameter space of the UJA, a further investigation was carried out by enhancing the calibrated numerical model and applying the *reduced basis* method. This enabled quantifying the effect of hydraulically active fault zones on the well-productivity-index (PI) in dependency of the UJA parameter space based on more than six million simulations. Further, it was possible to investigate the spatial distribution of flow regimes in the greater Munich area depending on different fault zone types and their

influence on the PI. An additional 81 million simulations based on maps of the hydraulic properties of the UJA were therefore deployed. The results of this secondary investigation suggest that hydraulically hidden fault zones can significantly increase the PI. The comparison with flow regime observations of geothermal wells in the greater Munich area suggests that a hydraulically active fault zone thickness of  $\geq 100$  m is unlikely for the UJA.

Finally, an open source Python tool (“uja\_faultzones” [github.com/Florian-Konrad/uja\\_faultzones](https://github.com/Florian-Konrad/uja_faultzones)) was developed that efficiently incorporates the numerical models and the methodology to derive flow regime and well productivity influence for an arbitrary fault zone type. Its fast calculation times of  $\sim 0.4$ s per simulation on a normal workstation enable reservoir engineers to quickly simulate a multitude of well tests of different fault zone realizations and derive their hydraulic influence.

## Zusammenfassung

Störungszonen im Oberjura Aquifer (UJA) des Nordalpinen Vorlandbeckens stellen Regionen mit potentiell günstigen hydraulischen Eigenschaften und erhöhter Wasserwegsamkeit dar. Sie sind daher häufig Teil der geothermischen Explorationskonzepte in diesem Gebiet und ein primäres Bohrziel, um hohe Fließraten in Geothermiebrunnen zu erzielen. Daten aus dem UJA, die aus durchgeführten Pumpversuchen stammen, zeigen jedoch, dass nur vier von 44 erfolgreichen Bohrungen einen hydraulischen Nachweis für das Vorhandensein einer solchen Störungzone im Sinne eines bi-/linearen Fließregimes erbringen. Jedoch kann neben technischen Effekten (z.B. Ungenauigkeiten in der Druckmessung, technisch bedingtes Oszillieren der Förderraten, Brunneneigenschaften) auch der Kontrast in den hydraulischen Eigenschaften selbst, der zwischen Störungzone und umgebendem Wirtsgestein (Matrix) auftritt, den Nachweis einer hydraulisch wirksamen Störungzone in den Pumpversuchsdaten verhindern. Das bedeutet, dass ein bestimmter Kontrast-Schwellenwert überschritten werden muss, bis der Störungseinfluss auf das Fließregime einer Geothermiebohrung deutlich sichtbar wird. Mit dieser Unsicherheit bei der Erkennung von Störungszonen in Druckdaten von Pumpversuchen geht auch die Frage nach ihrem Anteil an der Brunnenproduktivität einher. Besonders relevant ist diese Frage mit Blick auf hydraulisch aktive Störungszonen, die bei einem Pumpversuch generell unentdeckt bleiben (hydraulisch verborgene Störungszonen).

Um diese offenen Fragen zu untersuchen wurde ein vereinfachtes, aber dennoch realistisches, numerisches Modell erstellt und mit Druckdaten, die an einem Explorationsstandort im Süden von München während eines Pumpversuchs aufgezeichnet wurden, kalibriert. In einem ersten Schritt wurde dieses Modell verwendet, um das Vorhandensein von linearem und bilinearem Fließen in Abhängigkeit der hydraulischen Modelleigenschaften zu beobachten. Hierzu wurde der zugehörige Parameterraum, welcher aus den für den UJA tatsächlich möglichen hydraulischen Eigenschaftskombinationen vor allem von Störungszonen und der umgebenden Matrix besteht, systematisch abgetastet. Mit Hilfe eines HPC-Clusters (High Performance Computing) und durch automatisierte Erkennung des entsprechenden Hauptfließregimes konnten die Bereiche im Parameterraum ermittelt werden, in denen die gesuchten störungszonenbedingten Fließeffekte vorhanden sind. Durch die Untersuchung von mehr als 30000 Kombinationen der Modellparameter Störungszonen-Permeabilität, Matrix-Permeabilität, Störungszonen-Speicherkoeffizient, Matrix-Speicherkoeffizient und Störungszonen-Mächtigkeit wurde gezeigt, dass im Parameterraum des UJA erstmals ein bilineares Fließen nur dann beobachtet werden kann, wenn die Matrix-Permeabilität kleiner als

$2,0 \times 10^{-13} \text{ m}^2$  ist, und ein lineares Fließen, wenn die Matrix-Permeabilitätswerte unter  $6,0 \times 10^{-14} \text{ m}^2$  liegen. Darüber hinaus wurde gezeigt, dass Störungszonen, die bessere hydraulische Eigenschaften als die umgebende Matrix aufweisen, bei der Auswertung von Pumpversuchen aufgrund bestimmter hydraulischer Parameterkombination tatsächlich unentdeckt bleiben können.

Mit diesem Wissen über die Übergänge der Fließregime im Parameterraum des UJA wurde eine weitere Untersuchung im Rahmen dieser Arbeit durchgeführt, indem das zuvor kalibrierte numerische Modell durch Anwendung der *reduced basis* Methode erweitert wurde. Dies ermöglichte eine Quantifizierung des Einflusses hydraulisch aktiver Störungszonen auf den Brunnenproduktivitätsindex (PI) in Abhängigkeit vom UJA-Parameterraum auf der Basis von mehr als sechs Millionen Simulationen. Darüber hinaus war es im Anschluss möglich, die Verteilung der Fließregime im Großraum München in Abhängigkeit von verschiedenen Störungszonentypen und deren Einfluss auf den PI räumlich zu untersuchen. Hierfür wurden zusätzlich ca. 81 Millionen numerische Simulationen durchgeführt, welche Karten der hydraulischen Eigenschaften des UJA als Modelinput benutzten. Die Analyse des Störungseinflusses auf die Brunnenproduktivität im Zuge dieser Untersuchungen legen nahe, dass hydraulisch verborgene Störungszonen den PI deutlich erhöhen können. Der Vergleich der numerisch erzeugten Fließregime-Karten mit den beobachteten Fließregimen der geothermischen Bohrungen im Großraum München zeigt außerdem, dass eine hydraulisch aktive Störungszonenmächtigkeit von  $\geq 100 \text{ m}$  für den UJA eher als unwahrscheinlich angesehen werden kann.

Abschließend wurde ein open-source Python-Tool ("uja\_faultzones" [github.com/Florian-Konrad/uja\\_faultzones](https://github.com/Florian-Konrad/uja_faultzones)) entwickelt, das die im Rahmen dieser Arbeit aufgebauten numerischen Modelle und die Methodik zur Beschreibung des Störungszoneneinflusses auf das Fließregime und die Brunnenproduktivität für einen beliebigen Störzontentyp effizient integriert. Die schnellen Berechnungszeiten von  $\sim 0,4 \text{ s}$  (auf einer gängigen Workstation) pro Simulation ermöglichen es Reservoiringenieuren mit geringem Aufwand eine Vielzahl von Pumpversuchen für verschiedene Störungszonentypen zu simulieren und den möglichen hydraulischen Einfluss dieser Störungszonen auf einen Geothermiebrunnen abzuleiten.

## **Publications**

Some text, figures and tables have appeared previously in the following publications:

**Hydraulic behavior of fault zones in pump tests of geothermal wells: a parametric analysis using numerical simulations for the Upper Jurassic aquifer of the North Alpine Foreland Basin**

Florian Konrad, Alexandros Savvatis, Florian Wellmann and Kai Zosseder

*Geothermal Energy* (2019) 7:25

DOI: <https://doi.org/10.1186/s40517-019-0137-4>

**Productivity enhancement of geothermal wells through fault zones: efficient numerical evaluation of a parameter space for the Upper Jurassic aquifer of the North Alpine Foreland Basin**

Florian Konrad, Alexandros Savvatis, Denise Degen, Florian Wellmann, Florian Einsiedl and Kai Zosseder

*Geothermics* (2021) 95(2):102119

DOI: <https://doi.org/10.1016/j.geothermics.2021.102119>

## **Acknowledgements**

First, I would like to thank my supervisors Dr. Kai Zosseder and Prof. Dr. Florian Einsiedl for their support in every step of this work and for giving me this research opportunity. It was a great privilege being able to explore my ideas and to receive constant support. I highly appreciate all the valuable discussions and the patience over the last years. Kai, I would like to express my highest gratitude for introducing me to the world of fault zones and hydraulics in the field of deep geothermal energy exploration.

I would also like to thank Dr. Antoine B. Jaquey, Dr. Mauro Cacace and Dr. Guido Blöcher for technical support with MOOSE Framework, GOLEM and MeshIt, the RAVEN developers team and user community group for their helpful support in the software adaptation and Dr. Martin Ohlerich and Dr. Jens Weismüller for their guidance in the usage of the LRZ linux cluster and Supermuc.

Furthermore, I want to express my gratitude to Dr. Denise Degen for her guidance with DwarfElephant and the fruitful discussions. Moreover, I would like to thank my mentor Prof. Ph.D. Florian Wellmann for taking over my mentorship and the very useful advice as well as the valuable methodical input.

Thanks go to Theis Winter, Anne Imig, Manuel Gossler, Daniel Bohnsack, Felix Schölderle, Daniela Pfrang, Joachim Loy, Fabian Böttcher, Alejandra Pena, Markus Theel, Marco Kerl, Alberto Albarrán-Ordas, Dr. Arno Rein and all other colleagues at the Chair of Hydrogeology. I thank you for all the fun we had, for your constructive advices and intense discussions. Last but not least, I would like to thank my family and friends for their support over the last years.

## Table of contents

Abstract .....	I
Zusammenfassung .....	III
Publications .....	V
Acknowledgements .....	VI
Table of contents .....	VII
List of figures .....	X
List of tables .....	XVI
List of abbreviations .....	XVII
1 Introduction to deep hydro-geothermal energy exploration in Southern Germany and the Upper Jurassic aquifer .....	1
2 State of the art .....	5
2.1 Hydraulic situation of the greater Munich area .....	5
2.2 Fault zones and their role as hydraulic elements .....	8
2.3 The scope of pressure transient analysis in geothermal wells .....	13
2.4 The productivity of wells in the Upper Jurassic aquifer .....	17
2.5 Hydraulic numerical modeling of the Upper Jurassic aquifer .....	19
3 Aims and objectives .....	22
4 Material and methods .....	24
4.1 Geological framework of the study area and hydrogeological concept .....	26
4.2 Hydraulic numerical simulation of a fault zone inside the Upper Jurassic aquifer ..	28
4.2.1 Spatial and temporal discretization .....	28
4.2.2 Finite element simulator – GOLEM .....	32
4.3 Hydraulic properties of the Upper Jurassic aquifer .....	33
4.4 Numerical model calibration using field data .....	34
4.5 Flow regime analysis of simulated pumping tests .....	34

4.6	Parameter space investigation - Identifying limiting surfaces between flow regimes	37
4.6.1	Flow regime focused sensitivity analysis.....	37
4.6.2	Parameter space exploration – flow regimes.....	39
4.6.3	Identification of flow regime transitions in parameter space.....	40
4.7	The productivity index of a well and its alteration by a fault zone.....	42
4.8	Application of the reduced basis method to the finite element model.....	44
4.9	Fault zone induced productivity index change.....	48
4.9.1	Well productivity focused global sensitivity analysis.....	48
4.9.2	Parameter space exploration – productivity index.....	49
4.10	Spatial investigation of fault zone induced productivity index change and flow regime occurrences in the greater Munich area.....	49
4.11	Open source Python tool “uja faultzones”.....	51
5	Results.....	52
5.1	Model calibration results.....	52
5.2	Influence of hydraulic reservoir properties on the well flow regime.....	53
5.3	Identification of flow regime transitions in the parameter space.....	55
5.4	Characteristics of the flow regime distribution.....	58
5.5	Influence of hydraulic reservoir properties on the productivity index.....	60
5.6	Fault zone induced productivity index change.....	60
5.7	Spatial distribution of flow regimes and productivity index alteration associated with fault zones in the greater Munich area.....	65
5.8	Consequences for the geothermal exploration in the Upper Jurassic aquifer.....	68
6	Discussion of possible limitations of the numerical experiments.....	70
6.1	Model design.....	70
6.2	Uncertainties of the flow regime transitions.....	72
6.3	Numerical precision of the reduced basis method and consequences for the PI evaluation.....	73

6.4	Resolution of spatial information in the greater Munich area.....	73
7	Conclusions for the geothermal exploration of the Upper Jurassic aquifer and possible outlook.....	74
8	References.....	77
9	Appendix.....	89
9.1	Regression Predictors $\mathbf{x}_i$ , Dependent Variable $\mathbf{y}$ .....	89
9.2	Regression Scaling .....	89
9.3	Regression Functions .....	90
9.4	Temperature and depth of aquifer top in the investigation area.....	91
9.5	Evolution of rel. Fault zone PI influence – representative parameter space slices ..	92
9.6	Statistics of the fault zones relative PI change in dependency of fault zone thickness and matrix permeability .....	116
9.7	Statistics of the fault zones relative PI change for hydraulically hidden fault zones in dependency of fault zone thickness and matrix permeability .....	119
9.8	Statistics of the flow type distribution in dependency of fault zone thickness and matrix permeability .....	121
9.9	Spatial flow regime distributions for different fault zone types and specific matrix storage .....	123
9.10	Spatial relative PI improvement for different fault zone types and specific matrix storage .....	133

## List of figures

Fig. 1 Overview of the South German Molasse basin and its vertical structure together with a cross section illustrating the depth increase of the Upper Jurassic aquifer (Malm) from N to S (Fritzer, Settles, & Dorsch, 2012). Black location markers represent deep geothermal projects. ....	1
Fig. 2 Isolines showing the depth of top of the Upper Jurassic rocks based on the “UmweltAtlas Bayern” © Bayerisches Landesamt für Umwelt (Otto, 2021). ....	2
Fig. 3 Overview of the depositional environment of the Upper Jurassic during the Kimmeridgian (Mraz, 2019). Yellow isolines represent the large-scale spatial distribution of the hydraulic conductivity of the Upper Jurassic aquifer (Birner et al., 2012). ....	3
Fig. 4 Temperature isolines of the top of the Upper Jurassic rocks according to GeotIS (Agemar et al., 2014). ....	4
Fig. 5 Geothermals wells of the greater Munich area with their corresponding flow regime information and spatial distribution of fault zones based on five different data sets (data sources: Holzkirchen provided by Geothermie Holzkirchen GmbH; Sauerlach: Geothermal Alliance Bavaria (TUM, 2019); Geretsried provided by ENEX POWER GERMANY GmbH; GRAME after Bruss et al. (2018); UmweltAtlas: © Bayerisches Landesamt für Umwelt, <a href="http://www.lfu.bayern.de">www.lfu.bayern.de</a> ). ....	7
Fig. 6 Evolution of structural elements in carbonate rock-hosted normal fault zones after Micarelli et al. (2006) (IDDZ = Intensely deformed damage zone; WDDZ = weakly deformed damage zone). ....	8
Fig. 7 Exemplary observations of normal fault zones in carbonate rocks with different displacement and mechanically relevant rock facies ratios by Michie et al. (2014) (FSZ = fracture splay zone). ....	9

Fig. 8 Fault zone architecture models in dependency of different numbers of stratigraphic layers and ratios of thickness of weak:strong layers by Michie et al. (2014) (FSZ = fracture splay zone). ..... 10

Fig. 9 Concept for the hydraulic effect of fault zones according to Caine et al. (1996). ..... 12

Fig. 10 Overview of the fundamental analytical models used in PTA (IHS Markit, 2017), red thin line =  $\Delta p$  = pressure change (e.g. measured in a pumping test), thick colored lines = Bourdet Derivative/DER calculated from  $\Delta p$  according to equation (1), t = time..... 14

Fig. 11 Concept of the flow field geometry around a well inside a fault zone depending on the contrast in hydraulic properties between the fault zone and the surrounding reservoir-matrix (Bourdet, 2002). ..... 15

Fig. 12 Evaluation of the pressure buildup of a drill stem test at the Weilheim geothermal project. Green dots: measured pressure; Red dots: Bourdet Derivative (DER) calculated from measured pressure; red and black line: model fit for pressure and DER. A negative skin, reservoir transmissivity, well storage and a no flow boundary were interpreted..... 16

Fig. 13 Pressure data of two different geothermal wells of the UJA, red boxes indicate the fault zone associated flow (Savvatis, 2012). Left: bilinear flow. Right: linear flow. Black dots: measured pressure; Grey dots: Bourdet Derivative (DER) calculated from measured pressure. .... 17

Fig. 14 Inflow performance relationships of 13 geothermal wells in the central part of the Southern German Molasse Basin. Curves of the same color are wells of the same geothermal project. The curve labels represent the facies and fault zone throw: Facies: M = mass facies, B = basin facies ,  $\ddot{U}$  = transition facies / Fault zone throw: 1 = 0 m, 2 = smaller than 50 m, 3 = approx. 50 m, 4 = smaller than 100 m, 5 = approx. 100 m, 6 = above 100 m. (Steiner et al., 2012)..... 18

Fig. 15 Spatial discretization examples of fault zones inside the UJA using common software packages (FeFlow and Petrel) requiring geometric simplifications (Thuro et al., 2019; Wenderoth et al., 2005). .....	20
Fig. 16 Spatial discretization of the Mauerstetten geothermal project in the western central Molasse basin using an unstructured tetrahedral mesh representing seismic information without simplification (Cacace et al., 2013). .....	21
Fig. 17 Workflow 1: Fault zone associated flow regime investigation. ....	24
Fig. 18 Workflow 2: Fault zone induced well productivity change investigation. ....	25
Fig. 19 Schematic profile of the facies types and hydrostratigraphic groups of the Upper Jurassic rocks in the greater Munich area (Böhm et al., 2013). ....	27
Fig. 20 Hydrogeological model (right) and unstructured tetrahedral mesh (left, background) of the numerical simulation. ....	29
Fig. 21 Influence of temporal discretization on the simulation result of an example parameter combination exhibiting linear flow; initial timestep = 1 second; a high growth factor corresponds to less timesteps over the simulation timespan; unprecise numerical solutions can be observed by shortened and deviated dP and DER curves compared to simulation output with a higher number of timesteps. ....	31
Fig. 22 Example flow field of the numerical model with linear flow behavior, streamlines colorized after the flow velocity (v), induced pressure change as blue transparent isosurface. ....	32
Fig. 23 Flow regimes connected to fault zones; Left: pressure change (dP) of idealized pumping test, associated Bourdet Derivative and concept of flow field, see also Tab. 2 for a summary; Right: representative example during presence of each flow regime in the complex geometry of the 3D numerical model, numerically calculated pressure change isolines around the fault zone. ....	36

Fig. 24 Decision tree for the classification of DER curve based on the detection of a flow type in any of the cruvs data points.....37

Fig. 25 Visualization of the quantification basis of the DER shape change described in equation (8); y-axis = DER' = slope of the DER on the log-log-plot; x-axis = time..... 38

Fig. 26 Determination of optimal degree for polynomial regression; R<sup>2</sup> adjusted versus polynomial degree. .... 41

Fig. 27 Comparison between FE (GOLEM) and RB (DwarfElephant) model for four different parameter settings showcasing the different main flow regimes of interest. Each flow regime is represented by two pairs of curves, one pair (pressure change (dp) as solid line, Bourdet derivative (DER) as dotted line) for each of the two models in a log-log scale. The characteristic slopes of the main flow regime are indicated (see also Chapter 4.5). .... 47

Fig. 28 Regionalized matrix permeability and fluid viscosity of the greater Munich area based on the marked data points..... 50

Fig. 29 Calibration results; left: log-log plot of recovery phase; right: pressure and rate history of complete pumping test. .... 53

Fig. 30 Sensitivity plot;  $SC_{xi, min} - xi, s, Fj$  (see equation (5)) versus variable value change relative to individual parameter range..... 54

Fig. 31 Regression results for characteristic parameter combinations for the three observed flow regime transitions (1: radial to bilinear, 2: bilinear to linear, 3: linear to negative boundary); left: 50-meter fault zone thickness; right: 150-meter fault zone thickness; subplots have fixed specific matrix storage values; the specific fault zone storage is color coded; line styles represent the flow regime transitions; parameter combinations that fall on the transition line should be seen as combinations for which the flow regime above has still been observed. .... 57

Fig. 32 Flow regime distribution of three different fault zone thicknesses based on their associated parameter samples grouped into matrix permeability categories (see Chapter 4.9.2 for details regarding the sampling approach). ..... 59

Fig. 33 Global sensitivity analysis for the governing hydraulic model parameters: Delta index vs. random sample size. .... 60

Fig. 34 Relative fault zone *PI* increase ( $\Delta PI_{rel}$ ) grouped by matrix permeability categories for all tested fault zone thickness values. .... 61

Fig. 35 Relative fault zone *PI* increase ( $\Delta PI_{rel}$ ) grouped by matrix permeability categories only for samples with fault zone thickness values < 100 m and filtered for only radial flow regimes. .... 63

Fig. 36 Comparison between the “low” (represented by the 20-meter fault zone thickness case, left) and “high thickness group” (represented by the 100-meter fault zone thickness case, right) at a representative point in parameter space (fluid viscosity = 0.0001 Pa·s, spec. matrix storage =  $1 \times 10^{-10}$  1/Pa, spec. fault zone storage =  $1.6 \times 10^{-10}$  1/Pa) illustrating relative fault zone *PI* increase ( $\Delta PI_{rel}$ ) vs. matrix permeability for all sampled fault zone permeability values. .... 64

Fig. 37 Spatial flow regime distribution comparison illustrating the parameter influence of the hydraulically active fault zone thickness. Colored map areas represent the numerically derived flow regime for the globally applied fault zone type of each map (fault zone properties noted above each map). Data points are additionally shown and colored in the same way according to their actual flow regime field observation: blue = radial flow, yellow = bilinear flow, orange = linear flow, red = neg. boundary flow, grey = unspecified flow. .... 66

Fig. 38 Spatial flow regime distribution (left) and relative fault zone *PI* increase ( $\Delta PI_{rel}$ , right) for a 50-meter fault zone with  $1 \times 10^{-11}$  m<sup>2</sup> permeability and  $6.24 \times 10^{-12}$  1/Pa specific storage at  $3.55 \times 10^{-11}$  1/Pa specific matrix storage showcasing the best fit between calculated and observed (colorized data points) well flow regimes. .... 67

Fig. 39 Visualization of the reference matrix  $PI$  (at the reference time of 342h) vs. matrix permeability combining the influence of the ranges of fluid viscosity and specific matrix storage through a box-plot; transparent red bar marks minimal reservoir  $PI$  necessary for an economically successful well. .... 68

Fig. 40 Minimal fault zone permeability versus matrix permeability for different  $\Delta PI_{rel}$  thresholds and filtered only for hydraulically hidden fault zones below 100 meters thickness, thereby representing extreme values for the low thickness group. .... 69

## List of tables

Tab. 1 Possible ranges for the hydraulic parameters of the UJA; Unit conversions calculated for a fluid density of 971.82 kg/m <sup>3</sup> and a fluid viscosity of $2.89 \times 10^{-4}$ Pa*s (30 MPa pore pressure and 100°C reservoir temperature). .....	33
Tab. 2 Characteristic properties of the flow regimes of interest; analytical model versus classification for real world parameter space. ....	35
Tab. 3 Specification of the grid sampling for the flow regime focused investigation. ....	40
Tab. 4 Updated parameter ranges of the UJA and its fault zones, based on Tab. 1. ....	46
Tab. 5 Median values of $SC_{xi, min} - xi, s, Fj$ for the evenly/log-evenly spaced parameters. ....	55
Tab. 6 Median values of $SC_{xi, min} - xi, s, Fj$ for the unevenly spaced fault zone thickness. ....	55
Tab. 7 Matrix permeability values are shown below which the flow regime noted to its right is possible. The table has been derived from the corresponding regression functions for minimum and maximum values of specific fault and matrix storage and for a fault permeability of $1 \times 10^{-9}$ m <sup>2</sup> . ....	58
Tab. 8 Parameter ranges of the UJA and of its fault zones updated with results of this work. ....	74

## List of abbreviations

$b$	laminar flow coefficient [–]
$c$	turbulence coefficient [–]
$dp$	pressure change [MPa]
$dp_m$	pressure change matrix model [MPa]
$dp_{m,t_{last\ radial}}$	pressure change of point with latest radial flow behavior [MPa]
$dp_{m,t_{ref}}$	pressure change matrix model at reference time [MPa]
$dp_{fz}$	pressure change fault zone model [MPa]
$\Delta dp$	fault zone influence – pressure change difference [MPa]
$\Delta dp'$	slope of $\Delta dp$ [–]
DER	Bourdet Derivative [–]
$DER_{last\ radial}$	Bourdet Derivative value at latest radial flow pressure point [–]
$DER'$	slope of the Bourdet Derivative on the log-log-plot
$DER'_{x_{i,min},F_j}$	first derivative of DER curve for the hydraulic parameter combination ( $x_{i,min}$ and $F_j$ ) [–]
FE	finite element
FZ	fault zone
fz-k	fault zone permeability [ $m^2$ ]
fz-th	fault zone thickness [ $m$ ]
$F_j$	j-th fixation of the not investigated parameters of the sensitivity analysis
$g$	gravity vector [ $m/s^2$ ]
$h_{fault}$	fault zone thickness [ $m$ ]
HPC	high performance computing
LHS	latin hypercube sampling
MOR	model order reduction
$k$	permeability tensor [ $m^2$ ]
$K_f$	fluid bulk modulus [Pa]

$K_{fault/matrix}$	fault zone/matrix permeability [ $m^2$ ]
$n$	porosity [–]
PI	well productivity index [ $l/(s * MPa)$ ]
$PI_m$	PI matrix model [ $l/(s * MPa)$ ]
$PI_{m,ref}$	PI matrix model at reference time [ $l/(s * MPa)$ ]
$PI_{fz}$	PI fault zone model [ $l/(s * MPa)$ ]
$\Delta PI$	absolute PI Change [ $l/(s * MPa)$ ]
$\Delta PI_{rel}$	fault zone induced relative PI Change [–]
PTA	pressure transient analysis
$p_f$	pore pressure [ $Pa$ ]
$\rho_f$	fluid density [ $kg/m^3$ ]
$p_i$	average bottomhole pressure [ $MPa$ ]
$p_{wf}$	bottomhole flowing pressure [ $MPa$ ]
$q$	production rate [ $l/s$ ]
$q_d$	Darcy's velocity [ $m/s$ ]
$Q_f$	sink/source [ $l/s$ ]
RB	reduced basis method
$R^2_{adjusted}$	adjusted coefficient of determination [–]
SA	sensitivity analysis
SC	shape change measure between two DER curves [–]
$S_{s,fault/matrix}$	specific fault zone/matrix storage [ $1/Pa$ ]
$S_{sp}$	specific storage [ $1/Pa$ ]
s-fz-s	specific fault zone storage [ $1/Pa$ ]
s-m-s	specific matrix storage [ $1/Pa$ ]
$\sigma_i$	standard deviation of $X_i$
$t$	time [ $s$ ]

$t_k$	k-th time point of DER curve [s]
$t_{last\ radial}$	time of the latest radial flow pressure point [s ]
$t_{ref}$	reference time, 342 [h]
$\mu_f$	fluid viscosity [Pa * s]
UJA	Upper Jurassic aquifer
$v_f$	fluid velocity [ $m/s$ ]
$x_i$	hydraulic model property, regression predictor
$x_{i,s}$	s-th sampled value of $x_i$
$x_{i,min}$	minimum sampled value of $x_i$
$X_i$	regression training data set of i-th regression predictor ( $x_i$ )
$\bar{X}_i$	mean of $X_i$
$X_{i,j}$	j-th value of $X_i$
$y$	regression target variable
$Y$	regression training data set of target variable ( $y$ )

# 1 Introduction to deep hydro-geothermal energy exploration in Southern Germany and the Upper Jurassic aquifer

Our planet stores an enormous amount of thermal energy. With  $1.5 \times 10^{12}$  TWh (Armstead, 1978), the Earth's crust alone contains more energy than many generations of the entire world population could consume (total world energy consumption in 2019: 173,340 TWh) (Ritchie, 2021). Because this highly available and weather-independent resource is heterogeneously distributed, it is necessary to find a geological target located in an area with abundant thermal energy and suitable physical properties for an efficient extraction (Bauer, Freeden, Jacobi, & Neu, 2014; Quaschnig, 2010; Stober & Bucher, 2013).

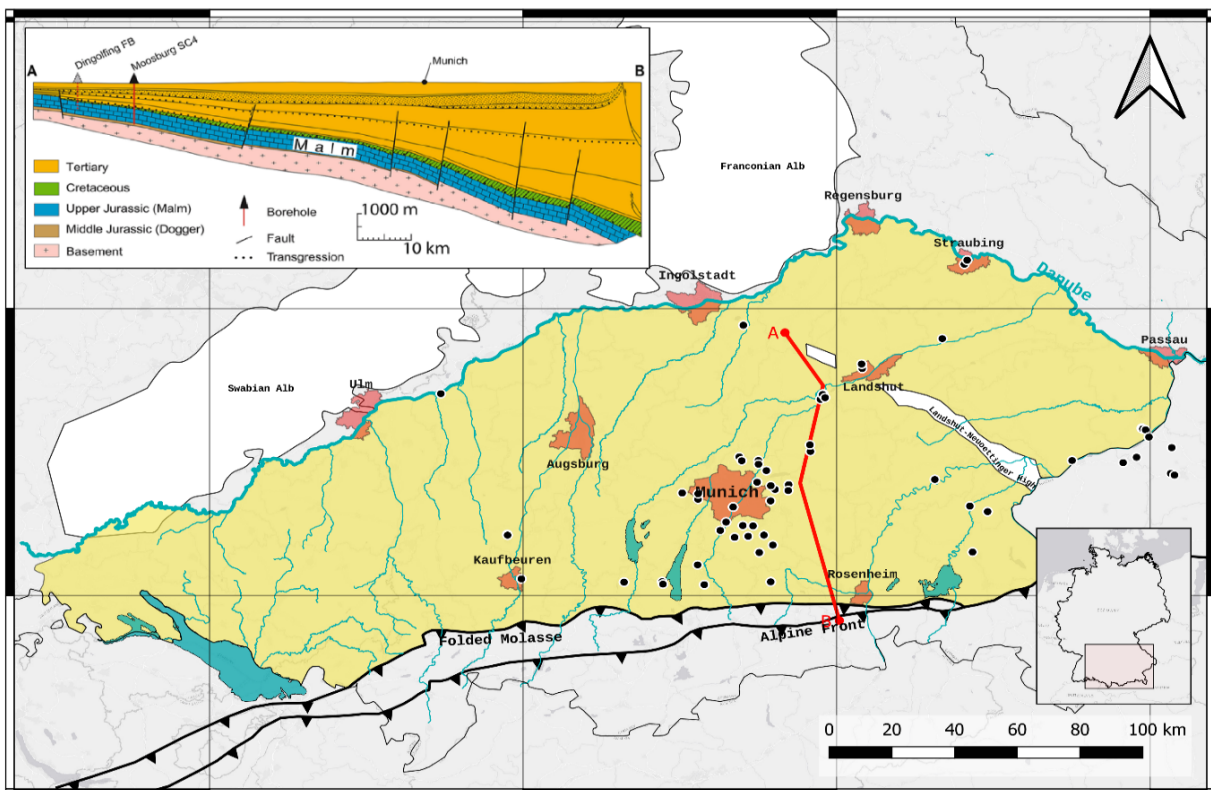


*Fig. 1 Overview of the South German Molasse basin and its vertical structure together with a cross section illustrating the depth increase of the Upper Jurassic aquifer (Malm) from N to S (Fritzer, Settles, & Dorsch, 2012). Black location markers represent deep geothermal projects.*

For a deep hydro-geothermal project, this essentially means tapping into an aquifer that has a sufficient combination of temperature and water volume that can be accessed through adequate hydraulic conductivity (Goldstein et al., 2013). In this context, different aquifer types present varying challenges. Deep carbonate reservoirs in mid-enthalpy sedimentary basins, in particular, are governed by intricate geological heterogeneities. Their complex sedimentary,

diagenetic and tectonic history makes predicting the aquifer’s hydraulic properties and its productivity at a possible drilling site difficult (Schneider & Thomas, 2012).

One of the most important aquifers for deep hydro-geothermal energy exploration in Europe is located in southern Germany in the North Alpine Foreland Basin (South German Molasse basin, see Fig. 1). Carbonatic rocks of the Upper Jurassic form a mid-enthalpy karstified and fractured porous reservoir. These rocks can be up to 600 meters thick and mainly consist of small-pored white limestones as well as fine- to coarse-grained dolomites (Agemar et al., 2014; Mraz, 2019; Wolfgramm et al., 2007). They exhibit a complex multi-phased diagenetic evolution depending on their sedimentary depositing facies (see Fig. 3 and refer to Chapter 4.1) and experienced a karstification in several phases that reaches up to 300 meters below their top (Frisch & Huber, 2000; Lemcke, 1988).

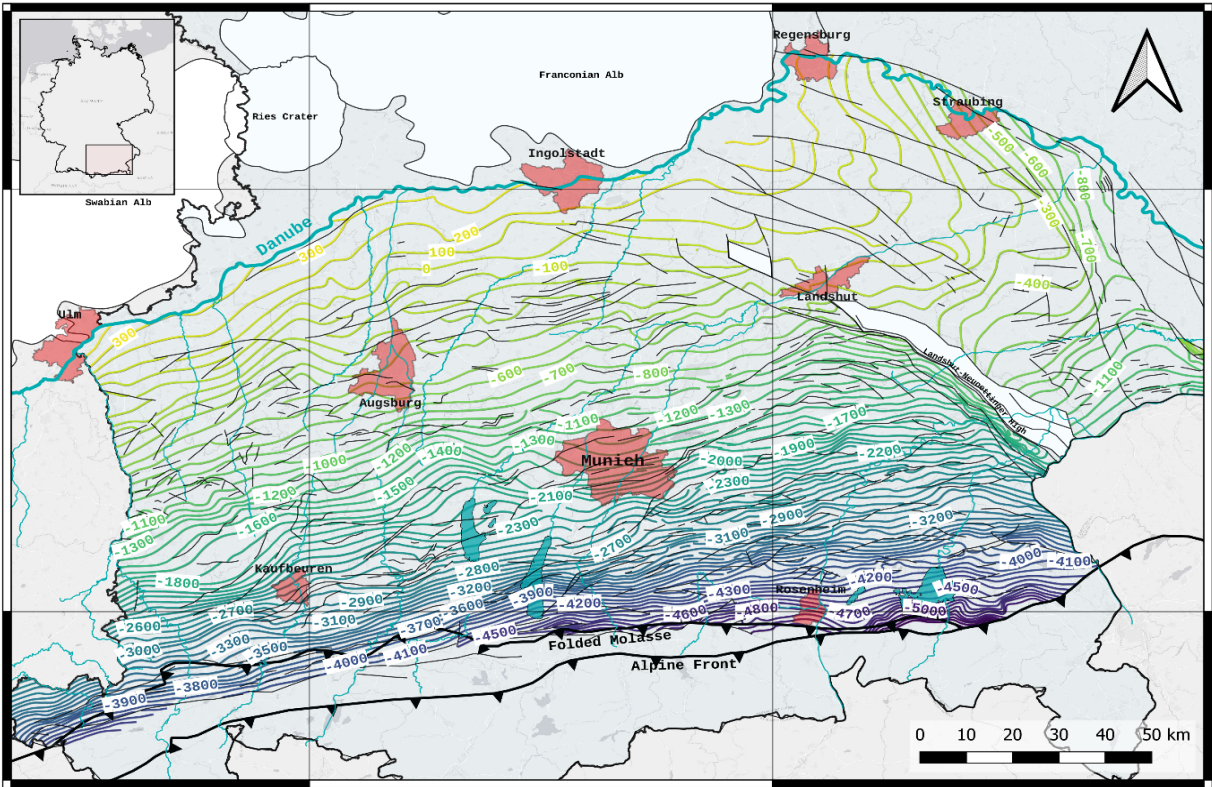


Fig. 2 Isolines showing the depth of top of the Upper Jurassic rocks based on the “UmweltAtlas Bayern” © Bayerisches Landesamt für Umwelt (Otto, 2021).

The reservoir rocks compose the ground surface at the northern border of the foreland basin (Franconian and Swabian Alb) and are inclined to the south due to lithospheric bending caused by the Alpine orogenesis (see Fig. 2). It is this flexural bending that caused the development of normal faults parallel to the Alps throughout the entire foreland basin also crossing the Upper Jurassic aquifer (UJA, also called Malm aquifer) creating important potential water pathways (Cacace et al., 2013; Fritzer et al., 2012). Close to the Alpine range, this reservoir can again be

found only at a depth of 5000 meters or more (Böhm, Savvatis, Steiner, Schneider, & Koch, 2013). Fig. 1 illustrates the location of the South German Molasse basin as well as the overall geometry of the Upper Jurassic aquifer through a cross section.

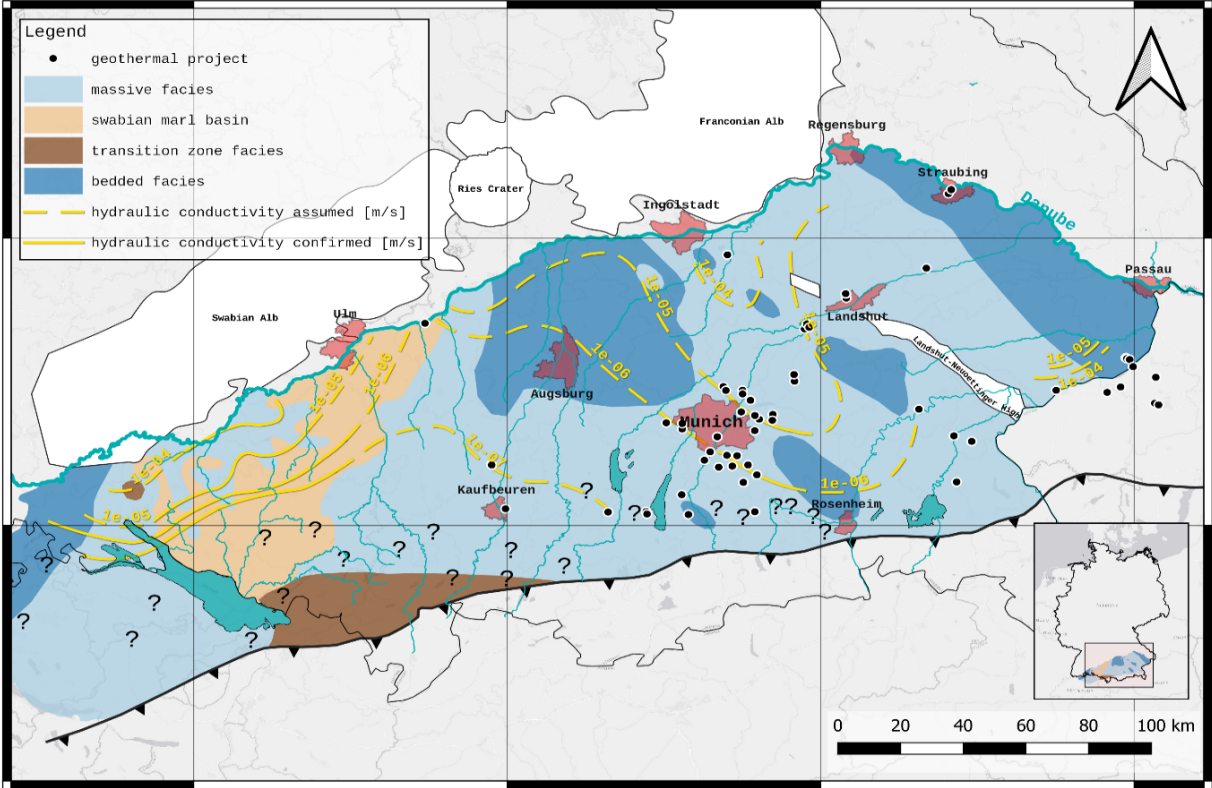


Fig. 3 Overview of the depositional environment of the Upper Jurassic during the Kimmeridgian (Mraz, 2019). Yellow isolines represent the large-scale spatial distribution of the hydraulic conductivity of the Upper Jurassic aquifer (Birner et al., 2012).

The task to economically extract the energy stored in the UJA is generally done by drilling a set of at least two wells (one injection and one extraction well, also called a well doublet) and can be broken down into two main factors, as briefly mentioned in the beginning of this chapter. First, enough thermal energy in the form of high reservoir temperatures must be present. The UJA’s inclination (see Fig. 2) and consequently a high depth in the middle and southern regions of the north Alpine foreland basin ensure such a sufficient temperature level. Already practically utilized temperatures range from around 40°C to more than 100°C (see Fig. 4) (Fritzer et al., 2012). However, the second factor - namely the aquifer’s productivity -, introduces significant uncertainty as it is controlled by the hydraulic reservoir properties, primarily by the reservoir permeability (Bauer et al., 2014), which vary strongly throughout the aquifer and are governed by the mentioned rock-evolutional factors. The consequence of this variation can be observed indirectly through the different production rates found at geothermal sites currently in operation (Agemar et al., 2014).

The measurement of the reservoir permeability in just one location alone is not easy to perform and is influenced by the selected method as shown in the southwestern area of the Molasse basin by Stober et al. (2013). Nevertheless, the most relevant and reliable way to spatially quantify the permeability distribution on the reservoir’s scale is based on the deployment and evaluation of pumping tests of geothermal wells (well tests) (Savvatis, 2012). These tests are mandatory after a well completion and they rely on the transient pressure response of the aquifer caused by the temporary change of the production rate to derive reservoir- and well-properties (Bauer et al., 2014; Bourdet, 2002) (the test design and evaluation methodology will be further explained in Chapter 2.3). Birner et al. (2012) collected such well test data from 98 wells in the Molasse basin and illustrated the complexity of the reservoir by describing the hydraulic conductivity distribution on a regional scale which is visualized in Fig. 3. However, sufficient knowledge and actual measured data must be gathered in a higher resolution in order to ensure a successful hydro-geothermal exploration.

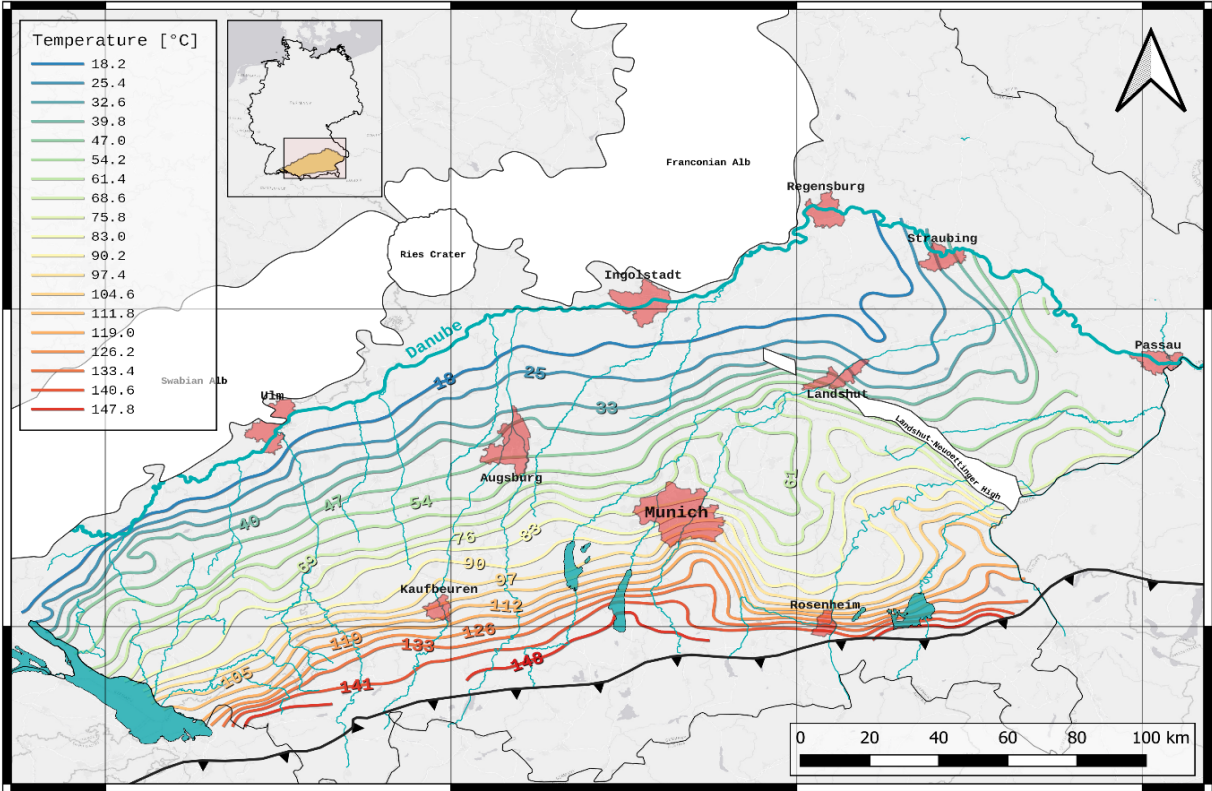


Fig. 4 Temperature isolines of the top of the Upper Jurassic rocks according to GeotIS (Agemar et al., 2014).

In summary, for the introductory presentation of the UJA in Southern Germany, a range of beneficial location factors make this thermal water reservoir an important resource for deep geothermal energy exploration. Carbonatic fractured porous rocks provide the basis for the potential extraction of high thermal water rates. Potentially high permeable fault zones and

karstification form regions of high interest to the exploration. Furthermore, the inclination of the Upper Jurassic rock layer and consequently the possibility for high temperatures allow for the opportunity to economically use weather independent geothermal energy in this area (Agemar et al., 2014; Birner, 2013).

## **2 State of the art**

The following five chapters cover the base topics and their current state of the art needed to understand and derive the research questions of this work. At first, the current state of the UJA in the Munich area is presented. This region represents a hotspot for geothermal exploration of the reservoir and provides hydraulic key observations. An important part in these observations form fault zones. Therefore, their structural properties and possible hydraulic influence are presented next. This is followed by the explanation of pressure transient analysis of well tests which is the primary tool to measure hydraulic reservoir properties around a well. Furthermore, a measure to quantify the productivity of a geothermal well is illustrated in the context of the greater Munich area. Finally, the importance and utilization of hydraulic numerical models for geothermal exploration are discussed.

### **2.1 Hydraulic situation of the greater Munich area**

The greater Munich area represents a special part of the South German Molasse Basin. High energy demand, driven by the growing capital city of Bavaria and its suburbs, and a favorable aquifer setting coincide. In the city's area, the reservoir's top is located at a depth between -1100 and -2200 meters above sea level according to the regional data set of the "UmweltAtlas Bayern" shown in Fig. 2 (Otto, 2021). The complementary approximate temperature range based on the GeotIS data set presented in Fig. 4 is between 70 and 110 °C (Agemar et al., 2014). The overall hydraulic reservoir conductivity ranges between  $10^{-5}$  and  $10^{-6}$  m/s (this corresponds to a permeability between  $3.345 \times 10^{-13}$  and  $3.345 \times 10^{-14}$  at a fluid density of  $974.18 \text{ kg/m}^3$  and a fluid viscosity of  $3.1975 \times 10^{-4} \text{ Pa}\cdot\text{s}$ ) according to Birner (2013). Consequently, the majority of the geothermal plants that tap into the Upper Jurassic aquifer can be found here (see Fig. 1). Hydrothermal doublets with an installed thermal output of more than 235 MWt and 26 MWe installed electric output access the energy stored in the subsurface (Agemar et al., 2014). Currently, 47 completed wells are located here (three of them are unsuccessful as of December 2021). The large scale maps presented in the introduction show only the rough overall conditions in the UJA. Recent data in higher resolution indicate that the detailed situation is far more heterogeneous (see Chapter 4.10 and Fig. 28 and Appendix 9.4).

Also important for the description of the hydraulic situation of the entire UJA, and especially around Munich, is the question regarding groundwater recharge and groundwater flow direction. This topic is still highly debated and contains several open research questions. Different works derive a different flow direction in parts of the large scale flow field of the UJA. At the northern border of the Molasse basin, groundwater recharge is considered to come from the North, the Swabian and Franconian Alb, where the groundwater flow follows the Danube in eastern direction (Birner et al., 2011; Frisch & Huber, 2000; Lemcke, 1976). In the central parts of the basin a groundwater flow mainly coming from the west with a minor component also flowing from the southeast towards Munich was postulated by Frisch & Huber (2000). However, Birner et al. (2011) conclude that there is a different flow path in that area: the overall flow towards Munich comes only from the northwest and continues in southeastern direction towards Lake Chiemsee. Overall, it can be observed that the thermal water in this central basin part exhibits an untypical low salinity. The current assumption is that this water consists of a mix of meteoric fresh water with crude oil associated water and with saliniferous water coming from the tertiary rock formations above the UJA (Balderer, 1990; Birner et al., 2011; Lemcke, 1976; Mayrhofer, 2013; Stober & Bucher, 2014). But different ideas exist for the actual infiltration and recharge area. Lake Constance in the western basin part (Heidinger et al., 2019) and the Northern Limestone Alps (Udluft, 1975) region are being considered. The recent works of Heine et al. (2021), Heine & Einsiedl (2021) and Winter & Einsiedl (2021) used novel methods (such as environmental isotopes for groundwater dating) to improve the understanding of the local and regional flow regime of the Molasse basin. They suggested in contrast to the mentioned earlier studies a groundwater recharge area in the southern part of the Molasse. Furthermore, by using isotope based ground water dating with the help of  $^{14}\text{C}$ -DOC and  $^{81}\text{Kr}$  the authors found that the thermal water of the UJA is composed of at least two water components with significant different apparent water ages. This ongoing investigation illustrates the complexity of the reservoir and its flow paths as well as the need for additional data gathering and extended research.

Another important factor to understand how the hydraulic situation around a well might look like is the impact of fault zones. Fault zones are hydraulically relevant but also complex structures that are often targets of geothermal exploration concepts in the UJA as they form regions of possibly favorable hydraulic properties. Fig. 5 illustrates the spatial distribution of fault zones in the greater Munich area. Different data sets with varying extents and resolution are shown. The “UmweltAtlas” data (publicly available for the Bavarian part of the UJA) is of

low resolution but it demonstrates nonetheless that large fault zones are present in the entire reservoir.

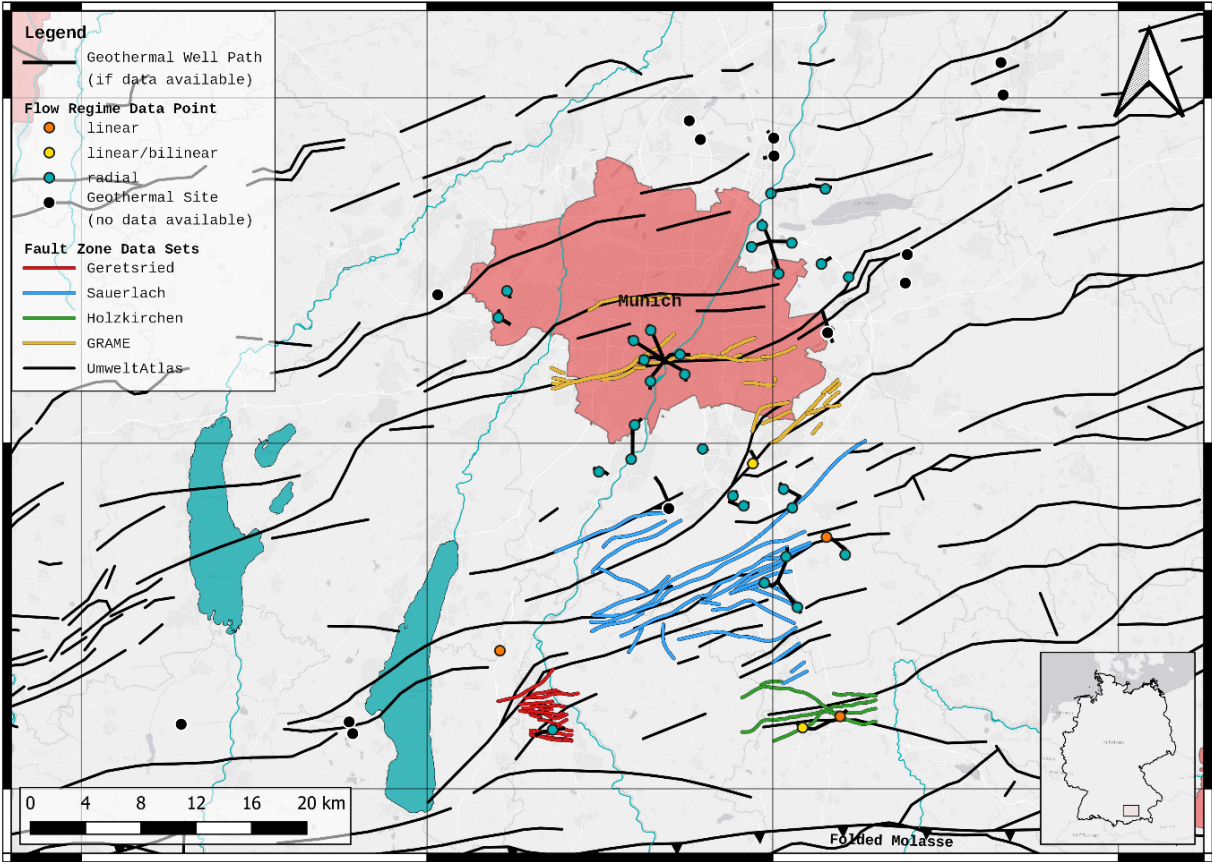


Fig. 5 Geothermals wells of the greater Munich area with their corresponding flow regime information and spatial distribution of fault zones based on five different data sets (data sources: Holzkirchen provided by Geothermie Holzkirchen GmbH; Sauerlach: Geothermal Alliance Bavaria (TUM, 2019); Geretsried provided by ENEX POWER GERMANY GmbH; GRAME after Bruss et al. (2018); UmweltAtlas: © Bayerisches Landesamt für Umwelt, www.lfu.bayern.de).

The additionally visualized fault zone records with higher resolution but smaller extent provide evidence that the reservoir is even more intensely faulted. In combination with the well paths shown, it becomes apparent that most of the geothermal wells directly develop fault zones. By investigating the geometry of the flow field around a well, it is possible to prove the hydraulic influence of a developed fault zone. The flow field geometry is analyzed based on pressure data from well tests. The basic idea in simple terms is, that if the pressure drawdown in the early period of such a well test occurs in an anisotropic oval shape (bilinear or linear flow, isotropic case = radial flow field, see concept in Fig. 11 and the detailed explanation in Chapter 2.3), the hydraulic impact of a fault zone can be verified. However, this type of analysis - as shown by the colored points in Fig. 5 - provides evidence for the fault zone’s presence only in a few cases. Most geothermal wells exhibit a radial flow regime suggesting a homogeneous reservoir.

## 2.2 Fault zones and their role as hydraulic elements

In order to understand how fault zones introduce anisotropy to a reservoir, it is important to assess their internal structure and derive how this structure alters the hydraulic properties of the aquifer's host rock and affects fluid flow. Fault zones are generally visible in seismic surveys and are very important for the geothermal exploration strategy as well as recommended exploration targets in the UJA (Böhm, Savvatis, & Steiner, 2012b; Shipilin, C. Tanner, Von Hartmann, & Moeck, 2020).

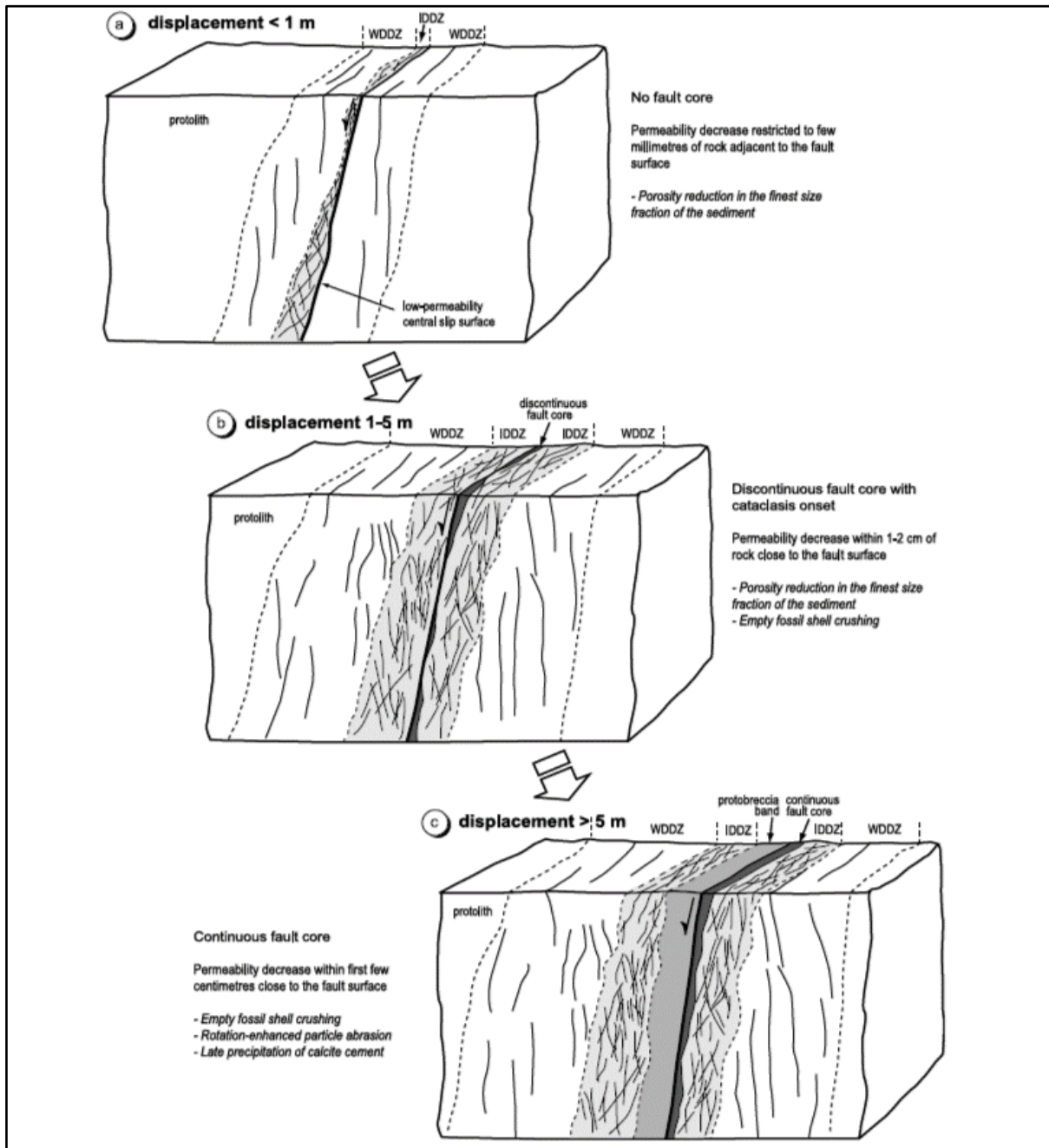


Fig. 6 Evolution of structural elements in carbonate rock-hosted normal fault zones after Micarelli et al. (2006) (IDDZ = Intensely deformed damage zone; WDDZ = weakly deformed damage zone).

A fault zone is generally defined as lithologically heterogeneous and structurally anisotropic discontinuity in the upper crust in which two blocks of rock moved relative to each other (Caine, Evans, & Forster, 1996; Grotzinger & Jordan, 2017; Peacock, Nixon, Rotevatn, Sanderson, & Zuluaga, 2016). Its general structure consists of a fault core surrounded by a damage zone that exponentially fades into the host rock, the protolith (Michie et al., 2014) (see Fig. 6). The displacement of the two involved protolith blocks is mainly located in the fault core forming a relatively narrow area of intensely deformed rocks, such as breccias, cataclasites and gouges (Choi, Edwards, Ko, & Kim, 2016). The term damage zone describes a region of less intense deformation enclosing the fault core. Here, second-order structures such as subsidiary faulting, fractures and tension gashes can be found (Billi, Salvini, & Storti, 2003; Faulkner et al., 2010).

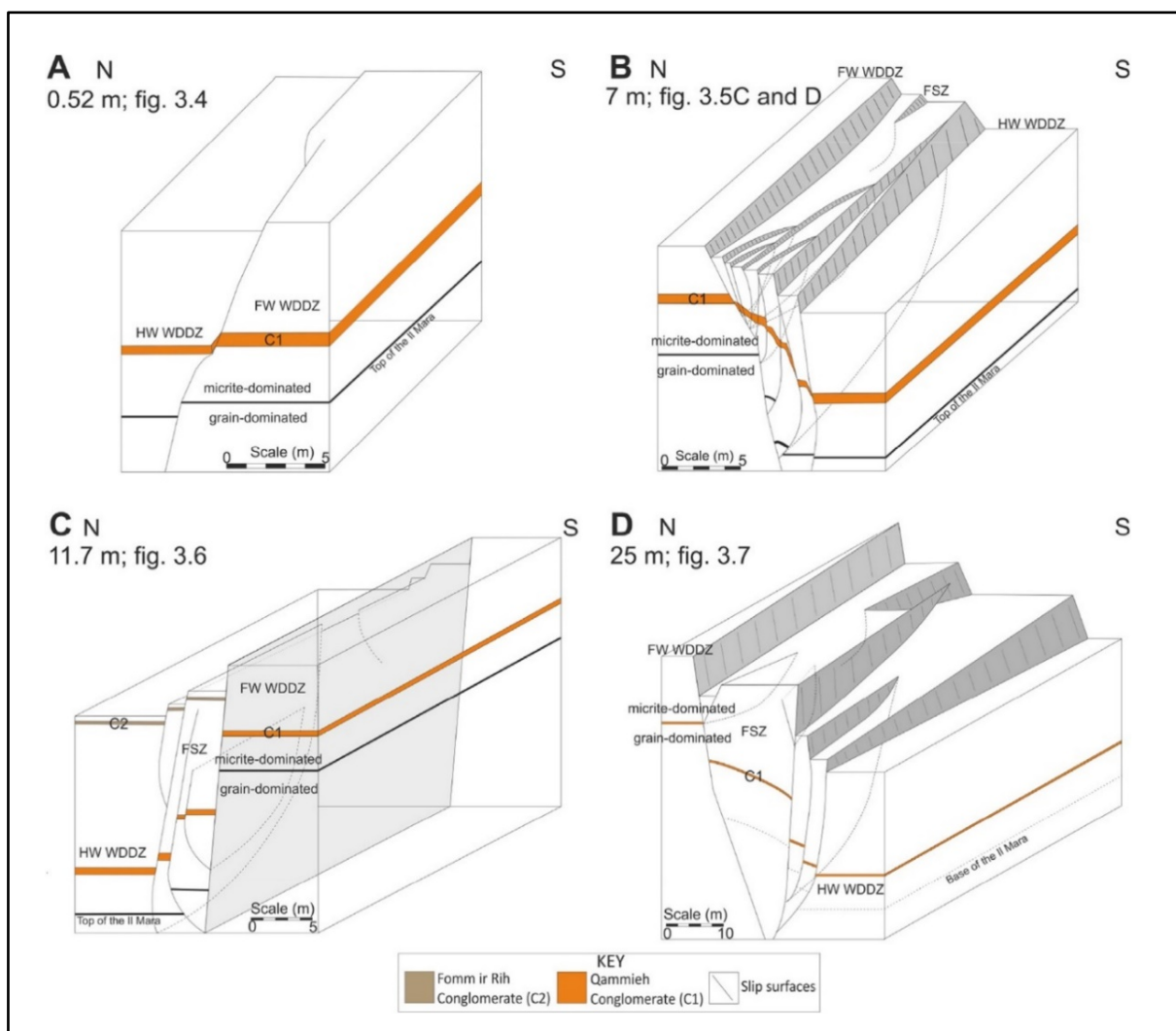


Fig. 7 Exemplary observations of normal fault zones in carbonate rocks with different displacement and mechanically relevant rock facies ratios by Michie et al. (2014) (FSZ = fracture splay zone).

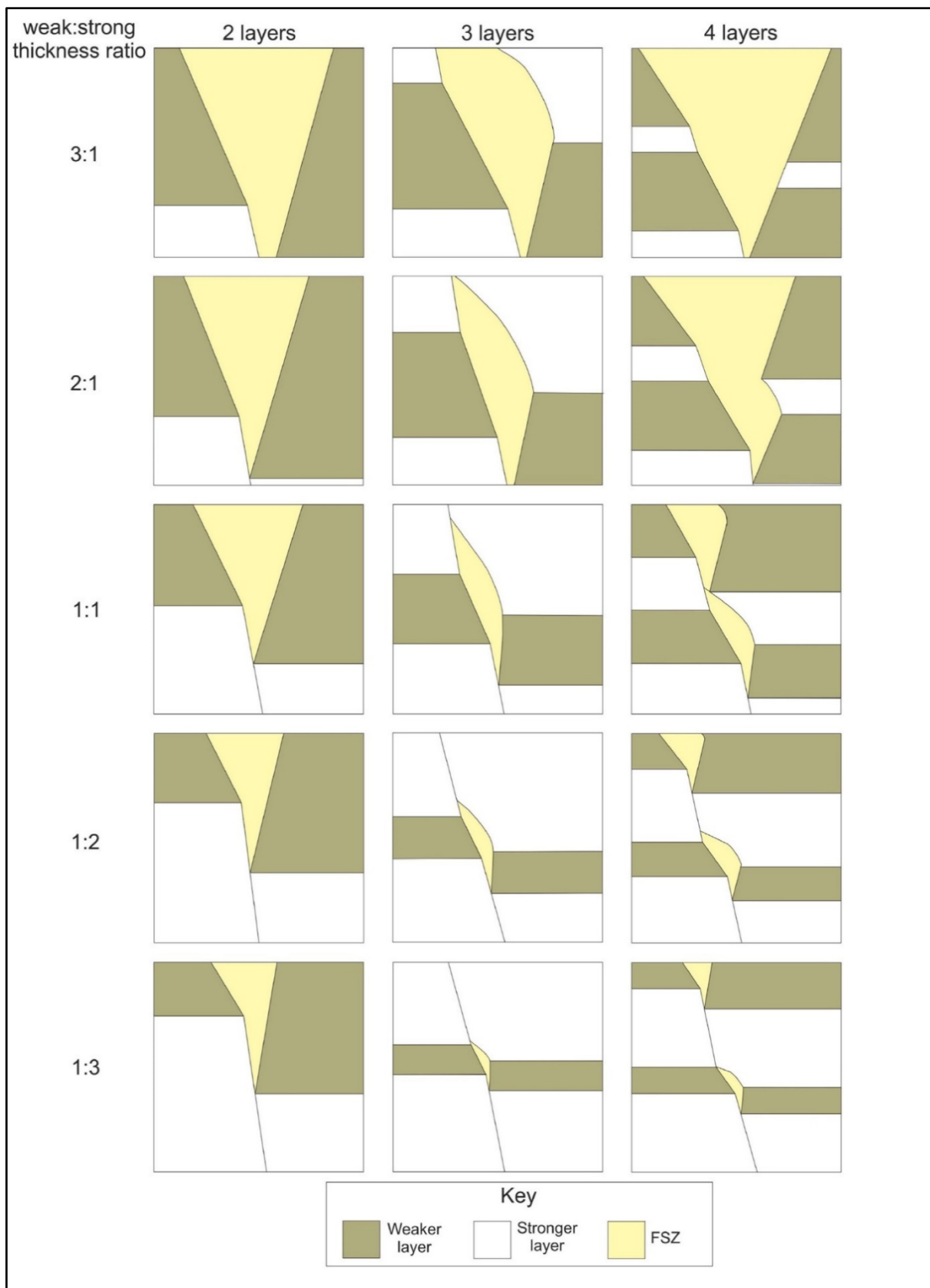


Fig. 8 Fault zone architecture models in dependency of different numbers of stratigraphic layers and ratios of thickness of weak:strong layers by Michie et al. (2014) (FSZ = fracture splay zone).

A wide variety of literature that describes and investigates fault zone architecture and evolution in different lithologies and tectonic settings exists. A good overview is given in Choi et al. (2016), Faulkner et al. (2010) and Wibberley et al. (2008). The authors demonstrate that the mechanical properties of the host rocks as well as the history of the stress regime causing a certain amount of throw define to what extent the ideal structural fault zone elements develop, if at all. Agosta & Aydin (2006), Bastesen & Braathen (2010), Micarelli et al. (2006) and Michie et al. (2014) demonstrate this complexity focusing on layered carbonate rocks. They show that with increasing throw and contrast in the mechanical properties of involved rock facies the complexity of the fault zone architecture also increases. Multiple fault cores can develop and form a complex geometry as shown in Fig. 7 and Fig. 8. Additionally, intensely (IDDZ) and weakly (WDDZ) deformed parts of the damage zone can be categorized as additional architectural elements (see Fig. 6).

Caine et al. (1996) and Micarelli et al. (2006) further describe the temporal evolution of fault zone elements and how they affect fluid flow. They derive four major hydraulic situational endmembers (see also Fig. 9):

- **Localized conduit:** a localized slip along a surface, without a fault core and damage zone or with only a poorly developed one
- **Distributed conduit:** the slip is accommodated on distributed surfaces, the fault core is missing or only poorly developed, the damage zone is well developed and contains slip surfaces and fracture networks
- **Localized barrier:** localized slip formed a cataclastic zone, resulting in a well-developed fault core, the damage zone is missing or only rudimentary present
- **Combined conduit-barrier:** a localized cataclastic zone surrounded by subsidiary distributed structures, a well-developed fault core, the damage zone is well developed and contains slip surfaces and fracture networks

The current knowledge about fault zone geometry of the UJA is primarily based on information from hydraulic, seismic and geophysical borehole data. Especially the latter two sources can potentially give an insight into fault zone geometry while seismic data is the only option for site-specific information during the planning phase of a geothermal well. Seismic surveys in the UJA provide at least three characteristic reflectors near the UJA top, which are commonly used to identify vertical displacement of the lithology and allow the interpretation of the position and extent of fault zones (Steiner, 2012). Further analysis after the drilling phase mainly using image logs allows one to derive detailed properties and the position of fault zones

relative to the well. However, this depends on data quality and might be subject to interpretation errors.

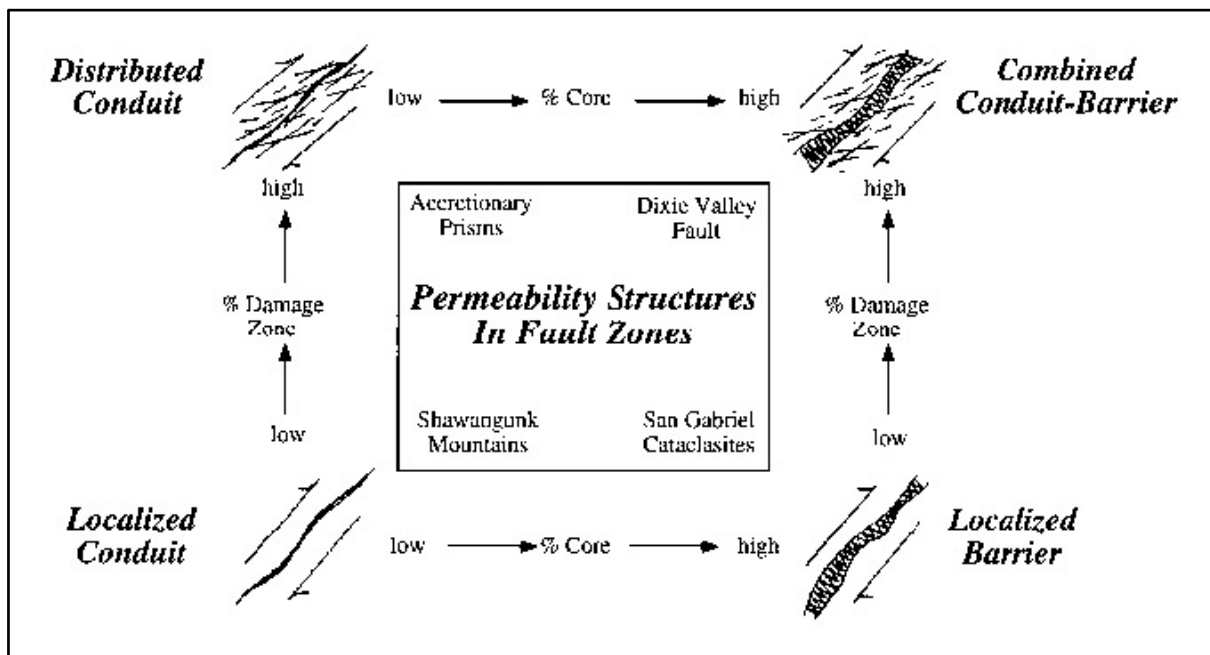


Fig. 9 Concept for the hydraulic effect of fault zones according to Caine et al. (1996).

Most UJA fault zones are generally WSW – ENE striking normal faults that can also be part of graben or ramp systems (Steiner, 2012). Different structural analysis based on 3-D seismic data at several separate locations suggests that these faults had a multiphase evolution that follows the stress field changes in the course of the Alpine orogeny (Budach, Wolfgramm, Moeck, & Lüschen, 2015; Moeck et al., 2015; Shipilin et al., 2020). In some areas, it is possible to observe more complex fault zone patterns with reactivated transpressively inverted fault zones. Additionally, a strike-slip system is postulated but no consistent evidence is yet found (Steiner, 2012). The general geometry of common UJA normal fault zones can be summarized in the following way:

- The dip angle varies between 60 and 85 degrees. This is based on available seismic data from five different locations (Weilheim, Dürrnhaar, Kirchstockach, Sauerlach, Geretsried) and also on the work of Moeck et al. (2015), von Hartmann et al. (2016) and Lüschen et al. (2014).
- Throw values range from 25 to 300 meters (Bachmann, Dohr, & Müller, 1982; Bachmann, Müller, & Weggen, 1987; Moeck et al., 2015; Schneider & Thomas, 2012).
- On the other hand, little data is available to quantify the lateral extent. But as correlations between throw and thickness or observations in similar rock layers suggest,

values between 10 and more than 100 meters are possible (Agosta & Aydin, 2006; Michie et al., 2014).

### **2.3 The scope of pressure transient analysis in geothermal wells**

The short description of the flow field geometry around a well in Chapter 2.1 and the relevance of well tests, as mentioned in the introductory Chapter 1, show that it is important understand how pressure data is used to derive crucial information about the reservoir. The corresponding techniques to analyze pressure data are summarized in the term “pressure transient analysis” (PTA). A “pressure transient” generally refers to a change of the temporal pressure evolution, whereas in well testing, this term points to a reservoir pressure disturbance caused by a change of the well flow rate. PTA uses the data of pressure und flow rate of a well test (production or injection) to obtain reservoir and well properties (reservoir transmissivity, skin factor, initial reservoir pressure, well productivity) by matching a model to the data set (Bourdet, 2002). The four common types to test a single well are (Zarrouk & McLean, 2019): the Drawdown test (sudden water production causes the well pressure to drop), the Build-up test (a producing well is abruptly shut-in), the Injection test (water is suddenly injected into a static well), and the Fall-off test (an injection is suddenly stopped).

PTA is also an established tool for the geothermal projects of the UJA. After the construction of a new geothermal well is finished, a next step is to assess its productivity and the resulting profitability. For this purpose, a long-term pumping test gets deployed right after a short cleaning-through-acidification period (no other stimulation treatments are applied for deep geothermal wells in the North Alpine Foreland Basin (Böhm, Savvatis, & Steiner, 2012a)). The goal of this test is to measure the pressure drawdown until a quasi-stabilization is reached followed by a shut-in and the observation of the pressure build-up. This data set is subsequently evaluated by the use of PTA with its key tool, the Bourdet Derivative (DER) (Bourdet, 2002). The aforementioned reservoir properties at the corresponding drilling site are thus identified. Additionally, the quality of communication between well and reservoir is determined and an understanding of the aquifer’s flow behavior is obtained (Bourdet, 2002). By putting those findings into a spatial context, future exploration strategies can be developed and improved (Savvatis, 2012). PTA is, in practice, mostly only applied on the recovery phase of a pumping test due to no fluctuations in the production rate.

The core tool for well-test interpretation of transient pressure data (pressure transient analysis, PTA) is the Pressure Derivative (DER), also called Bourdet derivative (Bourdet, 2002; Bourdet, Whittle, Douglas, & Pirard, 1983). It is defined as in (1).

$$\text{Bourdet Derivative (DER)} \quad \Delta p' = \frac{dp}{d \ln \Delta t} = \text{DER} \quad (1)$$

$p$  = pore pressure [MPa]

$t$  = time [h]

By plotting the DER together with the corresponding pressure change in the same log-log graph (diagnostic plot), characteristic shapes, defined by their slopes, for various flow regimes can be observed and quantified through analytical models. A selection of the most common flow regimes is given in Gringarten (2008) and visualized in Fig. 10. Bourdet (2002) summarized the definitions and use of corresponding interpretation models in a comprehensive overview. Additionally, Fig. 10 illustrates how such a diagnostic plot is temporally subdivided into early, middle and late time region. Each of these regions is characteristic for a certain group of effects that occur on specific time scales.

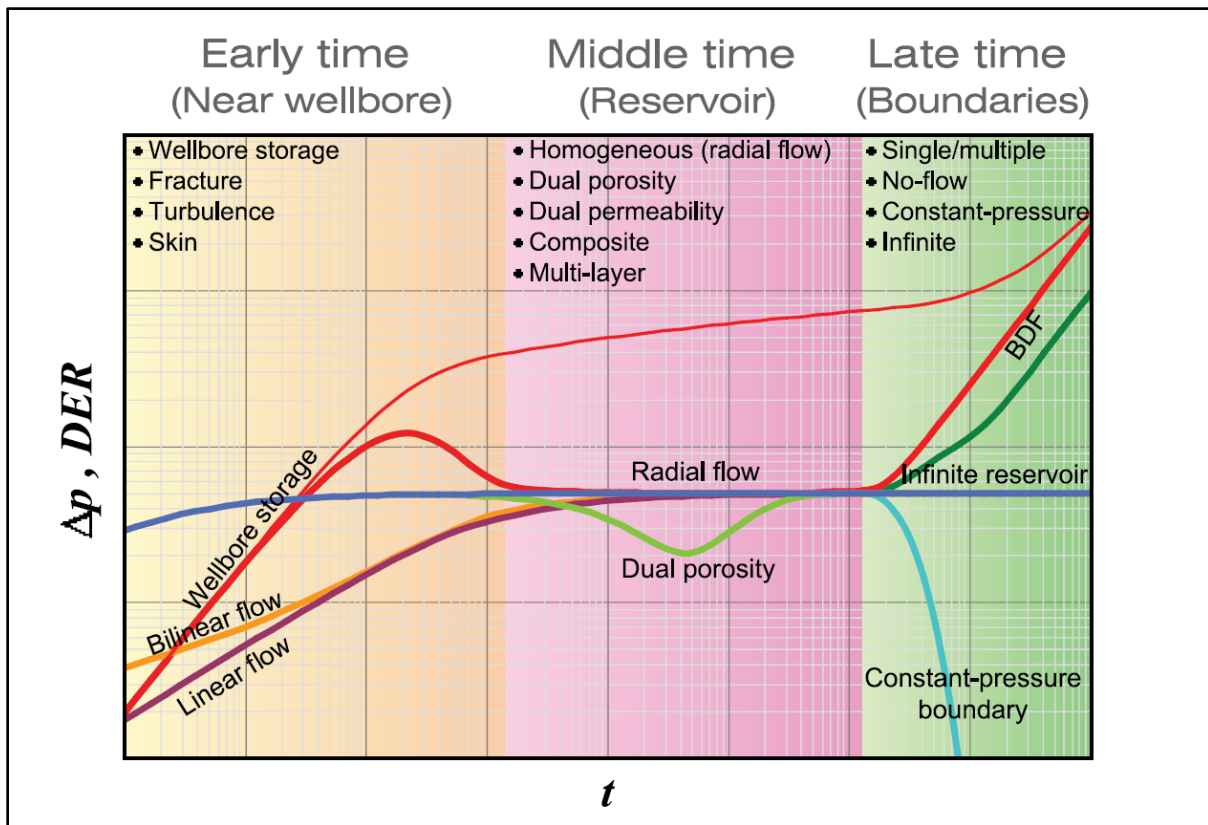


Fig. 10 Overview of the fundamental analytical models used in PTA (IHS Markit, 2017), red thin line =  $\Delta p$  = pressure change (e.g. measured in a pumping test), thick colored lines = Bourdet Derivative/DER calculated from  $\Delta p$  according to equation (1),  $t$  = time.

PTA is very widely used and many different models exist. The main models associated with a fault zone are the “infinite conductivity fracture” (linear flow) model developed by Gringarten et al. (1974) and the “finite-conductivity fracture” (bilinear flow) model developed by Cinco-Ley et al. (1978). There are additional models with increased complexity and for specific

reservoir situations that more or less extend the mentioned single fracture models. Dinh & Tiab (2010) for example extend the basic analytical solution for “linear flow” by an inclined fracture through which all fluid is produced. Based on this, Jia et al. (2016) added a slanted well to the inclined fracture. There are also models derived for very specific complex situations, as demonstrated by Wei et al. (2016) for “finite conductivity multi-staged fractured horizontal wells in fractured-vuggy carbonate reservoirs”. However, so far there is no analytical solution to a punctual intersection between a well and a fault zone with arbitrary inclinations and water extraction over the filter length of the well.

Fig. 11 shows how the flow field geometry around a well might be altered by a fault zone and introduces the contrast in hydraulic properties between the fault zone and the surrounding reservoir matrix (corresponding DER slopes are visualized in Fig. 10 and more detailed in Fig. 23). In the case of “radial flow”, this contrast is very weak and the fault zone is only slightly more conductive than the matrix. The result is a homogeneous pressure drawdown in every direction from the well in the same shape as if there was no fault zone. But as this contrast increases, a “bilinear flow” field becomes possible. The matrix flow becomes perpendicular to the fault zone in this case, as the fault zone directs the fluids to the well. Moreover, a significant gradient exists still inside the fault zone. This gradient will be neglectable in the “linear flow” case with very high fault zone conductivity and the fault zone acts as a well-extension. Even higher contrast is possible if the reservoir matrix is mainly impermeable. The fault zone alone forms the only conductive reservoir and the matrix behaves as a negative boundary. The underlying analytical models are further explained in the methods Chapter 4.5.

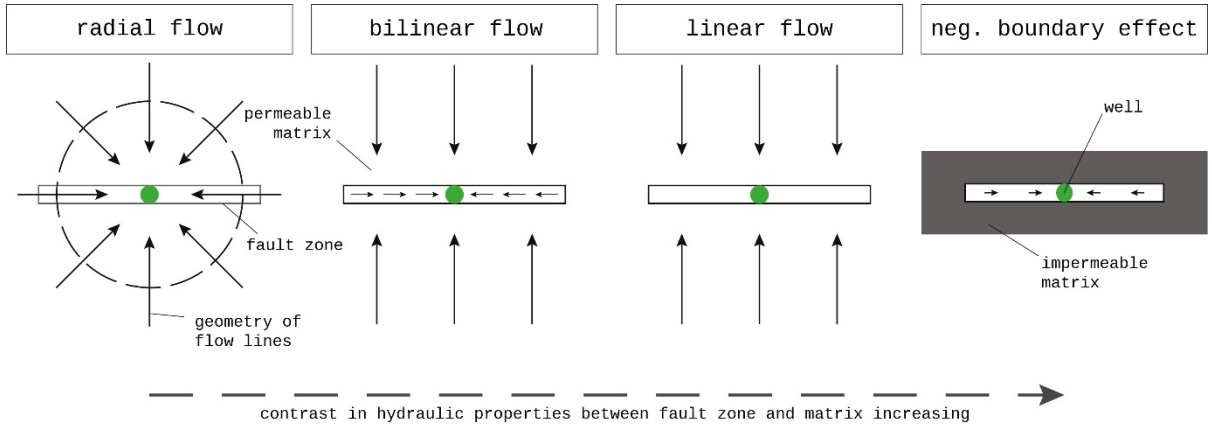


Fig. 11 Concept of the flow field geometry around a well inside a fault zone depending on the contrast in hydraulic properties between the fault zone and the surrounding reservoir-matrix (Bourdet, 2002).

The application of PTA in a real world case involves testing different models in combination with geological, geophysical and petrophysical information to find a reservoir model that is able to explain observations and which can be used for various prediction tasks (Bourdet, 2002). A good example is demonstrated by McClure & Horne (2011) in which PTA is used to investigate the permeability and structure of a fractured zone at the French geothermal project at *Soultz-sous-Forêts*. Enachescu et al. (2016) and Uematsu et al. (2012) present examples from the oil industry for complex carbonate reservoirs. The latter is also combining numerical models with standard analytical PTA.

The UJA pressure data of well tests and their interpretation are rarely published as they are often considered confidential reservoir information. Nevertheless, some publicly available data exists for the geothermal site *Bad Wörishofen* where transient pressure data is analyzed to derive the reservoir transmissivity (Stoyke et al., 2006). At the *Unterhaching* project Gt 2 well PTA of pumping tests was used in combination with geophysical borehole data to characterize and observe a fault zone (Rojas, Dussel, & Moeck, 2017). As part of the Geothermal Alliance Bavaria project, this work had access to pressure data of drill stem tests and their analysis at the geothermal project *Weilheim* (TUM, 2019).

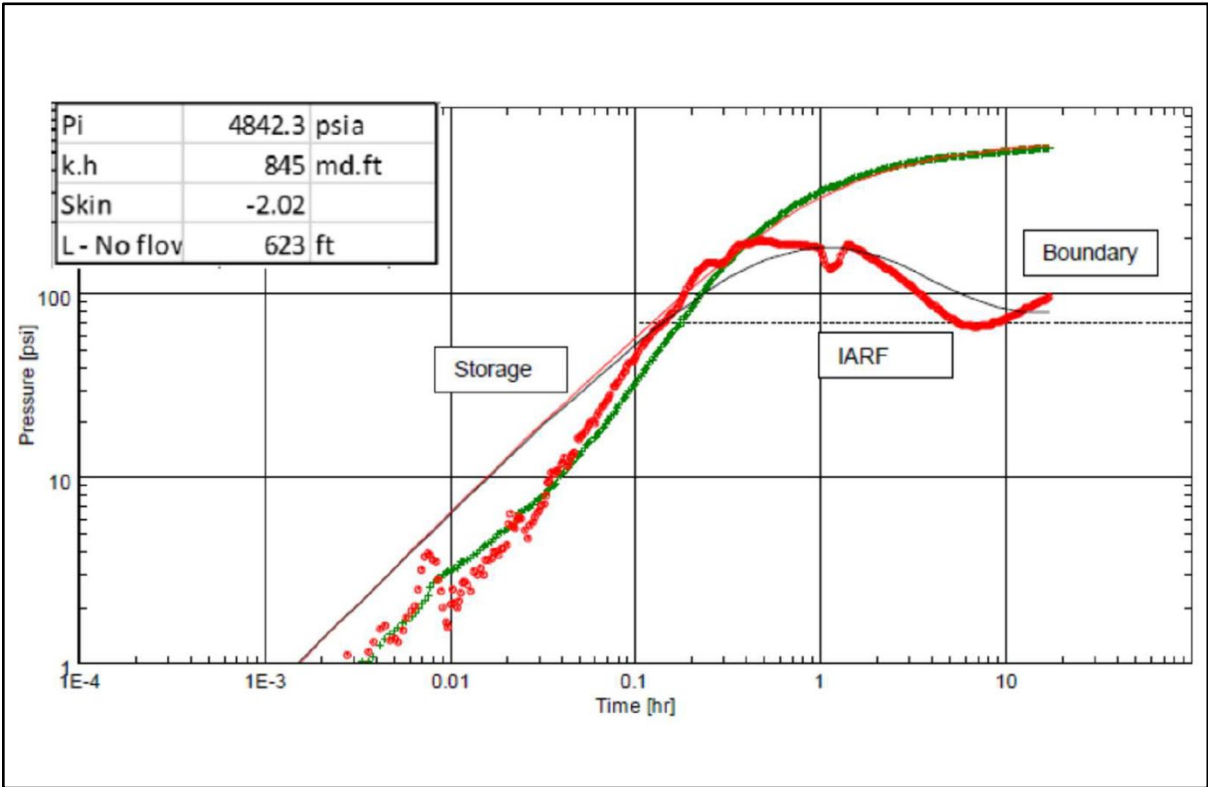


Fig. 12 Evaluation of the pressure buildup of a drill stem test at the *Weilheim* geothermal project. Green dots: measured pressure; Red dots: Bourdet Derivative (DER) calculated from measured pressure; red and black line: model fit for pressure and DER. A negative skin, reservoir transmissivity, well storage and a no flow boundary were interpreted.

An exemplary evaluation is shown in Fig. 12, which demonstrates how a model is fit to the pressure data to derive skin, transmissivity and well storage. The analysis indicates also a possible boundary effect, meaning a permeability decrease in the distance of the well (see also Fig. 10). Savvatis (2012) provides the most comprehensive set of analyzed well test data of the UJA in anonymized form. He illustrates the typical use cases of PTA with corresponding examples: Investigation of the results of acidification, derivation of reservoir properties, observation and quantification of boundaries and providing evidence for hydraulically active fault zones. The latter is exemplarily shown for a well with linear and another well with bilinear flow in the UJA in Fig. 13.

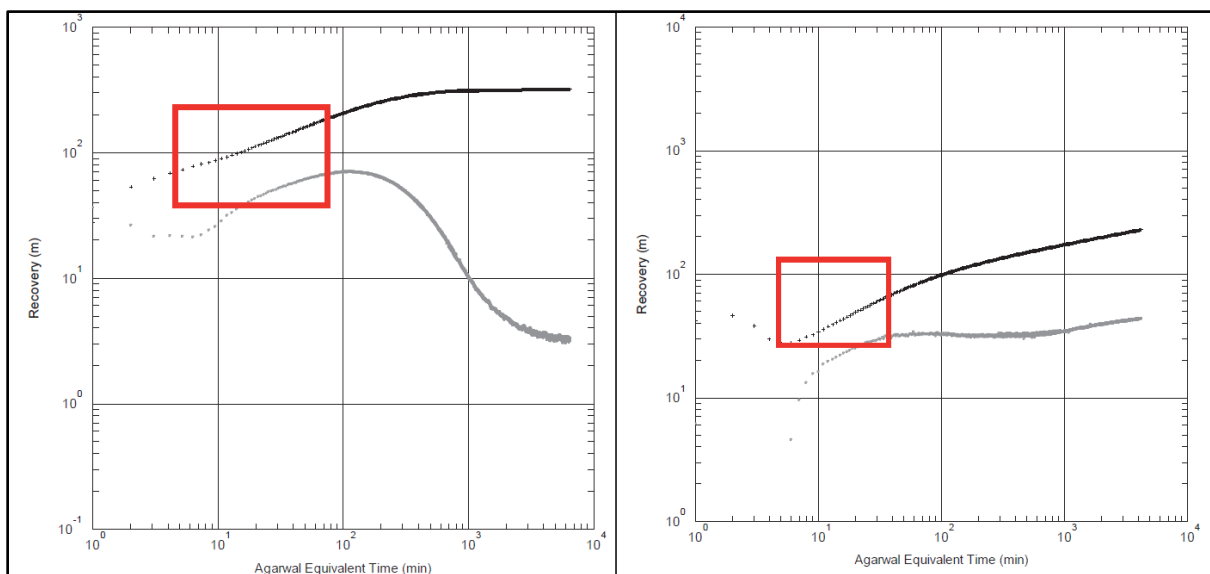


Fig. 13 Pressure data of two different geothermal wells of the UJA, red boxes indicate the fault zone associated flow (Savvatis, 2012). Left: bilinear flow. Right: linear flow. Black dots: measured pressure; Grey dots: Bourdet Derivative (DER) calculated from measured pressure.

## 2.4 The productivity of wells in the Upper Jurassic aquifer

In the context of geothermal exploration concepts, it is necessary to quantify the performance of a well and compare it with differently strategized wells. The common way to describe the performance of a well is to measure its drawdown (the pressure drop ( $dp$ ) relative to the unaltered reservoir pressure ( $p_i$ )) relative to the corresponding well flow rate ( $q$ ). This ratio is defined as the productivity index  $PI$  (2). It represents a combination of well and reservoir properties. The pressure drop ( $dp$ ) can generally be split into a linear and non-linear component as shown in the form of an inflow performance relationship (IPR) presented in equation (3) for a more realistic and well specific description. The non-linear term summarizes all turbulent effects such as flow inside the well tubing, skin and other near well effects. IPRs in combination with tubing performance curves allow the determination of the optimal operation point of a well

(Schlumberger, 2021). The *PI* or IPRs are further used to evaluate the effect of the cleaning-through-acidification phase and to search for correlations between reservoir properties of the UJA and well productivity. Steiner et al. (2012) present IPRs for 13 different wells in the UJA with respect to the reservoirs facies and throw values of fault zones (Fig. 14). They derive that the well performance is primarily driven by the depositing environment of the reservoir rocks and secondarily correlated to the fault zone throw.

productivity index (*PI*)  $PI = \frac{q}{dp}$  (2)

inflow performance relationship (*IPR*)  $dp = p_i - p_{wf} = bq + cq^2$  (3)

$q$  = production rate [l/s]  $dp$  = pressure change [MPa]  
 $p_i$  = average bottomhole pressure [MPa]  $p_{wf}$  = bottomhole flowing pressure [MPa]  
 $c$  = turbulence coefficient [-]  $b$  = laminar flow coefficient [-]

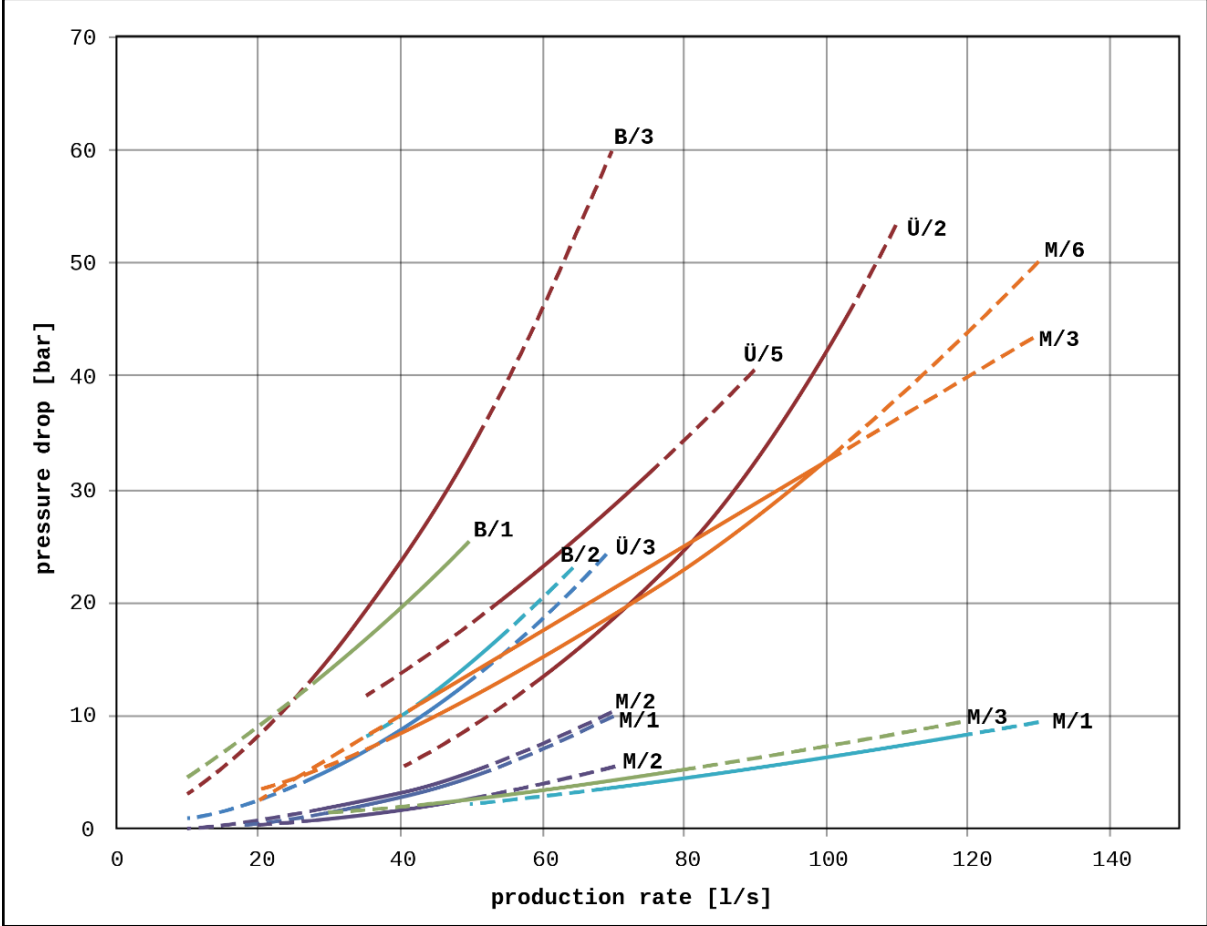


Fig. 14 Inflow performance relationships of 13 geothermal wells in the central part of the Southern German Molasse Basin. Curves of the same color are wells of the same geothermal project. The curve labels represent the facies and fault zone throw: Facies: M = mass facies, B = basin facies, Ü = transition facies / Fault zone throw: 1 = 0 m, 2 = smaller than 50 m, 3 = approx. 50 m, 4 = smaller than 100 m, 5 = approx. 100 m, 6 = above 100 m. (Steiner et al., 2012).

## 2.5 Hydraulic numerical modeling of the Upper Jurassic aquifer

Numerical models of geothermal wells and reservoir are an important part of the geothermal exploration in general and therefore also in the UJA. They are used for a multitude of different purposes. The general necessity for numerical UJA models was summarized by Steiner et al. (2012). Their arguments can be extended by the principles and goals presented by Cacace et al. (2013) to capture the current state of art:

- Optimization of the exploration strategy through calculation of different scenarios of well configurations and their influence on the hydraulic and thermal behavior
- Investigation of uncertainties in the geometric and hydraulic properties of the hydrogeological model of the exploration site and their influence on the hydraulic and thermal behavior
- Well productivity prediction (worst, business and best case scenario)
- Well management for a sustainable operation through calibration with in situ data during production
- Legally needed for permit application

The basis of such a reservoir model is the mathematical description of fluid flow in porous media. This is achieved by combining the principles of representative elementary volumes (REV) and mass conservation with Darcy's law and the concept of specific storage for confined aquifers. The resulting continuity equation (4), which cannot be solved analytically in real reservoir problems, is approximated by numerical methods (Bundschuh & Suárez Arriaga, 2010; Kolditz, 2002).

$$\text{fluid continuity equation} \quad \vec{\nabla} \left( \frac{\mathbf{k}}{\mu_f} (\vec{\nabla} p_f - \rho_f \mathbf{g}) \right) = S_{sp} \frac{\partial p_f}{\partial t} - Q_f \quad (4)$$

$p_f$  = pore pressure [Pa]

$t$  = time [s]

$\rho_f$  = fluid density [ $\text{kg}/\text{m}^3$ ]

$S_{sp}$  = specific storage [ $1/\text{Pa}$ ]

$\mathbf{g}$  = gravity vector [ $\text{m}/\text{s}^2$ ]

$\mu_f$  = fluid viscosity [Pa \* s]

$\mathbf{k}$  = permeability tensor of the porous medium [ $\text{m}^2$ ]

$Q_f$  = sink/source [ $\text{m}^3/\text{s}$ ]

There is a wide variety of different approaches in numerically approximating partial differential equations (PDEs) such as (4) (Bundschuh & Suárez Arriaga, 2010; Hesthaven & Warburton, 2008). Most notably known are the Finite Element Method (FEM) and the Finite Difference Method (FDM) on which the two most common commercial software packages to simulate groundwater flow in the UJA (portraying the actual reservoir geometry) are based on:

Petrel/Eclipse (FDM) and FeFlow (FEM). With such numerical tools, a hydrogeological model concept is transformed by discretizing the model domain spatially and the investigated timeframe temporally. Together with boundary conditions, the solution to the presented continuity equation can be approximated at each discrete point in space and time. The following reservoir models are examples of UJA models utilizing Feflow:

- Wenderoth et al. (2005) investigated the *Riem* geothermal site.
- Lafogler et al. (2016) worked at the *Pullach* project.
- Goldbrunner & Vasvári (2016) presented findings of the *Waldkraiburg* geothermal doublet.
- Schulz (2012) incorporated the greater Munich area and focused on the geothermal sites in *Pullach*, *Unterhaching*, *Oberhaching*, *Kirchstockach*, *Hofolding*, *Dürnhaar* and *Sauerlach*.
- Rioseco et al. (2018) on the other hand investigated the urban Munich area for an optimized geothermal multi-well pattern also using FeFlow.

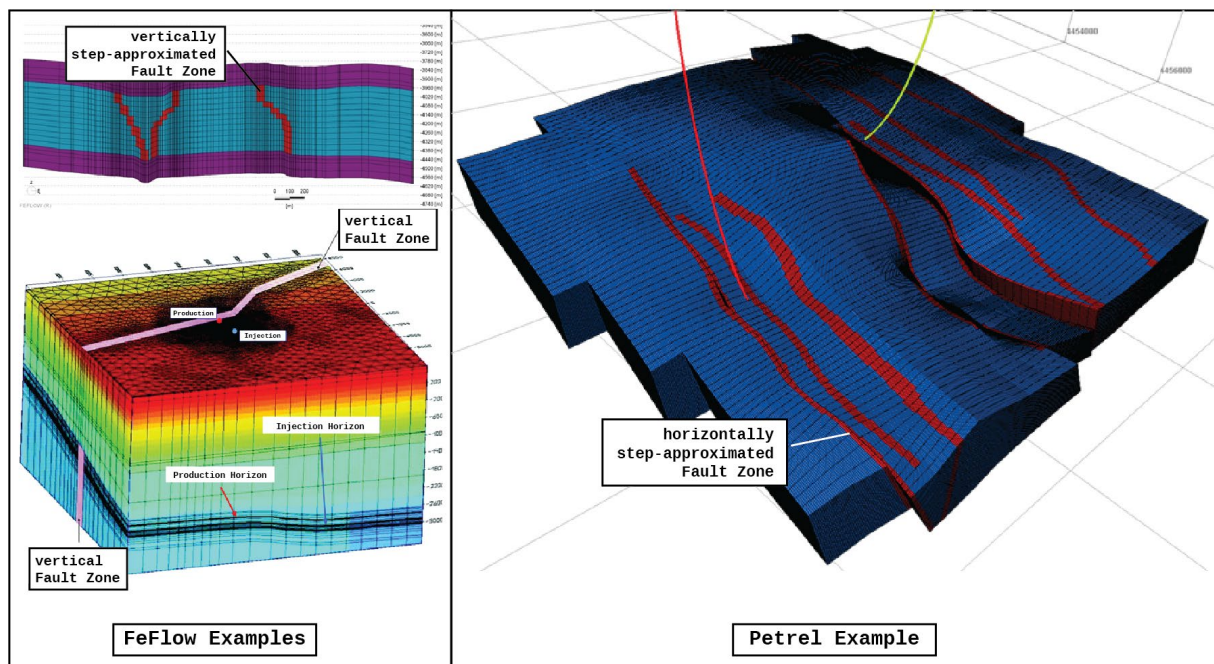
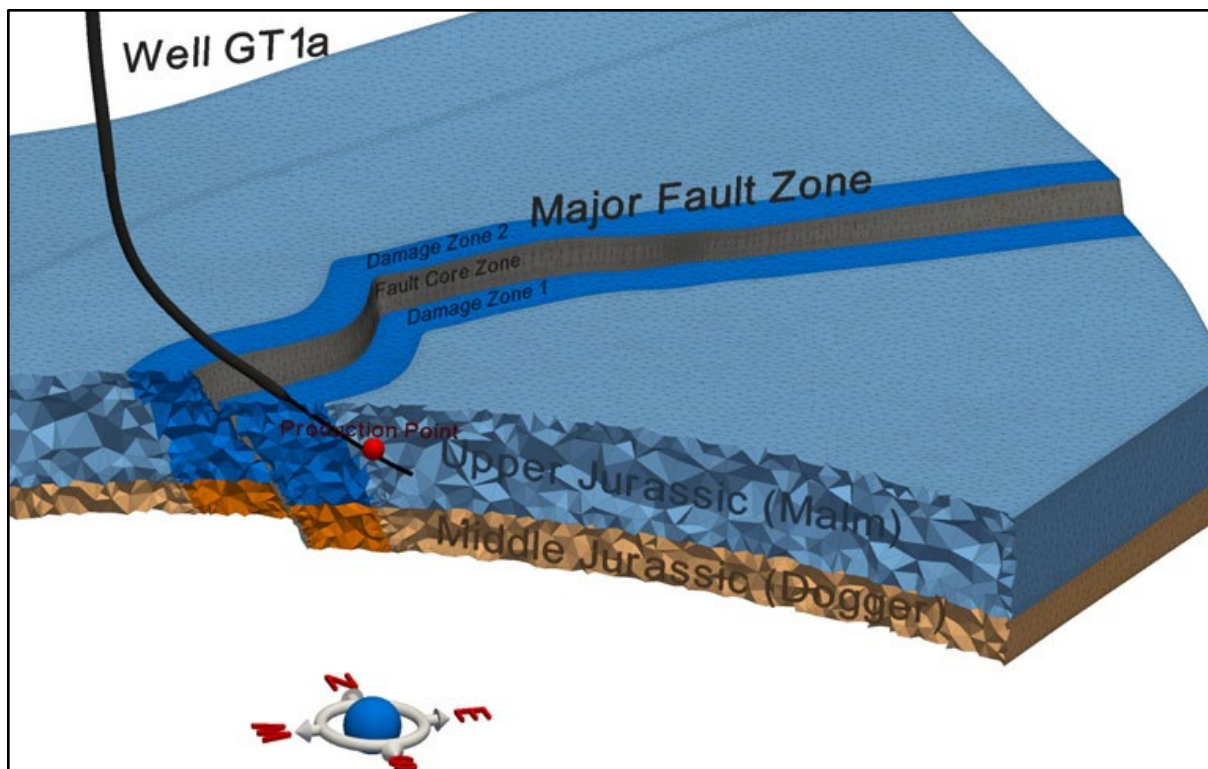


Fig. 15 Spatial discretization examples of fault zones inside the UJA using common software packages (FeFlow and Petrel) requiring geometric simplifications (Thuro et al., 2019; Wenderoth et al., 2005).

Published examples for the usage of Petrel/Eclipse are rare but its application is nonetheless very common in engineering offices working in the UJA (Steiner et al., 2012). The differences between these software packages are, besides the different user experiences based on the

incorporation of varying additional pre- and post-processing methodology, mainly the numerical solvers and the geometric constraints imposed by the numerical method. The FDM requires a structured mesh as spatial discretization of the model domain that generally requires less computation power but is also limited in its resolution to depict complex geometries. The FEM, in contrast, can additionally be applied to unstructured meshes but it is mathematically more complex and therefore computationally more expensive (Hesthaven & Warburton, 2008). Even though FeFlow is using the FEM, its native workflow is based on partially structured meshes (vertical layers and horizontal triangular mesh). Vertically complex structures are therefore generally simplified.



*Fig. 16 Spatial discretization of the Mauerstetten geothermal project in the western central Molasse basin using an unstructured tetrahedral mesh representing seismic information without simplification (Cacace et al., 2013).*

The result is that UJA models constructed using FeFlow normally simplify the inclination of fault zones to an upright geometry or approximate it in “steps” as can be seen in the mentioned examples above and in Fig. 15. However, as fault zones can appear in a variety of different hydraulic configurations, as presented in the introductory Chapter 1, it becomes more and more important to evaluate different scenarios during the planning phase of a geothermal project. A comparison between Petrel/Eclipse and FeFlow with a modern workflow using the open source simulation framework Moose/Golem (incorporating unstructured tetrahedral meshes) in

regards of numerically simulating a fault zone in the UJA showed that geometric approximations, such as the step-like representation of inclined fault zones, can result in severely altered simulation results (Thuro et al., 2019). At the *Mauerstetten* geothermal project site, Cacace et al. (2013) demonstrate a suitable way to evaluate different hydraulic situations of a fault zone of interest and further prove a high hydraulic influence of different fault zone configurations (see Fig. 16).

### **3 Aims and objectives**

As presented in detail in Chapter 2.2, fault zones inside the UJA are considered as key elements that can alter the reservoir flow in their proximity, while their exact role in the context of exploration strategies is not fully understood (Cacace et al., 2013; Caine et al., 1996; Michie et al., 2014; Savvatis, 2012). The main reason for this being the data sparsity regarding the complex interaction of geometric and hydraulic properties. Even by developing a deep understanding about the genesis of fault zones as well as the surrounding host rock and combining it with field investigations and laboratory measurements, the possibilities of their hydraulic behavior can only be roughly constrained. Furthermore, there are multiple additional local factors (e.g. stress field, actual tectonic history, rock facies and properties) which are difficult to determine precisely, but that greatly influence the hydraulic effect of fault zones. Therefore, mainly the interpretation of hydraulic data of well tests remains as a useful tool to derive and possibly quantify the fault zone influence on a geothermal well. However, as noted in Chapter 2.1, there is the non-intuitive observation that homogeneous flow fields around the geothermal wells of the greater Munich area are predominantly found within the reservoir, even though most of the wells develop large fault zones. On the one hand, these fault zones could just be unworthy exploration targets. On the other hand, there might also be significant thresholds (in the contrast of the hydraulic properties between fault zone and host rock) preventing a proper detection in pressure data. Additionally, the subsequent question arises if and to what extent UJA fault zones can contribute to the productivity of a geothermal well. In other words, are fault zones really promising exploration targets or is the surrounding host rock generally more important? Hence, this work focuses on the following questions:

- Which hydraulic parameter settings are necessary to observe bilinear or linear flow behavior of a fault zone during a well test within the Upper Jurassic aquifer in southern Germany?

- Is it possible that highly permeable fault zones are hidden in a radial flow regime observed in pressure data (further called hydraulically hidden fault zones)?
- To what extent can fault zones, and especially hydraulically hidden fault zones of the UJA, actually contribute to the productivity of a geothermal well?

The greatest challenge in answering these questions is the wide range of involved hydraulic properties, which lead to numerous possible hydraulic situations. A systematic investigation covering the entire natural parameter space is therefore necessary (Alfonsi et al., 2017). Based on it, the influence of fault zones on the pressure signal in a geothermal well must be observed and analyzed in order to shed light on this. There is no feasible real world experiment that can be used to test the many naturally possible fault zone realizations. However, numerical simulations provide a flexible tool to overcome this obstacle. This method can be used to hydraulically describe the Upper Jurassic aquifer and its fault zones while incorporating a realistic geometry.

In this work, a suitable model concept is transformed first into a hydraulic numerical model (using unstructured tetrahedral meshes and the finite element method) and its realistic nature is verified through calibration with field data. This model is then used to simulate pumping tests and evaluate them depending on the research question:

- By applying state-of-the-art pressure transient analysis methods to the model results in an automated fashion, the multitude of possible parameter settings is explored with a focus on flow regimes (see Chapters 2.3 and 4.5) and their transition in parameter space.
- The effect of a fault zone on well productivity (see Chapters 2.4 and 4.7) can be determined by comparing simulated pumping test results for an arbitrary parameter combination in two scenarios: 1. An aquifer with a geothermal well tapping in an inclined fault zone; 2. The same aquifer and well with the previously integrated fault zone removed.

Even though finite element (FE) simulations provide a practical approach in investigating the proposed system, the time needed to carry out those simulations is dominating the experiment design. Furthermore, this can lead to a low resolution in the evaluation of the desired parameter space. This work shows how this obstacle can be overcome in a first step by utilizing a high-performance computing (HPC) cluster. During the process of this work, new numerical methodology became available at a later stage: By constructing a low dimensional representation of a finite element (FE) simulation through the reduced basis (RB) method

additional to the HPC infrastructure application, an extremely detailed parameter space exploration could be carried out. This highly efficient numerical model (see Chapter 4.8) also allowed for detailed regional investigations based on input maps additional to the general parameter space investigation. This approach was then applied to the region of the Upper Jurassic aquifer with the highest geothermal usage and development: the greater Munich area. For this methodology to have the most effective relevance in the study area, new reservoir data was gathered, regionalized, and further used as model input, thereby allowing for the detailed spatial visualization of the fault zone influence on well productivity and flow behavior. The presented approach is also valid beyond the investigated location and illustrates the combination of very efficient numerical simulations on a high performance computer with well test analysis methodology to derive conclusions for hydraulic reservoir behavior observable in the field and the magnitude of fault zone influence on well productivity.

**4 Material and methods**

Now, the work steps applied to tackle the research questions as defined in Chapter 3 are summarized. These steps are grouped into two workflow packages that were approached successively over the course of several years: 1. fault zone associated flow regime workflow; 2. fault zone induced well productivity change workflow. The second work package was built upon knowledge gathered in the flow regime investigation and newly available methodology was applied.

**Workflow 1: Fault zone associated flow regime**

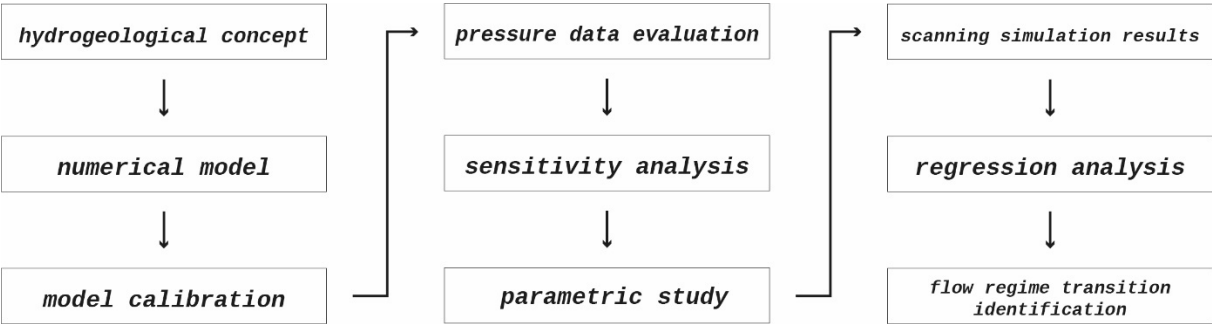


*Fig. 17 Workflow 1: Fault zone associated flow regime investigation.*

As foundation for all subsequent stages, a suitable hydrogeological concept was chosen that incorporates all hydraulic elements and their geometry as well as ranges for all relevant properties. This information was then transformed into a tetrahedral mesh describing the investigated aquifer spatially (Chapter 4.1). Combining this mesh with the physics of interest

(Chapter 4.2), a numerical model was set up for the simulation of well tests with different hydraulic property combinations (Chapter 4.3). To prove the plausibility of this model, field data of a geothermal well with linear flow was used for calibration and associated validation (Chapter 4.4). Next, an adaptation of the pressure transient analysis methodology was developed to automatically evaluate a large number of simulated well test data (Chapter 4.5). By investigating the sensitivity of the hydraulic model properties, all those of relevance could be retrieved and further used for a systematic parameter study (Chapter 4.6.1). The parameter space was then sampled and the corresponding model response, the well test, calculated with the flow regime associated research questions in mind (Chapter 4.6.2). The model results were further scanned for parameter combinations that mark the transitions between the occurring flow regimes. With the help of a regression analysis based on these identified parameter combinations, a continuous visualization for the input parameter space was possible (Chapter 4.6.3). A constitutive interpretation of the flow regime transitions was therefore possible. Fig. 17 summarizes the sequence of work steps in this first fault zone investigation.

**Workflow 2: Fault zone induced well productivity change**

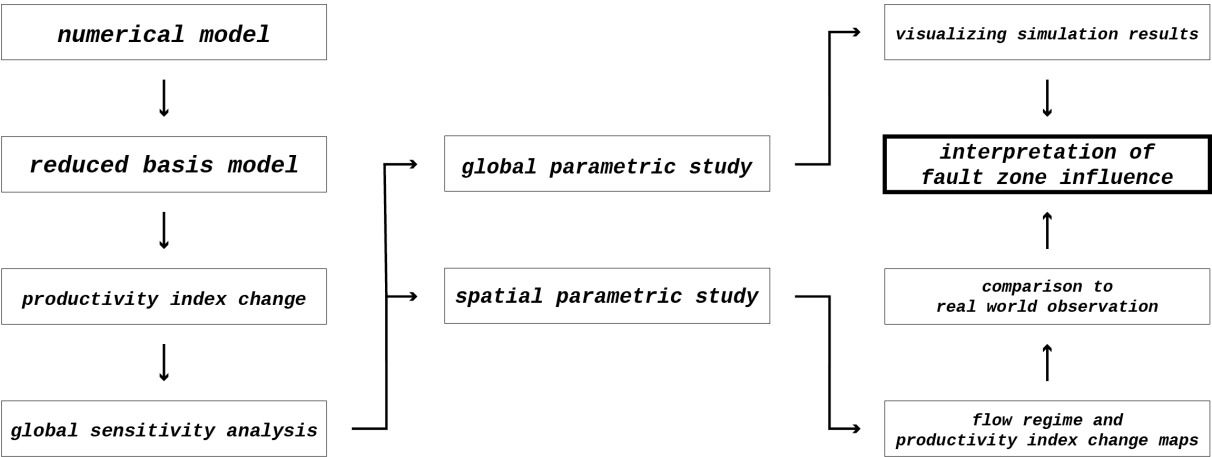


Fig. 18 Workflow 2: Fault zone induced well productivity change investigation.

Next, the question regarding fault zone influence on the well productivity was investigated. The main idea to tackle this problem was to compare simulated pressure curves of two versions of pumping tests (with and without hydraulically active fault zone) for a large number of hydraulic parameter combinations. The goal was to describe and quantify fault zone influence on well productivity in the entire UJA parameter space. The analysis is primarily focused on hydraulically active fault zones that do not develop a bi-/linear flow regime but only radial flow is observed in the well test evaluation (hydraulically hidden fault zones). The concept was to

calculate the pressure evolution during water extraction, first with a fault zone in the center of the aquifer and a well piercing through it and second with the fault zone removed by enhancing the previously developed numerical model. The difference in the resulting two pressure curves quantifies the hydraulic effect of the fault zone and was summarized in the alteration of the well productivity index (PI) (Chapter 4.7). Additionally, the simulated pressure curves were again examined by automated derivative analysis in order to determine the predominant flow regime and reveal possible correlations.

To cover the entire natural parameter space, it was necessary to facilitate a large number of simulations. In order to enable a very detailed parameter space investigation, quality controlled model order reduction was applied to the calibrated numerical model (Chapter 4.8). Very fast calculation times were achieved in this way, enabling a high-resolution investigation (Chapter 4.9). In a next step, this also permitted a global sensitivity analysis (Chapter 4.9.1). Information gathered by this is important for understanding the effect of the hydraulic model properties on the well PI and designing an efficient parameter space investigation. The findings of this sensitivity analysis were also used to visualize the simulation results in an appropriate way.

The reduced and fast performing model was further applied in an additional study. Investigating the change of the well productivity index induced by the fault zone is especially important in the greater Munich area. Therefore, new spatial information about reservoir permeability and fluid viscosity was gathered and regionalized into map grids. These spatial grids were used as model input to reduce the complexity of the parameter space (Chapter 4.10). By fixing the remaining hydraulic parameters (mainly hydraulic fault zone properties) for each spatial analysis, different fault zone types were then tested. Each type was simulated in each grid point of the entire investigation area. The simulation results thus represent maps of fault zone-induced well productivity index change as well as of the flow regime around the well of the respective fault zone type. By comparing the simulation results with observations in the local geothermal wells a more realistic fault zone configuration in terms of flow behavior could be derived. Its spatial effect on the well productivity index was then further studied. Fig. 18 summarizes the sequence of work steps in this second work package of the fault zone investigation.

#### **4.1 Geological framework of the study area and hydrogeological concept**

A conceptual model representing the main controlling hydraulic elements on a reservoir scale was first created as a basis for the numerical model representing the conditions in the targeted aquifer (Bundschuh & Suárez Arriaga, 2010). For the investigation of well tests in the UJA, those main elements are the aquifer matrix, the well and a fault zone. The basic purpose of this

concept, when transformed into a numerical model, is the hydraulic representation a fault zone within the UJA as realistically as possible, while enabling a variation of its properties to account for natural occurring ranges. Through a well located in the middle of this fault zone, water extraction must be applied in order to simulate a typical well test (see Chapters 2.3 and 4.5) that can be interpreted and analyzed.

The term aquifer matrix summarizes here all heterogeneities on a scale lower than the reservoir scale (e.g. small scale facies changes or individual fractures) and describes it as a continuum with averaged properties. Changes in rock types and properties on a scale relevant to the numerical simulation of the hydraulic reservoir behavior are controlled by the larger scale lithofacies and diagenesis in the southern German Molasse Basin. Böhm et al. (2013) presented a hydrostratigraphic classification of the UJA based on these two main factors and the data of 17 wells (Fig. 19). This classification followed the stratigraphic grouping of Quenstedt (1858). Here the two units Lower to Middle Malm (Malm  $\delta$  and  $\epsilon$ ) and Upper Malm (Malm  $\zeta$ ), are generally considered as the aquifer. The thickness and actual hydraulic properties are varying depending on the individual facies position. For the purpose of this investigation an average value of 500 meters (Böhm et al., 2013; Fritzer et al., 2012; Stier & Prestel, 1991) was considered as sufficient to represent the typical aquifer thickness. The hydraulic matrix properties (specific storage and permeability) were accordingly averaged on the chosen thickness, which also allows an application of the model results on different aquifer thicknesses.

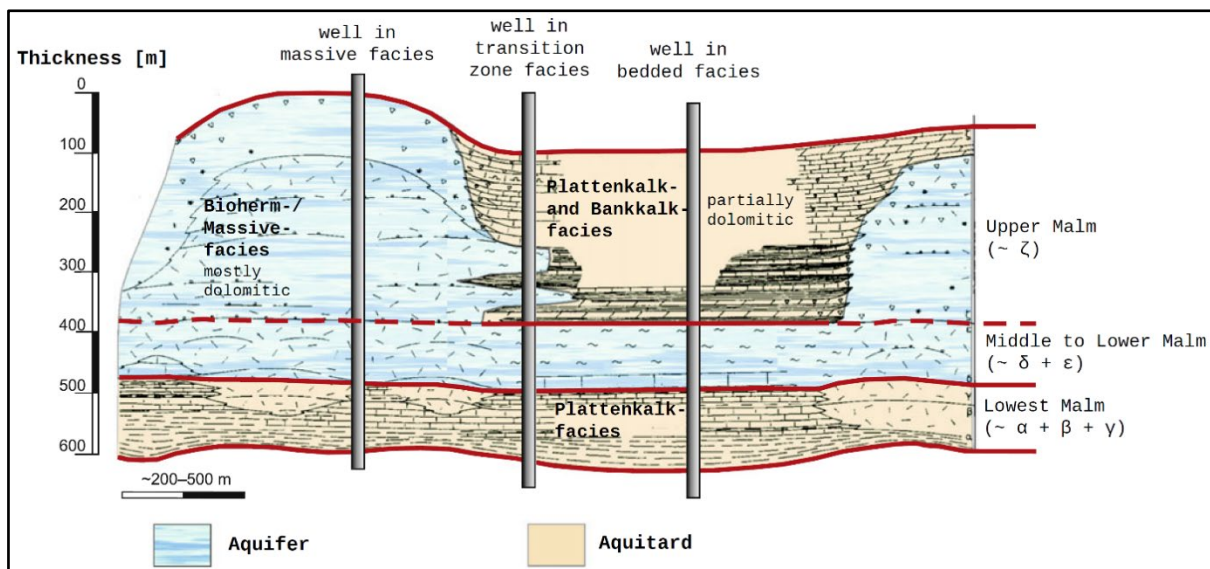


Fig. 19 Schematic profile of the facies types and hydrostratigraphic groups of the Upper Jurassic rocks in the greater Munich area (Böhm et al., 2013).

For the representation of fault zones in this hydrogeological concept, it is suitable to summarize all geological fault zone elements (see Chapter 2.2) into a single individual continuum. The

reason for it being that the detection of a fault zone in a well test relies on the interaction of an artificially introduced pressure transient with the heterogeneities of the reservoir (see Chapters 2.3 and 2.2). A geologically complex structured fault zone is thus reduced to its overall effect on the pressure front (Bourdet, 2002). The thickness of such a fault zone representation therefore equates to a hydraulically active thickness. As mentioned in the introduction (Chapter 1) various different fault zone types can exist depending on a complex interaction between many geological factors. Relevant for the description of the predominant flow regime and the improvement of the well PI (see Chapters 2.4 and 4.7) are all types that do not act as a barrier. These include narrow fault zones consisting mainly of a few open fractures without a properly developed fault core or damage zone corresponding to a smaller hydraulically active thickness (Caine et al., 1996). With higher throw values, significant damage zones can form (Choi et al., 2016). These damage zones span a greater area consisting of a highly interconnected fracture density (Agosta & Aydin, 2006; Knott et al., 1996; Moeck et al., 2015). High hydraulically active thickness values of the numerical model resemble this structural concept (see Chapter 2.2 and Fig. 9).

It is not necessary to incorporate the actual fault throw into the hydrogeological concept since these fault zones generally extend beyond the aquifer host rock. Hence, only the fault zone thickness remains as important geometric value and was therefore integrated into the numerical investigations based on a realistic range (see Chapters 4.2.1 and 2.2). The fault zone length has been fixed to a value of 1000 meters and the fault inclination to a value of 70 degrees. Both were derived from the previously mentioned seismic information and chosen as mean characteristic values (see Chapter 2.2).

## **4.2 Hydraulic numerical simulation of a fault zone inside the Upper Jurassic aquifer**

### *4.2.1 Spatial and temporal discretization*

As it is the aim to exactly reproduce the geometric complexity of the previously presented concept (see Chapter 4.1) while mathematically describing its hydraulic state, a numerical approach was favored over an analytical one due to its geometric freedom. For this the numerical simulator MOOSE framework (Gaston, Newman, Hansen, & Lebrun-grandié, 2009; Permann et al., 2020) combined with the reservoir simulation app GOLEM (Cacace & Jacquy, 2017), the mesh-generation-program MeshIT (Blöcher & Cacace, 2015) and the visualization-plus-pre-/post-processing-tool Paraview (Ahrens, Geveci, & Law, 2005) were chosen. The combination of these open source tools allows for a continuum approach together with discrete elements in an unstructured tetrahedral mesh, state-of-the-art numerical solvers and

preconditioners, as well as parallelization capacities, suitable for high-performance computing (HPC) clusters. This guarantees a precise consideration of the geometry and a fast and efficient approach to calculate the pressure evolution during a pumping test for different parameter combinations. Furthermore, the ability to facilitate a high number of well test simulations requires the usage of a HPC system and is necessary to investigate the UJA in its whole (see Chapter 4.6.1 and 4.6.2 for a description of the parameter space exploration).

The geometrical model concept can be summarized in the following way (Fig. 20). The aquifer is represented with homogeneous properties, a thickness of 500 meters and a lateral extent of 30 x 30 kilometers (no flow boundaries). A 70-degree-inclined and 1000-meter-long fault zone is located in the middle of this permeable rock layer, with a vertical well in its center (see Chapter 4.1). The fault zone thickness should be variable and is integrated as independent variable into the parameter study (see chapters 4.6.2 and 4.9.2 for detailed information of the thickness variation during the deployed numerical investigations).

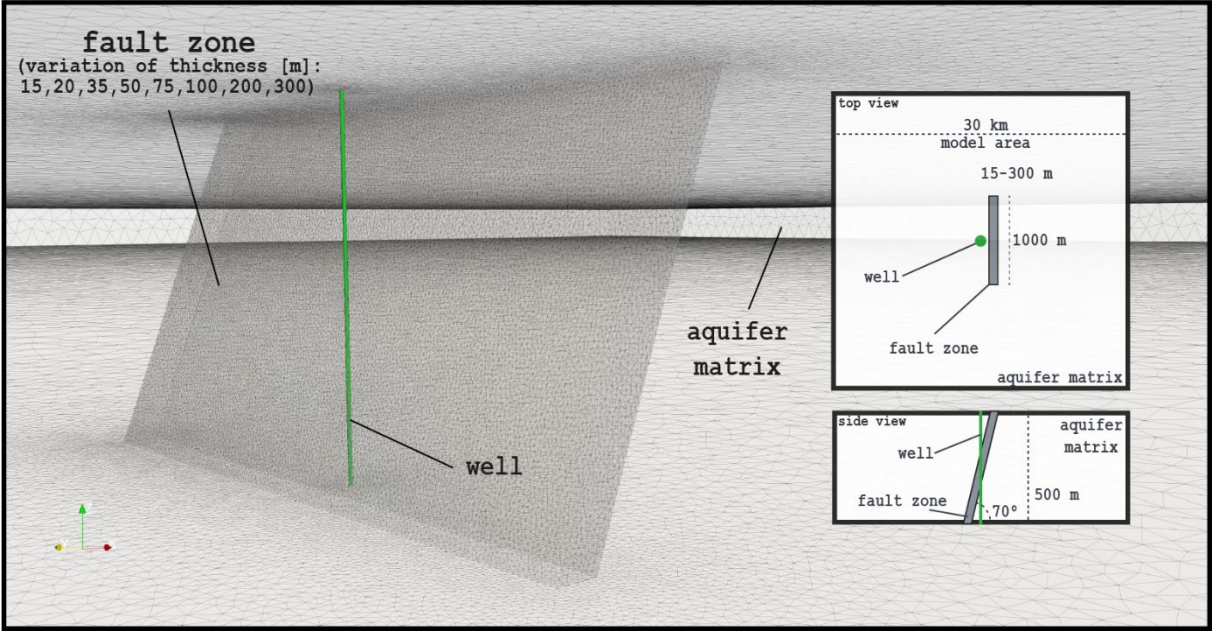


Fig. 20 Hydrogeological model (right) and unstructured tetrahedral mesh (left, background) of the numerical simulation.

To use available computational resources efficiently, an adequate spatial and temporal discretization of the individual numerical simulations is necessary without introducing numerical errors or unnecessary inaccuracies for further evaluation. The summarized geometry was represented in a tetrahedral mesh (Fig. 20) consisting of two continua: first, the host rock (further called matrix); second, the fault zone; and additionally a discrete lower dimensional element that depicts the borehole, at which the production sink was applied. For every fault zone thickness investigated in the parametric analysis a separate mesh had to be generated in

order to allow the variation of this variable. Regarding the quality of the spatial discretization, an optimization was conducted. In a first step, the main goal was to construct a visual appropriate representation of the desired geometry while keeping the total number of tetrahedral elements low to enable a fast simulation. This resulted in mesh-element-numbers ranging from ~0.45 million (300-meter fault zone thickness) to ~1.3 million (15-meter fault zone thickness) elements. To investigate if this discretization was sufficient a test case was calculated for each mesh and then compared against the same case but with a global mesh refinement of one level (each existing tetrahedral was split into four child elements). The results showed that the calculated pressure values varied between the refined and the normal mesh version by an average of about 0.02%. This variation influenced the Bourdet derivative evaluation only in the first two to four time steps while in the remaining ones no visual difference could be noticed. Because the early time behavior of the derivative is not of interest to the main analysis (see Chapter 4.5), the unrefined meshes were accepted for the main parametric analysis.

In order to choose a suitable temporal discretization, it is important to characterize simulation goal again. Well tests for as many parameter combinations as possible have to be simulated (see chapters 4.6.2 and 4.9.2 for details on the actual parameter space sampling). These tests must then be analyzed regarding their flow regime and, in the second workflow package, their temporal productivity evolution in dependency of the investigated parameter space. The time span over which pumping tests gather hydraulic data in practice is generally only a few days long. Additionally, in the field only the recovery phase data of these tests is suitable for a proper evaluation of the well and reservoir properties. The reason is that it is technically not possible to produce water under a constant rate during draw down (Alt & Kahnt, 2014; Bourdet, 2002). Therefore, the actual field data for evaluation by a reservoir engineer has an even shorter time span. For the simulated pumping tests, a time of 500 h was set as extreme value that would always be longer than any well test carried out in reality for the UJA. In addition, the difficulty of keeping a constant production rate does not apply for the numerical model. This allows for directly calculating only the pressure drawdown, which reduces the simulation time. The temporal discretization of the first workflow package (Fig. 21, temporal discretization of the second workflow will be explained in Chapter 4.8) was set by choosing an adaptive time stepping scheme based on the difficulty of the solution with an initial time step size of one second and an appropriate growth factor (the previous time steps gets multiplied by this factor if the number of iterations is below a maximum allowed iterations count) (Idaho National Laboratory, 2019). For the determination of a suitable value for this factor, an optimization was carried out. An example parameter combination that exhibits linear flow was chosen to compare

different growth factors to the resulting total number of time steps and the accuracy of the DER calculation (for information about der Bourdet Derivative and flow regimes refer to Chapters 2.3 and 4.5). As can be seen from Fig. 21, growth factors above 2.0 decrease the length and accuracy of the DER curve significantly. At the same time an exponential increase in the total number of time steps can be observed for the values 1.1 and 1.2. Therefore, a growth factor of 1.6 with a resulting total time step number of 30 was set for the discretization of the proposed 500 h simulation time.

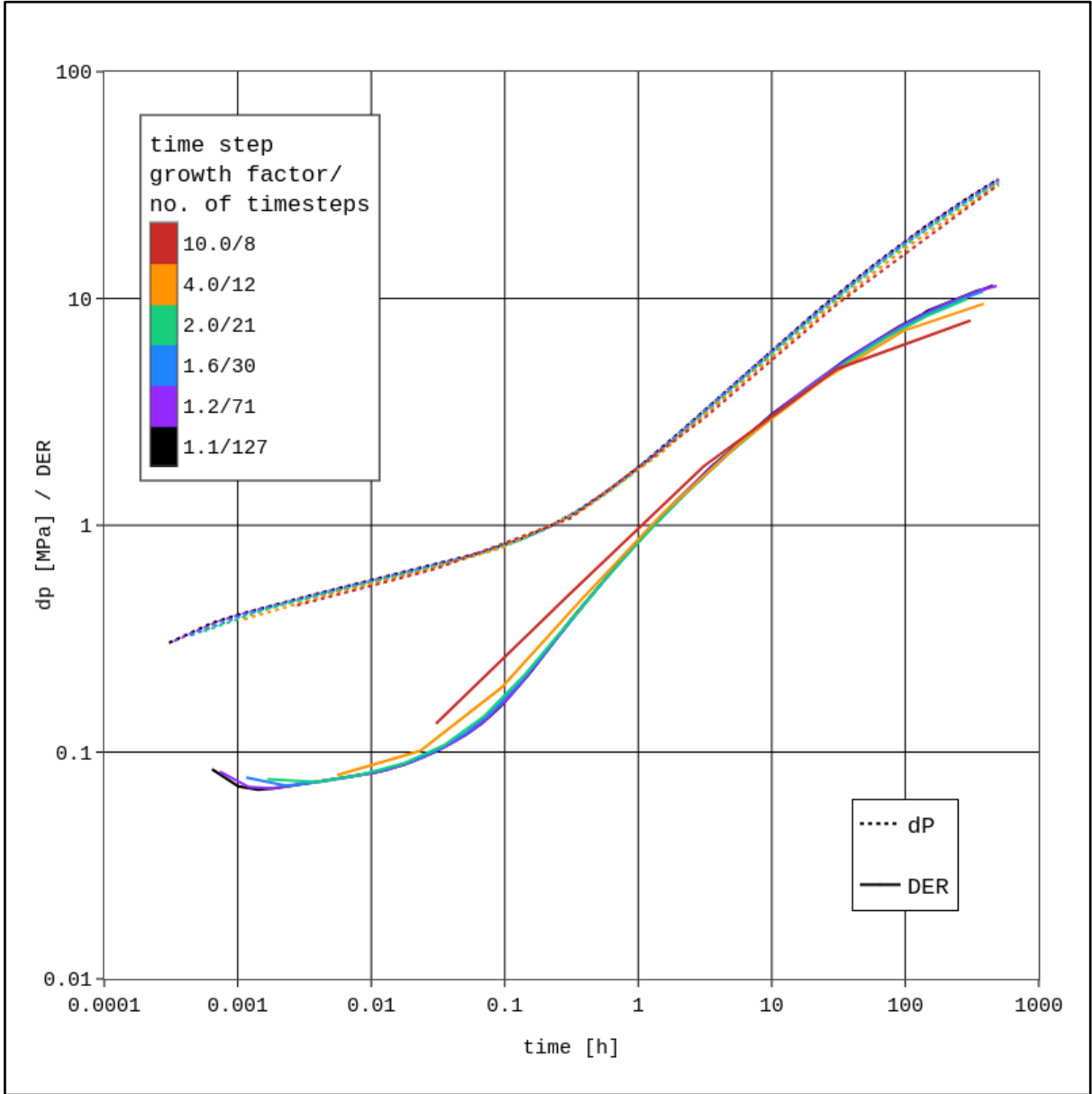


Fig. 21 Influence of temporal discretization on the simulation result of an example parameter combination exhibiting linear flow; initial timestep = 1 second; a high growth factor corresponds to less timesteps over the simulation timespan; unprecise numerical solutions can be observed by shortened and deviated dP and DER curves compared to simulation output with a higher number of timesteps.

#### 4.2.2 Finite element simulator – GOLEM

As the observation of the hydraulic response of a faulted reservoir to water extraction is the goal, a calculation of fluid flow by Darcy's law is sufficient (introduced in a general form in equation (4) in Chapter 2.5). Equation (5) presents the relevant mass balance equation as it is integrated in the GOLEM simulator (Cacace & Jacquey, 2017). Since GOLEM is capable of coupling thermal, hydraulic and mechanical behavior of a porous medium, (5) gets simplified for pure hydraulic calculations into equation (6) with the Darcy velocity as in (7). These two equations form again the continuity equation (4) presented in Chapter 2.5. In equation (6) porosity and fluid bulk modulus form the specific storage.

$$\text{Mass Balance Equation} \quad \frac{\partial (n \rho_f)}{\partial t} + \nabla \cdot (n \rho_f \mathbf{v}_f) - Q_f = 0 \quad (5)$$

$$\text{Pore Pressure Equation} \quad \frac{n}{K_f} \frac{\partial p_f}{\partial t} + \nabla \cdot \mathbf{q}_D - Q_f = 0 \quad (6)$$

$$\text{Darcy's Law} \quad \mathbf{q}_D = -\frac{\mathbf{k}}{\mu_f} (\nabla p_f - \rho_f \mathbf{g}) \quad (7)$$

$n$  = porosity [-]

$p_f$  = pore pressure [Pa]

$\rho_f$  = fluid density [ $\text{kg}/\text{m}^3$ ]

$t$  = time [s]

$\mu_f$  = fluid viscosity [ $\text{Pa} \cdot \text{s}$ ]

$\mathbf{v}_f$  = fluid velocity [ $\text{m}/\text{s}$ ]

$\mathbf{q}_D$  = Darcy's velocity [ $\text{m}/\text{s}$ ]

$Q_f$  = sink/source [ $\text{m}^3/\text{s}$ ]

$\mathbf{k}$  = permeability tensor [ $\text{m}^2$ ]

$\mathbf{g}$  = gravity vector [ $\text{m}/\text{s}^2$ ]

$K_f$  = fluid bulk modulus [Pa]

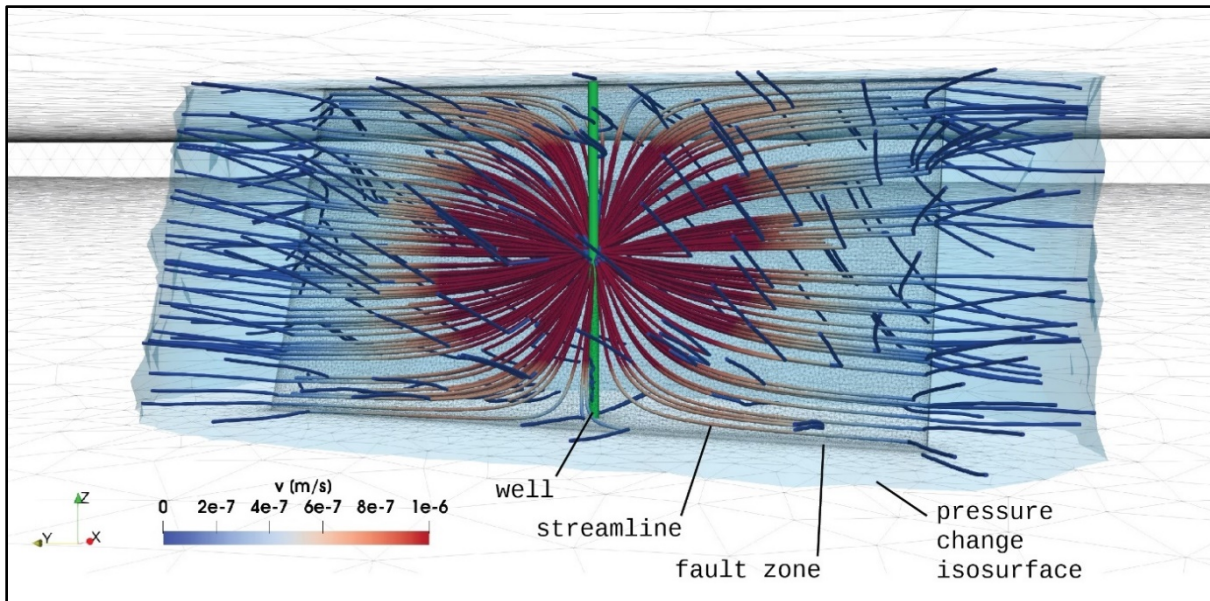


Fig. 22 Example flow field of the numerical model with linear flow behavior, streamlines colorized after the flow velocity ( $v$ ), induced pressure change as blue transparent isosurface.

Fig. 22 shows an example simulation result. The applied water extraction in the well induces a pressure change which is shown as a transparent isosurface while the corresponding streamlines are colorized according to the local flow velocity.

### 4.3 Hydraulic properties of the Upper Jurassic aquifer

Besides the information about the geometry of the introduced main hydraulic elements (see Chapters 2.2 and 4.1), it is necessary to know the relevant properties of their corresponding host rock. Available data was therefore gathered from literature and field engineers (ERDWERK GmbH) and summarized in Tab. 1 for all parameters relevant for a hydraulic simulation. Information about the fluid viscosity is based on pure water properties of the NIST Chemistry WebBook while production rates were taken from the Geothermal Information System (Agemar et al., 2014; Lemmon, McLinden, & Friend, 2018).

*Tab. 1 Possible ranges for the hydraulic parameters of the UJA; Unit conversions calculated for a fluid density of  $971.82 \text{ kg/m}^3$  and a fluid viscosity of  $2.89 \times 10^{-4} \text{ Pa*s}$  (30 MPa pore pressure and  $100^\circ\text{C}$  reservoir temperature).*

$x_i$	$i$	Min	Max	Unit	Source
Matrix permeability	1	$1.0 \times 10^{-17}$	$1.0 \times 10^{-12}$	$\text{m}^2$	Birner (2013) TUM (2019)
		$(3.3 \times 10^{-10})$	$3.3 \times 10^{-5}$	$\text{m/s}$	
Matrix storage	2	$2.0 \times 10^{-12}$	$1.6 \times 10^{-10}$	$1/\text{Pa}$	TUM (2019)
		$(2.0 \times 10^{-8})$	$1.6 \times 10^{-6}$	$1/\text{m}$	
Fault zone permeability	3	$1.0 \times 10^{-14}$	$1.0 \times 10^{-9}$	$\text{m}^2$	Birner (2013) TUM (2019)
		$(3.3 \times 10^{-7})$	$3.3 \times 10^{-2}$	$\text{m/s}$	
Fault zone storage	4	$2.0 \times 10^{-12}$	$1.6 \times 10^{-10}$	$1/\text{Pa}$	TUM (2019)
		$(2.0 \times 10^{-8})$	$1.6 \times 10^{-6}$	$1/\text{m}$	
Fault zone thickness	5	15	300	m	Agosta and Aydin, (2006); Michie et al. (2014)
Fluid viscosity	6	$1.0 \times 10^{-4}$	$3.0 \times 10^{-4}$	$\text{Pa*s}$	NIST (Lemmon et al. 2018)
Production rate	7	20	90	$1/\text{s}$	Geotis (Agemar et al. 2014)

A permeability range for the UJA is available in Birner (2013). A range for the permeability and specific storage values of the UJA was gathered from unpublished reports in collaboration with the research project Geothermal Alliance Bavaria and is based on the evaluation of 17 interference tests in the Munich area (TUM, 2019). The advantage of using the results from these tests is that they describe the average reservoir behavior between two exploration wells and therefore represent the properties of the numerical model's aquifer matrix (see Chapter 4.1). Small scale heterogeneities which would influence laboratory data are not of interest as

explained in Chapter 4.1. An extension by approximately an order of magnitude of these collected ranges assures a conservative approach (see Tab. 1).

#### **4.4 Numerical model calibration using field data**

Before the desired investigation of the behavior of fault zones in the UJA's well tests can be carried out with confidence, it is necessary to calibrate the numerical model (Bundschuh & Suárez Arriaga, 2010). Hydraulic data of a geothermal exploration site in the Munich area that exhibits a flow regime dominated by a fault zone was available for the verification of the chosen model concept. This data comprises the pressure evolution of a 96-h-long pumping test, which includes a 24-h-long recovery phase, and the associated production rates. By choosing a starting point inside the realistic parameter ranges (see Tab. 1 and Chapter 5.2) and varying fault zone thickness, specific fault zone storage and permeability as well as specific matrix storage and permeability until the pressure change and DER of the recovery phase could be matched and a first calibration was carried out (see also Chapter 4.5). Next, the calibration was tested against the actual production history. These two steps were repeated until recovery and production history could both be appropriately matched (calibration results can be found in Chapter 5.1).

#### **4.5 Flow regime analysis of simulated pumping tests**

For the investigation of a fault zone's influence in a real world parameter space on the hydraulic response of a geothermal well the following interpretation models are of main interest: Radial Flow, Bilinear Flow, Linear Flow and Negative Boundary Effect (also called closed homogenous reservoir) (see also Fig. 23 and Fig. 27). Naturally, it comes to mind that those mathematically defined models have smooth transitions from one to another inside the combinations of natural parameter ranges. The models and their behavior in the diagnostic plot (plot of pressure change and Bourdet Derivative in a log-log scale, see Chapter 2.3) are now further characterized (Bourdet, 2002):

1. If the fault zone exhibits only a slight improvement in its hydraulic properties (permeability and specific storage) compared with the matrix, it might not be observed in the DER, even though it actively contributes to well productivity. Only a normal radial flow regime with a DER slope of 0 can be observed.
2. Increasing hydraulic properties of the fault zone and contrast to the matrix start can be observed through a bilinear flow regime as the slope of the  $dp$  and DER both approach 0.25. The flow occurs both perpendicular (inside the matrix) and parallel (inside the fault zone itself) to the fault surface.

3. When flow along the fault zone starts dominating the pressure response inside a well, the pressure drop within the fault zone becomes negligible. Flow occurs mainly in the early time region perpendicular to the fault surface inside the matrix, and the slope of  $dp$  and DER tend to 0.5.
4. An increase in the thickness of the fault zone can also lead to a point where the volume inside the fault zone becomes relevant and bilinear or linear effects shift toward the late time region. These flow regimes are then related to a channel structure.
5. If one considers the hydraulic properties of the matrix surrounding the fault zones, there will come a point where it will start acting as a barrier while its values decrease. The slopes of  $dp$  and DER will increase up to 1.0. Here, the matrix behaves as an impermeable negative boundary.
6. Certain settings of low contrast between matrix and fault zone can also lead the evolution of the derivative without any of the characteristics being fulfilled. Especially unusual combinations of the specific storage values in combination with the chosen model geometry can lead to this point. Pressure data behaving like this is classified as unspecific and is associated between radial and bilinear flow belonging more to the first.

*Tab. 2 Characteristic properties of the flow regimes of interest; analytical model versus classification for real world parameter space.*

<b>Flow Type</b>	<b>Radial</b>	<b>Bilinear</b>	<b>Linear</b>	<b>Negative boundary</b>
<b><i>analytical model properties</i></b>				
<i>dP slope</i>	-	0.25	0.5	1
<i>DER slope</i>	0	0.25	0.5	1
<i>additional properties</i>	-	at the same time	at the same time	DER slope over a log cycle early at slope 1 than dP
<b><i>Classification for automated PTA</i></b>				
<i>dP slope</i>	-	0.15-0.375	0.375-0.6	0.6-1.0
<i>DER Slope</i>	0-0.15	0.15-0.375	0.375-0.6	0.6-1.0

A definition is necessary to classify which flow observations of simulated pumping tests are assigned to one of the above-defined flow regimes in a continuous parameter space. Tab. 2 shows the characteristic properties of the ideal mathematical flow regime models and also the definition that was chosen to automatically classify transient pressure observations in the

parameter space of the UJA. The selected classes are based on the analytical interpretation models (see Chapter 2.3 and Fig. 23) and should reflect how a field engineer would classify the pressure curves in practice.

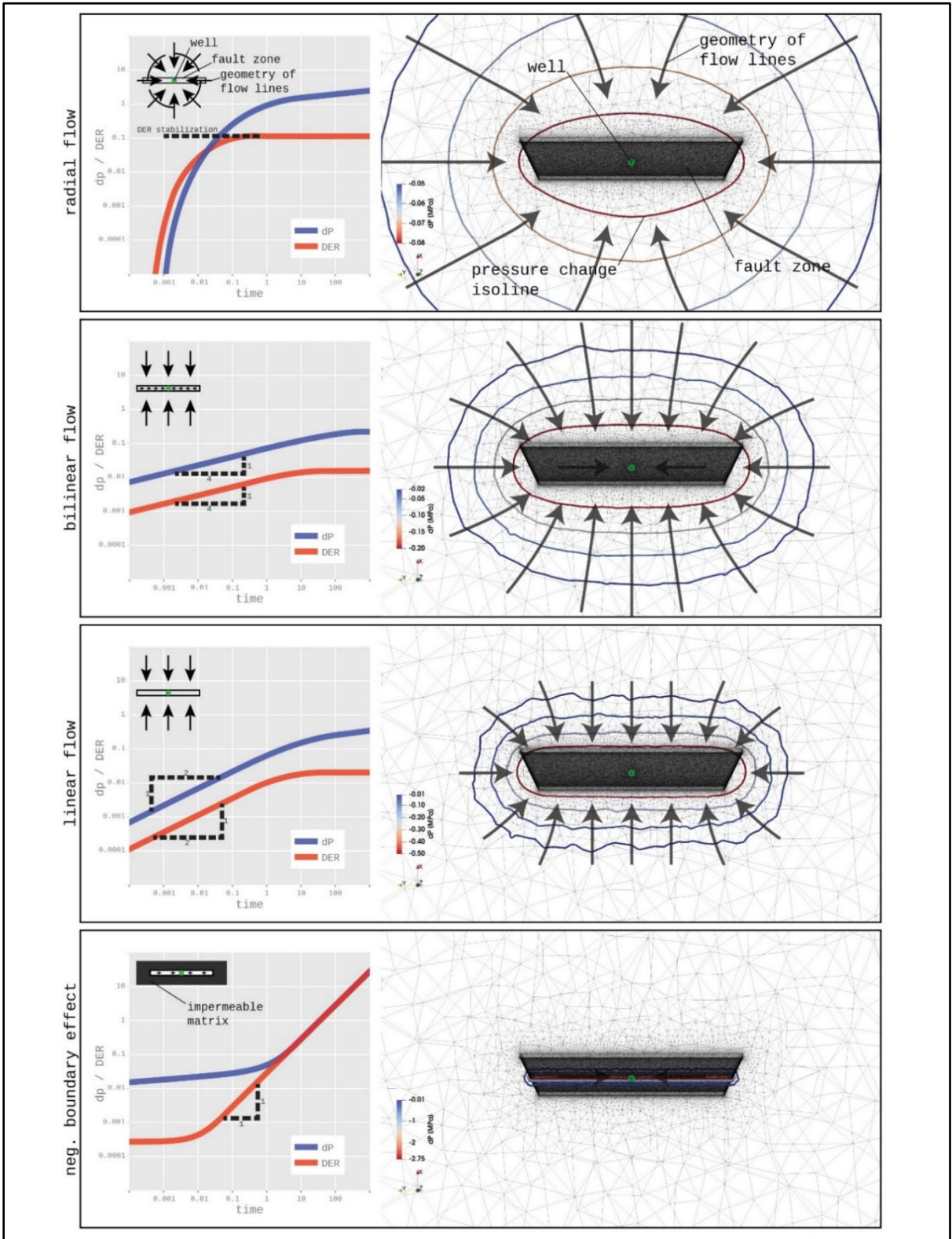
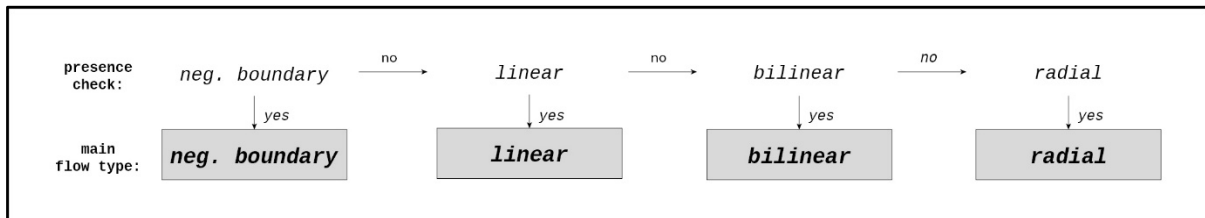


Fig. 23 Flow regimes connected to fault zones; Left: pressure change ( $dp$ ) of idealized pumping test, associated Bourdet Derivative and concept of flow field, see also Tab. 2 for a summary;

*Right: representative example during presence of each flow regime in the complex geometry of the 3D numerical model, numerically calculated pressure change isolines around the fault zone.*

This logic was then translated into a Python tool that iterates over the DER and  $dp$  slopes of a model result. In detail, for each sampled parameter combination, the DER was calculated and each DER-data point of an individual pumping test time series was classified based on the previously presented and practically oriented characteristics (Tab. 2). Afterwards, this DER-time-point-classification was reduced to the main occurring flow regime corresponding to the sampled parameter combination following a decision tree (Fig. 24). This automatization is necessary to enable the evaluation of large numbers of simulation results and identify where in the desired parameter space each flow regime is present.



*Fig. 24 Decision tree for the classification of DER curve based on the detection of a flow type in any of the cruvs data points.*

## 4.6 Parameter space investigation - Identifying limiting surfaces between flow regimes

### 4.6.1 Flow regime focused sensitivity analysis

The first step for an efficient exploration of a parameter space is the identification of all relevant parameters and the quantification of their influence on the researched quantity, the main flow regime of a pumping test (see Chapter 4.5). Therefore, a sensitivity analysis (SA) was carried out to find and describe all parameters that alter the shape of the Bourdet Derivative in the diagnostic plot, which forms the basis for the flow regime interpretation. There are generally two types of SA: local and global SA. Both aim to describe how a model output is affected by the variation of uncertain input parameters. While local SA looks at the model output variation related to small changes in the input, global SA investigates the entire input parameter space to provide reliable sensitivity measures while nonlinear effects and parameter interactions are present. This entails increased computational cost compared with local SA (Petropoulos & Srivastava, 2017; Saltelli et al., 2004). Because the computational cost of the underlying numerical model even on a HPC system is still too high to deploy a proper global SA, a local SA with a high sample size was deployed. Thus, each of the hydraulic properties listed in Tab.

1 ( $x_i, i = 1, 2, \dots, 7$ ) was sampled by six values ( $x_{i,s}, s = 1, 2, \dots, 6$ ) evenly spaced (log spaced for fault zone and matrix permeability) over its possible range for each combination among maxima and minima of the remaining parameters (further called fixations  $F_j, j = 1, 2, \dots, 2^{i_{max}-1}=6$ ) and their corresponding ranges. Six parameter perturbations in this one-at-a-time approach were chosen compared to the recommended minimal number of three (endpoints and midpoint of parameter range) to increase the accuracy of the sensitivity analysis (Petropoulos & Srivastava, 2017).

$$DER \text{ shape change} \quad SC_{x_{i,min}-x_{i,s},F_j} = \sum_{k=1}^{max} (DER'_{x_{i,min},t_k} - DER'_{x_i,t_k})^2 \quad (8)$$

$SC$  = shape change measure

$x_{i,s}$  =  $s$ -th sampled ( $s = 1, 2, \dots, 6$ ) value of the investigated parameter  $x_i$  ( $i = 1, 2, \dots, 7$ )

$x_{i,min}$  = minimum value of the investigated parameter range

$F_j$  =  $j$ -th fixation of the currently not investigated parameters,  $j = 1, 2, \dots, 2^{i_{max}-1}=6$

$t_k$  =  $k$ -th data point in time

$DER'$  = slope of the Bourdet Derivative on the log-log-plot

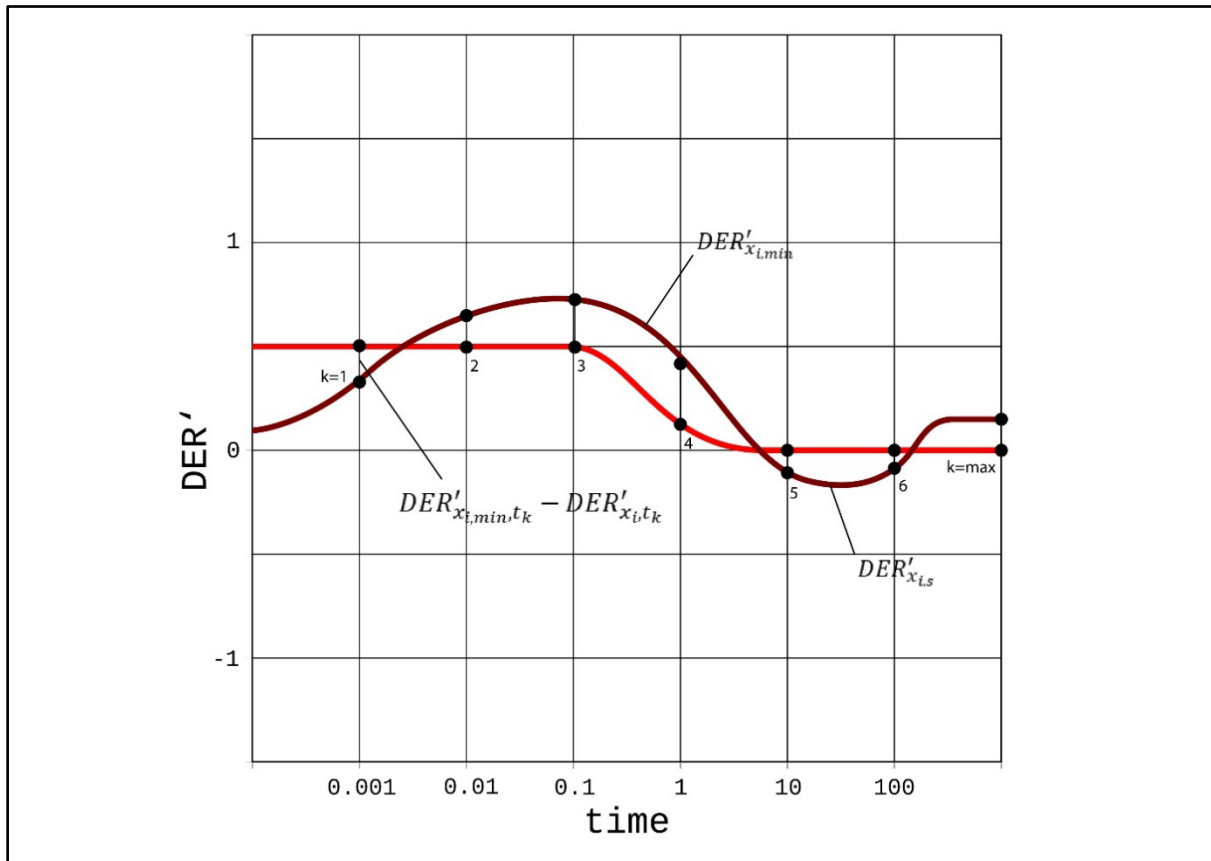


Fig. 25 Visualization of the quantification basis of the DER shape change described in equation (8); y-axis =  $DER'$  = slope of the DER on the log-log-plot; x-axis = time.

That resulted in the calculation of  $6 * 2^6 = 384$  simulations and their DER curves for all parameters of interest with the exception of the fault zone thickness since it is necessary to generate a new mesh every time this parameter needs to be varied (see Chapters 4.2.1 and 4.3). Additionally, fault zone thickness values below 100 meters are more realistic as stated before (see Chapters 4.1 and 2.2). This eventually resulted in a manual perturbation for this parameter of five unevenly spaced values (20, 35, 50, 100 and 200 meters) with the focus on lower fault zone thicknesses ( $5 * 2^6 = 320$ ). The DER shape changes between the six, respectively five, values of the investigated parameters were compared relative to the DER curve at parameter range minimum,  $DER_{x_{i,min},F_j}$ . The quantification of the DER shape change between the two compared curves ( $SC_{x_{i,min}-x_{i,s},F_j}$ ) was done according to equation (8), by summarizing the quadratic differences of the first derivative of the DER in each data point in time (see Fig. 25). This resulted in five (four, for fault zone thickness) DER shape change values per investigated parameter for each of the  $2^6 = 64$  fixations ( $F_j$ ). Through normalizing each parameter variation on its parameter range, a comparison of the sensitivity between all hydraulic properties is possible (Petropoulos & Srivastava, 2017).

#### 4.6.2 Parameter space exploration – flow regimes

With the application of RAVEN, an open source software framework for parametric and stochastic analysis (Alfonsi et al., 2017), and the use of an HPC cluster (LRZ linux cluster and supermuc (Leibniz-Rechenzentrum, 2017)) it was possible to automate and calculate a great number of artificial pumping tests in a reasonable time. On a normal workstation (Intel® Core™ i7-4790K CPU @ 4.00GHz), simulation times ranged from ~37 minutes (15-meter fault zone thickness) to ~9 minutes (300-meter fault zone thickness). By running the numerical model on an HPC system (lrz linux cluster; Intel® Xeon® E5-2697 v3) these times reduced to ~24 minutes (15-meter fault zone thickness) and ~4 minutes (300-meter fault zone thickness). Additionally, many simulations could be calculated simultaneously, which reduced the overall time needed drastically.

After the basic numerical model was set up and the flow regime analysis automated, a sampling scheme had to be chosen to scan the input space. A full factorial design sampling approach (hereinafter referred to as grid sampling) is suitable for this. In other words, each input parameter range is divided into levels, and all possible combinations of these levels across all input parameters are evaluated (Montgomery, 2013). The grid was set, limited by the simulation time and the available computational resources and based on the possible parameter ranges

listed in Tab. 1 as given in Tab. 3. The resulting parameter-grid is made up of 30,492 input-space-coordinates/parameter-combinations.

*Tab. 3 Specification of the grid sampling for the flow regime focused investigation.*

<b>Parameter</b>	<b>Spacing-Type</b>	<b>Steps = No. of Samples</b>
fault zone and matrix permeability	log, even	11
specific fault zone and matrix storage	linear, even	6
fault zone thickness	manual pick (15, 20, 35, 50, 100, 200 and 300 meters)	7

#### 4.6.3 Identification of flow regime transitions in parameter space

The next step after carrying out the parametric study is the investigation of the produced simulation results (see Fig. 17). First, sampled points at the boundary between the occurring flow regimes were extracted from the 30492 input-space-coordinates and as individual data sets separated for each flow regime boundary (radial-to-bilinear, bilinear-to-linear, linear-to-neg.-boundary). These data sets represent the transition between the fault zone related flow regimes as point data. To get a functional relationship for a continuous visualization of the boundary data sets in the investigated parameter space a polynomial regression was applied. In other words, the regressions in this case are a means to mathematically describe the limit surfaces in the parameter space that separate the occurrence of the different flow regimes (Alfonsi et al., 2017). These functions enable the prediction of a flow regime at a parameter perturbation that has not been sampled in the previous parameter space exploration. To perform such a polynomial regression, one target variable ( $y$ , see Appendix 9.1) among all the investigated hydraulically sensitive parameters ( $x_i$ , see Appendix 9.1) had to be chosen while the remaining ones were used as explanatory/predicting variables. Since the matrix permeability has the highest relevance for the field application, as it is one of the main results of pumping tests, and exhibits high sensitivity (see Chapter 5.3) it was set as  $y$ . Depending on these two variable types each boundary data set was split into a predictor data set ( $X$ ) and a target data set ( $Y$ ) on which the regression model was fit. Since a polynomial regression is a special case of a linear regression the same principle of minimization of residual sum of squares between observed dataset responses and by the regression model predicted responses through fitting coefficients applies (Draper & Smith, 1998). The Python package “scikit-learn” was utilized to achieve this (Pedregosa, Weiss, & Brucher, 2011). Scaling of the underlying data set (extracted flow regime boundary data points) according to equation (9) was introduced to increase numerical stability

of the regression (Buitinck et al., 2013; “scikit-learn user guide: preprocessing data,” 2018). The respective scaling information which forms the base for all further steps of the regression analysis is provided in Appendix 9.2. The determination of a suitable polynomial degree was done by calculation of the adjusted coefficient of determination for the degrees from 1 to 12.

Data set scaling 
$$X_{i,j,scaled} = \frac{X_{ij} - \bar{X}_i}{\sigma_i} \quad (9)$$

$X_{i,j,scaled}$  =  $j$ -th scaled value of  $i$ -th predictor ( $x_i$ ) training data set

$X_{ij}$  =  $j$ -th value of  $i$ -th predictor ( $x_i$ ) training data set

$\sigma_i$  = standard deviation of training data set for  $i$ -th predictor

$\bar{X}_i$  = mean of training data set for  $i$ -th predictor

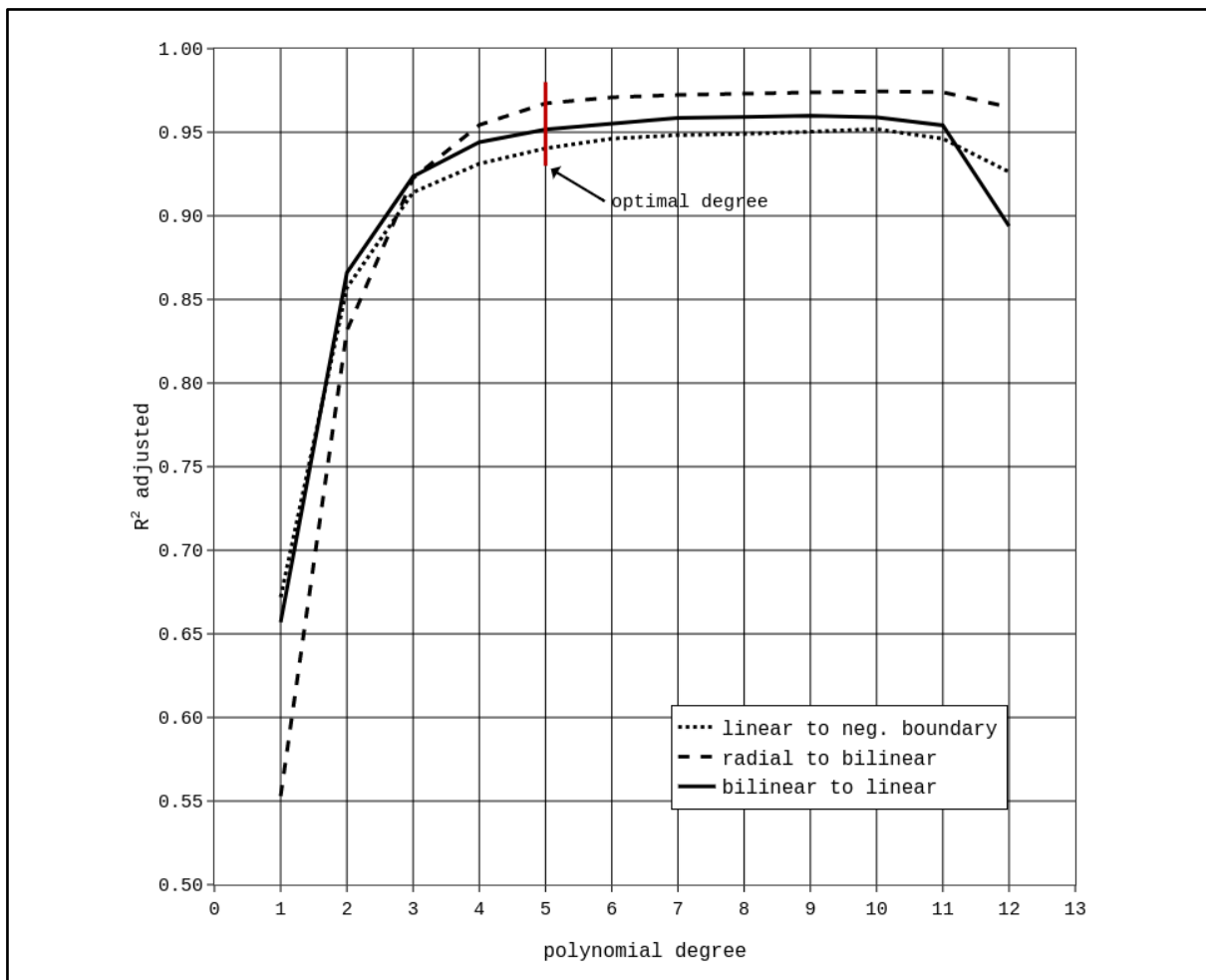


Fig. 26 Determination of optimal degree for polynomial regression;  $R^2$  adjusted versus polynomial degree.

Fig. 26 shows the adjusted coefficient of determination ( $R_{adjusted}^2$ ) versus the polynomial degree for the regression of the three transitions of interest (between the radial, bilinear, linear and neg. boundary flow regime). The change of  $R_{adjusted}^2$  from degree five to degree six of the polynomial drops below 1% for all three transitions. Hence, degree five was used for the

regression analysis. Subsequent visualization and interpretation of the presence of a flow regime in the investigated parameter space was built upon the resulting polynomial relationship. The corresponding regression functions are provided in Appendix 9.3.

#### **4.7 The productivity index of a well and its alteration by a fault zone**

This section marks the start of the second workflow package as explained above (Fig. 18). It therefore starts with an explanation how the productivity index (see the state of the art Chapter 2.4) can be used to quantify the influence of a fault zone on the productivity of a well. In this context it is important to note, that the focus is on the relationship between a fault zone and the surrounding reservoir matrix, which means that well effects (e.g. well storage & skin) were not considered. By using downhole pressure and assuming an ideal well with no storage and skin, the *PI* is further seen as a pure reservoir measure. Additionally, the presence of turbulent flow in the UJA parameter space had to be ruled out in order to neglect the non-linear part of equation (3) completely. The Reynolds number can be used to see whether turbulent flow occurs in the subsequent analysis. According to Bundschuh & Suárez Arriaga (2010), any flow with a Reynolds number below 10 is clearly laminar. The most extreme parameter combination for the numerical model of the Upper Jurassic aquifer shows the following: For a 15-meter fault zone thickness, fault zone permeability of  $1.0 * 10^{-9} \text{ m}^2$ , the lowest viscosity of  $0.0001 \text{ Pa} * \text{ s}$ , a very high fluid density of  $990 \text{ kg/m}^3$ , applying a production rate of  $30 \text{ l/s}$  (this value was fixed for all simulations based on the findings of the sensitivity analysis, see Chapters 4.6.1 and 5.2) only to the well surface inside the  $70^\circ$  inclined fault zone and assuming conservatively a low porosity at this high permeability of 0.1 (Bohnsack, Potten, Pfrang, Wolpert, & Zosseder, 2020; Homuth, Götz, & Sass, 2015) the Reynolds number can be calculated as 1.48. This value quickly decreases below 1.0 as soon as the parameter combination or flow geometry changes or the distance to the well is accounted for. This allows the turbulence term in equation (3) to be ignored and also confirms the application of Darcy's law for the desired description of the *PI* of the reservoir.

The idea to derive the actual influence of a fault zone on well productivity for a given combination of hydraulic properties is based on the comparison of a set of two simulated pumping tests. For the first simulation, both the matrix and fault zone are parametrized. In the second, the fault zone continuum is replaced by the matrix. The difference between the resulting pressure curves is a measure for the fault zone influence, which can then be expressed as a *PI* change value ( $\Delta PI$ )(10).

For the individually calculated pressure curves of the numerical model,  $dp$  will never be constant during radial flow since only a production well in a closed system is integrated. During pseudo steady state conditions,  $dp$  is strongly influenced by the chosen reservoir geometry. The model extent is designed for the general investigation between matrix and fault zone and to prevent early pressure alterations by boundary effects. Additionally, only a production well is integrated. However, in reality, there is a complex setting with multiple production and injection wells influencing each other. The numerically calculated pseudo steady state is therefore not useful for comparison with real world cases. However, the  $\Delta dp$  (11) between the fault zone and matrix model can become constant at some point during radial or pseudo steady state flow. This depends on the parameter setting, which implies that the pressure transient has moved past the fault zone and that both models experience the same pressure evolution. Notably, this is the case for parameter settings in which the fault zone is hidden in the pumping test data and only radial flow can be observed. By calculating the slope of  $\Delta dp$  ( $\Delta dp'$ ) and extracting  $\Delta dp$  where  $\Delta dp'$  approaches zero,  $\Delta PI$  can be derived (12). It can also be proposed that  $\Delta dp'$  will not approach zero if the flow system is dominated by the fault zone and the majority of well productivity comes from it. It is not possible to calculate  $\Delta PI$  for these parameter settings.

$$\text{Absolute PI Change} \quad \Delta PI = PI_m - PI_{fz} \quad (10)$$

$$\text{Fault Zone Influence} \quad \Delta dp = dp_m - dp_{fz} \quad (11)$$

$$\Delta PI = \frac{q}{dp_m} - \frac{q}{dp_m - \Delta dp} \quad (12)$$

$$\text{Reference PI} \quad PI_{m,ref} = \frac{q}{dp_{m,t_{ref}}} \quad (13)$$

$$\text{Relative PI Change} \quad \Delta PI_{rel} = \Delta PI / PI_{m,ref} \quad (14)$$

$PI_m = \text{matrix model PI } [^1/(s * MPa)]$

$dp_m = \text{pressure change matrix model [MPa]}$

$PI_{fz} = \text{fault zone model PI } [^1/(s * MPa)]$

$dp_{fz} = \text{pressure change fault zone model [MPa]}$

$PI_{m,ref} = \text{matrix model PI at reference time } [^1/(s * MPa)]$

$\Delta dp = \text{pressure change difference [MPa]}$

$t_{ref} = \text{reference time, 342 [h]}$

Nevertheless, interpreting  $\Delta dp$  alone could lead to misconceptions because the magnitude of  $PI_m$  is important. This is because that  $\Delta PI$  is, of course, dependent on  $dp_m$  and therefore also on  $PI_m$ . For example, for a small  $PI_m$ , it is more likely that the fault zone will have a high  $PI$ -influence, thereby resulting in a high  $\Delta dp$ . This value cannot be applied to a high  $PI_m$  of a very

permeable aquifer because this would lead to an incorrect conclusion. It is therefore important to calculate  $PI_m$  for each parameter case, even though it cannot be determined precisely. By choosing a reference point ( $t_{ref}$ ),  $dp_{m,ref}$  can be extracted, and  $PI_{m,ref}$  (13) can be calculated in the same manner for each hydraulic scenario for comparison. For most parameter combinations, the best possible  $t_{ref}$  should not be affected by the model boundaries and should not be located in the early time region but rather only after most fault zone effects have passed. Considering that  $dp_m$  is still increasing at this point, the resulting  $PI_{m,ref}$  is decreasing. The influence of the fault zone can then be described as relative change in  $PI$ ,  $\Delta PI_{rel}$  (14), in a conservative fashion (no fault zone influence overestimation) by putting  $\Delta PI$  into relation to  $PI_{m,ref}$ . A  $t_{Ref}$  of 342 h was found as suitable reference time. This is the time-step of the numerical model in the middle to late time region, in which most parameter samples show radial flow and in which there are no early time effects because of the chosen geometry of well and fault zone. For high matrix permeability values (greater than  $\sim 1.0 \times 10^{-13} \text{ m}^2$ ), it is not possible to calculate  $PI_{m,ref}$  directly at this point because the pressure response is dominated by model boundaries. The last point of the pressure curve that shows radial flow is therefore extrapolated and used to calculate  $dp_{m,t_{ref}}$  (equation (15) (Bourdet, 2002)).

$$\begin{aligned} \text{Extrapolation of} & & dp_{m,t_{ref}} &= DER_{last\ radial} * (\ln t_{ref} - \ln t_{last\ radial}) \\ \text{pressure change at} & & & + dp_{m,t_{last\ radial}} \\ \text{reference time} & & & \end{aligned} \quad (15)$$

$dp_{m,t_{last\ radial}}$  = pressure change with latest radial flow behavior

$DER_{last\ radial}$  = Bourdet Derivative value at latest radial flow pressure point

$t_{last\ radial}$  = time of the latest radial flow pressure point

#### 4.8 Application of the reduced basis method to the finite element model

For a proper assessment on how different types of fault zones alter the well productivity index for various aquifer matrix properties, a rigorous exploration of the parameter space is necessary. The amount of samples that can be taken is primarily limited by calculation time of the underlying numerical model (as shown previously in Chapter 4.6.2). Naturally, more samples are better in order to ensure a high-resolution investigation. The computational cost of a minimal parameter space exploration based on grid sampling and the previously presented numerical model for the well-productivity-focused study can be estimated as follows:

Considering simulations on at least all combinations of maxima, minima, and mean values of the six governing input parameters (see further explanation in Chapter 4.9.1) as the smallest sample size that might be evaluated. The result would be  $3^6 + 3^3 = 756$  simulations. Because two model runs (with and without a fault zone) must be conducted. Based on the average calculation time of the GOLEM model of 23 minutes per run (see also Chapter 4.6.2), a continuous computation of ~12 days on a standard workstation would be necessary.

Ideally, a higher temporal discretization would be deployed for the productivity-focused study to enable a precise model result evaluation resulting in even longer simulation times. In addition, a greater sample size is needed for a proper assessment of the desired fault zone influence (Petropoulos & Srivastava, 2017). However, this quickly leads to large computational cost. Even with an HPC infrastructure, a significant calculation time is necessary if the normal FE model is used.

A possible way to overcome this high computational cost as a limiting factor is to apply the principle of model order reduction (MOR). The goal of MOR is to capture just the essential features of the input/output behavior of the desired system through some form of approximation while keeping the errors introduced by the approximation under control (e.g. neglectable for the desired system investigation) (Alfonsi et al., 2017; Manzoni, Quarteroni, & Rozza, 2012). This way, the overall time consumption can be lowered drastically. A comprehensive parameter study with a realistic fault zone setting becomes possible. Many different techniques to reduce a model's order exist, such as surrogate models, geometrical reduction, model reduction and computational reduction (Manzoni et al., 2012). A MOR technique of the computational type that allows for a certified approximation of a FE model is the reduced basis method (RB Method) in the here presented form. Low-dimensional approximations to solutions of parametrized partial differential equations are computed with a user-defined error bound (Hesthaven, Rozza, & Stamm, 2016; Prud'homme et al., 2002; Quarteroni, Manzoni, & Negri, 2015). The RB method used here is split into two stages:

- The offline stage; here, the computational expensive FE solution is calculated at several training points over the desired parameter space following a Greedy approach (a well-known algorithm to construct a reduced subspace (Degen, Veroy, & Wellmann, 2020; Manzoni et al., 2012), used to find the optimal training points). The amount of full FE simulations needed depends on the underlying parameter complexity and the defined approximation accuracy. A reduced model is then built based on these FE solutions. This reduced model is physics-preserving and maintains a high accuracy.

- The online stage; here, the reduced model is used to solve the problem with many different parameter values yielding a speed-up of several orders of magnitude compared with the full FE solutions. The reduced model is thus ideal for exploring the parameter space.

Degen et al. (2020) implemented this methodology as an application for the MOOSE framework, DwarfElephant, and demonstrated its speed-up as well as an example usage in geoscience. DwarfElephant was therefore used to build a low-order model for the previous FE model considering the possible parameter range.

As new data became available at this stage of the presented work, the parameter ranges shown in Tab. 1 were slightly adjusted. The updated possible ranges of the UJA used for the productivity focused workflow (Fig. 18) are summarized in Tab. 4.

*Tab. 4 Updated parameter ranges of the UJA and its fault zones, based on Tab. 1.*

	Min	Max	Unit
<b>Matrix permeability</b>	$1.0 \times 10^{-17}$	$2.0 \times 10^{-11}$	m <sup>2</sup>
<b>Matrix storage</b>	$2.0 \times 10^{-12}$	$1.6 \times 10^{-10}$	1/Pa
<b>Fault zone permeability</b>	$1.0 \times 10^{-14}$	$1.0 \times 10^{-9}$	m <sup>2</sup>
<b>Fault zone storage</b>	$2.0 \times 10^{-12}$	$1.6 \times 10^{-10}$	1/Pa
<b>Fault zone thickness</b>	15	300	m
<b>Fluid viscosity</b>	$1.0 \times 10^{-4}$	$5.0 \times 10^{-4}$	Pa*s

For each individual fault zone thickness, a separate reduced-order model had to be constructed because of the different underlying tetrahedral meshes. During the course of this work, a 75-meter fault zone thickness mesh was added to the existing range of discrete thickness values (see Chapter 4.6.2) in order to increase the possible sample resolution. The model contains now individually meshed fault zone thicknesses of 15, 20, 35, 50, 75, 100, 200, and 300 m.

The resulting reduced models have a maximum relative error tolerance of  $5.0 \times 10^{-4}$ . A comparison between a GOLEM (FE) and a DwarfElephant (RB) solution for exemplary input parameter combinations presenting the different flow regime types is shown in Fig. 27. Using

the RB method speeds up the calculation by four orders of magnitude, while the corresponding DER of the pressure curves still allows a proper pressure transient analysis (PTA). Only narrow differences in the very early or very late time region of the DER were found. Because these time regions are not used to derive the main flow regime or the  $\Delta PI_{rel}$ , they do not alter the subsequent analysis.

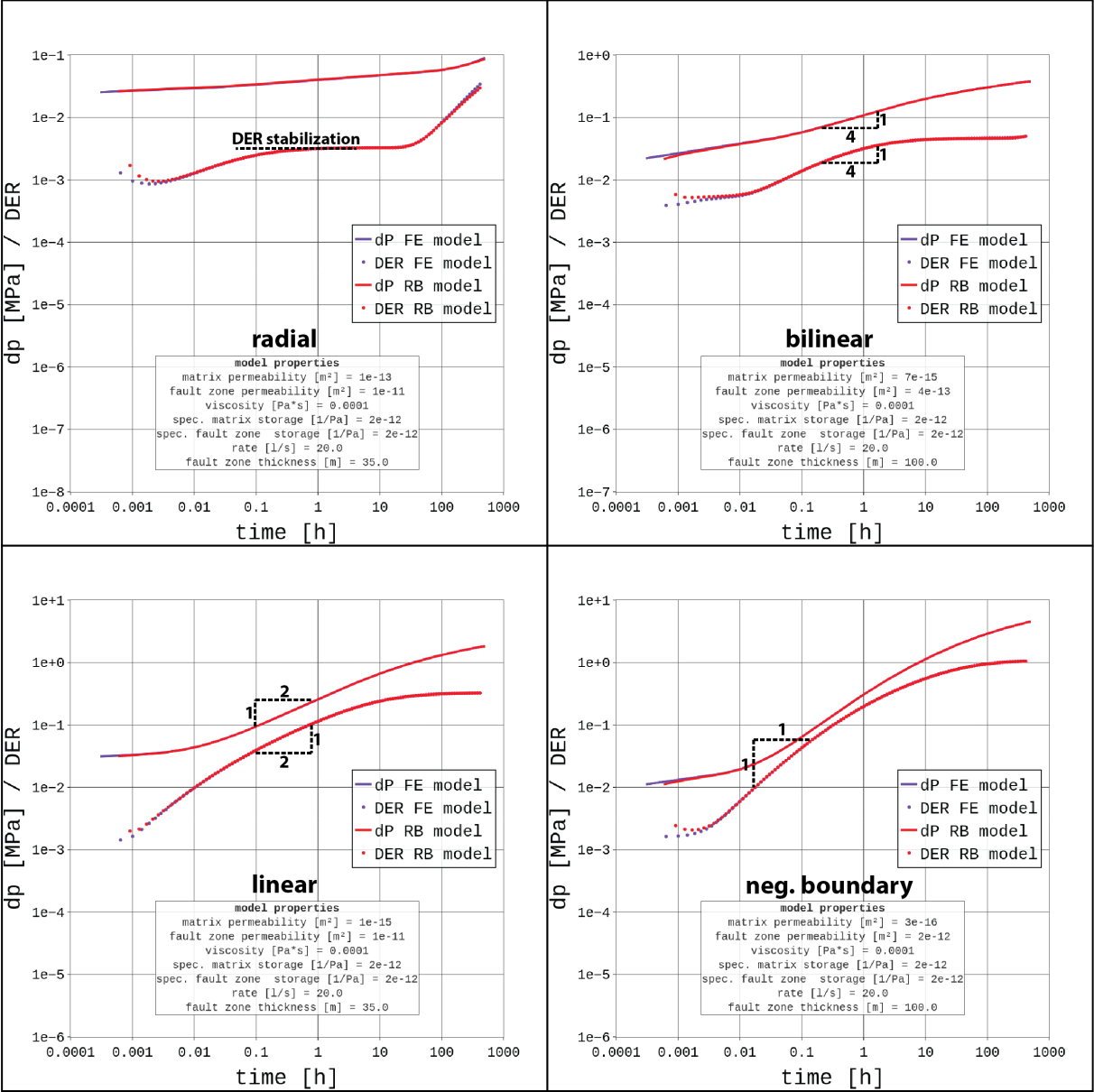


Fig. 27 Comparison between FE (GOLEM) and RB (DwarfElephant) model for four different parameter settings showcasing the different main flow regimes of interest. Each flow regime is represented by two pairs of curves, one pair (pressure change ( $dp$ ) as solid line, Bourdet derivative (DER) as dotted line) for each of the two models in a log-log scale. The characteristic slopes of the main flow regime are indicated (see also Chapter 4.5).

## 4.9 Fault zone induced productivity index change

### 4.9.1 Well productivity focused global sensitivity analysis

Because this part of the presented work centers on the *PI* (see Chapters 2.4 and 4.7) the sensitivity of the model input had to be reevaluated. As local SA tends to overestimate the influence of the input parameters (Degen et al., 2021; Wainwright, Finsterle, Jung, Zhou, & Birkholzer, 2014) and fast simulation times together with HPC infrastructure could be utilized (see Chapter 4.8), a more optimal global SA approach was chosen here. The aim was again to identify the importance of all parameters and focus the *PI* change analysis and results visualization on those with the greatest influence. The nature of the *PI* change definition presented here implies that the value of interest cannot be determined for every randomly sampled parameter combination (see Chapter 4.7). Additionally, the fault zone thickness could not be varied freely because it is linked to a new mesh generation and is therefore predefined (see Chapters 4.2.1 and 4.8). Because of these factors, variance-based global sensitivity indices such as the Sobol indices could not be considered as a sensitivity measure as they rely on a specific sampling scheme and require always a *PI* change model result (Petropoulos & Srivastava, 2017; Saltelli, 2002; Saltelli et al., 2010; Sobol, 2001; Usher, 2016). Better suited for this kind of analysis is the density-based Delta Moment-Independent Measure (Delta indices), which allows the use of samples that have predefined values for the fault zone thickness and which are filtered after the simulation runs in order to exclude those without a *PI* change result (Plischke, Borgonovo, & Smith, 2013; Sobol & Kucherenko, 2009). This global SA can be randomly sampled because only the visualization of the sensitivity measures is of interest. Latin hypercube sampling (LHS) provides an efficient way to choose near-random samples. It was thus used to generate samples for calculating the Delta indices. The sensitivity of all parameters was then evaluated in the following order:

1. Generation of random samples for each fault zone thickness individually
2. Calculation of the results of the model on these samples
3. Filtering of the results of the model results by removing those where the *PI* change calculation was unsuccessful (see Chapter 4.7) and combining the results of all fault zone thickness types into one data set
4. Calculation of the Delta indices on this combined data set
5. Increase of the number of random samples and repeating steps 1-4 until the calculated sensitivity indices converge

#### 4.9.2 Parameter space exploration – productivity index

To investigate the natural parameter space of the UJA once more with the *PI* as the new target parameter, a grid sampling approach was chosen again. Its big advantage is that, unlike with random sampling strategies, individual parameter effects can be isolated and visualized. Here, the level-resolution used to scan each parameter range needs to be high enough to assess the parameter effect on the model results. It was expected that the *PI* change and the DER curve exhibit a steady shift in parameter space. For example, if the hydraulic properties of the fault zone (specific storage and permeability) increase, the change in *PI* will also increase. Together with the experience gathered in the sensitivity analysis, a resolution of 15 levels was considered high for this parametric analysis (which is later proven in the results visualization). The fault zone thickness had to be treated differently as it is limited to the mentioned eight values (15, 20, 35, 50, 75, 100, 200, and 300 m, see Chapter 4.8). The specific storage of fault zone and matrix as well as fluid viscosity were sampled linearly, while fault zone and matrix permeability samples were logarithmically evenly spaced. Production rates were not expected to influence the calculation of the change in *PI*. This is because only the description of the reservoirs *PI* is of interest for this work. Turbulence effects do not need to be considered as explained in equation (3) in Chapter 4.7. The production rate was thus fixed to a value of 20 l/s.

The parameter grid containing all variations incorporating eight fixed fault zone thickness values therefore has a sample size of  $8 * 15^5 = 6,075,000$ . For each perturbation of matrix properties and fluid viscosity, an additional pure matrix model result was needed in order to compare pressure curves and isolate the influence of fault zone. This means that an additional  $15^3$  parameter combinations had to be calculated. In total, 6,078,375 numerical simulations were carried out during the “online stage” of the RB models.

#### **4.10 Spatial investigation of fault zone induced productivity index change and flow regime occurrences in the greater Munich area**

The greater Munich area represents the region with the highest geothermal development located inside the Upper Jurassic aquifer (Thomas, 2012). Especially here, the question regarding the effect of fault zones on well productivity is of particular interest for the ongoing reservoir exploration. A new set of reservoir data of existing wells in this area was gathered for this work. This data was used to generate updated maps for reservoir permeability and fluid viscosity. The confidential data of 34 wells was used because this work is part of the Geothermal Alliance Bavaria research project in cooperation with Erdwerk GmbH.

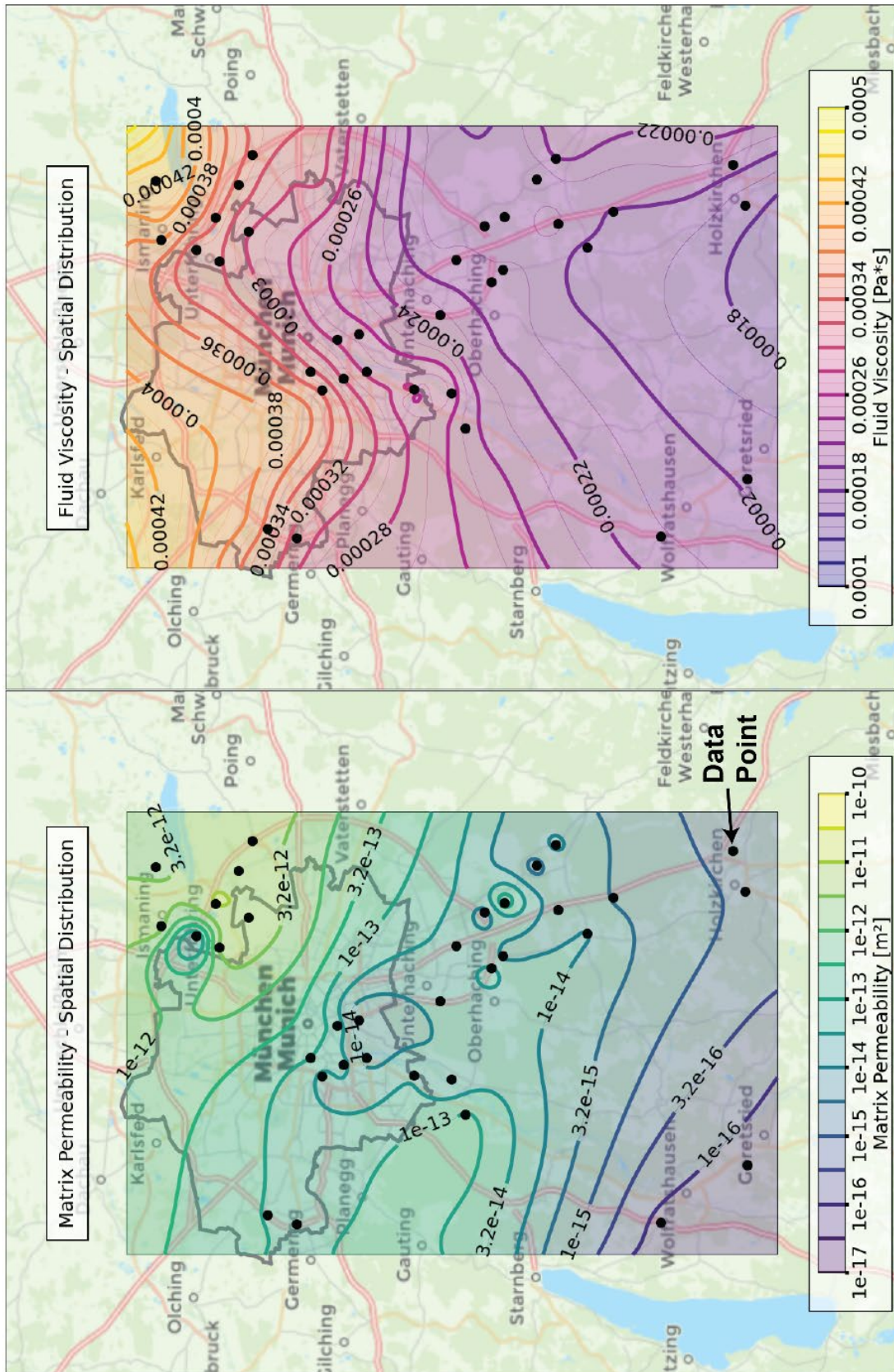


Fig. 28 Regionalized matrix permeability and fluid viscosity of the greater Munich area based on the marked data points.

The information compiled is currently the most comprehensive data set on the hydraulic behavior of the Upper Jurassic aquifer (State: January 2022). Pumping test data from these geothermal wells is interpreted using pressure transient analysis in order to calculate the local reservoir transmissibility. This point information is then used to derive a spatial data set and convert it to a permeability map grid assuming a reservoir thickness of 500 m. Reservoir depth and temperature information available from the same wells is transformed into spatial information in the same manner. The depth information is then used to calculate water pressure at the top of the reservoir assuming pure water of an average density of  $935 \text{ kg/m}^3$  and a water table at 500 m below sea level.

This pressure information together with the temperature data thus allows the computation of fluid viscosity according to IAWPS (Romera, 2020; Wagner et al., 2000). The spatial information of matrix permeability and fluid viscosity (Fig. 28) is used to reduce the complexity of the governing parameter space from six to four uncertain input parameters. For different spatially fixed perturbations of specific matrix storage and hydraulic fault zone properties (specific storage, permeability and thickness), the *PI* change and flow regime occurrences are calculated as presented above (Chapter 4.7) at each point of the input map grid (~1 million simulations are carried out for one map). The result is a *PI* change and flow regime map for each perturbation. Because this kind of spatial analysis is oriented towards describing the regional trends and behavior for different fault zone types, it is not necessary to sample the ranges of the four uncertain input parameters in an extremely detailed manner. Instead, specific matrix and fault zone storage are varied by their minima, maxima, and medians, while fault zone thicknesses of 20, 50, and 100 m and fault zone permeability in three logarithmically evenly spaced samples are investigated. Therefore,  $3^4 = 81$  maps are calculated and interpreted in comparison with the real world flow regime observations at the geothermal wells in the greater Munich area.

#### **4.11 Open source Python tool “uja faultzones”**

During the course of this work, the methodology presented here to evaluate pumping test data had to be applied in several iterations to different and large data sets. This has only been possible by automatization. With the generation of the reduced numerical models (see Chapter 4.8), the necessity of complex software installations depending on different numerical libraries was removed. This led to the development of a stand-alone Python tool (named `uja_faultzones`) for the Upper Jurassic aquifer that can easily be used on different computer systems. It provides the user a fast and precise way to evaluate a custom combination of the governing hydraulic

model parameters and removes the need for inaccurate regression functions to share the findings of this work. It incorporates nine reduced basis models (eight different fault zone thicknesses plus the pure reservoir case) and calculates two pumping tests (with and without fault zone) for a given set of model properties inside the UJA parameter range. The simulation results are directly analyzed regarding flow regime and fault zone related well productivity increase. The pressure curves of the two pumping tests can be visualized and stored in a diagnostic plot. Furthermore, an arbitrary list of model properties can be supplied and `uja_faultzones` will evaluate the different situations automatically one after the other. Calculation times for one parameter combination are generally below 1 second (~0.4s per simulation) depending on the computer system. `uja_faultzones` can be obtained via GitHub ([https://github.com/Florian-Konrad/uja\\_faultzones](https://github.com/Florian-Konrad/uja_faultzones)) under an open source GPL 3.0 license.

## 5 Results

In this chapter the results of the two workflows are presented in detail. These results are explained and further evaluated as well as interpreted. The first three subchapters (5.1, 5.2, 5.3) summarize the findings of “workflow one”, while Chapters 5.4, 5.5, 5.6, 5.7 and 5.8 present “workflow two”.

### 5.1 Model calibration results

As previously explained, a calibration and validation against a pumping test of a geothermal well in the south of Munich that exhibits linear flow was done before the desired parametric study could be tackled with confidence. After approximately 500 simulation runs a best fit between modelled and measured pumping test data could be achieved. Fig. 29 shows a comparison between the two. The “log-log plot of recovery phase” illustrates the calibration fit on the recovery pressure data. The validation is shown in “complete pumping test history” where the calibration was tested against the varying production rates of the test. The final calibration/validation values are:

- 15 m fault zone thickness
- $8.8 \times 10^{-16}$  m<sup>2</sup> matrix permeability
- $2.2 \times 10^{-12}$  1/Pa specific matrix storage
- $1.0 \times 10^{-9}$  m<sup>2</sup> fault zone permeability
- $2.0 \times 10^{-12}$  1/Pa specific fault zone storage
- and positive boundary with a distance of approximately 400 m to the well.

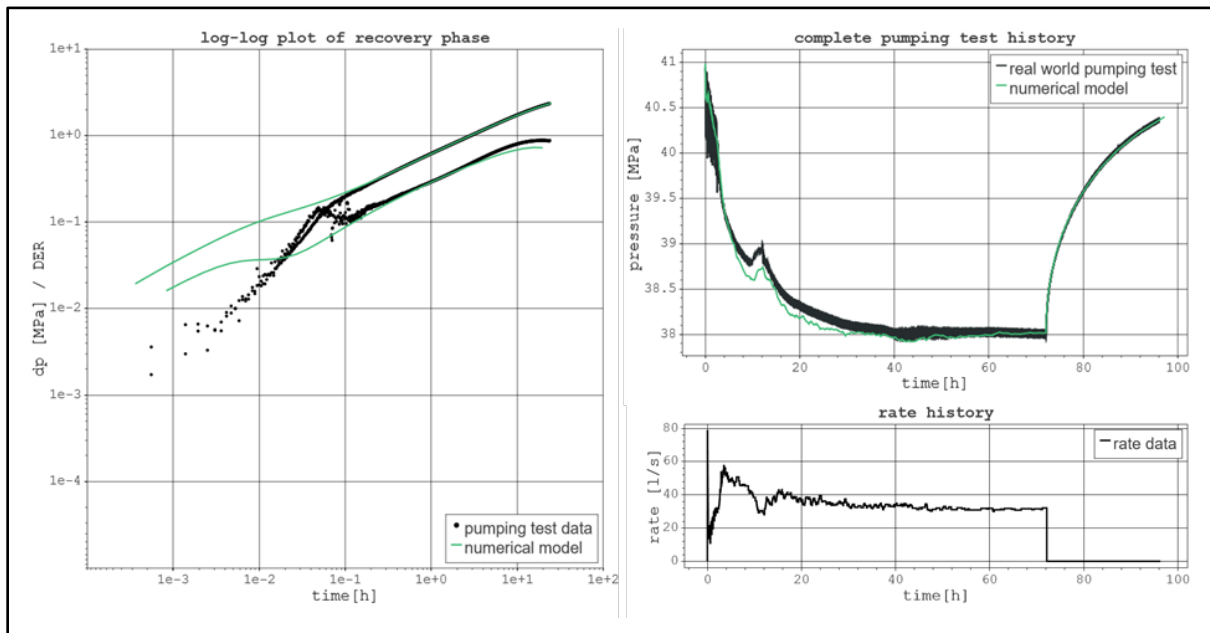


Fig. 29 Calibration results; left: log-log plot of recovery phase; right: pressure and rate history of complete pumping test.

For the evaluation of the calibration results, it is important to note that the model focus is on fault zone and aquifer-matrix while technical well conditions were simplified. Therefore, it can be seen that in the early time region of the recovery phase on the log-log-plot less fit had been achieved. Also, in the history match of the validation, there is a difference obvious in the draw down phase that is resulting from the practical complexity of the technical pumping test execution that could not be accounted for. Having said this, the numerical model is overall able to reproduce the field behavior, with the same pressure difference between the start and end of the production phase. Also, the recovery phase of the pumping test data was reproduced well which can be seen in the middle time region of the log-log plot and in the history matching plot. This confirms the underlying hydrogeological concept and also the realistic nature of the created numerical model.

## 5.2 Influence of hydraulic reservoir properties on the well flow regime

As previously stated, a determination of all sensitive parameters is necessary (see Chapter 4.6.1). In the context of pressure transient analysis, the individual parameter influence can be measured by the shape change of the DER curve depending on that parameter's variation. The following parameters were subject to this sensitivity analysis:

- specific storage of fault zone and matrix
- permeability of fault zone and matrix

- production rate
- fault zone thickness
- fluid viscosity.

The spectrum of these properties was gathered for the UJA in Tab. 1 (see Chapter 4.3). Fig. 30 illustrates the calculated changes in the DER shape (see Chapter 4.6.1) depending on specific storage, permeability and fluid viscosity. Specific matrix storage (max. median of  $SC_{x_{2,min}-x_{2,s},F_j} = 3.7$ ), fault zone (max. median of  $SC_{x_{3,min}-x_{3,s},F_j} = 8.9$ ) and matrix (max. median of  $SC_{x_{1,min}-x_{1,s},F_j} = 9.8$ ) permeability show the biggest influence on the shape of the DER. Specific fault zone storage (max. median of  $SC_{x_{4,min}-x_{4,s},F_j} = 0.6$ ), on the other hand, shows only low sensitivity, while fluid viscosity (max. median of  $SC_{x_{6,min}-x_{6,s},F_j} = 0.2$ ) appears to have the lowest. From Tab. 5, it is noticeable that the production rate has no influence, which was already to be expected as Bourdet et al. (1989) states that the speed of the pressure front propagating into the reservoir is independent of the flow rate. Fault zone thickness (max. median of  $SC_{x_{5,min}-x_{5,s},F_j} = 0.8$ , see Tab. 5) and specific fault zone storage have an influence in the same low order of magnitude.

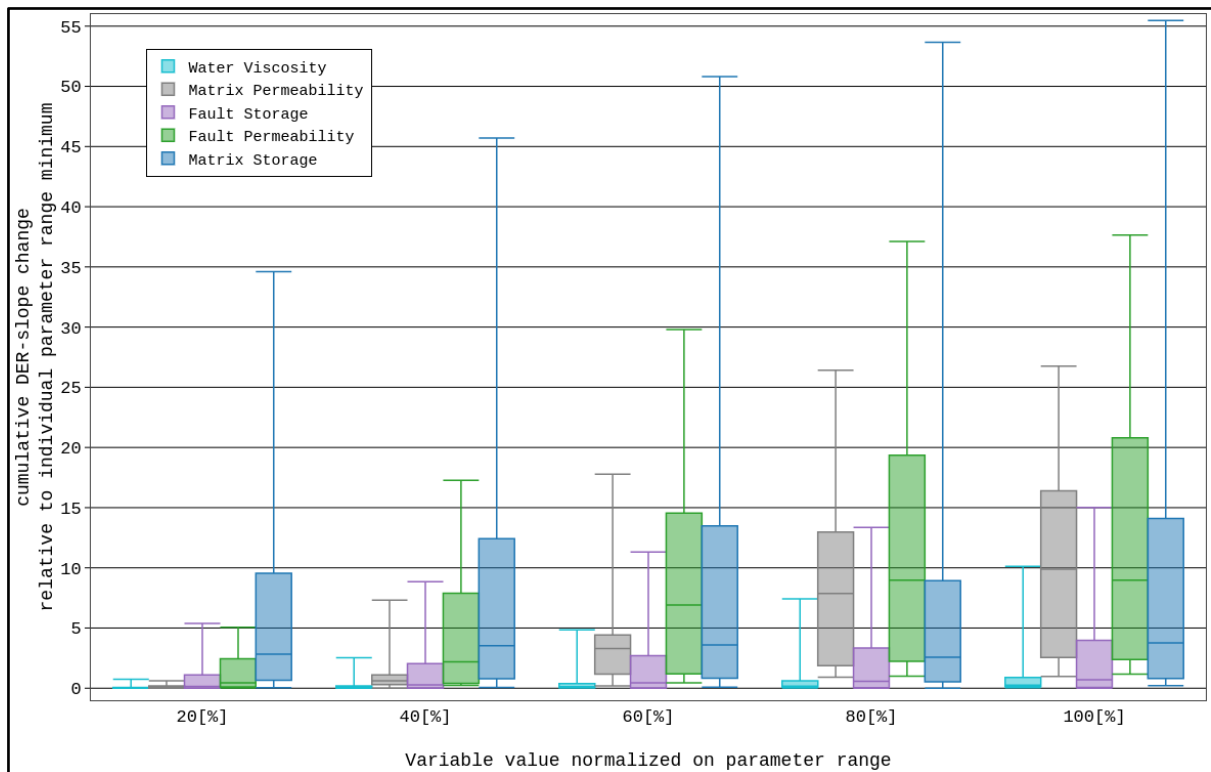


Fig. 30 Sensitivity plot;  $SC_{x_{i,min}-x_{i,s},F_j}$  (see equation (5)) versus variable value change relative to individual parameter range.

Fluid viscosity can have an influence on the derivative shape but only to such a small extent that it was excluded from the further flow regime analysis. The resulting parameters, considered as sensitive, are the permeability and specific storage of the fault zone and matrix as well as the fault zone thickness. The remaining insensitive parameters have been fixed for the flow regime analysis (production rate:  $30 \frac{l}{s}$ , fluid viscosity:  $0.0002897 Pa * s$ ).

Tab. 5 Median values of  $SC_{x_{i,min}-x_{i,s},F_j}$  for the evenly/log-evenly spaced parameters.

Variable value normalized on parameter range [%]	Water Viscosity	Matrix Permeability	Fault Zone Storage	Fault Zone Permeability	Matrix Storage	Production Rate
20	0.017	0.058	0.149	0.441	2.819	0.000
40	0.058	0.620	0.270	2.189	3.522	0.000
60	0.113	3.297	0.444	6.914	3.590	0.000
80	0.177	7.870	0.570	8.968	2.578	0.000
100	0.245	9.893	0.691	8.972	3.759	0.000

Tab. 6 Median values of  $SC_{x_{i,min}-x_{i,s},F_j}$  for the unevenly spaced fault zone thickness.

Variable value normalized on parameter range [%]	Median of cumulative DER-slope changes [-]
	Fault Zone Thickness
8	0.114
17	0.251
44	0.476
100	0.804

### 5.3 Identification of flow regime transitions in the parameter space

As discussed previously, through grid sampling the parameter space (Tab. 1), calculation of the numerical model response, automated flow regime classification of the model output, extraction of parameter combinations at the flow regime transitions and a subsequent regression analysis an appropriate visualization of these interfaces was possible (see methods Chapter 4.6).

The results of this regression are shown in Fig. 31 for selected characteristic settings. To show the fault zone thickness influence, two representative values (left column: 50 meters, right column: 150 meters) were visualized. Three graphs were generated for each fault thickness while every individual graph has a fixed specific matrix storage. The visualized axes were chosen with respect to the highest practical relevance which is on permeability values. The shift

of the flow regime transitions due to specific fault zone storage is shown by four different line colors and the line style depends on the flow regime transition type. Each drawn line represents the regression of parameter combinations at the transition between flow regimes according to the legend. Below that line (lower matrix permeability values), the occurrence of another flow regime is possible. Linear flow can be found, for example, below the solid and above or on the dotted line. It can be observed that there is a nearly constant logarithmic slope present at each flow regime transition for small permeability values of fault zone and matrix. This slope starts to decrease at some point, while permeability values increase which means that the influence of the increasing fault zones permeability declines until it is no longer present. Thus, only the matrix permeability controls which flow regime is present when keeping a constant specific storage and a fixed fault zone thickness. The slope value itself is controlled by fault zone thickness and also the specific storage of fault and matrix. In some cases of the transition between linear flow and negative boundary flow, it can be seen that the slope is not constant for extreme low permeability combinations. It is also noticeable that for higher fault zone thickness and specific matrix storage values below  $1.6 \times 10^{-10}$  1/Pa, the slope does not reach zero for all flow regime transitions anymore.

Focusing on specific storage, it can be seen that the values of the matrix and the fault zone are contradictory in its effects. Higher specific matrix storage lowers the permeability values at the flow regime transitions while higher specific fault zone storage raises them. This contradicting effect is also visible by looking at the size of the parameter region where linear flow is present. It can be noted that decreasing specific storage values of the matrix are reducing its area while a decreasing storage in the fault zone is increasing the linear flow region slightly.

Tab. 7 summarizes matrix permeability values at the flow regime transitions for extreme settings. The flow regime noted in the column to its right is possible if matrix permeability values are smaller than this extreme value and equal to or bigger than the extreme value in the next column. Tab. 7 has been derived from the corresponding regression functions for minimum and maximum values of specific fault and matrix storage and for the extreme fault permeability of  $1 \times 10^{-9}$  m<sup>2</sup>.

The usage of Tab. 7 can be illustrated exemplary by looking at the bilinear flow observation, which represents the weakest in pumping tests visible influence of a fault zone. A highly permeable ( $1 \times 10^{-11}$  m<sup>2</sup> -  $1 \times 10^{-9}$  m<sup>2</sup> fault zone permeability) 15 meter thick fault zone alters the flow regime around the well to a bilinear one at a specific matrix and fault zone storage of  $2 \times 10^{-12}$  1/Pa if the matrix permeability is below  $4 \times 10^{-14}$  m<sup>2</sup> and equal or above  $3 \times 10^{-15}$  m<sup>2</sup>.

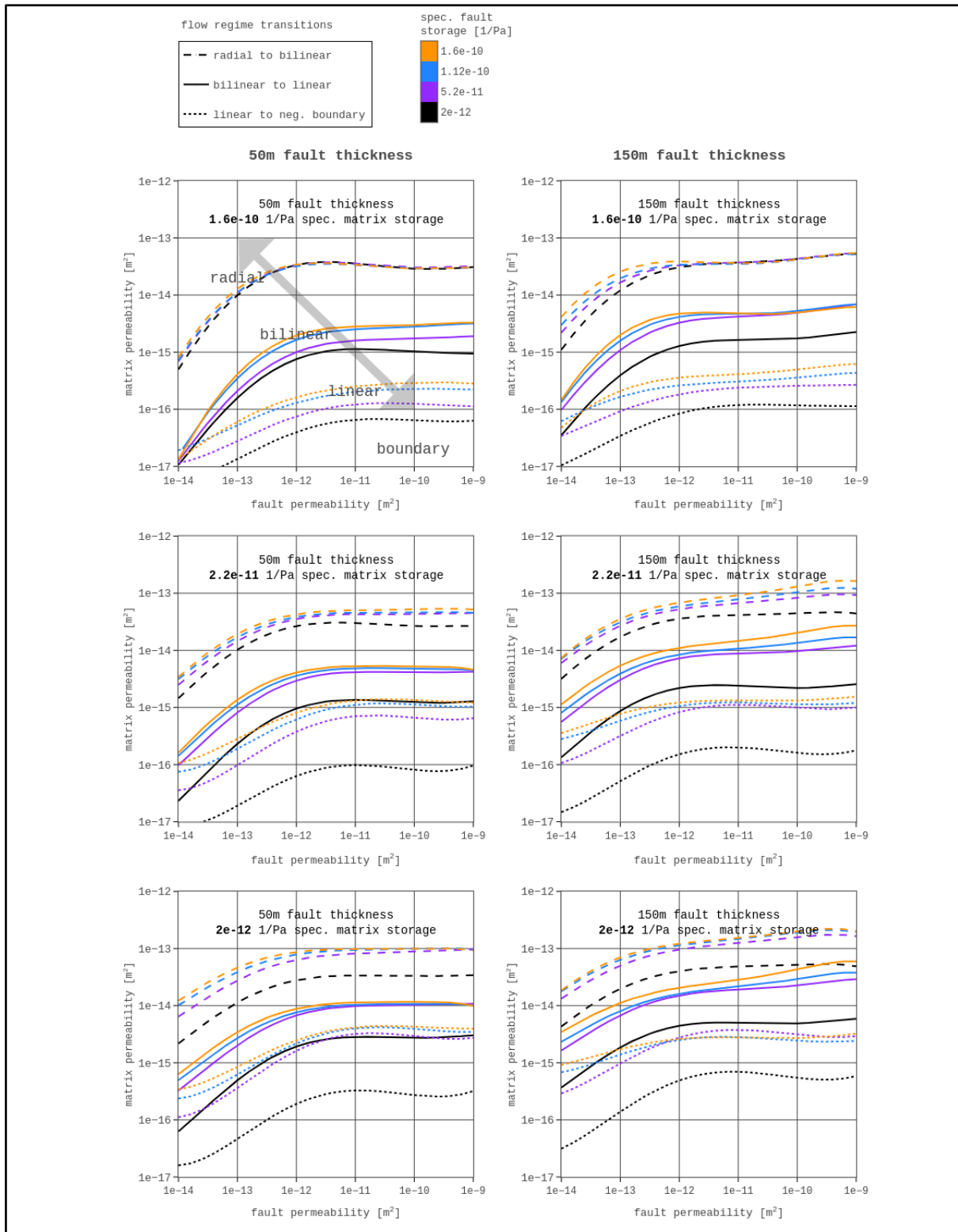


Fig. 31 Regression results for characteristic parameter combinations for the three observed flow regime transitions (1: radial to bilinear, 2: bilinear to linear, 3: linear to negative boundary); left: 50-meter fault zone thickness; right: 150-meter fault zone thickness; subplots have fixed specific matrix storage values; the specific fault zone storage is color coded; line styles represent the flow regime transitions; parameter combinations that fall on the transition line should be seen as combinations for which the flow regime above has still been observed.

Tab. 7 Matrix permeability values are shown below which the flow regime noted to its right is possible. The table has been derived from the corresponding regression functions for minimum and maximum values of specific fault and matrix storage and for a fault permeability of  $1 \times 10^{-9} \text{ m}^2$ .

spec. matrix storage [1/Pa]	spec. fault storage [1/Pa]	fault zone thickness [m]		matrix permeability [ $\text{m}^2$ ]		matrix permeability [ $\text{m}^2$ ]		matrix permeability [ $\text{m}^2$ ]	
$2.0 \times 10^{12}$	$1.6 \times 10^{10}$	15	radial	$9 \times 10^{-14}$	bilinear	$9 \times 10^{-15}$	linear	$3 \times 10^{-15}$	matrix as boundary
		35		$9 \times 10^{-14}$		$1 \times 10^{-14}$		$4 \times 10^{-15}$	
		50		$9 \times 10^{-14}$		$1 \times 10^{-14}$		$4 \times 10^{-15}$	
		100		$1 \times 10^{-13}$		$2 \times 10^{-14}$		$3 \times 10^{-15}$	
		150		$2 \times 10^{-13}$		$6 \times 10^{-14}$		$3 \times 10^{-15}$	
		200		$1 \times 10^{-13}$		$5 \times 10^{-14}$		$5 \times 10^{-15}$	
		300		$1 \times 10^{-13}$		$4 \times 10^{-14}$		$6 \times 10^{-15}$	
	$2.0 \times 10^{12}$	15		$4 \times 10^{-14}$		$3 \times 10^{-15}$		$1 \times 10^{-16}$	
		35		$4 \times 10^{-14}$		$3 \times 10^{-15}$		$2 \times 10^{-16}$	
		50		$3 \times 10^{-14}$		$3 \times 10^{-15}$		$3 \times 10^{-16}$	
		100		$4 \times 10^{-14}$		$3 \times 10^{-15}$		$4 \times 10^{-16}$	
		150		$5 \times 10^{-14}$		$6 \times 10^{-15}$		$6 \times 10^{-16}$	
		200		$4 \times 10^{-14}$		$3 \times 10^{-15}$		$7 \times 10^{-16}$	
		300		$3 \times 10^{-14}$		$3 \times 10^{-15}$		$9 \times 10^{-16}$	
$1.6 \times 10^{10}$	$1.6 \times 10^{10}$	15	$3 \times 10^{-14}$	$3 \times 10^{-15}$	$1 \times 10^{-16}$				
		35	$3 \times 10^{-14}$	$3 \times 10^{-15}$	$2 \times 10^{-16}$				
		50	$3 \times 10^{-14}$	$3 \times 10^{-15}$	$3 \times 10^{-16}$				
		100	$4 \times 10^{-14}$	$4 \times 10^{-15}$	$5 \times 10^{-16}$				
		150	$5 \times 10^{-14}$	$6 \times 10^{-15}$	$6 \times 10^{-16}$				
		200	$4 \times 10^{-14}$	$3 \times 10^{-15}$	$9 \times 10^{-16}$				
		300	$4 \times 10^{-14}$	$4 \times 10^{-15}$	$1 \times 10^{-16}$				
	$2.0 \times 10^{12}$	15	$3 \times 10^{-14}$	$8 \times 10^{-16}$	$3 \times 10^{-17}$				
		35	$3 \times 10^{-14}$	$9 \times 10^{-16}$	$5 \times 10^{-17}$				
		50	$3 \times 10^{-14}$	$9 \times 10^{-16}$	$6 \times 10^{-17}$				
		100	$4 \times 10^{-14}$	$1 \times 10^{-15}$	$1 \times 10^{-16}$				
		150	$5 \times 10^{-14}$	$2 \times 10^{-15}$	$1 \times 10^{-16}$				
		200	$4 \times 10^{-14}$	$1 \times 10^{-15}$	$1 \times 10^{-16}$				
		300	$4 \times 10^{-14}$	$1 \times 10^{-15}$	$1 \times 10^{-16}$				

By looking closer at the radial-to-bilinear transition in Fig. 31 (marked with the dashed lines), it can be seen that there is an area above that line which consists of parameter combinations with higher fault zone than matrix permeability. This means a pumping test observes only radial flow at those combinations even though the fault zone holds better hydraulic properties compared to the surrounding matrix. The size of this area in parameter space containing those hydraulically hidden fault zones is decreasing with a decline of the specific matrix storage. Extreme cases from Tab. 7 suggest that the observation of bilinear flow for the UJA is possible for the first time if matrix permeability values are below  $2 \times 10^{-13} \text{ m}^2$  and if they drop below  $6 \times 10^{-14} \text{ m}^2$ , linear flow becomes feasible.

#### 5.4 Characteristics of the flow regime distribution

Fig. 32 illustrates the flow regime distribution over the entire parameter space filtered only for three different fault zone thicknesses. As seen during the sensitivity analysis of the second workflow, after the hydraulically active fault zone thickness, the matrix permeability has the second highest relevance. Flow regimes are therefore plotted in categories (each for one of the

15 levels of the sample grid, see Chapter 4.9.2) of matrix permeability with their fractions relative to all samples at that fixed fault zone thickness and matrix permeability.

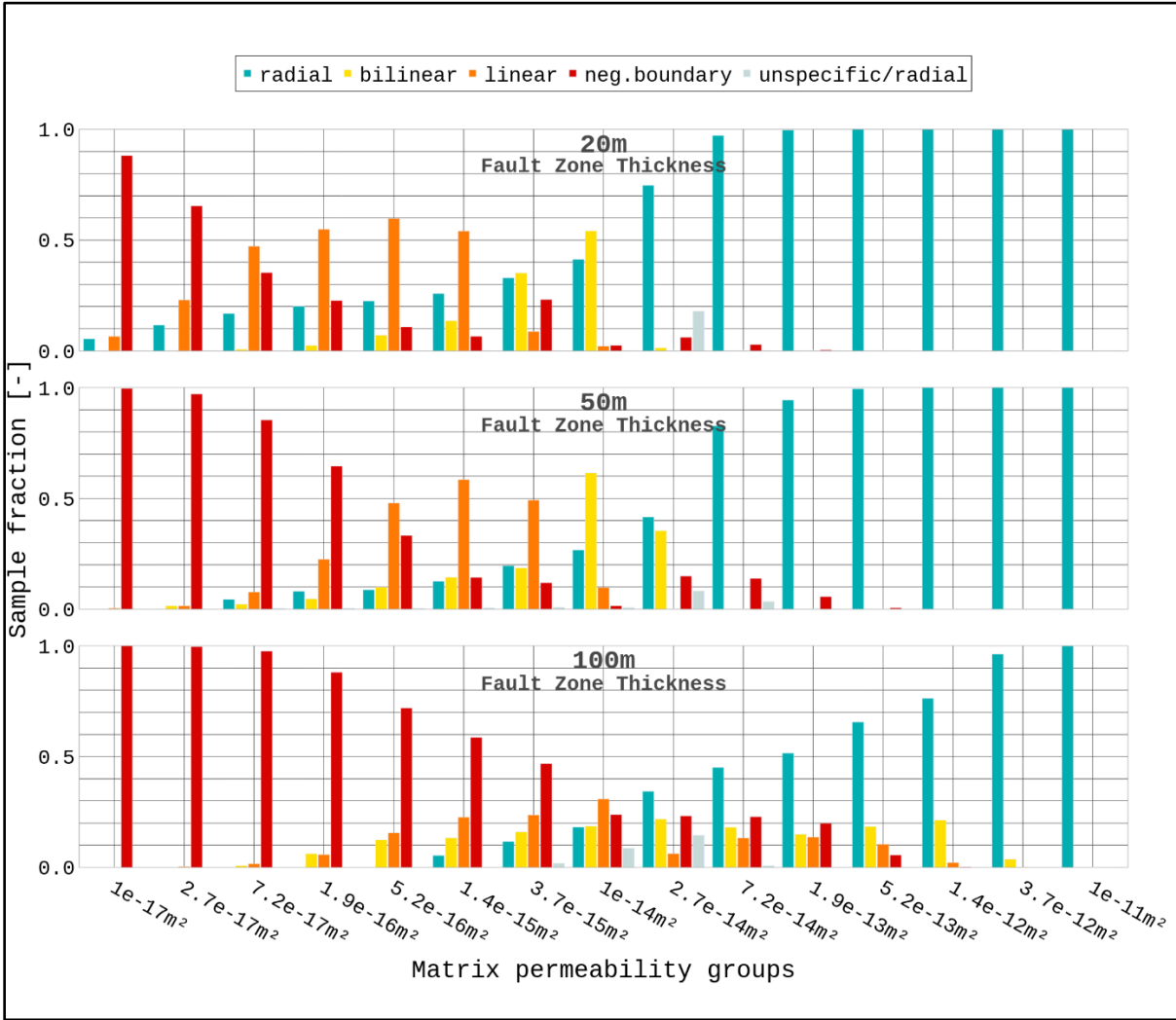


Fig. 32 Flow regime distribution of three different fault zone thicknesses based on their associated parameter samples grouped into matrix permeability categories (see Chapter 4.9.2 for details regarding the sampling approach).

It can be seen that, for low fault zone thicknesses of 20 m, the parameter space for matrix permeability values above  $2.68 \times 10^{-14} \text{ m}^2$  is dominated by radial flow which means that almost all tested combinations of fault zone permeability and fluid viscosity result in pressure signals of the well in which the fault zone is hydraulically hidden and not really detected by traditional PTA. The highest occurrence of bilinear flow (55%) can be found at  $1 \times 10^{-14} \text{ m}^2$ , while the highest occurrence of linear flow (60%) is located around  $5.18 \times 10^{-16} \text{ m}^2$ . Below  $1 \times 10^{-17} \text{ m}^2$  matrix permeability, the flow is dominated by the interface of the fault zone to the matrix through negative boundary flow. Increasing fault zone thickness generally shifts the main presence of these flow regimes in the direction of higher matrix permeability:

- negative boundary flow moves to  $1 \times 10^{-16} \text{ m}^2$  for 50 m and  $1 \times 10^{-17} \text{ m}^2$  for 100 m
- linear flow moves to  $1.39 \times 10^{-15} \text{ m}^2$  for 50 m and  $1 \times 10^{-14} \text{ m}^2$  for 100 m
- radial flow that dominates the system is present at and above  $1.93 \times 10^{-13} \text{ m}^2$  for 50 m and  $1.39 \times 10^{-12} \text{ m}^2$  for 100 m.

Between 50 m and 100 m fault zone thickness, the spread of bilinear and linear flow regime presence increases, while their maxima (in terms of fraction values) decrease.

### 5.5 Influence of hydraulic reservoir properties on the productivity index

Fig. 33 illustrates the findings of the sensitivity study. The fault zone thickness proves to be the parameter with the highest influence on the desired  $PI$  change value with a Delta index of 0.45. The matrix permeability shows a Delta index of 0.2 followed by the fault zone permeability of 0.18. The lowest sensitivity is registered in the following decreasing order for fluid viscosity (0.15), specific matrix storage (0.14), and specific fault zone storage (0.12). These Delta indices change only by an insignificant amount between a sample size increase from  $\sim 0.5$  to  $>2$  million. The magnitude as well as the order of parameter importance can therefore be considered to be reliable.

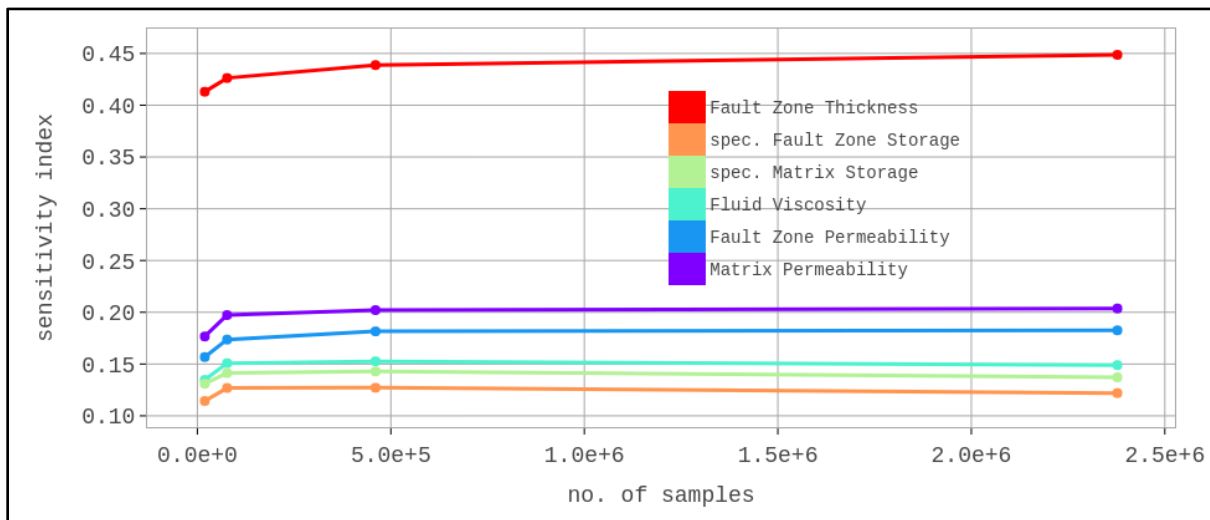


Fig. 33 Global sensitivity analysis for the governing hydraulic model parameters: Delta index vs. random sample size.

### 5.6 Fault zone induced productivity index change

Results of the investigation of the global parameter space with respect to the influence of fault zones on well productivity is shown in Fig. 34. First, it is important to consider the additionally visualized fraction of samples for which the attempt to calculate  $\Delta PI_{rel}$  was unsuccessful (see

Chapter 4.7). At  $1.93 \times 10^{-13} \text{ m}^2$  matrix permeability, it is basically not present, which means that all sampled parameter combinations were evaluated and  $\Delta PI_{rel}$  calculated. As the matrix permeability decreases, there is an increase in the portion of samples for which the difference between the pressure curve of the pure matrix and the fault zone model is still changing. These samples are parameter combinations in which the fault zone introduces a dominant alteration of the hydraulic system that is not stabilizing in terms of  $\Delta dp'$  reaching zero (see Chapter 4.7). This is confirmed by the rise of the bilinear, linear, and negative boundary flow regimes (Fig. 33). Thus, especially below  $1.39 \times 10^{-15} \text{ m}^2$  matrix permeability, it is not possible to quantify fault zone induced  $PI$  change. From  $1.93 \times 10^{-13} \text{ m}^2$ , increasing matrix permeability values slightly increase the proportion of unsuccessful samples mainly only for high fault zone thicknesses ( $> 75 \text{ m}$ ). This effect is related to the model design; for extreme combinations of high fault zone and high matrix permeability, the model boundary becomes visible in the pressure signal very early, thereby preventing the pressure difference between fault zone and matrix model from becoming constant.

The dynamic of the fault zone related  $PI$  change can be split into two groups that show different characteristics over the parameter space (Fig. 34).

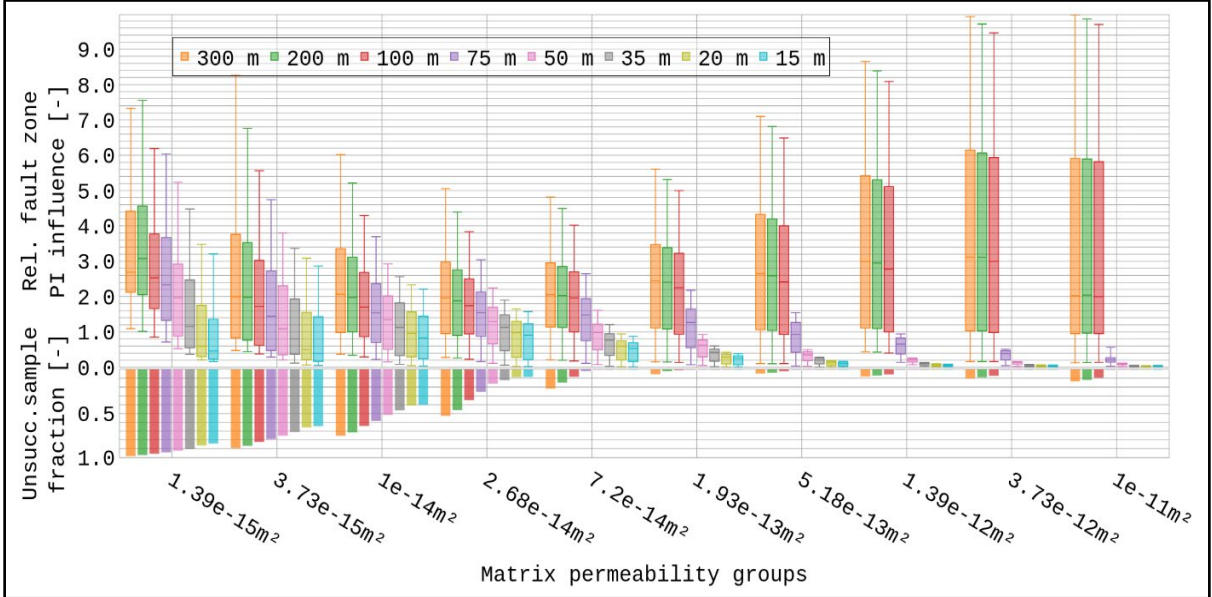


Fig. 34 Relative fault zone  $PI$  increase ( $\Delta PI_{rel}$ ) grouped by matrix permeability categories for all tested fault zone thickness values.

First, fault zone thicknesses of 100 m or higher (“high thickness group”) generally have quite a high influence with the majority of mean  $\Delta PI_{rel} > 2$ . As before, a good starting point to describe them is at  $1.93 \times 10^{-13} \text{ m}^2$  matrix permeability (mean  $\Delta PI_{rel}$  at 100-m fault zone thickness: 2.16; at 200 m: 2.3; at 300 m: 2.35). Higher matrix permeability causes the  $\Delta PI_{rel}$

first to rise as well until  $3.73 \times 10^{-12} \text{ m}^2$  (100m fault zone thickness mean  $\Delta PI_{rel}$ : 3.46; at 200 m: 3.56; at 300 m: 3.61). For even higher matrix permeability ( $1.0 \times 10^{-11} \text{ m}^2$ ), a decrease of the mean  $\Delta PI_{rel}$  can be observed (100 m fault zone thickness mean  $\Delta PI_{rel}$ : 3.35; at 200 m: 3.38; at 300 m: 3.37; note that the 300-m value drops below the 200-m value indicating the limits of the presented evaluation which are further discussed in Chapter 6.3). Below  $1.93 \times 10^{-13} \text{ m}^2$  matrix permeability, the mean  $\Delta PI_{rel}$  of the “high thickness group” scatters between 1.88 and 3.41. With lower matrix permeability, mostly only the interquartile range and the amount of unsuccessful sample evaluations increases.

The second group comprises fault zone thicknesses from 15 to 75 m (“low thickness group”) and is additionally visualized separately only for hydraulically hidden fault zones (only radial flow regimes observed in the pumping test) in Fig. 35. For this low fault zone thickness group, a more obvious relationship between matrix permeability and  $\Delta PI_{rel}$  is visible. At  $3.73 \times 10^{-12} \text{ m}^2$  and  $1.0 \times 10^{-11} \text{ m}^2$  matrix permeability, only a well  $PI$  increase below 5% is present for 15-m to 35-m fault zone thickness; 50 m shows ~10% increase while 75 m is higher with 20 and 34%. All fault zones in this group now have a higher mean  $\Delta PI_{rel}$  with decreasing matrix permeability. At  $7.20 \times 10^{-14} \text{ m}^2$  matrix permeability, the following mean values can be derived:

- 15-m thickness: 0.45
- 20-m thickness: 0.50
- 35-m thickness: 0.66
- 50-m thickness: 0.87
- 75-m thickness: 1.37

As shown before, with a matrix permeability greater than and equal to  $7.20 \times 10^{-14} \text{ m}^2$ , most samples behave as hydraulically hidden fault zones for this thickness group. Below  $7.20 \times 10^{-14} \text{ m}^2$  matrix permeability, the same trend is visible (but not as fast as for the high fault zone thickness group). The interquartile range, in particular, and the unsuccessful sample fraction increase. Detailed tables with the statistics for all sampled parameter combinations as well as hydraulically hidden fault zones can be found in Appendices 9.6, 9.7, and 9.8. Additional detailed plots of the complete parameter space can be found in Appendix 9.5. The behavioral shift between the two groups happens between 75 and 100 m in thickness. The 75-m case is already separated with a significantly higher mean  $\Delta PI_{rel}$  than the remaining smaller thickness values, which all have their means at high matrix permeability close together. However, the same decreasing  $\Delta PI_{rel}$  with higher matrix permeability can be seen. To illustrate

the characteristics of the two fault zone thickness groups and their different dependency of  $\Delta PI_{rel}$  on fault zone and matrix permeability, a visualization with greater detail is given in Fig. 36.

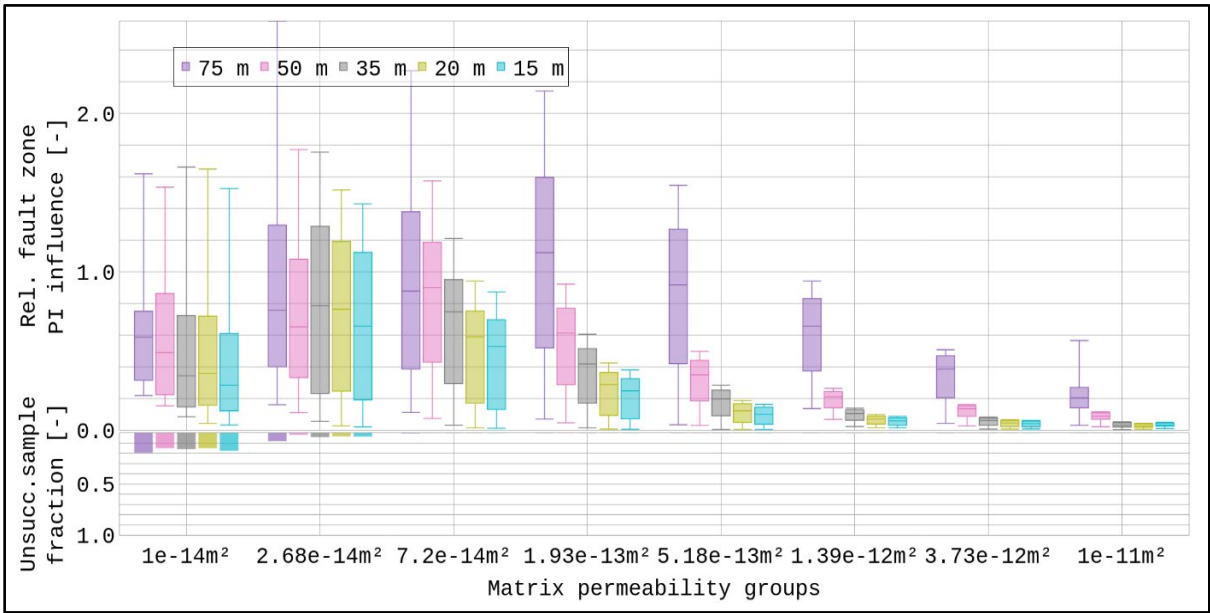


Fig. 35 Relative fault zone PI increase ( $\Delta PI_{rel}$ ) grouped by matrix permeability categories only for samples with fault zone thickness values < 100 m and filtered for only radial flow regimes.

The “low thickness group” represented by the 20-meter case behaves as would naturally be expected: The PI improvement for high matrix permeability associated with the fault zone is very low and can be considered negligible (below 5%). The matrix permeability clearly dominates the system. An asymptotic rise of  $\Delta PI_{rel}$  is observed as the matrix permeability decreases, thereby confirming the idea that the contrast between matrix and fault zone becomes greater and that the matrix is losing its effect on well productivity. At a certain point (which is different for each applied fault zone type and marked as the first scatter point next to the PI influence line in Fig. 36) while matrix permeability is decreasing, it is not possible to calculate  $\Delta PI_{rel}$  anymore (see Chapter 4.7). The fault zone thus has a strong influence on the well PI. In addition, the flow field around the well is no longer radial. From Fig. 35 it can be derived that for a matrix permeability below  $1.93 \times 10^{-13} \text{ m}^2$ , most fault zone types of this group provide a hydraulic improvement of more than 30% to the well.

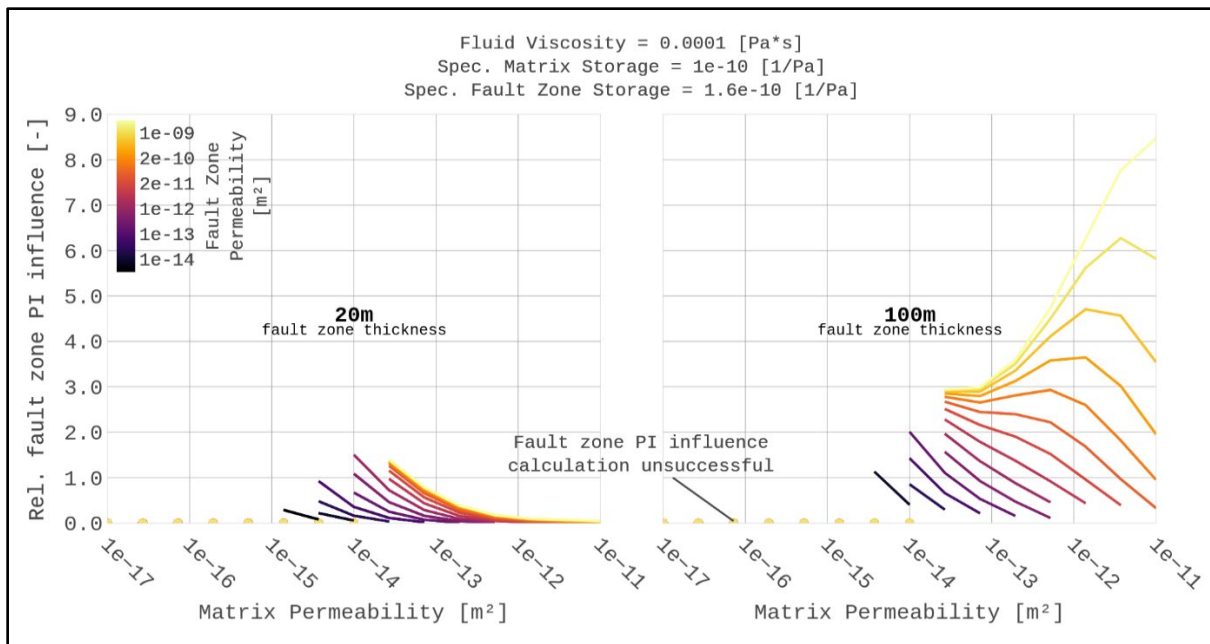


Fig. 36 Comparison between the “low” (represented by the 20-meter fault zone thickness case, left) and “high thickness group” (represented by the 100-meter fault zone thickness case, right) at a representative point in parameter space (fluid viscosity = 0.0001 Pa·s, spec. matrix storage =  $1 \times 10^{-10}$  1/Pa, spec. fault zone storage =  $1.6 \times 10^{-10}$  1/Pa) illustrating relative fault zone PI increase ( $\Delta PI_{rel}$ ) vs. matrix permeability for all sampled fault zone permeability values.

The “high thickness group” represented by the 100-meter case in Fig. 36 also shows this characteristic but with a steeper increase in  $\Delta PI_{rel}$  for decreasing matrix permeability only for the lower half of the fault zone permeability range tested. Fault zone permeability settings above  $7 \times 10^{-12}$  m<sup>2</sup> behave oppositely until they reach a maximum value after which the  $\Delta PI_{rel}$  decreases again. The visualization of the results of the entire parameter space confirm this value (see Appendix 9.5). This behavior can be interpreted by the idea that these fault zones have such a high volume and react so fast to the pressure transient introduced by the well that the increasing matrix permeability - and thus the reservoir improvement - is amplified. Fault zones of the “high thickness group” above this permeability threshold are therefore likely to make up a considerable part of the *PI* of a well independently of the remaining parameters. Samples with lower fault zone permeability in this group quickly begin to have a high effect on *PI*. It can thus be reasoned that only a little increase in fault zone permeability compared with the surrounding host rock is enough to improve the *PI* of the well by more than 20%.

## 5.7 Spatial distribution of flow regimes and productivity index alteration associated with fault zones in the greater Munich area

The 81 parameter sets tested (27 different fault zone configurations at three different specific matrix storage values, based on the matrix permeability and fluid viscosity presented in Fig. 28, see also Chapter 4.10) can be found in Appendices 9.9 and 9.10. To highlight the influence of the fault zone thickness, a comparison of the 50-meter and 100-meter case for three different fault zone permeabilities is illustrated in Fig. 37. An increase in fault zone permeability only slightly shifts the location of the flow regimes for a 50-meter thick fault zone. In contrast, with an in the greater Munich area globally applied 100-meter fault zone thickness, a heavy northward shift of the fault zone associated flow regimes (bi- and linear flow) is observed in concert with an increase in fault zone permeability. The comparison between the calculated flow regimes and the actual field observation (data points and labels) obviously favors lower fault zone thickness values.

By matching the 81 parameter sets (perturbations of different fault zone types and specific matrix storage) and their simulated spatial flow regime distribution with the flow field information from the actual geothermal wells located in the greater Munich area, a best fit can be derived. This flow regime fit together with the corresponding  $\Delta PI_{rel}$  map is shown in Fig. 38. The latter shows very low  $\Delta PI_{rel}$  values ( $< 10\%$ ) in the northeastern corner of the study area with the exception of a small isolated area around a data point with lower matrix permeability. From northwest to southeast in the middle of Munich, the 0.5 isoline can be seen. This implies a 50% well  $PI$  increase related to the globally simulated 50-meter-thick fault zone with  $1 \times 10^{-11} \text{ m}^2$  permeability and  $6.24 \times 10^{-12} \text{ 1/Pa}$  specific storage as well as for a specific matrix storage of  $3.55 \times 10^{-11} \text{ 1/Pa}$ . The southern region of the  $\Delta PI_{rel}$  map consists of parameter combinations with low and decreasing matrix permeability for which the  $\Delta PI_{rel}$  cannot be calculated because the influence of the fault zone is already too large and hence no isolines are visible in that area. This correlates with the occurrence of the bilinear and linear flow regimes as shown in the left map of Fig. 38.

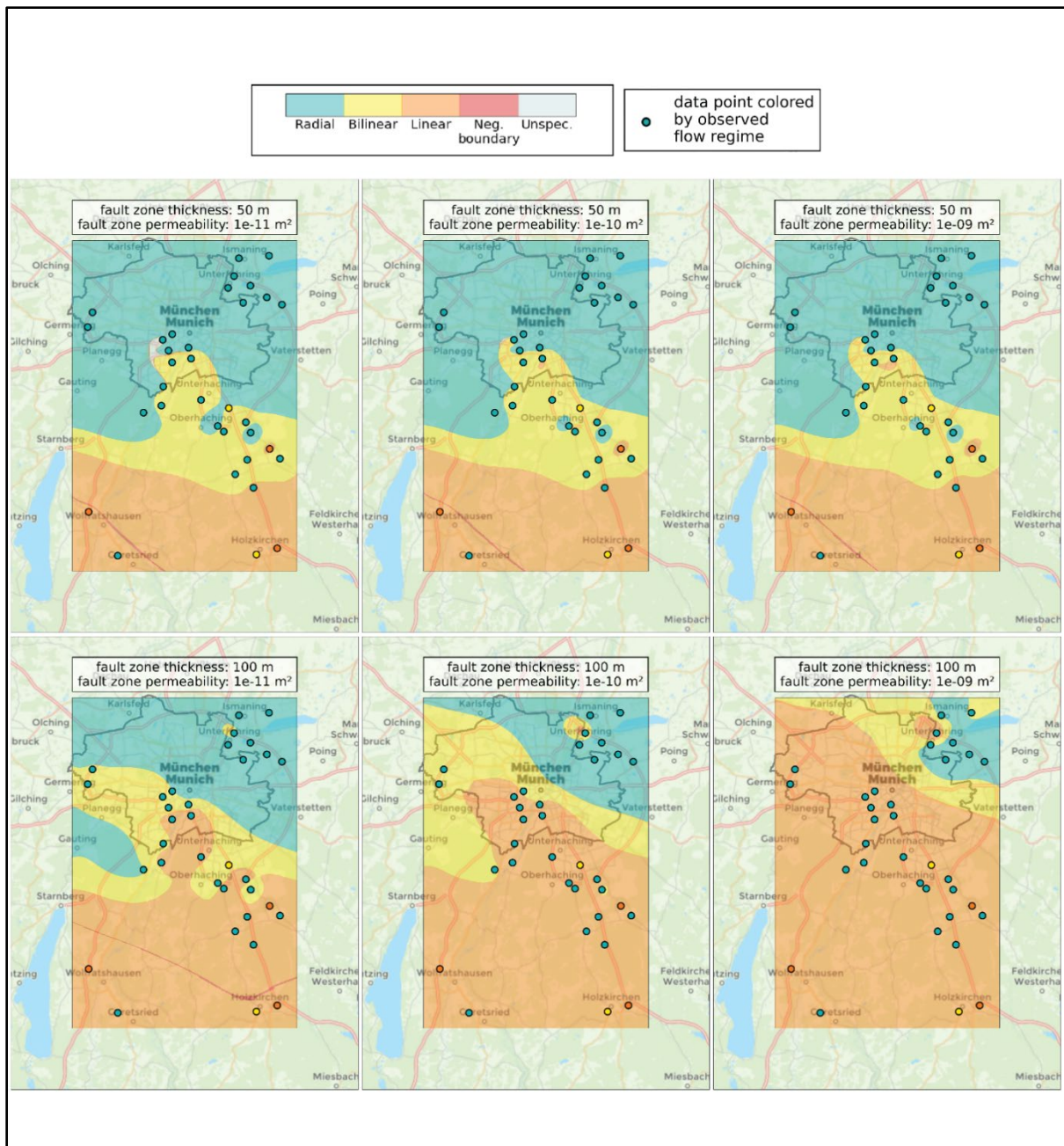


Fig. 37 Spatial flow regime distribution comparison illustrating the parameter influence of the hydraulically active fault zone thickness. Colored map areas represent the numerically derived flow regime for the globally applied fault zone type of each map (fault zone properties noted above each map). Data points are additionally shown and colorized in the same way according to their actual flow regime field observation: blue = radial flow, yellow = bilinear flow, orange = linear flow, red = neg. boundary flow, grey = unspecified flow.

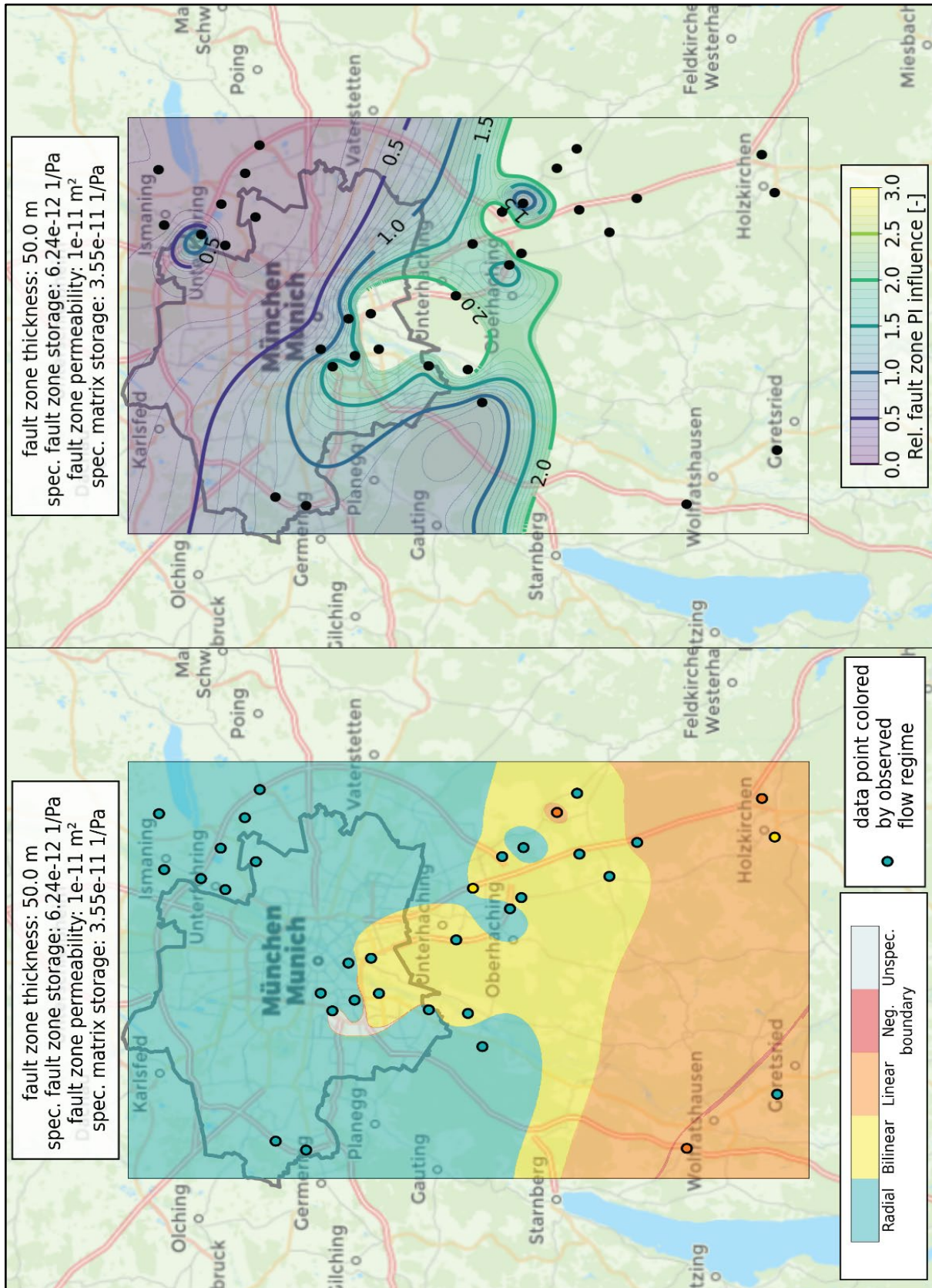


Fig. 38 Spatial flow regime distribution (left) and relative fault zone PI increase ( $\Delta PI_{rel}$ , right) for a 50-meter fault zone with  $1 \times 10^{-11}$  m<sup>2</sup> permeability and  $6.24 \times 10^{-12}$  1/Pa specific storage at  $3.55 \times 10^{-11}$  1/Pa specific matrix storage showcasing the best fit between calculated and observed (colored data points) well flow regimes.

## 5.8 Consequences for the geothermal exploration in the Upper Jurassic aquifer

By comparing the simulated reference  $PI$  values with the actual IPRs (see Chapter 2.4) of geothermal wells, it is possible to describe a rough threshold for a necessary matrix permeability needed for a commercially successful geothermal well. From the IPR curves presented in Savvatis (2012) (Fig. 14), minimal reservoir  $PI$  values around 20-30 l/s/MPa can be estimated. Non-linear effects are able to reduce them to 10 or less l/s/MPa at economical rates of around 70 l/s. A matrix permeability between  $1.0 \times 10^{-14} \text{ m}^2$  and  $2.68 \times 10^{-14} \text{ m}^2$  marks this threshold (Fig. 39) which is also confirmed by Bauer et al. (2014). The realization of a successful geothermal well below would be economically feasible only by developing a fault zone with increased hydraulic properties.

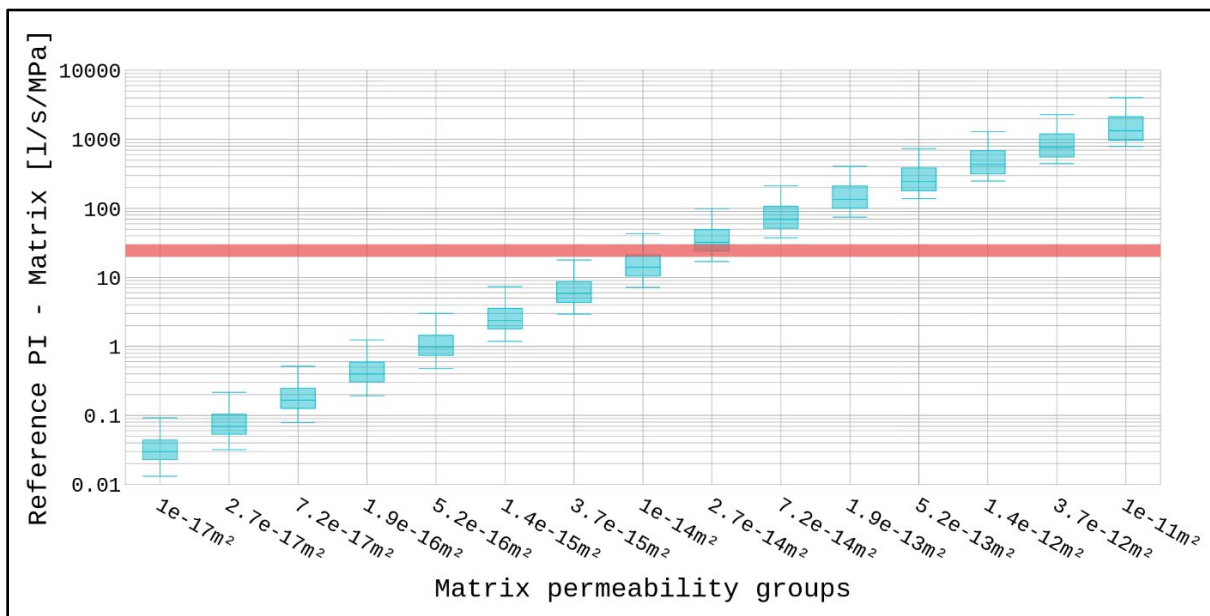


Fig. 39 Visualization of the reference matrix  $PI$  (at the reference time of 342h) vs. matrix permeability combining the influence of the ranges of fluid viscosity and specific matrix storage through a box-plot; transparent red bar marks minimal reservoir  $PI$  necessary for an economically successful well.

From the observations in flow regime distributions over the entire parameter space as well as over the spatial extent of the study site, it can be deduced that fault zones with a hydraulically active thicknesses of 100 m or higher are unlikely for the Upper Jurassic aquifer. On the one hand, the spatial flow regime comparison endorses only smaller fault zone thicknesses (Fig. 37 and Appendices 9.9 and 9.10). On the other hand, bilinear and linear flow regimes for the “high thickness group” tend more to the late time region of the pumping test and thus tend to be associated with channel structures for which no real world evidence is known for the Upper Jurassic aquifer so far. This hypothesis is supported by the borehole measurements at the

geothermal drilling sites Geretsried and Unterhaching which suggest fault zone thickness values of 80 meters and 94 meters (Dussel, Moeck, Wolfgramm, & Straubinger, 2018; Rojas et al., 2017).

Another important consequence from the simulation results is associated with hydraulically hidden fault zones of the more likely “low thickness group”. While these settings show only a radial flow regime, they can still significantly improve the well  $PI$  which makes them valuable targets for the exploration. Their mean maximum increase in  $PI$  is:

- 104% at a matrix permeability of  $1.93 \times 10^{-13} \text{ m}^2$  (75-meter case)
- 81% at  $7.2 \times 10^{-14} \text{ m}^2$  (50-meter case)
- 80% at  $2.68 \times 10^{-14} \text{ m}^2$  (35-meter case)
- 72% at  $2.68 \times 10^{-14} \text{ m}^2$  (20-meter case)
- 66% also at  $2.68 \times 10^{-14} \text{ m}^2$  (15-meter case)

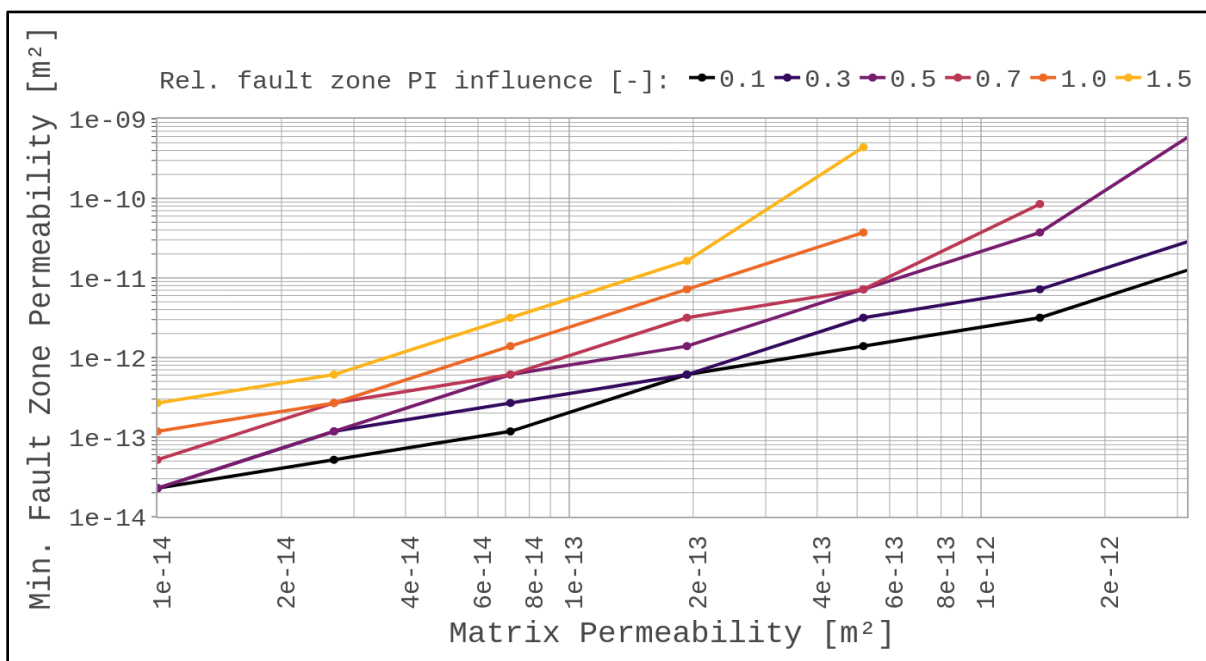


Fig. 40 Minimal fault zone permeability versus matrix permeability for different  $\Delta PI_{rel}$  thresholds and filtered only for hydraulically hidden fault zones below 100 meters thickness, thereby representing extreme values for the low thickness group.

Hydraulically hidden fault zones that are generally not relevant for the exploration are located in the parameter space below 50-meter thickness and in combination with a matrix permeability greater than  $5.18 \times 10^{-13} \text{ m}^2$  because they provide only an insignificant  $\Delta PI_{rel}$ . Additionally, a necessary minimal contrast between matrix and fault zone permeability needed to make a certain  $\Delta PI_{rel}$  threshold possible can be derived. Fig. 40 shows the minimally observed fault

zone permeability versus the investigated matrix permeability levels for hydraulically hidden fault zones as well as all fault zone thicknesses below 100 m combined. The latter causes the oscillations in the plotted lines, which are constrained to the values of the fault zone permeability sampled. Upon inspection of the 0.1 threshold line, which implies a 10% increase in well productivity, it can be observed that fault zone permeability must be at least around two times that of the matrix. This can be seen as a highly useful magnitude of fault zone and matrix permeability ratios for the exploration.

The spatial analysis of the greater Munich area shows that a large portion of the map is strongly influenced (more than 50% *PI* improvement) by the 50-meter fault zone that provided the best flow regime fit. Even an increase in well productivity of more than 100% can be found for this low thickness scenario for more than half of the total area. This confirms the interpretation that even fault zones of low thickness values remain highly beneficial for the exploration if they are hydraulically active and have an increased permeability compared with the surrounding matrix. Especially the southern area of the investigated domain proves to be always hydraulically dominated by fault zones because bi-/linear or negative boundary flow regimes are present in all scenarios tested.

## **6 Discussion of possible limitations of the numerical experiments**

The following four chapters are discussing the limitations of the results of both workflows as they share underlying methodology.

### **6.1 Model design**

In addition to the interpretation and synthesis of the results, it is important to discuss possible limitations of the workflow. First, the underlying model assumptions should be mentioned again. As explained in the beginning, fault zones develop in different sizes and geometries depending on numerous local and temporal conditions (see Chapter 2.2). A crucial fundamental assumption made here is that a hydraulically active fault zone is tapped by the geothermal well. Especially the current stress field and the orientation of a fault zone relative to it also control the hydraulic situation (Steiner, 2012). While the local stress field can also vary over time and fault zones can reactivate because of effects caused by the geothermal exploration itself (Seithel, Gaucher, Mueller, Steiner, & Kohl, 2019). However, this is outside the scope of this work.

The presented numerical model is limited by its fundamental assumptions especially regarding the chosen geometry of well and fault zone. But through the application of characteristic fault

zone sizes and a punctual intersection between well and fault zone (as it is always the case for geothermal wells in the UJA), the goal of capturing the basic hydraulic fault zone behavior was reached. Further investigations are now possible by increasing the complexity of additional geometric variables, such as the inclination of the fault zone and well. Future studies could also benefit from more high-resolution seismic information and refine the appearance of fault zones into more than one characteristic geometric type.

Alternatively, it could be helpful to investigate this topic through analytical models, for example, as derived by Cinco-Ley, Ramey, and Miller (1975), and compare them to the numerical approach shown here. This could especially be helpful in order to derive the influence of the geometrical model assumptions (fault zone and well inclination, fault zone length) for detecting hydraulically hidden fault zones during the workflow.

In addition to assumptions in the underlying geometrical model concept, the design of the simulated pumping test introduces inaccuracies to some extent. In terms of flow regimes around the well, the simulation time had been chosen way longer than a normal pumping test would last (Savvatis, 2012). This makes it possible for some parameter combinations to observe flow types on different time scales than compared to the field (Bourdet, 2002). In combination with the absence of well effects, this means that more of the fault zone related flow regimes have been discovered in this analysis than it would be possible in a real pumping test. The determined transitions in parameter space should hence be seen as theoretical values portraying flow regimes under ideal conditions. The consequence of this is that there are conceivable parameter combinations that should indicate a fault zone related flow regime in a pumping test (see again Chapter 2.3 and Fig. 10) based on the findings of this work while in reality they can be masked by well effects or remain undetected due to the time scale of the pumping test (Zarrouk & McLean, 2019).

Regarding the productivity-focused investigation, the pumping test duration of 500 h might not be long enough in certain extreme slow reacting parameter combinations (especially at medium to low matrix permeability). The model boundaries of 15 km from the well might also cloud the pressure data for high matrix permeability settings. Especially at matrix permeabilities above  $10^{-13}$  m<sup>2</sup>, the model boundaries might alter the pressure signal after around 100 hours as could be observed and confirmed by calculating the radius of investigation (Earlougher, 1977; Kuchuk, 2009; Miyan & Pant, 2015). However, because the focus of this work is on fault zones that are hidden in a radial flow field of a well, these inaccuracies or limitations mostly apply only to the additionally calculated parameter combinations that exhibit bi-/linear or negative boundary flow. Finally, the *PI* in the approach presented here is purely a measure for the

reservoir. No well effects were considered to provide comparability independent of individual borehole properties (skin and wellbore storage).

## **6.2 Uncertainties of the flow regime transitions**

A great challenge in the search for flow regime transitions was a sufficient sampling over the UJA parameter space. Since an individual model run took on average ten minutes to finish, it was only possible to carry out an analysis like this by utilizing an HPC cluster. Even though a total number of 30492 simulations were carried out, an inaccuracy in discovering the flow regime transition depending on the parameter grid resolution remains. The polynomial regression model introduced an additional error for the adjacent interpretation, which is also partly based on the amount of simulations as well as on the regression model type itself (Draper & Smith, 1998).

Furthermore, the chosen flow regime classes are constrained by several hard-defined values for  $dp$  and DER slopes and time scales based on an interpretation coming from a practical point of view and the assessment of real world pressure data, which, to some degree, depends on how it is interpreted. In addition, their translation into Python has been derived by manually examining a training data set of several hundred samples for most types of parameter combinations as well as careful evaluation of transitions and outliers in the final results. However, the focus of this work is on identifying the parameter space in which a given flow regime is possible. Choosing the classes on which the automated PTA is based differently would mainly just change the intercept of the regression functions. In addition, by approaching the data evaluation conservatively and interpreting the regression functions as limiting surfaces below (lower matrix permeability) which the associated flow type is very likely to be observed, it is still valid to pursue an interpretation as done here.

An advantage of using numerical simulations in the context presented here is the possibility to account for the complexity of realistic geometries, meaning an inclined fault and water production over the whole filter length of the well, based on geological and field data and then investigating the actual parameter space of the researched aquifer. A conclusion that the effect of a low conductivity fracture is magnified with higher matrix permeability values found by Heber Cinco et al. (1978) through analytical investigations is in agreement with the observations based on the numerical simulations of realistic aquifer geometries calculated in this work.

### **6.3 Numerical precision of the reduced basis method and consequences for the PI evaluation**

With focus on the PI investigation, an important topic to cover is numerical precision. The RB model was trained with a maximum relative error tolerance of  $5 \times 10^{-4}$  relative to the FE solution. This value was accepted as the best possible one because it is not a trivial task to find a numerically stable combination of this accuracy value and integrate all input parameter ranges during the “offline stage” of the RB approach (the greater the parameter ranges, the higher the risk of extreme combinations leading to problems in finding a numerical solution) (Degen et al., 2020). For most parameter combinations, this accuracy is more than sufficient to compare the pressure result between the matrix and the fault zone model without introducing a considerable error. However, for a very small difference between the two pressure curves, they might become relevant. This applies to very high matrix permeabilities in general ( $\sim 1 \times 10^{-11} \text{ m}^2$ ) as well as to cases where the properties of the fault zone are very similar compared to those of the surrounding matrix, thereby causing only a very small difference between the two pumping tests. Taking this into account, it means that  $\Delta PI_{rel}$  values below 0.05 should be considered altered. However, either way, such small  $\Delta PI_{rel}$  can be interpreted as insignificant fault zone influence and therefore do not introduce errors into the overall interpretation.

### **6.4 Resolution of spatial information in the greater Munich area**

Considering the simulated maps in the Munich area, it is fundamental to note the precision of the underlying input maps and the design of these spatial investigations. Even though the point reservoir data is the currently most comprehensive data set for the study site compared with previous works (Birner, 2013) and represents the state of the art, it is only a fraction of the reality. Additionally, the regionalized versions generated from it and used as input are only as good as the quality of the data points. The pumping test data used to derive matrix permeability is often quite challenging to evaluate because technical effects and short pumping test duration increase the difficulty of the interpretation (Savvatis, 2012; Wolfgramm et al., 2007). As it is usually the case with spatial point information in geosciences, a higher point density is desirable and would increase the precision of the regionalization applied (Isaaks & Srivastava, 1989). However, the errors associated with this problem are hard to grasp, and additional data would help to quantify and reduce them. This can be solved only by drilling more wells. With respect to the design of the spatial investigations, model properties for which no spatial information was available had to be applied for each map globally. Fault zone properties, in particular,

should be mentioned here. The comparison between the calculated and real world flow regimes should thus be used only as an indication for the plausibility of the fault zone types tested and the general understanding. Because of the characteristics of the fault zone genesis (see Chapter 2.2), it is quite likely that different fault zone types are present at the same time in the study and map area.

## 7 Conclusions for the geothermal exploration of the Upper Jurassic aquifer and possible outlook

In general it can be concluded that the presented model concept (inclined fault zone with punctual well intersection inside of a reservoir matrix) proved to be valid to describe real world situations and capture the general hydraulic behavior of fault zones in the UJA. It is therefore possible to use the findings, methods and tools of this work in a general manner and during the planning of new geothermal wells. A special advantage lies in the potential to understand and quantify the hydraulic impact of a fault zone in various conditions by efficiently evaluating large numbers of possible scenarios that can be quickly adjusted if new reservoir knowledge becomes available.

*Tab. 8 Parameter ranges of the UJA and of its fault zones updated with results of this work.*

	Min	Max	Unit
<b>Matrix permeability</b>	$1.0 \times 10^{-17}$	$2.0 \times 10^{-11}$	m <sup>2</sup>
<b>Matrix storage</b>	$2.0 \times 10^{-12}$	$1.6 \times 10^{-10}$	1/Pa
<b>Fault zone permeability</b>	$1.0 \times 10^{-14}$	$1.0 \times 10^{-9}$	m <sup>2</sup>
<b>Fault zone storage</b>	$2.0 \times 10^{-12}$	$1.6 \times 10^{-10}$	1/Pa
<b>Fault zone thickness (hydr. active)</b>	15	100	m
<b>Fluid viscosity</b>	$1.0 \times 10^{-4}$	$5.0 \times 10^{-4}$	Pa*s

Another conclusion can be drawn regarding the hydraulic properties of the UJA. During the course of this work, it was possible to gather the currently most comprehensive data set of hydraulic aquifer properties in the greater Munich area and derive possible parameter ranges. Additionally, the hydraulically relevant properties of fault zones were derived from literature sources, analyzed and compared to the real world situation. This allowed to derive an upper limit of the hydraulically relevant thickness of fault zones at 100 meters. A summary of

hydraulic parameter ranges considered characteristic for the greater Munich area are given in Tab. 8.

To answer open questions in regards to the hydraulic effect of fault zones, an intensive investigation of the UJA parameter space was deployed. Over 30,000 FE-based and more than 90 million numerical simulations based on high precision model order reduction were carried out on an HPC cluster.

On the one hand, this resulted in a successful identification of occurring flow regime transitions. These results can be further used to determine reservoir conditions in which the hydraulic behavior around a well is dominated by fault zones. The use of the resulting regression functions allows a convenient investigation of individual hydraulic parameters in the planning phase of a geothermal exploration site. Additionally, extreme values for the observation of fault zone related flow regimes have been identified. This means that a bilinear flow can only be observed for the UJA if the matrix permeability is less than  $2.0 \times 10^{-13} \text{ m}^2$ . For a matrix permeability less than  $6.0 \times 10^{-14} \text{ m}^2$ , linear flow can occur while negative boundary flow can be detected for values smaller than  $6.0 \times 10^{-15} \text{ m}^2$ . In addition, it was shown that there is an area in parameter space that allows for a fault zone with better hydraulic properties than those of the matrix while only radial flow can still be observed in the pressure derivative of a pumping test. It seems possible now that some of the geothermal wells in the greater Munich area tap into productivity improving fault zones that are hidden in their pumping tests. This is a crucial information for the development of future drilling targets.

On the other hand, it was shown that hydraulically active fault zones can significantly improve well productivity, even if they are hidden in the radial flow of pumping tests and even if they have only a low hydraulically relevant thickness. Fault zones with a thickness of  $\geq 100 \text{ m}$  generally have a different dynamic in terms of flow regimes and *PI* improvement than those with smaller values. It was observed that these high fault zones thicknesses can even amplify increasing hydraulic matrix properties at high fault zone permeability values. However, flow regime analysis and spatial investigations suggest lower thickness values ( $< 100\text{m}$ ) for the Upper Jurassic aquifer, which can still have a considerable effect on the *PI*. For the Munich area, a fault zone of 50-meter hydraulically active thickness was used to best replicate the real world flow regime observations. The spatial analysis of this fault zone type suggests that to the south and southwest of Munich's downtown, an increase in well *PI* of more than 50% would be possible if such a hydraulically active fault zone were developed in this area. Furthermore, it can be concluded that an observation of a fault zone in a pumping test is not likely in the Munich urban area but only south of it. In addition to these spatial findings, it was possible to

derive that hydraulically hidden fault zones of the “low thickness group” must generally be at least twice as permeable as the surrounding matrix or more in order to cause a productivity increase of 10% or more. It could also be seen that below  $3.73 \times 10^{-15} \text{ m}^2$  matrix permeability, it is possible to realize an economically successful geothermal well only by developing a high permeable fault zone. In combination with the newly generated spatial reservoir permeability map in the greater Munich area (see Fig. 28), it is possible to locate regions for the geothermal exploration where it is mandatory to develop a highly permeable fault zone to construct an economically successful geothermal well.

The findings of this work were also shared publicly in a highly detailed way with very little technical requirements through the open source tool “uja faultzones”. By using Python, everyone interested can run high precision numerical simulations of pumping tests of the presented fault zone model. Custom parameter combinations can be investigated without the need for fast computing hardware. Well flow regimes and the alteration of the well PI through a fault zone can now be checked during the planning of a new geothermal site without much effort and complement the workflow of a reservoir engineer.

The relevance of fault zones for the geothermal exploration in general but especially in the UJA could be demonstrated in the course of this work. The workflow presented here is not limited to the UJA and could easily be applied to a different aquifer and parameter space. Its principles could also be used to evaluate effects of other hydraulic aquifer structures, such as karstification. Additionally, future research could on the one hand improve the investigative detail by analyzing even more parameter samples based on improved hardware or software. On the other hand, newly gathered reservoir data should be used to update the numerical models as it becomes available in the coming years. Furthermore, the presented analysis could be extended to fault zones with reduced hydraulic properties compared to the surrounding host rock. It would also be worth attempting to overcome the re-meshing limitations and investigate additional geometric model factors, such as fault zone length, fault zone inclination and well inclination. This could be achieved by automating mesh generation or by training more reduced order models based on systematically handpicked geometry realizations. Finally, the investigation of heat transport dependent on the hydraulic setting around fault zones could be addressed. Such a systematic analysis could provide a relationship between aquifer as well as fault zone properties and geometry or maximum propagation of a cold water injection front around a geothermal well. Such a knowledge would help to improve future exploration concepts in terms of thermal breakthrough and sustainable reservoir usage.

## 8 References

- Agemar, T., Alten, J., Ganz, B., Kuder, J., Kühne, K., Schumacher, S., & Schulz, R. (2014). The Geothermal Information System for Germany – GeotIS. *Zeitschrift Der Deutschen Gesellschaft Für Geowissenschaften*, 165(2), 129–144. <https://doi.org/10.1127/1860-1804/2014/0060>
- Agosta, F., & Aydin, A. (2006). Architecture and deformation mechanism of a basin-bounding normal fault in Mesozoic platform carbonates, central Italy. *Journal of Structural Geology*, 28(8), 1445–1467. <https://doi.org/10.1016/j.jsg.2006.04.006>
- Ahrens, J., Geveci, B., & Law, C. (2005). *ParaView: An End-User Tool for Large Data Visualization*, *Visualization Handbook*. Elsevier.
- Alfonsi, A., Rabiti, C., Mandelli, D., Cogliati, J., Wang, C., Talbot, P. W., ... Smith, C. (2017). *RAVEN Theory Manual and User Guide*. Idaho National Laboratory.
- Alt, W., & Kahnt, R. (2014). Hydraulische Untersuchungen. In M. Bauer, W. Freeden, H. Jacobi, & T. Neu (Eds.), *Handbuch Tiefe Geothermie* (pp. 609–658). Berlin Heidelberg: Springer.
- Armstead, H. C. H. (1978). *Geothermal energy: Its past, present and future contributions to the energy needs of man*.
- Bachmann, G. H., Dohr, G., & Müller, M. (1982). Exploration in a classic thrust belt and its foreland Bavarian Alps, Germany. *The American Association of Petroleum Geologists Bulletin*, 66(12), 2529–2542.
- Bachmann, G. H., Müller, M., & Weggen, K. (1987). Evolution of the Molasse Basin (Germany, Switzerland). *Tectonophysics*, 137(1–4), 77–92. [https://doi.org/10.1016/0040-1951\(87\)90315-5](https://doi.org/10.1016/0040-1951(87)90315-5)
- Balderer, W. (1990). Hydrogeologische Charakterisierung der Grundwasservorkommen innerhalb der Molasse der Nordostschweiz aufgrund von hydrochemischen und Isotopenuntersuchungen. [Hydrogeological Characterization of the Groundwater Reservoirs in the Molasse of the North-East. *Steir. Beitr. z. Hydrogeologie*. Graz.
- Bastesen, E., & Braathen, A. (2010). Extensional faults in fine grained carbonates - analysis of fault core lithology and thickness-displacement relationships. *Journal of Structural Geology*, 32(11), 1609–1628. <https://doi.org/10.1016/j.jsg.2010.09.008>
- Bauer, M., Freeden, W., Jacobi, H., & Neu, T. (2014). *Handbuch Tiefe Geothermie*. (M. Bauer, W. Freeden, H. Jacobi, & N. Thomas, Eds.), *Handbuch Tiefe Geothermie*. Springer Berlin Heidelberg. <https://doi.org/10.1007/978-3-642-54511-5>

- Billi, A., Salvini, F., & Storti, F. (2003). The damage zone-fault core transition in carbonate rocks: Implications for fault growth, structure and permeability. *Journal of Structural Geology*, 25(11), 1779–1794. [https://doi.org/10.1016/S0191-8141\(03\)00037-3](https://doi.org/10.1016/S0191-8141(03)00037-3)
- Birner, J. (2013). *Hydrogeologisches Modell des Malmaquifers im Süddeutschen Molassebecken*. Freie University Berlin.
- Birner, J., Fritzer, T., Jodocy, M., Savvatis, A., Schneider, M., Ingrid Stober, ... Stober, I. (2012). Hydraulische Eigenschaften des Malmaquifers im Süddeutschen Molassebecken und ihre Bedeutung für die geothermische Erschließung. *Z Geol Wiss.*, 40(2/3), 133–156.
- Birner, J., Mayr, C., Thomas, L., Schneider, M., Baumann, T., & Winkler, A. (2011). Hydrochemie und Genese der tiefen Grundwaesser des Malmaquifers im bayerischen Teil des sueddeutschen Molassebeckens. *Zeitschrift Fuer Geologische Wissenschaften*.
- Blöcher, G., & Cacace, M. (2015). MeshIt - A software for three dimensional volumetric meshing of complex faulted reservoirs. *Computers and Geosciences*, 74(6), 5191–5209. <https://doi.org/10.1007/s12665-015-4537-x>
- Böhm, F., Savvatis, A., & Steiner, U. (2012a). Handlungsempfehlungen. In M. Schneider & L. Thomas (Eds.), *Verbundvorhaben: Wissenschaftliche und technische Grundlagen zur strukturgeologischen und hydrogeologischen Charakterisierung tiefer geothermisch genutzter Grundwasserleiter am Beispiel des süddeutschen Molassebeckens* (pp. 215–217).
- Böhm, F., Savvatis, A., & Steiner, U. (2012b). Innovative Explorationsstrategie. In *Verbundvorhaben: Wissenschaftliche und technische Grundlagen zur strukturgeologischen und hydrogeologischen Charakterisierung tiefer geothermisch genutzter Grundwasserleiter am Beispiel des süddeutschen Molassebeckens* (pp. 129–154).
- Böhm, F., Savvatis, A., Steiner, U., Schneider, M., & Koch, R. (2013). Lithofazielle Reservoircharakterisierung zur geothermischen Nutzung des Malm im Großraum München. *Grundwasser*, 18(1), 3–13. <https://doi.org/10.1007/s00767-012-0202-4>
- Bohnsack, D., Potten, M., Pfrang, D., Wolpert, P., & Zosseder, K. (2020). Porosity–permeability relationship derived from Upper Jurassic carbonate rock cores to assess the regional hydraulic matrix properties of the Malm reservoir in the South German Molasse Basin. *Geothermal Energy*, 8(1). <https://doi.org/10.1186/s40517-020-00166-9>
- Bourdet, D. (2002). *Well test analysis : the use of advanced interpretation models*. (1st ed.). Amsterdam: Elsevier Science B.V.
- Bourdet, D., Ayoub, J. A., & Pirard, Y. M. (1989). Use of Pressure Derivative in Well Test

- Interpretation. *SPE Formation Evaluation*. <https://doi.org/10.2118/12777-PA>
- Bourdet, D., Whittle, T. M., Douglas, A. A., & Pirard, Y. M. (1983). A new set of type curves simplifies well test analysis. *World Oil*. <https://doi.org/10.2118/16812-PA>
- Bruss, D., Barenth, F., Greller, M., Hecht, C., Koschel, H., Kröper, T., & SWM Services GmbH. (2018). *Verbundvorhaben : Ganzheitlich optimierte und nachhaltige Reservoirerschließung für tiefengeothermische Anlagen im bayerischen Molassebecken Teilvorhaben : Entwicklung eines 50 MW el Kraftwerks und Erschließung von 400 MW th für die Fernwärme in München E. München.*
- Budach, I., Wolfgramm, M., Moeck, I., & Lüschen, E. (2015). Die Strukturentwicklung des Malm in Unterhaching ( Bayern ) aus 3D-seismischen Daten, (November).
- Buitinck, L., Louppe, G., Blondel, M., Pedregosa, F., Mueller, A., Grisel, O., ... Varoquaux, G. (2013). API design for machine learning software: experiences from the scikit-learn project, 1–15. Retrieved from <http://arxiv.org/abs/1309.0238>
- Bundschuh, J., & Suárez Arriaga, M. C. (2010). *Introduction to the Numerical Modeling of Groundwater and Geothermal Systems: Fundamentals of Mass, Energy and Solute Transport in Poroelastic Rocks.*
- Cacace, M., Blöcher, G., Watanabe, N., Moeck, I., Börsing, N., Scheck-Wenderoth, M., ... Huenges, E. (2013). Modelling of fractured carbonate reservoirs: Outline of a novel technique via a case study from the Molasse Basin, southern Bavaria, Germany. *Environmental Earth Sciences*, 70(8), 3585–3602. <https://doi.org/10.1007/s12665-013-2402-3>
- Cacace, M., & Jacquy, A. B. (2017). Flexible parallel implicit modelling of coupled thermal-hydraulic-mechanical processes in fractured rocks. *Solid Earth*, 8(5), 921–941. <https://doi.org/10.5194/se-8-921-2017>
- Caine, J. S., Evans, J. P., & Forster, C. B. C. B. C. B. (1996). Fault zone architecture and permeability structure. *Geology*, 24(11), 1025–1028. [https://doi.org/10.1130/0091-7613\(1996\)024<1025](https://doi.org/10.1130/0091-7613(1996)024<1025)
- Choi, J. H., Edwards, P., Ko, K., & Kim, Y. S. (2016). Definition and classification of fault damage zones: A review and a new methodological approach. *Earth-Science Reviews*, 152, 70–87. <https://doi.org/10.1016/j.earscirev.2015.11.006>
- Cinco-Ley, H., Ramey, H. J., & Miller, F. G. (1975). Unsteady-State Pressure Distribution Created by a Well with an Inclined Fracture. *Society of Petroleum Engineers Journal*, 5591.
- Cinco-Ley, H., Samaniego V., F., & Dominguez A., N. (1978). Transient Pressure Behavior for

- a Well With a Finite-Conductivity Vertical Fracture. *Society of Petroleum Engineers Journal*, 18(04), 253–264. <https://doi.org/10.2118/6014-PA>
- Degen, D., Veroy, K., Freymark, J., Scheck-Wenderoth, M., Poulet, T., & Wellmann, F. (2021). Global sensitivity analysis to optimize basin-scale conductive model calibration – A case study from the Upper Rhine Graben. *Geothermics*, 95(March), 102143. <https://doi.org/10.1016/j.geothermics.2021.102143>
- Degen, D., Veroy, K., & Wellmann, F. (2020). Certified reduced basis method in geosciences. *Computational Geosciences*, 24(1), 241–259. <https://doi.org/10.1007/s10596-019-09916-6>
- Dinh, A. V., & Tiab, D. (2010). Pressure-Transient Analysis of a Well With an Inclined Hydraulic Fracture. *Spe Reservoir Evaluation & Engineering*, 13(March), 845–860.
- Draper, N. R., & Smith, H. (1998). Applied Regression Analysis, 3rd Edition. *John Wiley & Sons, Inc.* Retrieved from <http://eu.wiley.com/WileyCDA/WileyTitle/productCd-0471170828.html>
- Dussel, M., Moeck, I., Wolfgramm, M., & Straubinger, R. (2018). Characterization of a Deep Fault Zone in Upper Jurassic Carbonates of the Northern Alpine Foreland Basin for Geothermal Production (South Germany). In *43rd Workshop on Geothermal Reservoir Engineering* (pp. 12–14). Stanford.
- Earlougher, J. R. (1977). Advances in Well Test Analysis. *SPE Monograph Series*, 5, 264.
- Enachescu, C., Dmour, H., & Ács, V. (2016). Integrated well test interpretation of a naturally fractured carbonate reservoir Integrated well test interpretation of a naturally fractured carbonate reservoir – A case study. *MOLGROUP*, (February). Retrieved from [https://www.researchgate.net/publication/290391450\\_Integrated\\_well\\_test\\_interpretation\\_of\\_a\\_naturally\\_fractured\\_carbonate\\_reservoir\\_-\\_A\\_case\\_study](https://www.researchgate.net/publication/290391450_Integrated_well_test_interpretation_of_a_naturally_fractured_carbonate_reservoir_-_A_case_study)
- Faulkner, D. R., Jackson, C. A. L., Lunn, R. J., Schlische, R. W., Shipton, Z. K., Wibberley, C. A. J., & Withjack, M. O. (2010). A review of recent developments concerning the structure, mechanics and fluid flow properties of fault zones. *Journal of Structural Geology*, 32(11), 1557–1575. <https://doi.org/10.1016/j.jsg.2010.06.009>
- Frisch, H., & Huber, B. (2000). Ein hydrogeologisches Modell und der Versuch einer Bilanzierung des Thermalwasservorkommens für den Malmkarst im süddeutschen und im angrenzenden oberösterreichischen Molassebecken. *Hydrogeologie Und Umwelt*, 20, 25–43.
- Fritzer, T., Settles, E., & Dorsch, K. (2012). *Bayerischer Geothermieatlas – Hydrothermale Energiegewinnung*. Bayerisches Staatsministerium für Wirtschaft, Infrastruktur, Verkehr

- und Technologie. Retrieved from [papers://16b01535-c16e-4b49-9060-33c1aad71bf3/Paper/p3381](https://papers://16b01535-c16e-4b49-9060-33c1aad71bf3/Paper/p3381)
- Gaston, D., Newman, C., Hansen, G., & Lebrun-grandié, D. (2009). MOOSE : A parallel computational framework for coupled systems of nonlinear equations. In *International Conference on Mathematics, Computational Methods & Reactor Physics (M&C 2009)* (Vol. 239, pp. 1768–1778). <https://doi.org/10.1016/j.nucengdes.2009.05.021>
- Goldbrunner, J. E., & Vasvári, V. (2016). Hydrogeology and geothermic simulation of the geothermal doublet at Waldkraiburg (Bavaria). *Austrian Journal of Earth Sciences*, *109*(1), 99–113. <https://doi.org/10.17738/ajes.2016.0007>
- Goldstein, B., Hiriart, G., Tester, J., Gutiérrez-Negrín, L., Bertani, R., Bromley, C., ... Muraoka, H. (2013). Geothermal energy, nature, use, and expectations. In M. Kaltschmitt, N. J. Themelis, L. Y. Bronicki, L. Söder, & L. A. Vega (Eds.), *Renewable Energy Systems* (pp. 772–782). New York, NY: Springer New York. [https://doi.org/10.1007/978-1-4614-5820-3\\_309](https://doi.org/10.1007/978-1-4614-5820-3_309)
- Gringarten, A. C. (2008). From Straight Lines to Deconvolution: The Evolution of the State of the Art in Well Test Analysis. *SPE Reservoir Evaluation & Engineering*, *11*(April 2007), 18. <https://doi.org/10.2118/102079-PA>
- Gringarten, A. C., Ramey, H. J., & Raghavan, R. (1974). Unsteady-State Pressure Distributions Created by a Well With a Single Infinite-Conductivity Vertical Fracture. *Society of Petroleum Engineers Journal*, *14*(04), 347–360. <https://doi.org/10.2118/4051-PA>
- Grotzinger, J., & Jordan, T. (2017). *Press/Siever Allgemeine Geologie* (7th ed.). Berlin Heidelberg: Springer Spektrum.
- Heidinger, M., Eichinger, F., Purtschert, R., Mueller, P., Zappala, J., Wirsing, G., ... Groß, D. (2019). 81Kr/85Kr-Dating of thermal groundwaters in the Upper Jurassic (Molasse Basin). *Grundwasser*, *24*(4), 287–294. <https://doi.org/10.1007/s00767-019-00431-0>
- Heine, F., & Einsiedl, F. (2021). Groundwater dating with dissolved organic radiocarbon: A promising approach in carbonate aquifers. *Applied Geochemistry*, *125*(August 2020), 104827. <https://doi.org/10.1016/j.apgeochem.2020.104827>
- Heine, F., Zosseder, K., & Einsiedl, F. (2021). Hydrochemical zoning and chemical evolution of the deep upper jurassic thermal groundwater reservoir using water chemical and environmental isotope data. *Water (Switzerland)*, *13*(9). <https://doi.org/10.3390/w13091162>
- Hesthaven, J. S., Rozza, G., & Stamm, B. (2016). *Certified Reduced Basis Methods for Parametrized Partial Differential Equations*. <https://doi.org/10.1007/978-3-319-22470-1>

- Hesthaven, J. S., & Warburton, T. (2008). *Nodal Discontinuous Galerkin Methods: Algorithms, Analysis, and Applications*. *Computational Seismology* (1st ed.). Springer-Verlag New York. <https://doi.org/10.1093/acprof:oso/9780198717409.003.0009>
- Homuth, S., Götz, A. E., & Sass, I. (2015). Reservoir characterization of the Upper Jurassic geothermal target formations (Molasse Basin, Germany): role of thermofacies as exploration tool. *Geothermal Energy Science*, 3(1), 41–49. <https://doi.org/10.5194/gtes-3-41-2015>
- Idaho National Laboratory. (2019). mooseframework.org: IterationAdaptiveDT. Retrieved April 3, 2019, from <https://www.mooseframework.org/source/timesteppers/IterationAdaptiveDT.html#iterationadaptivedt>
- IHS Markit. (2017). Well Testing Fundamentals. Retrieved from <http://cdn.ihs.com/www/pdf/Well-Test-Fundamentals-Poster.pdf>
- Isaaks, E. H., & Srivastava, R. M. (1989). *Applied geostatistics*. New York: Oxford University Press.
- Jia, P., Cheng, L., Huang, S., & Liu, H. (2016). Pressure-transient analysis of a finite-conductivity inclined fracture connected to a slanted wellbore. *SPE Journal*, 21(2). [https://doi.org/10.1016/S0929-6441\(09\)60019-9](https://doi.org/10.1016/S0929-6441(09)60019-9)
- Knott, S. D., Beach, A., Brockbank, P. J., Lawson Brown, J., McCallum, J. E., & Welbon, A. I. (1996). Spatial and mechanical controls on normal fault populations. *Journal of Structural Geology*, 18(2–3), 359–372. [https://doi.org/10.1016/S0191-8141\(96\)80056-3](https://doi.org/10.1016/S0191-8141(96)80056-3)
- Kolditz, O. (2002). *Computational Methods in Environmental Fluid Mechanics*. <https://doi.org/10.1007/978-3-662-04761-3>
- Kuchuk, F. J. (2009). Radius of investigation for reserve estimation from pressure transient well tests. *SPE Middle East Oil and Gas Show and Conference, MEOS, Proceedings*, 3, 1157–1178. <https://doi.org/10.2118/120515-ms>
- Lafogler, M., Bartels, J., Wenderoth, F., Savvatis, A., Steiner, U., Schubert, A., ... Baumann, T. (2016). Quantifizierung der lokalen und Prognose der regionalen hydraulischen und hydrochemischen Reservoireigenschaften des Malmaquifers auf Basis eines Push-Pull-Tests am Standort Pullach ( Puma ) Schlussbericht, 90.
- Leibniz-Rechenzentrum. (2017). Leibniz Supercomputing Centre. Retrieved April 23, 2019, from <https://www.lrz.de/services/compute/>
- Lemcke, K. (1976). Übertiefe Grundwässer im süddeutschen Alpenvorland. *Bull. Ver. Schweiz. Petroleum-Geol. u. -Ing.*, 42(103), 9–18.

- Lemcke, K. (1988). *Das Bayerische Alpenvorland vor der Eiszeit*. Stuttgart, Germany: Schweizerbart Science Publishers.
- Lemmon, E. W., McLinden, M. O., & Friend, D. G. (2018). Thermophysical Properties of Fluid Systems. In P. J. Linstrom & W. G. Mallard (Eds.), *NIST Chemistry WebBook, NIST Standard Reference Database Number 69*. Gaithersburg MD: National Institute of Standards and Technology. <https://doi.org/10.18434/T4D303>
- Lüschen, E., Wolfgramm, M., Fritzer, T., Dussel, M., Thomas, R., & Schulz, R. (2014). 3D seismic survey explores geothermal targets for reservoir characterization at Unterhaching, Munich, Germany. *Geothermics*, *50*, 167–179. <https://doi.org/10.1016/j.geothermics.2013.09.007>
- Manzoni, A., Quarteroni, A., & Rozza, G. (2012). Computational Reduction for Parametrized PDEs: Strategies and Applications. *Milan Journal of Mathematics*, *80*(2), 283–309. <https://doi.org/10.1007/s00032-012-0182-y>
- Mayrhofer, C. (2013). *Hydrochemische Untersuchungen im Malmaquifer im bayerischen Molassebecken*. Technische Universität München.
- McClure, M. W., & Horne, R. N. (2011). Pressure transient analysis of fracture zone permeability at Soultz-sous-Forêts. *Transactions - Geothermal Resources Council*, *35* 2.
- Micarelli, L., Benedicto, A., & Wibberley, C. A. J. (2006). Structural evolution and permeability of normal fault zones in highly porous carbonate rocks. *Journal of Structural Geology*, *28*(7), 1214–1227. <https://doi.org/10.1016/j.jsg.2006.03.036>
- Michie, E. A. H. A. H., Haines, T. J. J., Healy, D., Neilson, J. E. E., Timms, N. E., Wibberley, C. A. J. A. J., ... Wibberley, C. A. J. A. J. (2014). Influence of carbonate facies on fault zone architecture. *Journal of Structural Geology*, *65*(February 2015), 82–99. <https://doi.org/10.1016/j.jsg.2014.04.007>
- Miyan, M., & Pant, P. K. (2015). Diffusion Equation for Fluid Flow in Porous Rocks. *Journal of Science*, *4*(4), 418–425.
- Moeck, I. S., Uhlig, S., Loske, B., Jentsch, A., Mählmann, R. F., Ferreiro-Maehlmann, R., & Hild, S. (2015). Fossil Multiphase Normal Faults - Prime Targets for Geothermal Drilling in the Bavarian Molasse Basin? *World Geothermal Congress 2015*, (April), 19–25.
- Montgomery, D. C. (2013). *Design and Analysis of Experiments* (8th ed.).
- Mraz, E. (2019). *Reservoir Characterization to Improve Exploration Concepts of the Upper Jurassic in the Southern Bavarian Molasse Basin*. Technical University Munich.
- Otto, A. (2021). UmweltAtlas Bayern. Bayerisches Landesamt für Umwelt. Retrieved from <https://www.lfu.bayern.de/umweltdaten/kartendienste/umweltatlas/>

- Peacock, D. C. P., Nixon, C. W., Rotevatn, A., Sanderson, D. J., & Zuluaga, L. F. (2016). Glossary of fault and other fracture networks. *Journal of Structural Geology*, *92*, 12–29. <https://doi.org/10.1016/j.jsg.2016.09.008>
- Pedregosa, F., Weiss, R., & Brucher, M. (2011). Scikit-learn : Machine Learning in Python, *12*, 2825–2830.
- Permann, C. J., Gaston, D. R., Andrš, D., Carlsen, R. W., Kong, F., Lindsay, A. D., ... Martineau, R. C. (2020). MOOSE: Enabling massively parallel multiphysics simulation. *SoftwareX*, *11*, 100430. <https://doi.org/https://doi.org/10.1016/j.softx.2020.100430>
- Petropoulos, G. P., & Srivastava, P. K. (2017). *Sensitivity Analysis in Earth Observation Modelling*. Amsterdam: Elsevier.
- Plischke, E., Borgonovo, E., & Smith, C. L. (2013). Global sensitivity measures from given data. *European Journal of Operational Research*, *226*(3), 536–550. <https://doi.org/10.1016/j.ejor.2012.11.047>
- Prud'homme, C., Rovas, D. V, Veroy, K., Machiels, L., Maday, Y., Patera, A. T., ... Turinici, G. (2002). Reliable Real-Time Solution of Parametrized Partial Differential Equations: Reduced-Basis Output Bound Methods. *Journal of Fluids Engineering*, *124*(1), 70. <https://doi.org/10.1115/1.1448332>
- Quarteroni, A., Manzoni, A., & Negri, F. (2015). *Reduced basis methods for partial differential equations: An introduction*. <https://doi.org/10.1007/978-3-319-15431-2>
- Quaschnig, V. (2010). *Renewable Energy and Climate Change*. <https://doi.org/10.1002/9781119994381>
- Quenstedt, F. A. (1858). *Der Jura*. Tübingen: Laupp. Retrieved from <https://books.google.de/books?id=Y7sQAAAAIAAJ>
- Rioseco, E. M., Ziesch, J., Wawerzinek, B., Hartmann, H. Von, Thomas, R., & Bunes, H. (2018). 3-D Geothermal Reservoir Modeling of the Upper Jurassic Carbonate Aquifer in the City of Munich ( Germany ) under the Thermal-Hydraulic Influence of Optimized Geothermal Multi- Well Patterns – Project GeoParaMoL. *43rd Workshop on Geothermal Reservoir Engineering Stanford University*, 1–12.
- Ritchie, H. (2021). Energy Production and Consumption. Retrieved from <https://ourworldindata.org/energy-production-consumption>
- Rojas, A. E. O., Dussel, M., & Moeck, I. (2017). Borehole geophysical characterisation of a major fault zone in the geothermal Unterhaching Gt 2 well , South German Molasse Basin, *169*(September), 445–463. <https://doi.org/10.1127/zdgg/201>
- Romera, J. J. G. (2020, March). Python library for IAPWS standard calculation of water and

- steam properties. Zenodo. <https://doi.org/10.5281/zenodo.3734292>
- Saltelli, A. (2002). Making best use of model evaluations to compute sensitivity indices. *Computer Physics Communications*, 145(2), 280–297. [https://doi.org/10.1016/S0010-4655\(02\)00280-1](https://doi.org/10.1016/S0010-4655(02)00280-1)
- Saltelli, A., Annoni, P., Azzini, I., Campolongo, F., Ratto, M., & Tarantola, S. (2010). Variance based sensitivity analysis of model output. Design and estimator for the total sensitivity index. *Computer Physics Communications*, 181(2), 259–270. <https://doi.org/10.1016/j.cpc.2009.09.018>
- Savvatis, A. (2012). Hydraulik. In M. Schneider & L. Thomas (Eds.), *Verbundvorhaben: Wissenschaftliche und technische Grundlagen zur strukturgeologischen und hydrogeologischen Charakterisierung tiefer geothermisch genutzter Grundwasserleiter am Beispiel des süddeutschen Molassebeckens* (pp. 129–154).
- Schlumberger. (2021). inflow performance relationship. Retrieved from [https://glossary.oilfield.slb.com/en/Terms/i/inflow\\_performance\\_relationship.aspx](https://glossary.oilfield.slb.com/en/Terms/i/inflow_performance_relationship.aspx)
- Schneider, M., & Thomas, L. (2012). Verbundvorhaben : Wissenschaftliche und technische Grundlagen zur strukturgeologischen und hydrogeologischen Charakterisierung tiefer geothermisch genutzter Grundwasserleiter am Beispiel des süddeutschen Molassebeckens. *Endbericht--BMU Forschungsvorhaben*, 237.
- Schulz, R. (2012). *Geothermische Charakterisierung von karstig-klüftigen Aquiferen im Großraum München. Leibniz-Institut für Angewandte Geophysik Hannover*.
- scikit-learn user guide: preprocessing data. (2018). Retrieved April 3, 2019, from <https://scikit-learn.org/stable/modules/preprocessing.html>
- Seithel, R., Gaucher, E., Mueller, B., Steiner, U., & Kohl, T. (2019). Geothermics Probability of fault reactivation in the Bavarian Molasse Basin. *Geothermics*, 82(May), 81–90. <https://doi.org/10.1016/j.geothermics.2019.06.004>
- Shipilin, V., C. Tanner, D., Von Hartmann, H., & Moeck, I. (2020). Multiphase, decoupled faulting in the southern German Molasse Basin - Evidence from 3-D seismic data. *Solid Earth*, 11(6), 2097–2117. <https://doi.org/10.5194/se-11-2097-2020>
- Sobol, I. M. (2001). Global sensitivity indices for nonlinear mathematical models and their Monte Carlo estimates. *Mathematics and Computers in Simulation*, 55(1–3), 271–280. [https://doi.org/10.1016/S0378-4754\(00\)00270-6](https://doi.org/10.1016/S0378-4754(00)00270-6)
- Sobol, I. M., & Kucherenko, S. (2009). Derivative based global sensitivity measures and their link with global sensitivity indices. *Mathematics and Computers in Simulation*, 79(10), 3009–3017. <https://doi.org/10.1016/j.matcom.2009.01.023>

- Steiner, U. (2012). Strukturgeologie. In M. Schneider & L. Thomas (Eds.), *Verbundvorhaben: Wissenschaftliche und technische Grundlagen zur strukturgeologischen und hydrogeologischen Charakterisierung tiefer geothermisch genutzter Grundwasserleiter am Beispiel des süddeutschen Molassebeckens* (pp. 29–59).
- Steiner, U., Böhm, F., & Savvatis, A. (2012). Hydrogeologisches Modell. In M. Schneider & L. Thomas (Eds.), *Verbundvorhaben: Wissenschaftliche und technische Grundlagen zur strukturgeologischen und hydrogeologischen Charakterisierung tiefer geothermisch genutzter Grundwasserleiter am Beispiel des süddeutschen Molassebeckens* (pp. 196–220).
- Stier, P., & Prestel, R. (1991). Der Malmkarst im Süddeutschen Molassebecken – Ein hydrogeologischer Überblick. In *Hydrogeothermische Energiebilanz und Grundwasserhaushalt des Malmkarstes im Süddeutschen Molassebecken (Schlussbericht - Forschungsvorhaben 03 E 6240 A/B)* (p. 12). München, Freiburg: Bay. L.-Amt Wasserwirtschaft & geol. L.-Amt Baden-Württemberg.
- Stober, I., & Bucher, K. (2013). Geothermal Energy. Springer Berlin Heidelberg. <https://doi.org/10.1007/978-3-642-13352-7>
- Stober, I., & Bucher, K. (2014). Hydrochemische Untersuchungen. In *Geothermie* (pp. 261–279). Berlin, Heidelberg: Springer Berlin Heidelberg. [https://doi.org/10.1007/978-3-642-41763-4\\_14](https://doi.org/10.1007/978-3-642-41763-4_14)
- Stober, I., Jodocy, M., & Hintersberger, B. (2013). Gegenüberstellung von Durchlässigkeiten aus verschiedenen Verfahren im tief liegenden Oberjura des südwestdeutschen Molassebeckens. *Z. Dt. Ges. Geowiss.*, 164, 663–679. <https://doi.org/10.1127/1860-1804/2013/0033>
- Stoyke, R., Schubert, A., Vater, H., Böhm, F., Dorsch, K., & Hanke, K. (2006). Neue Erkenntnisse zum Malm Tiefengrundwasserleiter in der Westmolasse aus der Tiefbohrung Bad Wörishofen GT2 und ihr Bedeutung für die Geothermie. *Erdwerk*.
- Thomas, L. (2012). Projektbeschreibung. In M. Schneider & L. Thomas (Eds.), *Verbundvorhaben: Wissenschaftliche und technische Grundlagen zur strukturgeologischen und hydrogeologischen Charakterisierung tiefer geothermisch genutzter Grundwasserleiter am Beispiel des süddeutschen Molassebeckens* (pp. 13–16).
- Thuro, K., Zosseder, K., Bohnsack, D., Heine, F., Konrad, F., Mraz, E., & Stockinger, G. (2019). *Abschlussbericht zu den Arbeitspaketen der Technischen Universität München zum Verbundprojekt: Dolomitkluft - Erschließung, Test und Analyse des ersten kluftdominierten Dolomitaquifers im tiefen Malm des Molassebeckens zur Erhöhung der*

- Erfolgsaussichten* : München. <https://doi.org/https://doi.org/10.2314/KXP:1687930376>
- TUM. (2019). Geothermal-Alliance Bavaria. Retrieved April 23, 2019, from <https://www.mse.tum.de/gab/>
- Udluft, P. (1975). Das tiefere Grundwasser zwischen Vindelicischem Rücken und Alpenrand. *Geologisches Jahrbuch*, C(11), 82. Retrieved from [http://www.schweizerbart.de/publications/detail/isbn/9783510962457/Geologisches%5C\\_Jahrbuch%5C\\_Reihe%5C\\_C%5C\\_Heft](http://www.schweizerbart.de/publications/detail/isbn/9783510962457/Geologisches%5C_Jahrbuch%5C_Reihe%5C_C%5C_Heft)
- Uematsu, H., Iino, A., Iizuka, R., Corporation, I., & Hashemi, M. Al. (2012). Uncertainty Identification Using Pressure Transient Analysis for a Complex Carbonate Reservoir. *Society of Petroleum Engineers*.
- Usher, W. (2016). *The Value of Learning about Critical Energy System Uncertainties, An exploration of dynamic uncertainty in the energy system*.
- von Hartmann, H., Tanner, D. C., & Schumacher, S. (2016). Initiation and development of normal faults within the German alpine foreland basin: The inconspicuous role of basement structures. *Tectonics*, 35(6), 1560–1574. <https://doi.org/10.1002/2016TC004176>
- Wagner, W., Cooper, J. R., Dittmann, A., Kijima, J., Kretschmar, H. J., Kruse, A., ... Willkommen, T. (2000). The IAPWS industrial formulation 1997 for the thermodynamic properties of water and steam. *Journal of Engineering for Gas Turbines and Power*, 122(1), 150–180. <https://doi.org/10.1115/1.483186>
- Wainwright, H. M., Finsterle, S., Jung, Y., Zhou, Q., & Birkholzer, J. T. (2014). Computers & Geosciences Making sense of global sensitivity analyses. *Computers and Geosciences*, 65, 84–94. <https://doi.org/10.1016/j.cageo.2013.06.006>
- Wei, M., Duan, Y., Zhou, X., & Fang, Q. (2016). Pressure Transient Analysis for Finite Conductivity Multi-staged Fractured Horizontal Well in Fractured-Vuggy Carbonate Reservoirs. *International Journal of Oil, Gas and Coal Engineering*, 4(1), 1. <https://doi.org/10.11648/j.ogce.s.2016040101.11>
- Wenderoth, F., Fritzer, T., Gropius, M., Huber, B., & Schubert, A. (2005). Numerische 3D-modellierung eines geohydrothermalen dublettenbetriebs im malmkarst. *Geothermische Energie*, 48, 12.
- Wibberley, C. A. J., Kurz, W., Imber, J., Holdsworth, R. E., & Collettini, C. (2008). *The Internal Structure of Fault Zones: Implications for Mechanical and Fluid-Flow Properties*. *Special Publications*, (Vol. 299). London: Geological Society.
- Winter, T., & Einsiedl, F. (2021). Using hydrochemical and environmental isotope data to

characterize the thermal reservoir of the Upper Jurassic aquifer in the South German Molasse Basin on the Pleistocene timescale. In *Goldschmidt virtual 2021*. Retrieved from <https://2021.goldschmidt.info/goldschmidt/2021/meetingapp.cgi/Paper/5010>

- Wolfgramm, M., Bartels, J., Hoffmann, F., Kittl, G., Lenz, G., Seibt, P., ... Unger, H. J. (2007). Unterhaching geothermal well doublet: structural and hydrodynamic reservoir characteristic; Bavaria (Germany). *European Geothermal Congress*, 47(May 2014).
- Zarrouk, S. J., & McLean, K. (2019). *Geothermal Well Test Analysis. Geothermal Well Test Analysis* (1st ed.). London: Academic Press. <https://doi.org/10.1016/c2017-0-02723-4>

## 9 Appendix

### 9.1 Regression Predictors $x_i$ , Dependent Variable $y$

$$x_0 = S_{S,\text{fault}} \times 5 \times 10^8$$

$$x_1 = \log(K_{\text{fault}})$$

$$x_2 = S_{S,\text{matrix}} \times 5 \times 10^8$$

$$x_3 = h_{\text{fault}}$$

$$y = \log(K_{\text{matrix}})$$

$S_s$  = specific storage coefficient [1/Pa]

$K$  = permeability [ $\text{m}^2$ ]

$h$  = thickness [m]

### 9.2 Regression Scaling

transition		$x_0$	$x_1$	$x_2$	$x_3$
radial to bilinear	mean	<b>0.04051</b>	<b>-11.49910</b>	<b>0.04049</b>	<b>102.88885</b>
	standard deviation	<b>0.02698</b>	<b>1.58071</b>	<b>0.02698</b>	<b>100.21314</b>
bilinear to linear	mean	<b>0.03954</b>	<b>-11.19080</b>	<b>0.03990</b>	<b>102.99182</b>
	standard deviation	<b>0.02692</b>	<b>1.41923</b>	<b>0.02714</b>	<b>99.20036</b>
linear to neg. boundary	mean	<b>0.04239</b>	<b>-11.20684</b>	<b>0.03899</b>	<b>113.19850</b>
	standard deviation	<b>0.02658</b>	<b>1.48145</b>	<b>0.02721</b>	<b>102.18529</b>

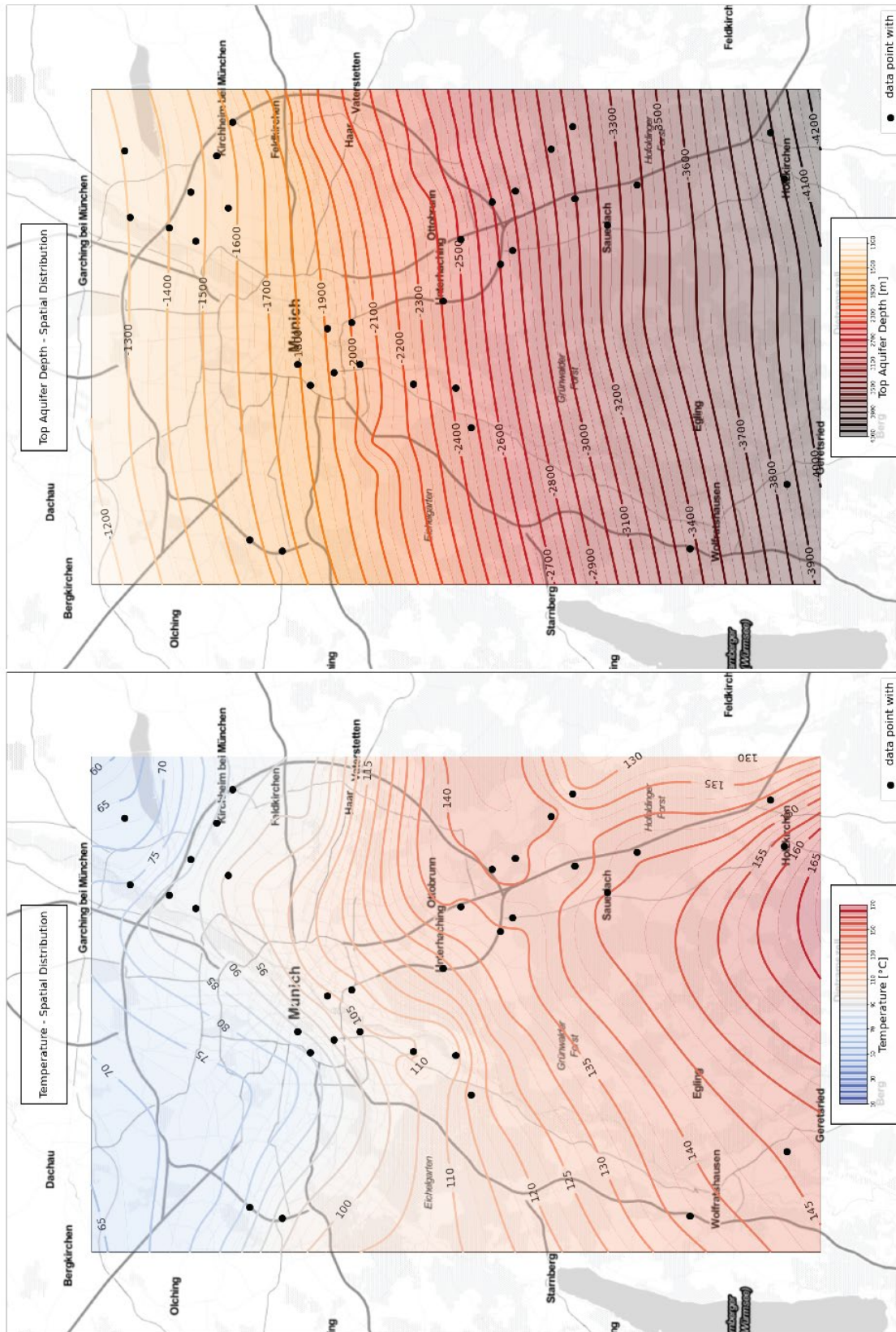
# 1 9.3 Regression Functions

indeterminates of each term	1	$X_0$	$X_1$	$X_2$	$X_3$	$X_0^2$	$X_0*X_1$	$X_0*X_2$	$X_0*X_3$	$X_1^2$	$X_1*X_2$	$X_1*X_3$	$X_2^2$	$X_2*X_3$	$X_3^2$	$X_0^3$	$X_0^2*X_1$	$X_0^2*X_2$	
coefficient of surface 1	-2.01 *10 <sup>-15</sup>	3.14 *10 <sup>-2</sup>	-3.57 *10 <sup>-2</sup>	-2.29 *10 <sup>-2</sup>	9.63 *10 <sup>-2</sup>	3.89 *10 <sup>-2</sup>	-1.16 *10 <sup>-3</sup>	-8.34 *10 <sup>-3</sup>	3.07 *10 <sup>-2</sup>	-1.17 *10 <sup>-1</sup>	-9.83 *10 <sup>-2</sup>	1.39 *10 <sup>-1</sup>	4.15 *10 <sup>-2</sup>	-1.39 *10 <sup>-1</sup>	4.18 *10 <sup>-1</sup>	-1.92 *10 <sup>-2</sup>	-2.27 *10 <sup>-3</sup>	-4.83 *10 <sup>-2</sup>	
coefficient of surface 2	-3.95 *10 <sup>-15</sup>	6.91 *10 <sup>-2</sup>	1.21 *10 <sup>-2</sup>	-1.13 *10 <sup>-1</sup>	4.13 *10 <sup>-1</sup>	-4.00 *10 <sup>-2</sup>	-6.89 *10 <sup>-3</sup>	2.12 *10 <sup>-2</sup>	-8.16 *10 <sup>-2</sup>	-1.20 *10 <sup>-1</sup>	6.59 *10 <sup>-3</sup>	3.22 *10 <sup>-2</sup>	-6.13 *10 <sup>-3</sup>	-3.97 *10 <sup>-2</sup>	4.83 *10 <sup>-1</sup>	2.40 *10 <sup>-2</sup>	-6.70 *10 <sup>-3</sup>	-3.50 *10 <sup>-2</sup>	
coefficient of surface 3	4.84 *10 <sup>-16</sup>	2.15 *10 <sup>-1</sup>	1.45 *10 <sup>-1</sup>	-2.81 *10 <sup>-1</sup>	1.20 *10 <sup>-1</sup>	-5.02 *10 <sup>-2</sup>	-2.40 *10 <sup>-2</sup>	4.57 *10 <sup>-2</sup>	-5.98 *10 <sup>-2</sup>	-1.93 *10 <sup>-1</sup>	3.24 *10 <sup>-2</sup>	-9.00 *10 <sup>-2</sup>	-1.58 *10 <sup>-2</sup>	3.10 *10 <sup>-2</sup>	-1.14 *10 <sup>-1</sup>	-2.21 *10 <sup>-2</sup>	-2.04 *10 <sup>-2</sup>	-2.20 *10 <sup>-2</sup>	
	$X_0^2*X_3$	$X_0*X_1^2$	$X_0*X_1*X_2$	$X_0*X_1*X_3$	$X_0*X_2^2$	$X_0*X_2*X_3$	$X_0*X_3^2$	$X_1^3$	$X_1^2*X_2$	$X_1^2*X_3$	$X_1*X_2^2$	$X_1*X_2*X_3$	$X_1*X_3^2$	$X_2^3$	$X_2^2*X_3$	$X_2*X_3^2$	$X_3^3$	$X_0^4$	
	-1.51 *10 <sup>-4</sup>	3.65 *10 <sup>-2</sup>	-3.69 *10 <sup>-2</sup>	1.77 *10 <sup>-2</sup>	-2.63 *10 <sup>-2</sup>	-2.60 *10 <sup>-2</sup>	3.57 *10 <sup>-3</sup>	2.00 *10 <sup>-1</sup>	-8.58 *10 <sup>-3</sup>	1.95 *10 <sup>-1</sup>	5.31 *10 <sup>-2</sup>	-3.84 *10 <sup>-2</sup>	1.50 *10 <sup>-1</sup>	-9.66 *10 <sup>-3</sup>	3.43 *10 <sup>-2</sup>	3.19 *10 <sup>-2</sup>	-2.19 *10 <sup>-1</sup>	-8.30 *10 <sup>-3</sup>	
	2.23 *10 <sup>-2</sup>	3.80 *10 <sup>-2</sup>	-2.81 *10 <sup>-2</sup>	2.55 *10 <sup>-2</sup>	4.39 *10 <sup>-3</sup>	-9.66 *10 <sup>-2</sup>	5.50 *10 <sup>-2</sup>	1.66 *10 <sup>-1</sup>	-1.06 *10 <sup>-2</sup>	1.27 *10 <sup>-1</sup>	1.98 *10 <sup>-3</sup>	-4.50 *10 <sup>-2</sup>	1.59 *10 <sup>-1</sup>	3.51 *10 <sup>-2</sup>	2.38 *10 <sup>-2</sup>	-3.86 *10 <sup>-2</sup>	-5.23 *10 <sup>-1</sup>	-2.85 *10 <sup>-2</sup>	
	-0.94 *10 <sup>-2</sup>	7.03 *10 <sup>-2</sup>	5.89 *10 <sup>-3</sup>	-3.29 *10 <sup>-2</sup>	-7.99 *10 <sup>-2</sup>	3.25 *10 <sup>-2</sup>	4.33 *10 <sup>-2</sup>	7.54 *10 <sup>-2</sup>	0.56 *10 <sup>-1</sup>	1.63 *10 <sup>-1</sup>	-4.35 *10 <sup>-2</sup>	4.26 *10 <sup>-2</sup>	8.15 *10 <sup>-2</sup>	3.37 *10 <sup>-2</sup>	-7.35 *10 <sup>-2</sup>	2.68 *10 <sup>-2</sup>	3.57 *10 <sup>-1</sup>	-1.84 *10 <sup>-2</sup>	
	$X_0^3*X_1$	$X_0^3*X_2$	$X_0^3*X_3$	$X_0^2*X_1^2$	$X_0^2*X_1*X_2$	$X_0^2*X_1*X_3$	$X_0^2*X_2^2$	$X_0^2*X_2*X_3$	$X_0^2*X_3^2$	$X_0*X_1^3$	$X_0*X_1^2*X_2$	$X_0*X_1^2*X_3$	$X_0*X_1*X_2^2$	$X_0*X_1*X_2*X_3$	$X_0*X_1*X_3^2$	$X_0*X_2^3$	$X_0*X_2^2*X_3$	$X_0*X_2*X_3^2$	$X_0*X_3^3$
	9.98 *10 <sup>-4</sup>	-1.42 *10 <sup>-2</sup>	3.52 *10 <sup>-3</sup>	-1.02 *10 <sup>-2</sup>	5.21 *10 <sup>-3</sup>	5.88 *10 <sup>-3</sup>	-2.98 *10 <sup>-2</sup>	3.60 *10 <sup>-3</sup>	0.24 *10 <sup>-2</sup>	-3.59 *10 <sup>-3</sup>	2.89 *10 <sup>-3</sup>	1.12 *10 <sup>-2</sup>	-1.12 *10 <sup>-2</sup>	-2.30 *10 <sup>-2</sup>	7.44 *10 <sup>-3</sup>	-9.02 *10 <sup>-3</sup>	-1.10 *10 <sup>-2</sup>	1.35 *10 <sup>-2</sup>	
	7.86 *10 <sup>-3</sup>	-3.32 *10 <sup>-2</sup>	4.97 *10 <sup>-2</sup>	-5.94 *10 <sup>-3</sup>	-4.54 *10 <sup>-3</sup>	-5.90 *10 <sup>-4</sup>	-3.08 *10 <sup>-3</sup>	-3.37 *10 <sup>-2</sup>	3.78 *10 <sup>-2</sup>	-7.26 *10 <sup>-3</sup>	-4.19 *10 <sup>-3</sup>	9.48 *10 <sup>-3</sup>	-5.32 *10 <sup>-3</sup>	-3.76 *10 <sup>-2</sup>	3.86 *10 <sup>-2</sup>	1.22 *10 <sup>-2</sup>	8.96 *10 <sup>-4</sup>	-2.46 *10 <sup>-2</sup>	
	1.08 *10 <sup>-2</sup>	-3.80 *10 <sup>-2</sup>	2.47 *10 <sup>-2</sup>	-2.47 *10 <sup>-3</sup>	1.67 *10 <sup>-3</sup>	1.79 *10 <sup>-2</sup>	-4.57 *10 <sup>-3</sup>	-1.88 *10 <sup>-2</sup>	7.72 *10 <sup>-3</sup>	-6.52 *10 <sup>-3</sup>	-9.84 *10 <sup>-3</sup>	3.25 *10 <sup>-2</sup>	-9.16 *10 <sup>-3</sup>	4.80 *10 <sup>-3</sup>	3.17 *10 <sup>-2</sup>	1.87 *10 <sup>-2</sup>	-4.06 *10 <sup>-2</sup>	-2.07 *10 <sup>-2</sup>	
	$X_0^3*X_3$	$X_1^4$	$X_1^3*X_2$	$X_1^3*X_3$	$X_1^2*X_2^2$	$X_1^2*X_2*X_3$	$X_1^2*X_3^2$	$X_1*X_2^3$	$X_1*X_2^2*X_3$	$X_1*X_2*X_3^2$	$X_1*X_3^3$	$X_2^4$	$X_2^3*X_3$	$X_2^2*X_3^2$	$X_2*X_3^3$	$X_3^4$	$X_0^5$	$X_0^4*X_1$	
	-1.98 *10 <sup>-2</sup>	-2.40 *10 <sup>-2</sup>	3.56 *10 <sup>-2</sup>	-2.85 *10 <sup>-2</sup>	8.93 *10 <sup>-3</sup>	3.99 *10 <sup>-2</sup>	-2.24 *10 <sup>-1</sup>	1.74 *10 <sup>-2</sup>	1.88 *10 <sup>-3</sup>	5.36 *10 <sup>-2</sup>	-4.45 *10 <sup>-1</sup>	3.39 *10 <sup>-2</sup>	2.98 *10 <sup>-2</sup>	-2.06 *10 <sup>-2</sup>	5.15 *10 <sup>-2</sup>	-5.48 *10 <sup>-1</sup>	2.53 *10 <sup>-3</sup>	1.79 *10 <sup>-3</sup>	
	3.01 *10 <sup>-2</sup>	-1.74 *10 <sup>-2</sup>	1.86 *10 <sup>-2</sup>	-9.72 *10 <sup>-3</sup>	1.70 *10 <sup>-2</sup>	2.76 *10 <sup>-3</sup>	-1.26 *10 <sup>-1</sup>	-7.30 *10 <sup>-3</sup>	8.53 *10 <sup>-3</sup>	4.01 *10 <sup>-3</sup>	-3.17 *10 <sup>-1</sup>	5.32 *10 <sup>-2</sup>	2.54 *10 <sup>-2</sup>	8.17 *10 <sup>-3</sup>	5.67 *10 <sup>-2</sup>	-8.23 *10 <sup>-1</sup>	1.51 *10 <sup>-2</sup>	-3.20 *10 <sup>-3</sup>	
	4.82 *10 <sup>-2</sup>	2.28 *10 <sup>-2</sup>	-6.81 *10 <sup>-3</sup>	1.64 *10 <sup>-2</sup>	-8.23 *10 <sup>-3</sup>	-4.39 *10 <sup>-3</sup>	8.96 *10 <sup>-3</sup>	-6.79 *10 <sup>-3</sup>	-1.67 *10 <sup>-2</sup>	-3.91 *10 <sup>-2</sup>	-7.61 *10 <sup>-2</sup>	8.89 *10 <sup>-2</sup>	3.53 *10 <sup>-2</sup>	4.22 *10 <sup>-2</sup>	-1.77 *10 <sup>-2</sup>	-2.72 *10 <sup>-1</sup>	2.24 *10 <sup>-2</sup>	-5.14 *10 <sup>-3</sup>	
	$X_0^4*X_2$	$X_0^4*X_3$	$X_0^3*X_1^2$	$X_0^3*X_1*X_2$	$X_0^3*X_1*X_3$	$X_0^3*X_2^2$	$X_0^3*X_2*X_3$	$X_0^3*X_3^2$	$X_0^2*X_1^3$	$X_0^2*X_1^2*X_2$	$X_0^2*X_1^2*X_3$	$X_0^2*X_1*X_2^2$	$X_0^2*X_1*X_2*X_3$	$X_0^2*X_1*X_3^2$	$X_0^2*X_2^3$	$X_0^2*X_2^2*X_3$	$X_0^2*X_2*X_3^2$	$X_0^2*X_3^3$	
	1.04 *10 <sup>-2</sup>	7.92 *10 <sup>-4</sup>	4.86 *10 <sup>-3</sup>	-6.24 *10 <sup>-3</sup>	-4.21 *10 <sup>-3</sup>	2.07 *10 <sup>-2</sup>	-1.31 *10 <sup>-3</sup>	-2.32 *10 <sup>-3</sup>	7.11 *10 <sup>-3</sup>	8.25 *10 <sup>-4</sup>	-2.79 *10 <sup>-3</sup>	-7.97 *10 <sup>-3</sup>	1.63 *10 <sup>-3</sup>	-2.25 *10 <sup>-4</sup>	2.66 *10 <sup>-2</sup>	-2.30 *10 <sup>-3</sup>	2.53 *10 <sup>-3</sup>	-1.26 *10 <sup>-3</sup>	
	2.16 *10 <sup>-2</sup>	-1.90 *10 <sup>-2</sup>	1.82 *10 <sup>-3</sup>	7.73 *10 <sup>-4</sup>	2.62 *10 <sup>-3</sup>	5.57 *10 <sup>-3</sup>	2.32 *10 <sup>-2</sup>	-2.44 *10 <sup>-2</sup>	3.83 *10 <sup>-3</sup>	-1.50 *10 <sup>-3</sup>	4.34 *10 <sup>-3</sup>	-2.81 *10 <sup>-3</sup>	2.15 *10 <sup>-3</sup>	5.18 *10 <sup>-4</sup>	4.79 *10 <sup>-4</sup>	-4.29 *10 <sup>-3</sup>	2.05 *10 <sup>-2</sup>	-1.68 *10 <sup>-2</sup>	
	3.36 *10 <sup>-2</sup>	-1.31 *10 <sup>-2</sup>	-1.05 *10 <sup>-2</sup>	-4.77 *10 <sup>-3</sup>	7.02 *10 <sup>-3</sup>	2.61 *10 <sup>-2</sup>	1.01 *10 <sup>-2</sup>	-7.13 *10 <sup>-3</sup>	8.56 *10 <sup>-3</sup>	-9.10 *10 <sup>-3</sup>	-1.07 *10 <sup>-2</sup>	1.40 *10 <sup>-2</sup>	-1.00 *10 <sup>-2</sup>	-6.16 *10 <sup>-3</sup>	-6.51 *10 <sup>-3</sup>	3.81 *10 <sup>-2</sup>	1.07 *10 <sup>-2</sup>	-2.84 *10 <sup>-3</sup>	
	$X_0^4*X_1$	$X_0^3*X_1^3$	$X_0^3*X_1^2*X_2$	$X_0^3*X_1^2*X_3$	$X_0^3*X_1*X_2^2$	$X_0^3*X_1*X_2*X_3$	$X_0^3*X_1*X_3^2$	$X_0^3*X_2^3$	$X_0^3*X_2^2*X_3$	$X_0^3*X_2*X_3^2$	$X_0^3*X_3^3$	$X_0^2*X_1^4$	$X_0^2*X_1^3*X_2$	$X_0^2*X_1^3*X_3$	$X_0^2*X_1^2*X_2^2$	$X_0^2*X_1^2*X_2*X_3$	$X_0^2*X_1^2*X_3^2$	$X_0^2*X_1*X_2^3$	$X_0^2*X_1*X_2^2*X_3$
	-8.23 *10 <sup>-3</sup>	1.47 *10 <sup>-3</sup>	2.74 *10 <sup>-3</sup>	-6.92 *10 <sup>-4</sup>	5.60 *10 <sup>-3</sup>	-8.51 *10 <sup>-3</sup>	1.65 *10 <sup>-2</sup>	-7.76 *10 <sup>-3</sup>	8.92 *10 <sup>-3</sup>	-2.25 *10 <sup>-3</sup>	9.23 *10 <sup>-3</sup>	1.70 *10 <sup>-2</sup>	-4.00 *10 <sup>-3</sup>	-7.91 *10 <sup>-3</sup>	9.93 *10 <sup>-3</sup>	-2.17 *10 <sup>-2</sup>	-5.63 *10 <sup>-3</sup>	-3.25 *10 <sup>-2</sup>	
	-1.07 *10 <sup>-2</sup>	8.15 *10 <sup>-3</sup>	-6.17 *10 <sup>-3</sup>	1.50 *10 <sup>-3</sup>	-2.13 *10 <sup>-3</sup>	-6.06 *10 <sup>-3</sup>	2.70 *10 <sup>-3</sup>	-1.85 *10 <sup>-3</sup>	1.47 *10 <sup>-2</sup>	-1.99 *10 <sup>-2</sup>	-5.05 *10 <sup>-3</sup>	1.87 *10 <sup>-2</sup>	-8.15 *10 <sup>-3</sup>	1.44 *10 <sup>-2</sup>	-1.36 *10 <sup>-2</sup>	-1.67 *10 <sup>-2</sup>	-3.71 *10 <sup>-3</sup>	-1.71 *10 <sup>-2</sup>	
	-1.73 *10 <sup>-2</sup>	7.51 *10 <sup>-3</sup>	3.81 *10 <sup>-3</sup>	1.34 *10 <sup>-2</sup>	-6.21 *10 <sup>-3</sup>	-9.50 *10 <sup>-3</sup>	2.84 *10 <sup>-3</sup>	5.60 *10 <sup>-4</sup>	-5.04 *10 <sup>-3</sup>	-1.72 *10 <sup>-2</sup>	-9.37 *10 <sup>-3</sup>	-2.48 *10 <sup>-3</sup>	2.32 *10 <sup>-2</sup>	5.41 *10 <sup>-3</sup>	-3.18 *10 <sup>-2</sup>	-1.04 *10 <sup>-2</sup>	-1.45 *10 <sup>-2</sup>	-3.10 *10 <sup>-2</sup>	
	$X_1^3*X_2^2$	$X_1^3*X_2*X_3$	$X_1^3*X_3^2$	$X_1^2*X_2^3$	$X_1^2*X_2^2*X_3$	$X_1^2*X_2*X_3^2$	$X_1^2*X_3^3$	$X_1*X_2^4$	$X_1*X_2^3*X_3$	$X_1*X_2^2*X_3^2$	$X_1*X_2*X_3^3$	$X_1*X_3^4$	$X_2^5$	$X_2^4*X_3$	$X_2^3*X_3^2$	$X_2^2*X_3^3$	$X_2*X_3^4$	$X_3^5$	
	-0.13 *10 <sup>-1</sup>	-1.12 *10 <sup>-2</sup>	2.54 *10 <sup>-2</sup>	-3.29 *10 <sup>-3</sup>	-2.08 *10 <sup>-2</sup>	-2.45 *10 <sup>-2</sup>	8.24 *10 <sup>-2</sup>	-7.97 *10 <sup>-3</sup>	1.84 *10 <sup>-2</sup>	-7.88 *10 <sup>-3</sup>	-1.79 *10 <sup>-2</sup>	1.68 *10 <sup>-1</sup>	-2.53 *10 <sup>-2</sup>	-1.14 *10 <sup>-2</sup>	-6.35 *10 <sup>-3</sup>	1.07 *10 <sup>-2</sup>	-2.21 *10 <sup>-2</sup>	2.74 *10 <sup>-1</sup>	
	-1.13 *10 <sup>-2</sup>	3.82 *10 <sup>-3</sup>	-5.94 *10 <sup>-3</sup>	-3.16 *10 <sup>-5</sup>	-7.07 *10 <sup>-4</sup>	-4.17 *10 <sup>-3</sup>	4.26 *10 <sup>-2</sup>	8.32 *10 <sup>-3</sup>	3.71 *10 <sup>-3</sup>	-7.36 *10 <sup>-3</sup>	2.32 *10 <sup>-3</sup>	1.19 *10 <sup>-1</sup>	-4.03 *10 <sup>-2</sup>	-7.08 *10 <sup>-3</sup>	-7.53 *10 <sup>-3</sup>	-5.05 *10 <sup>-3</sup>	-1.88 *10 <sup>-2</sup>	4.61 *10 <sup>-1</sup>	
	1.12 *10 <sup>-3</sup>	-2.15 *10 <sup>-3</sup>	-2.01 *10 <sup>-2</sup>	4.13 *10 <sup>-3</sup>	4.55 *10 <sup>-3</sup>	-3.61 *10 <sup>-3</sup>	-1.57 *10 <sup>-2</sup>	7.45 *10 <sup>-3</sup>	-4.22 *10 <sup>-3</sup>	1.62 *10 <sup>-2</sup>	1.12 *10 <sup>-2</sup>	2.52 *10 <sup>-2</sup>	-4.93 *10 <sup>-2</sup>	-7.10 *10 <sup>-3</sup>	-3.65 *10 <sup>-2</sup>	-1.25 *10 <sup>-2</sup>	1.07 *10 <sup>-2</sup>	5.93 *10 <sup>-2</sup>	
intercept of surface 1	-1.35 *10 <sup>1</sup>																		
intercept of surface 2	-1.45 *10 <sup>1</sup>																		
intercept of surface 3	-1.53 *10 <sup>1</sup>																		

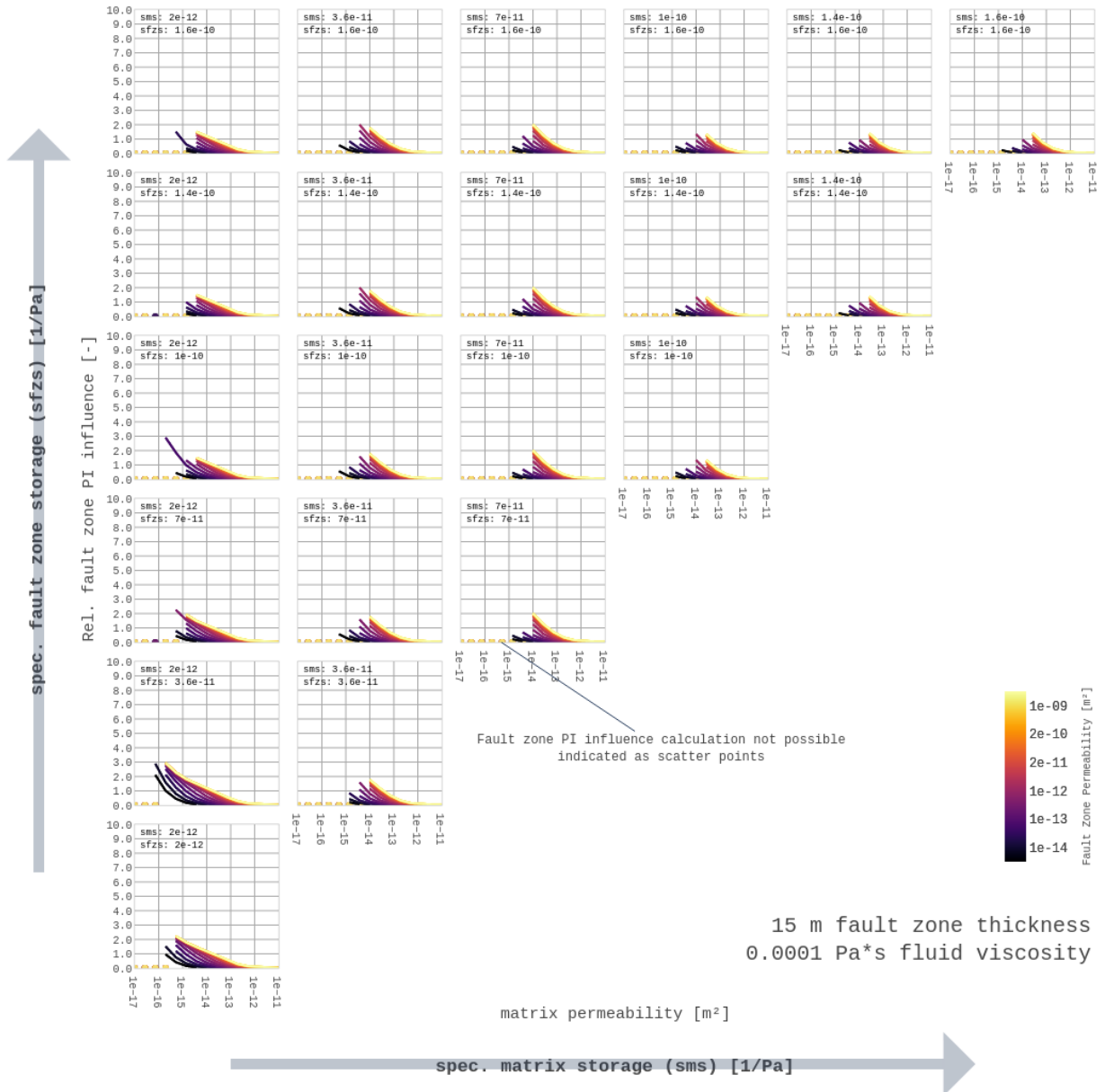
Legend: surface 1 = boundary surface between radial and bilinear flow  
 surface 2 = boundary surface between bilinear and linear flow  
 surface 3 = boundary surface between linear and boundary flow

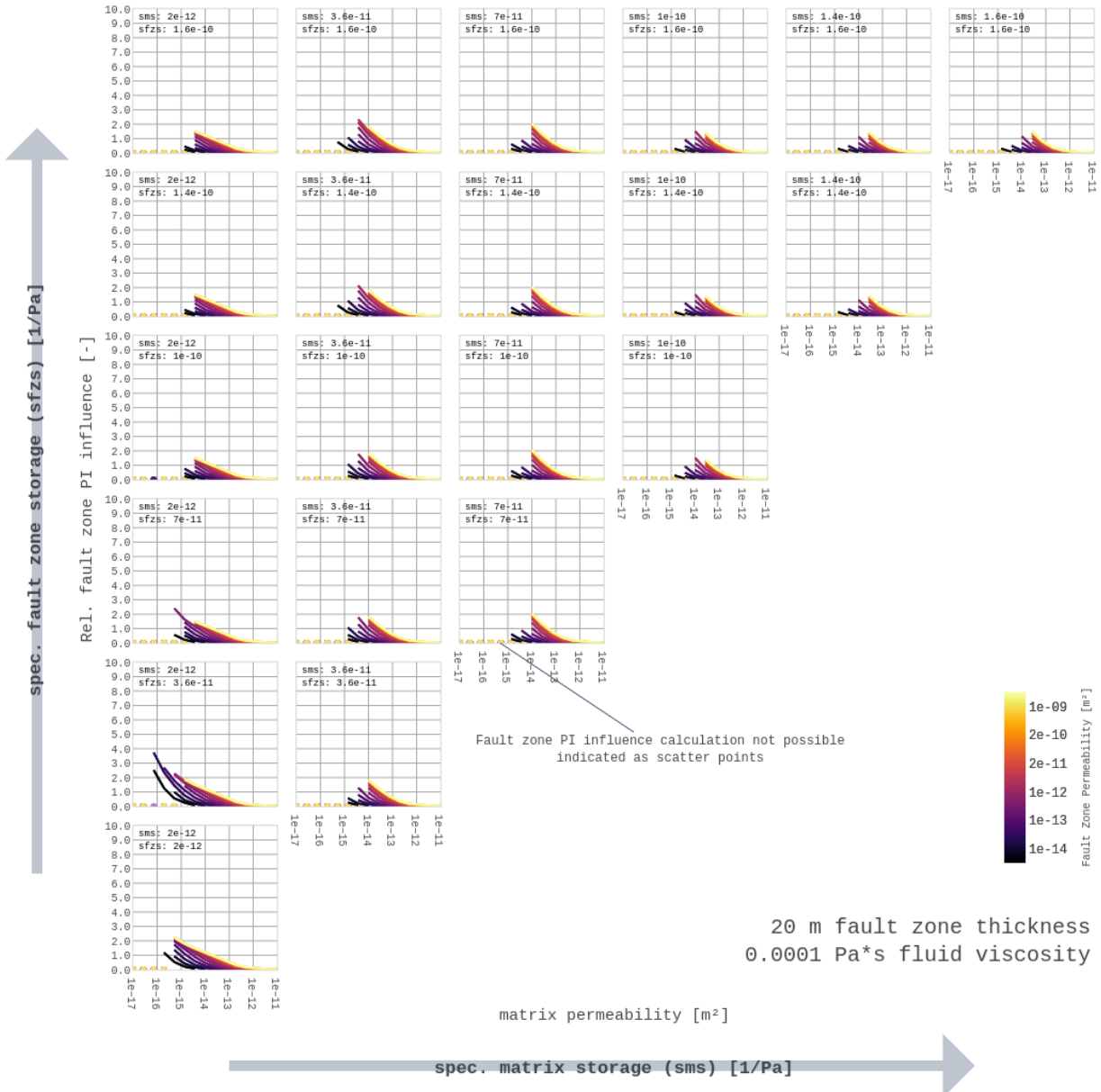
2

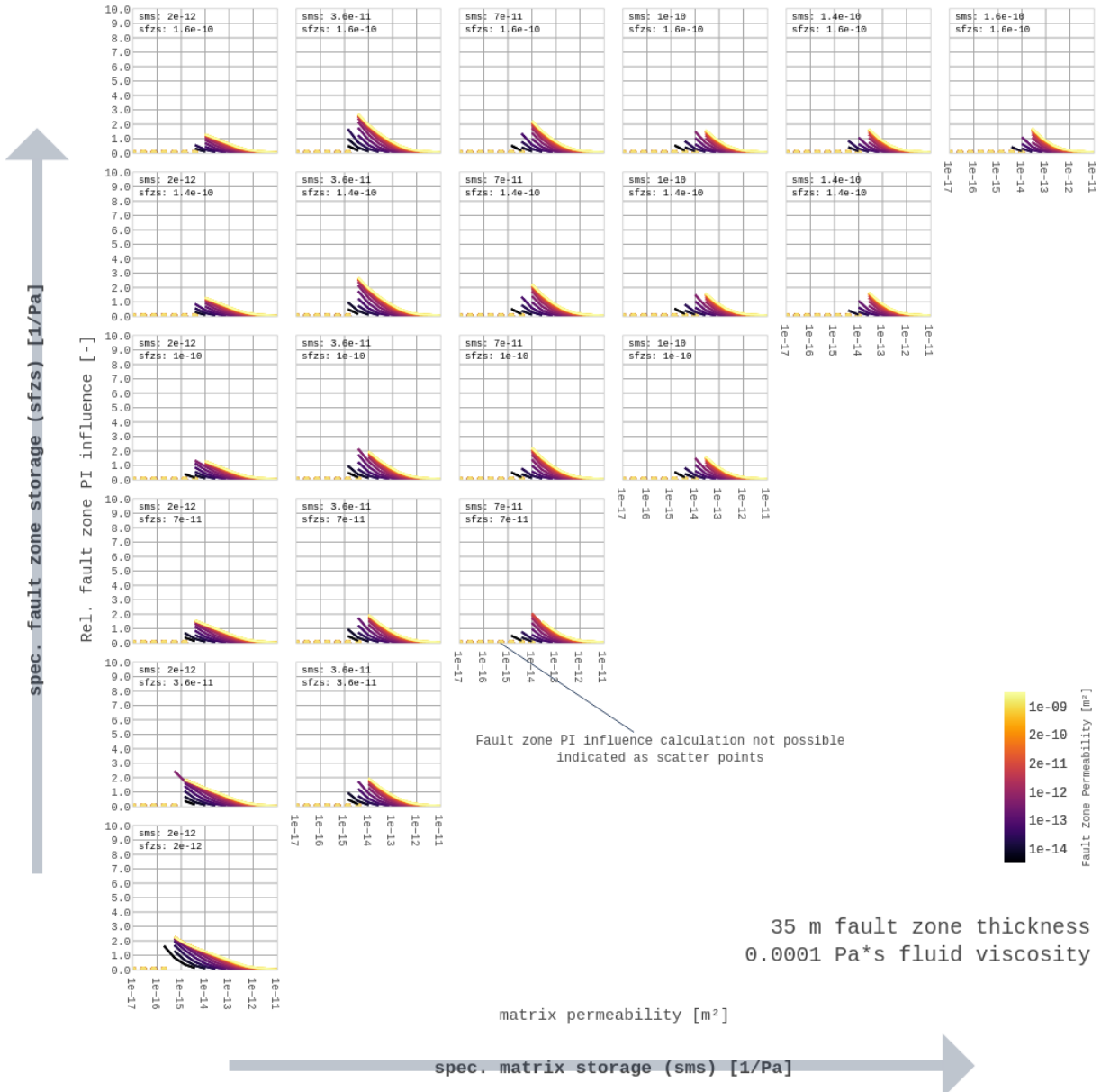
## 9.4 Temperature and depth of aquifer top in the investigation area

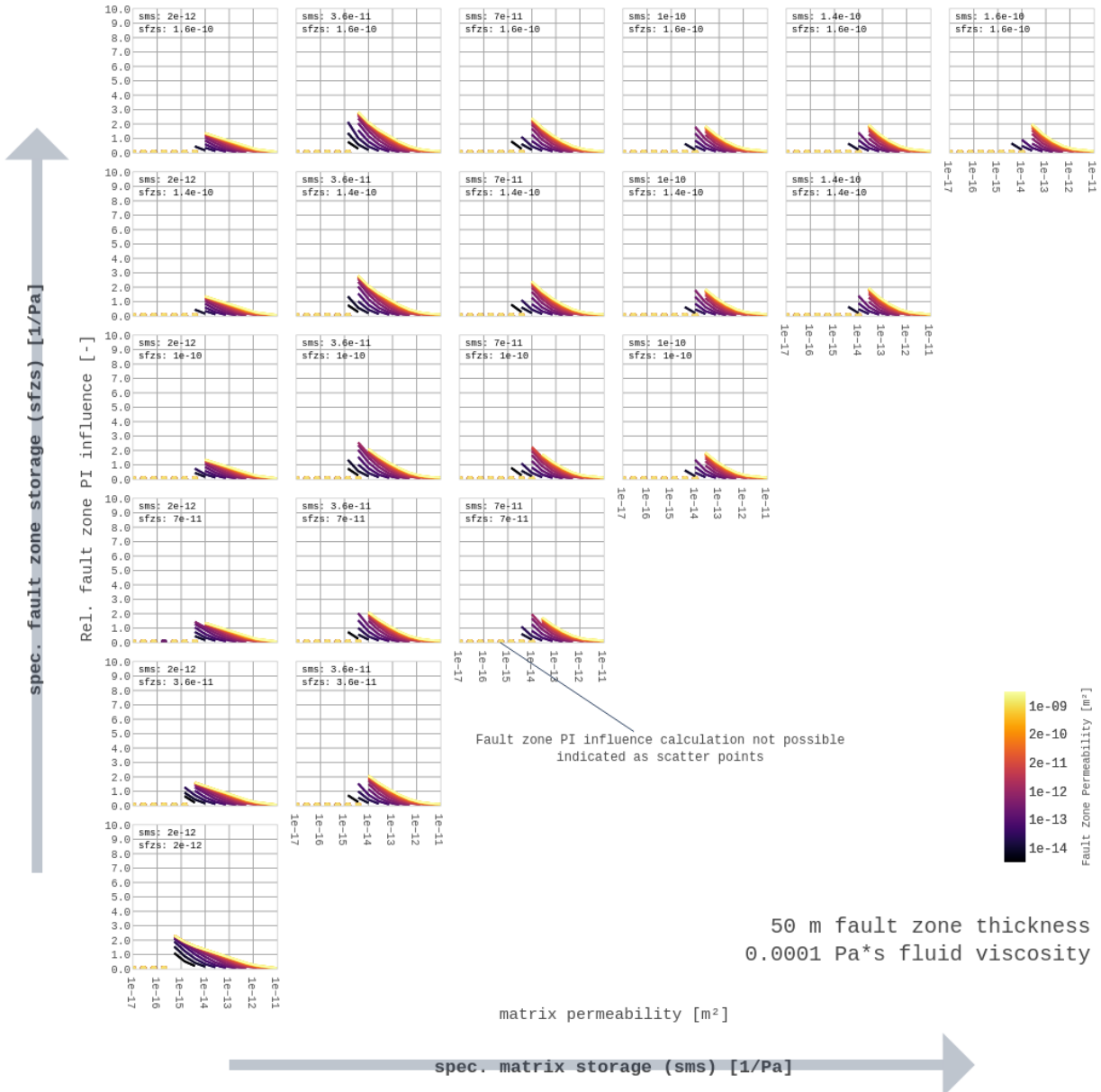


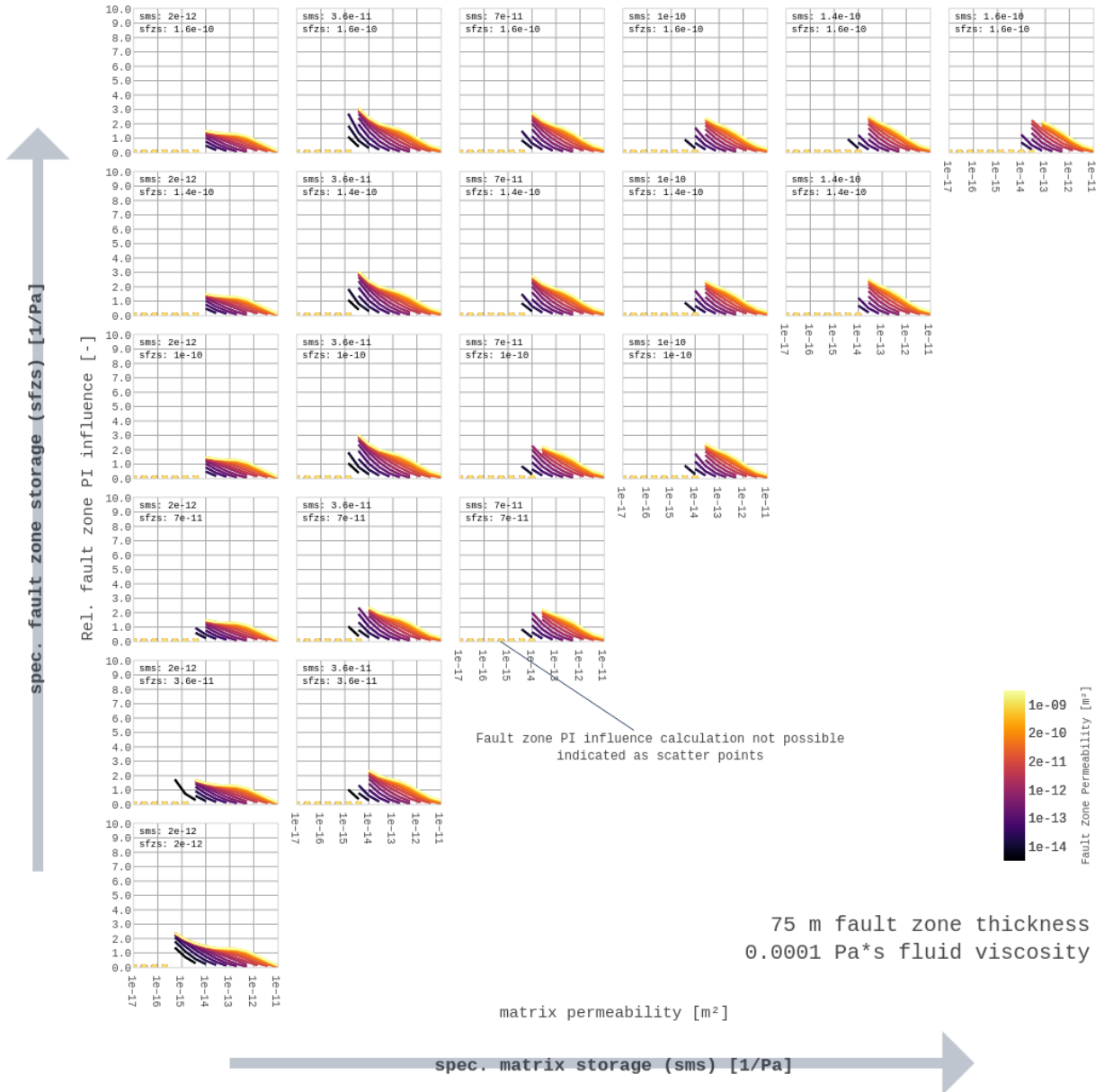
## 9.5 Evolution of rel. Fault zone PI influence – representative parameter space slices

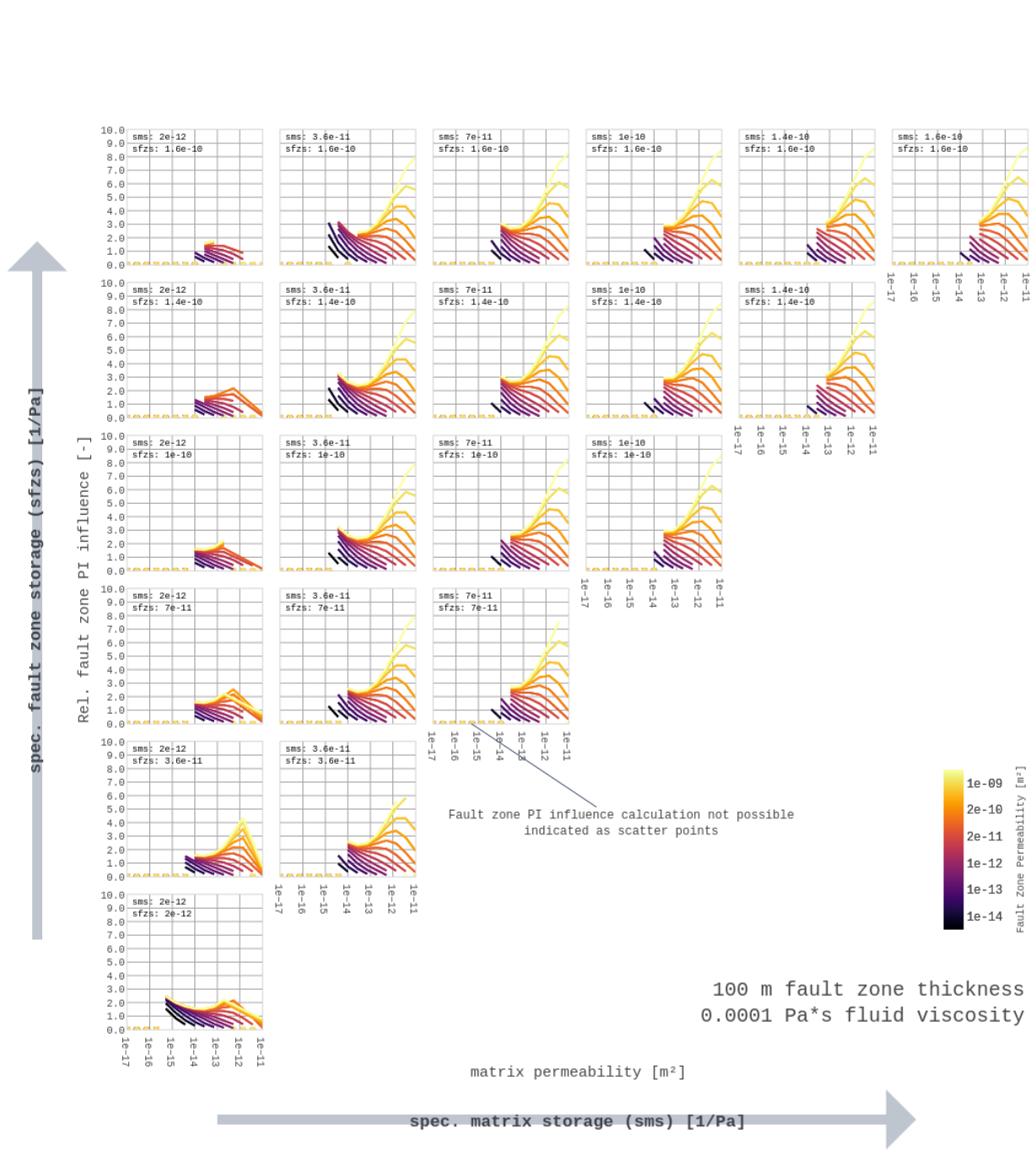


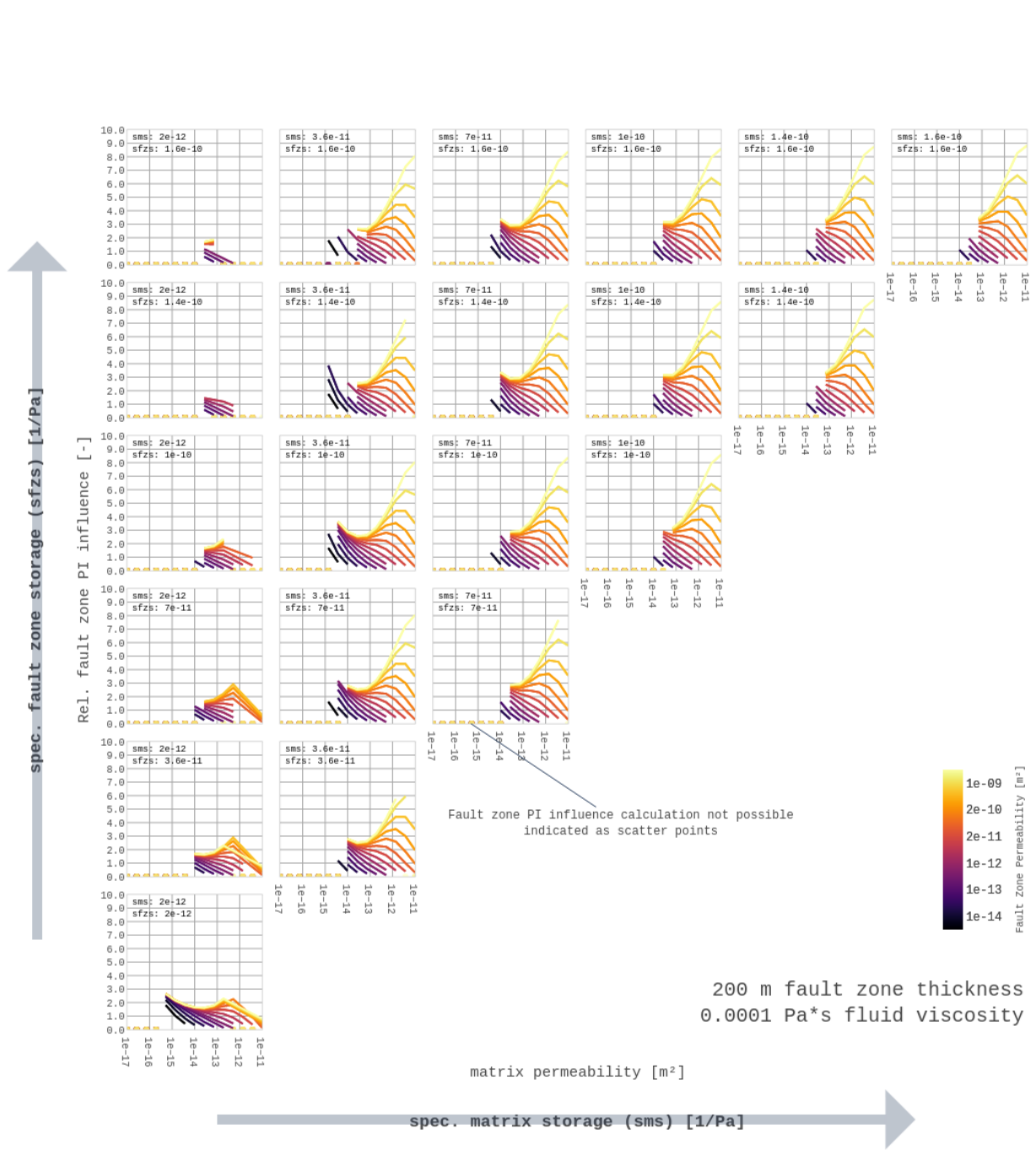


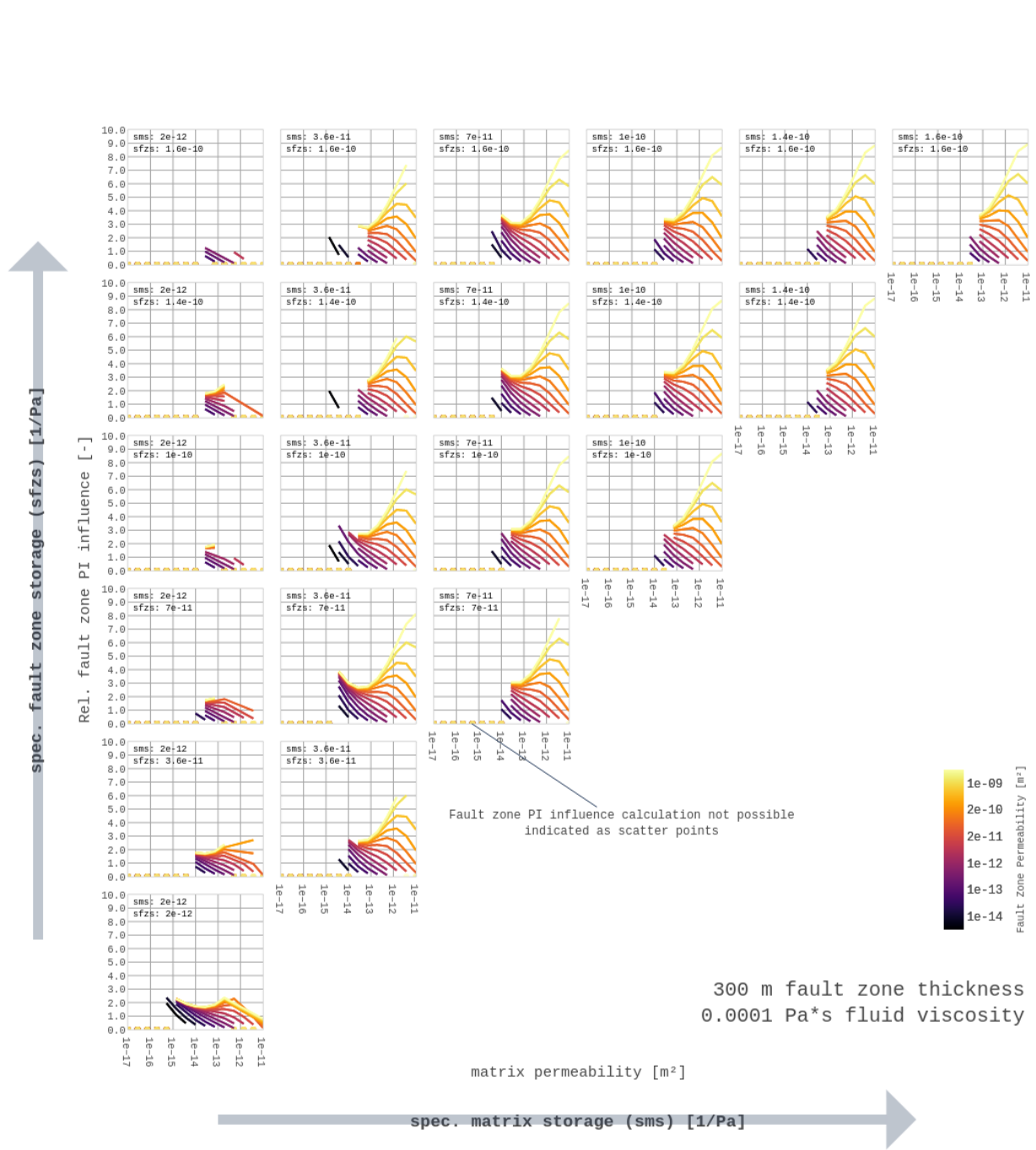


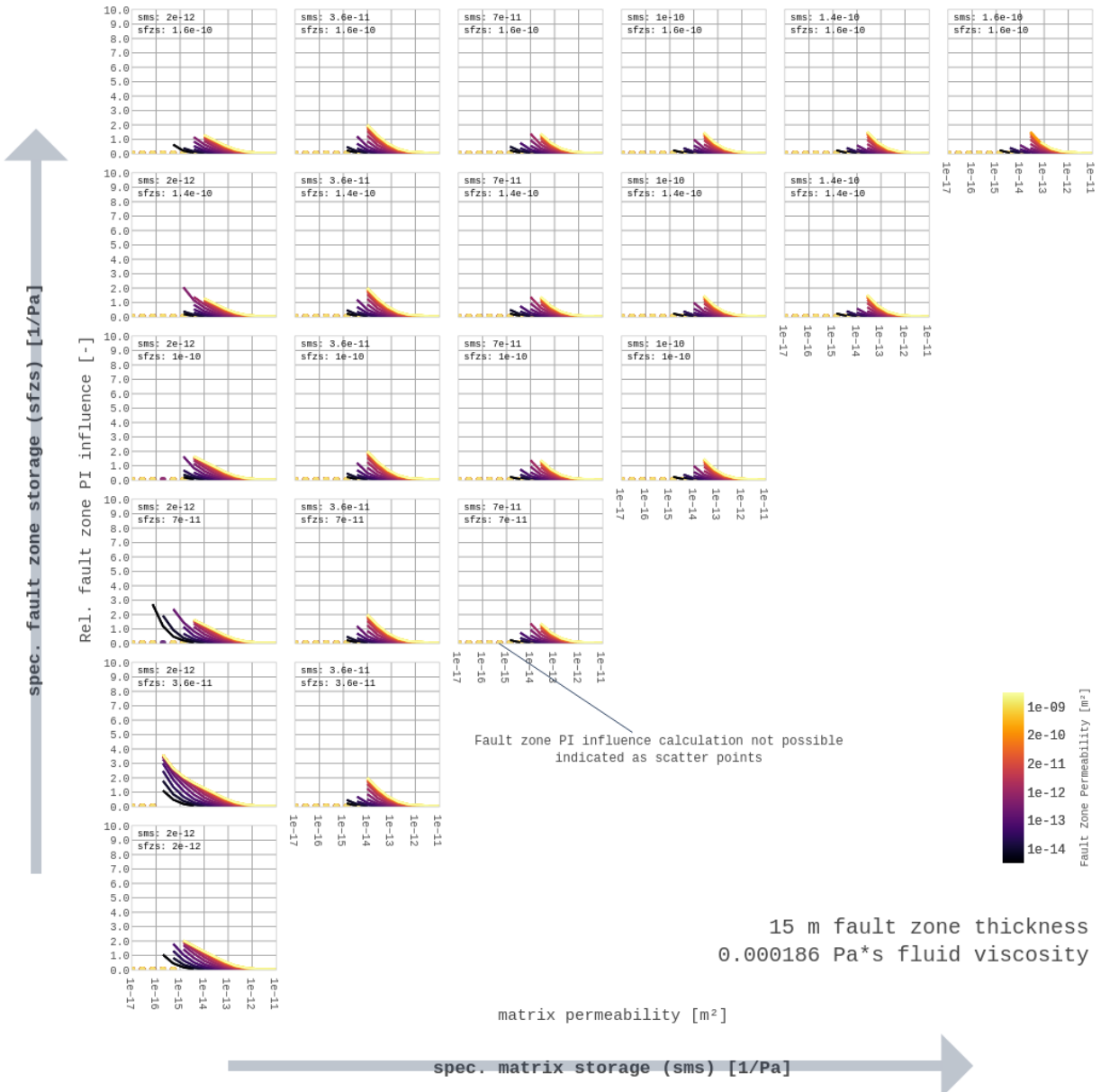


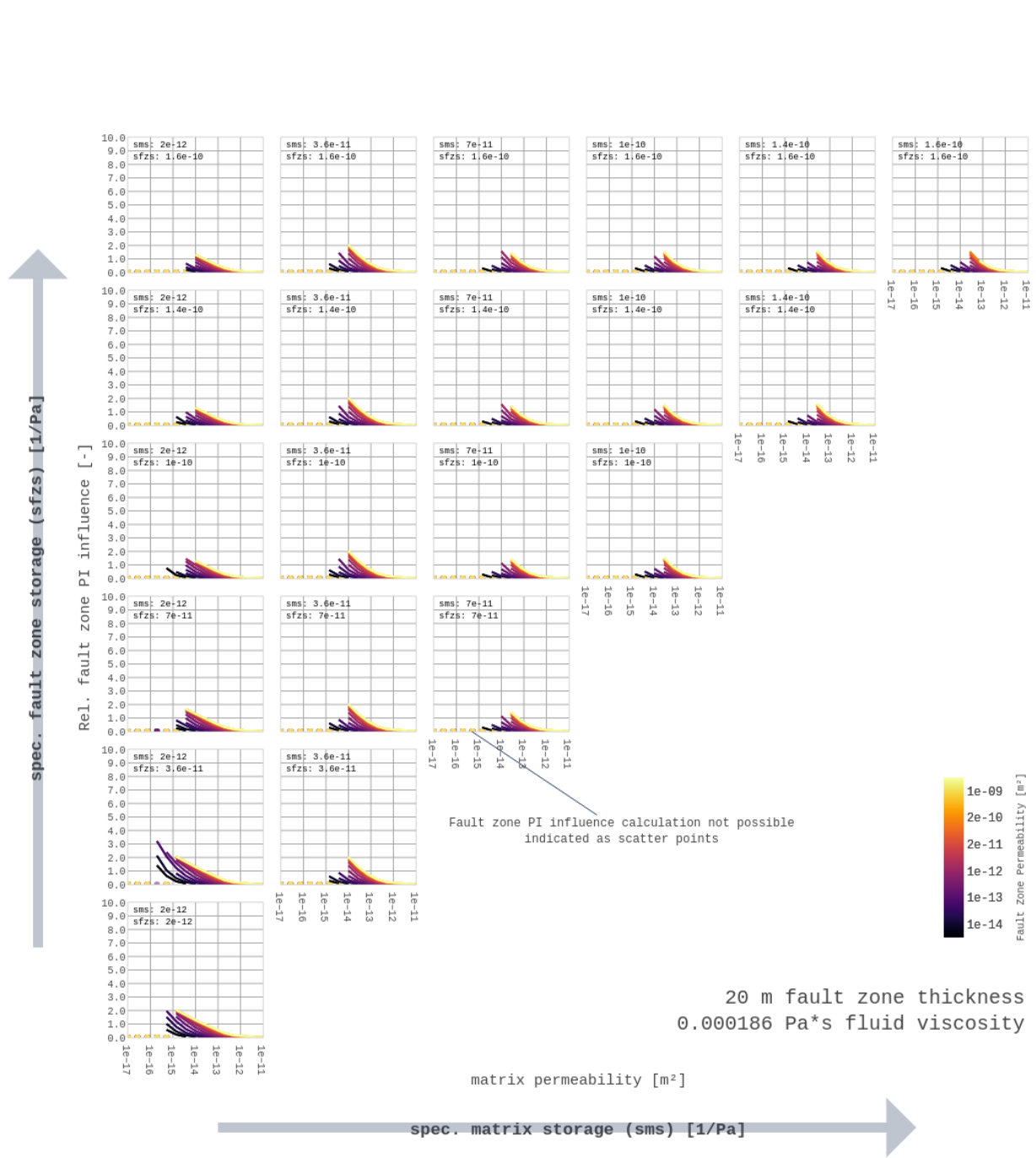


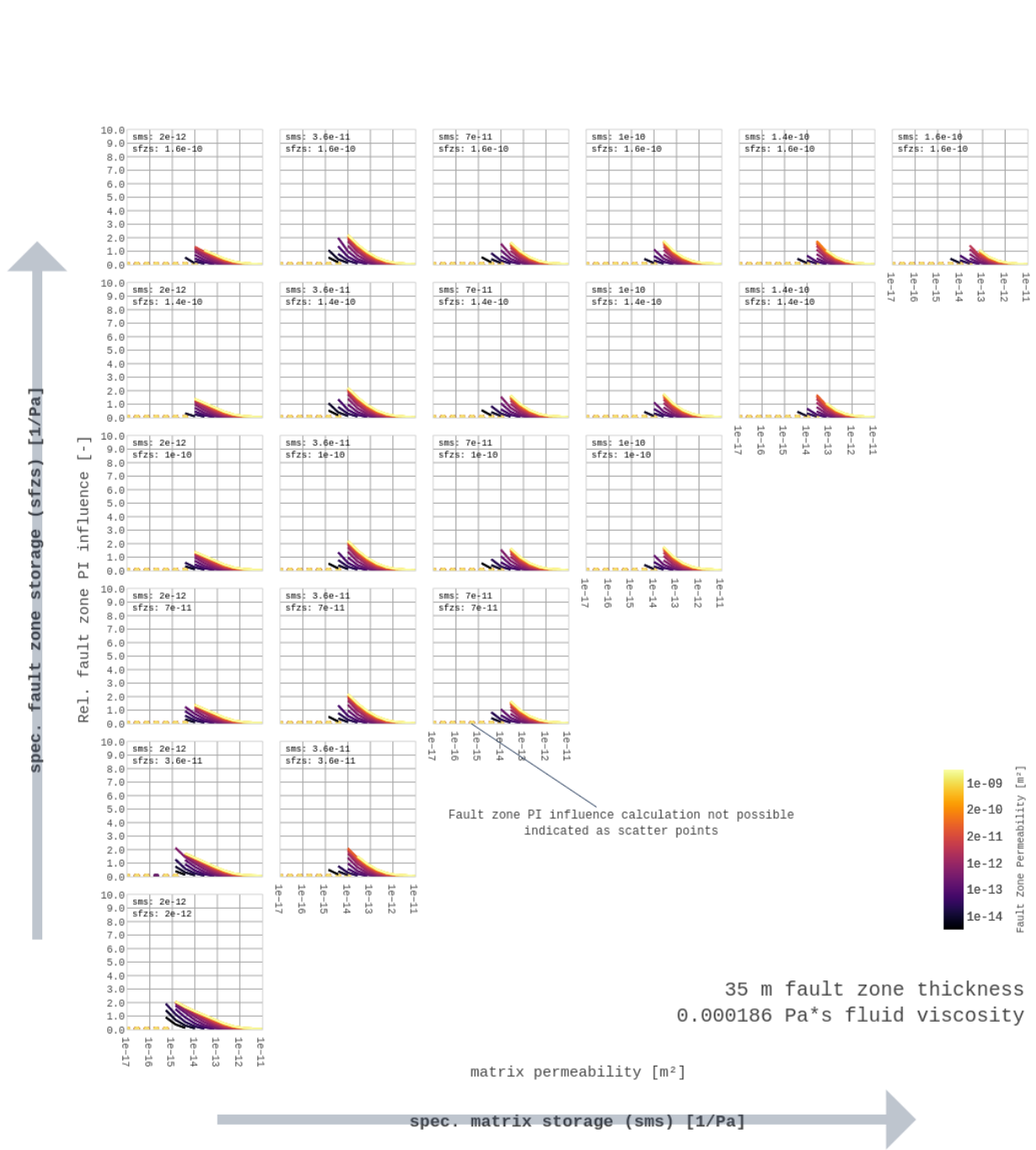


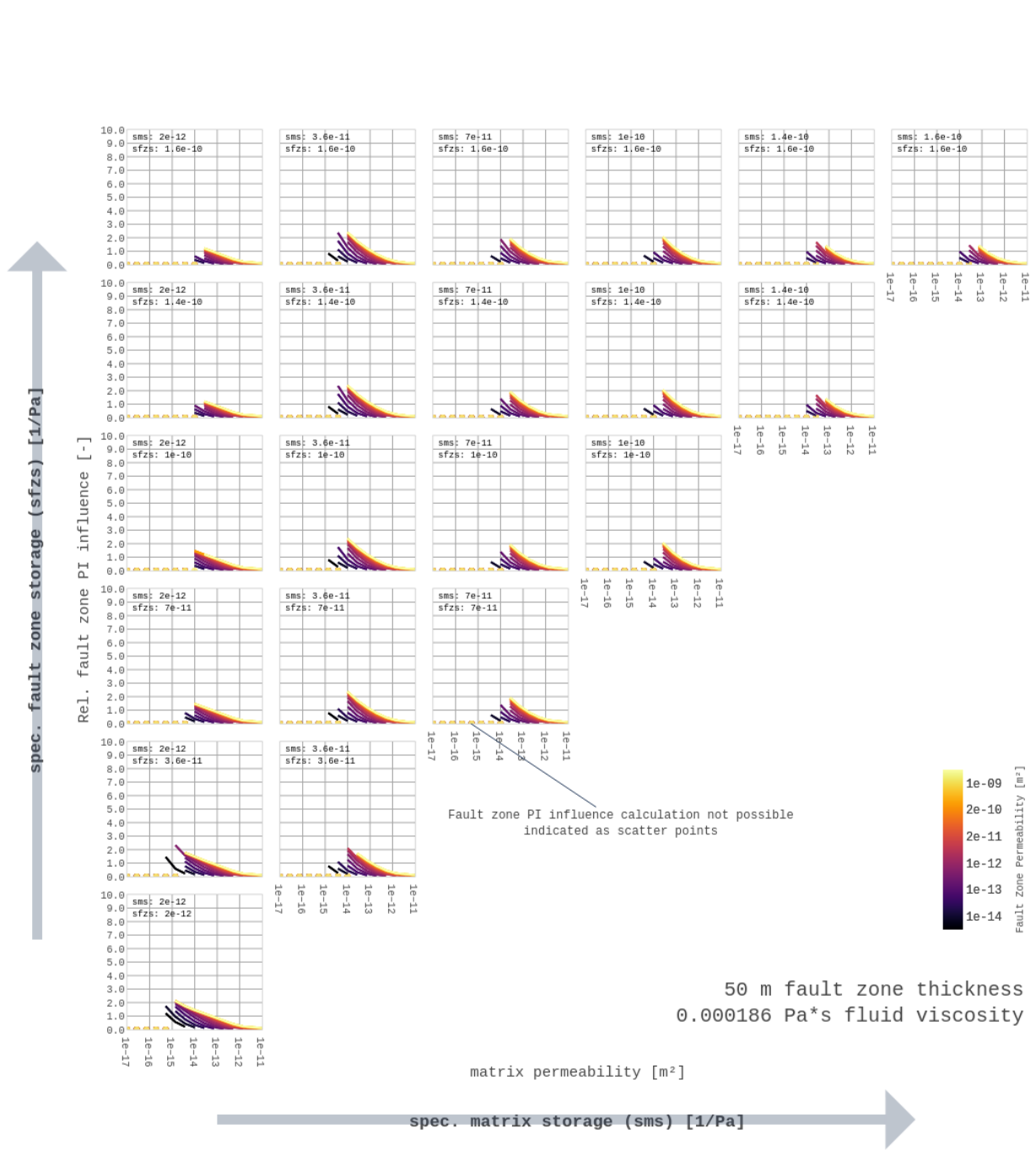


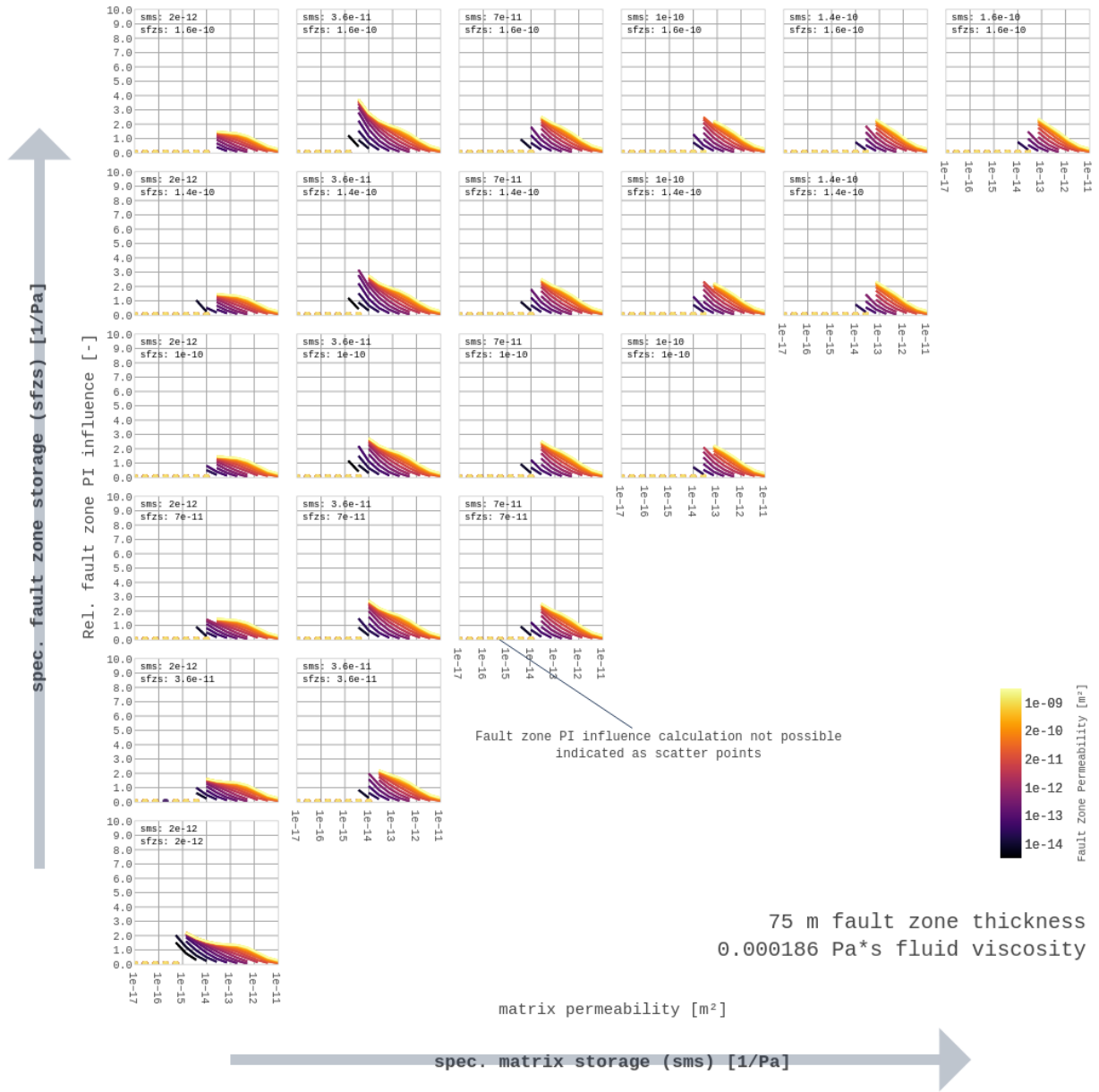


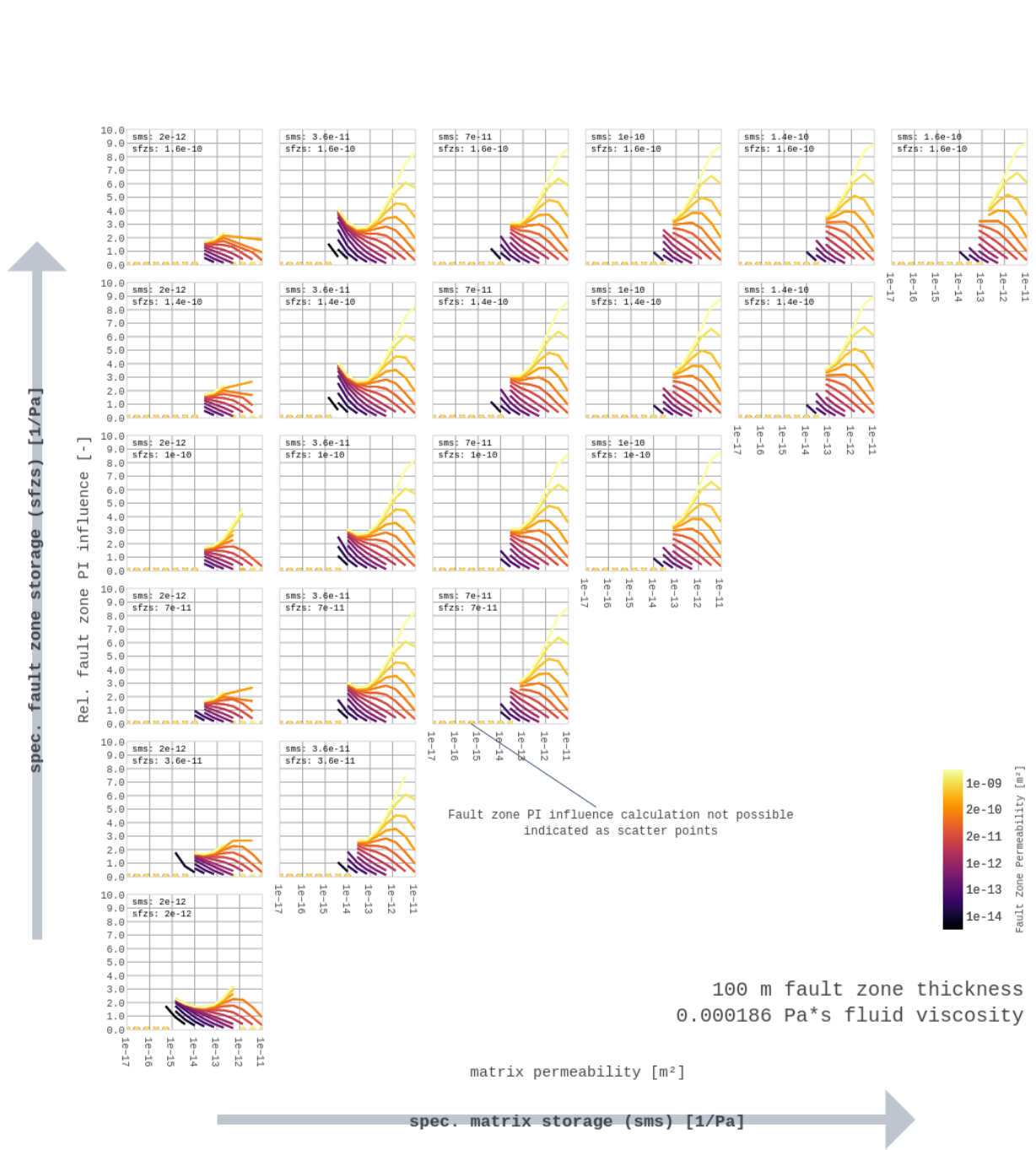












100 m fault zone thickness  
 0.000186 Pa\*s fluid viscosity

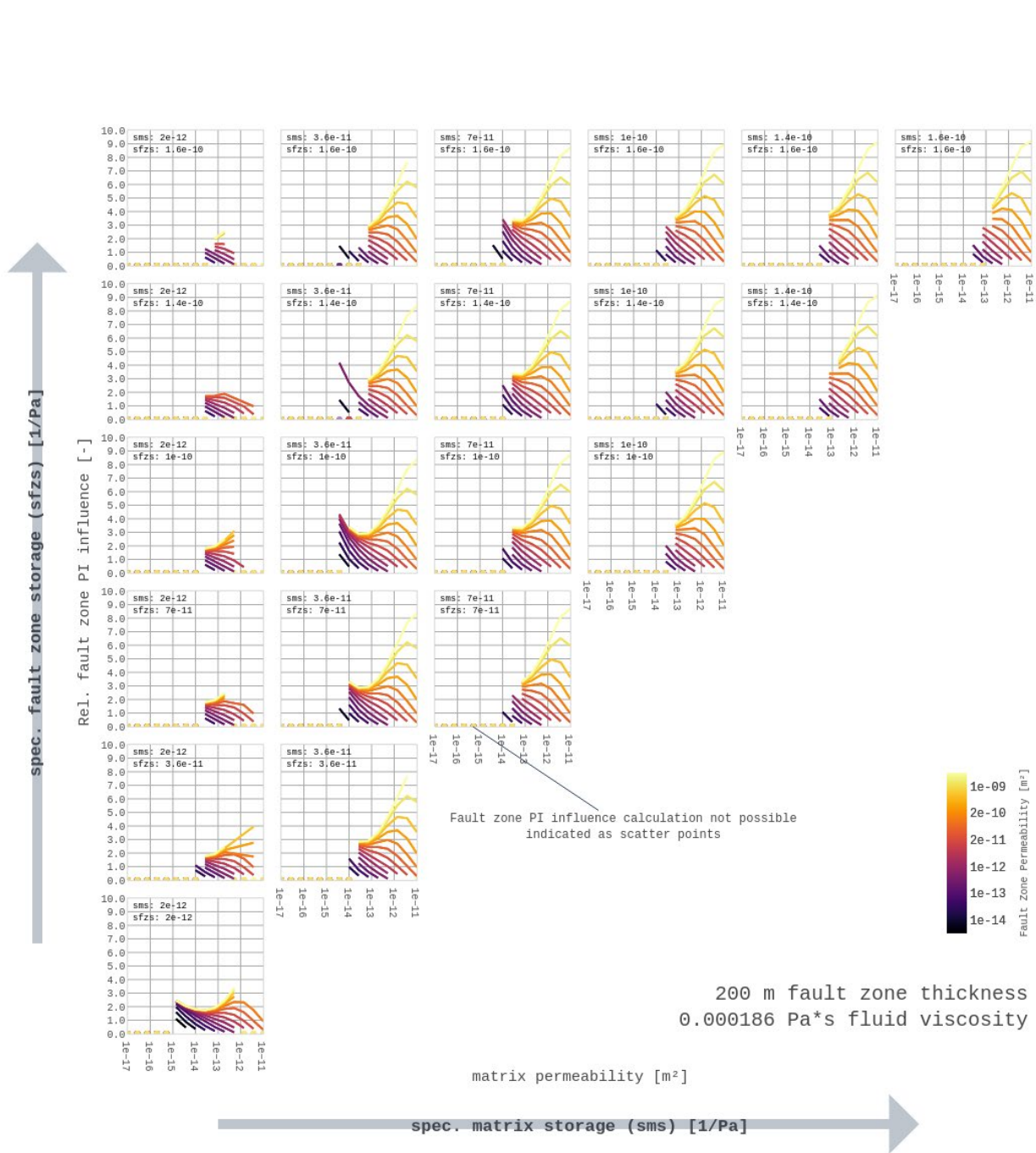
matrix permeability [m²]

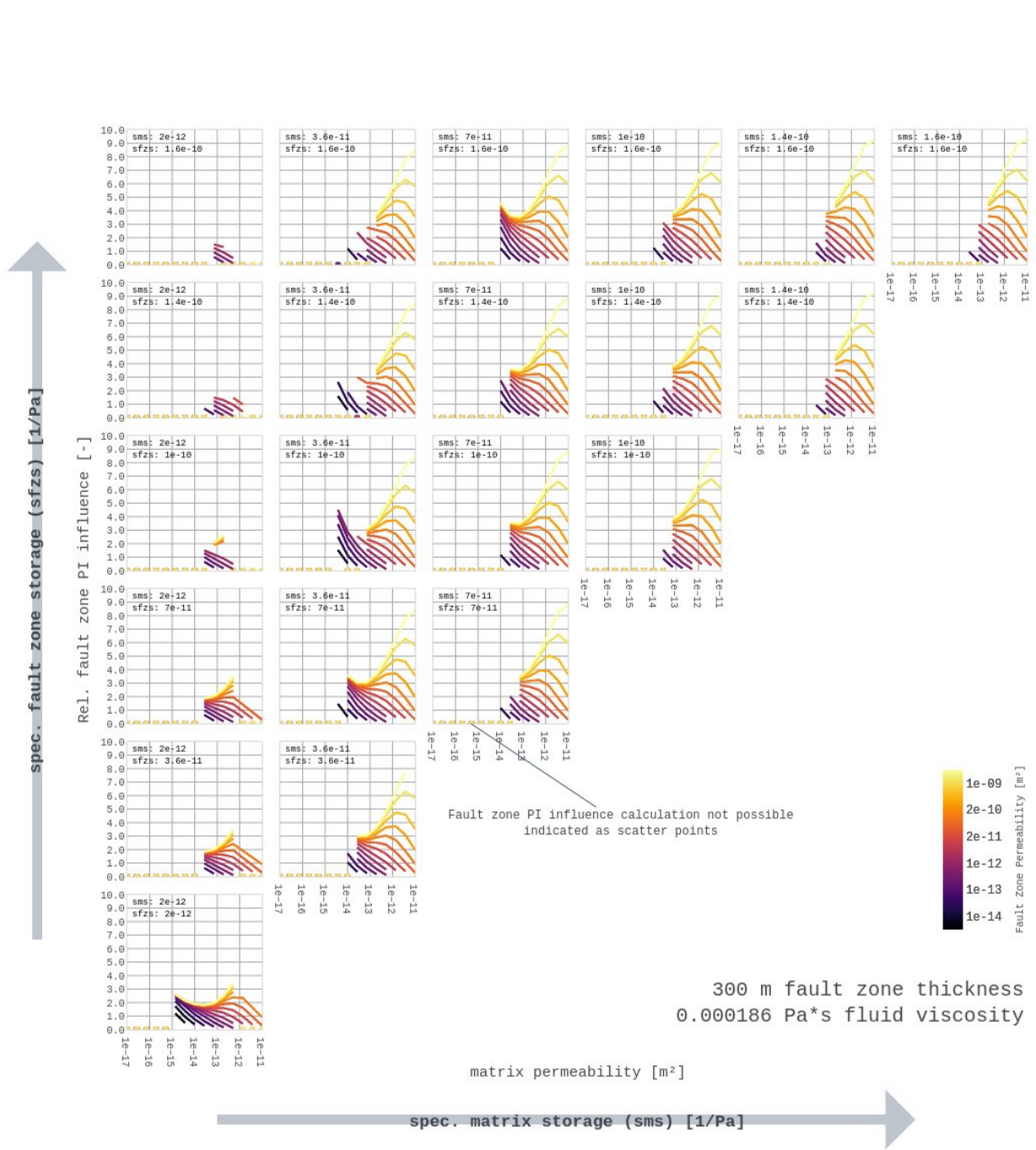
spec. matrix storage (sms) [1/Pa]

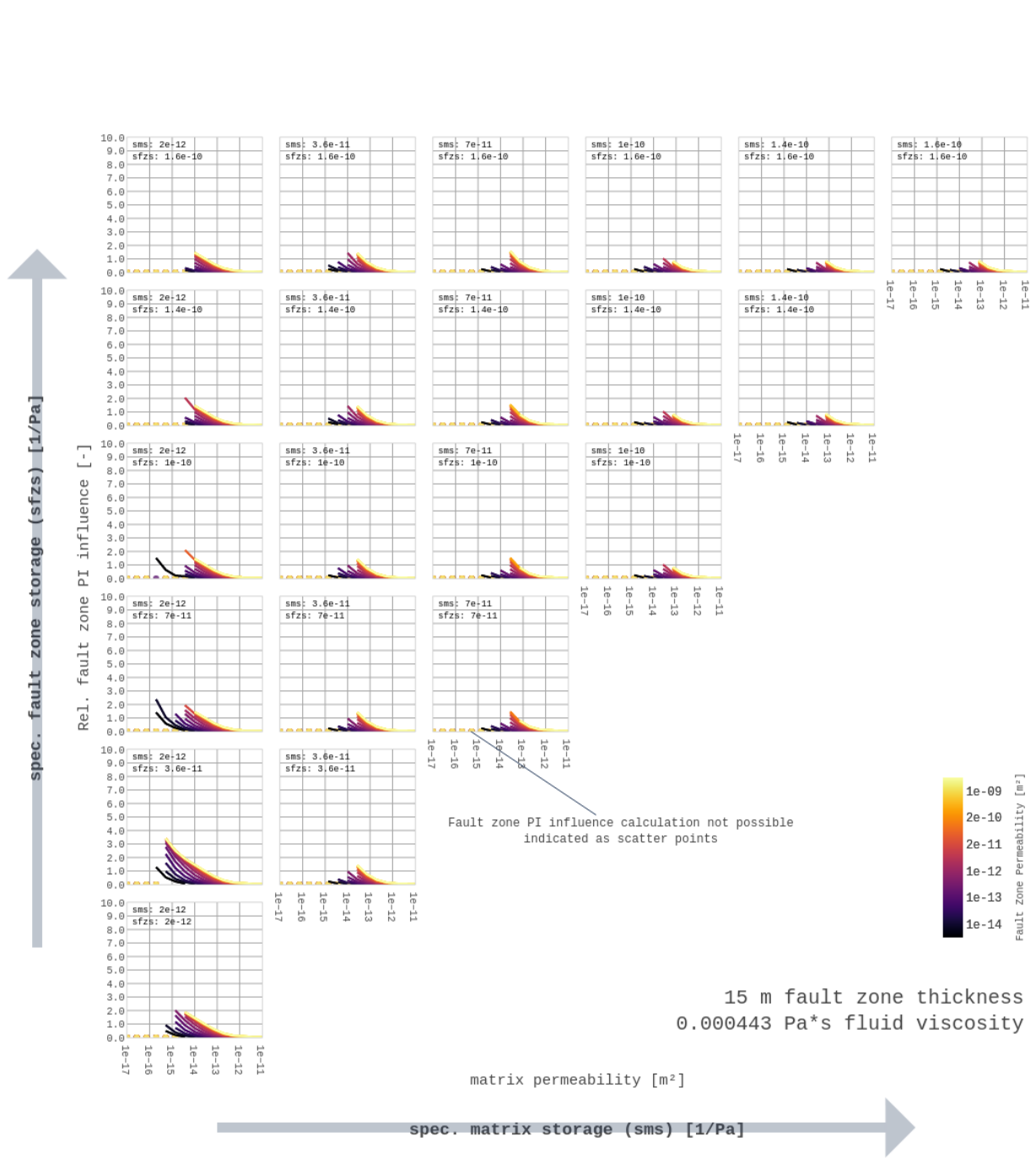
spec. fault zone storage (sfzs) [1/Pa]

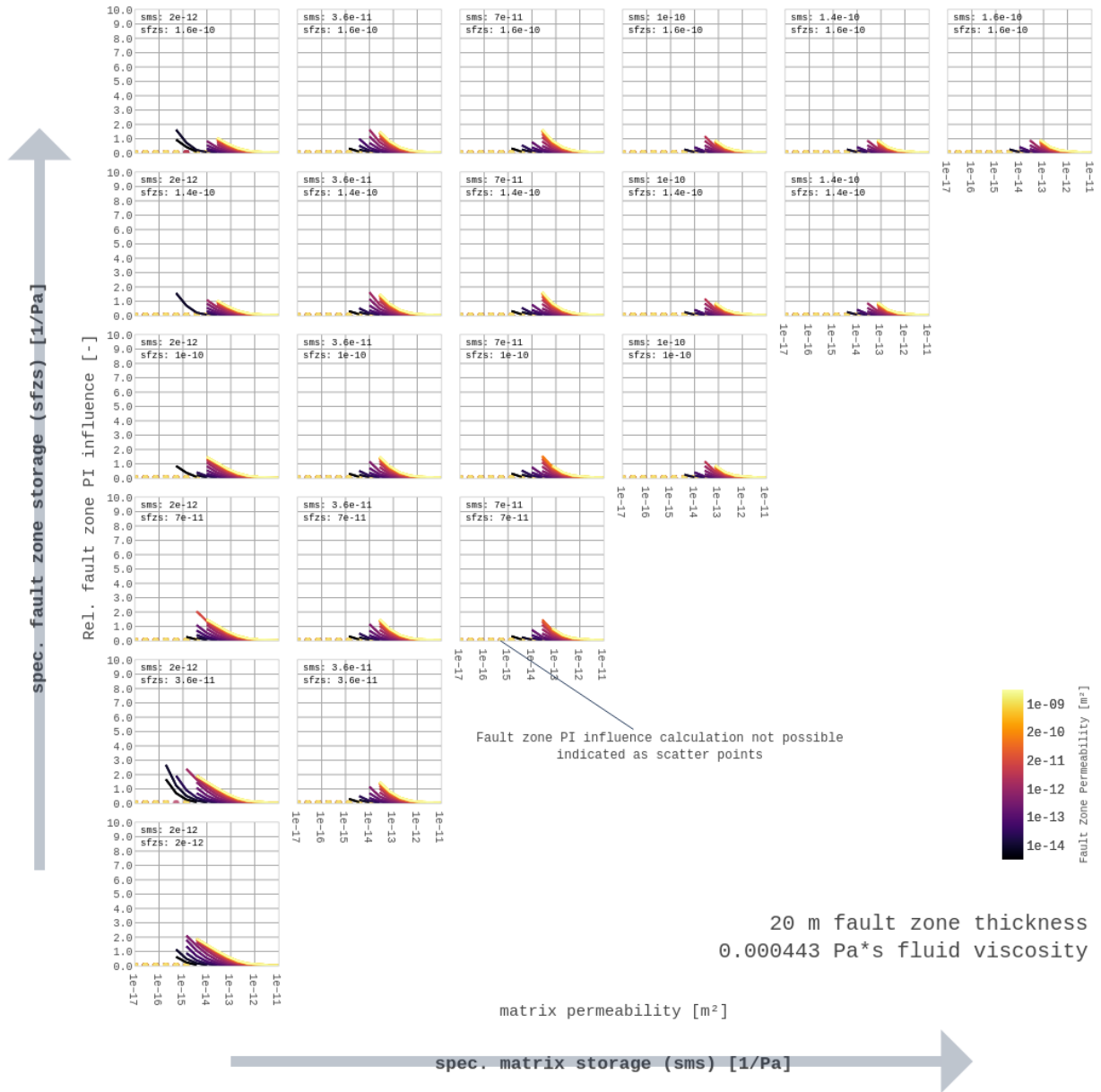
Rel. fault zone PI influence [-]

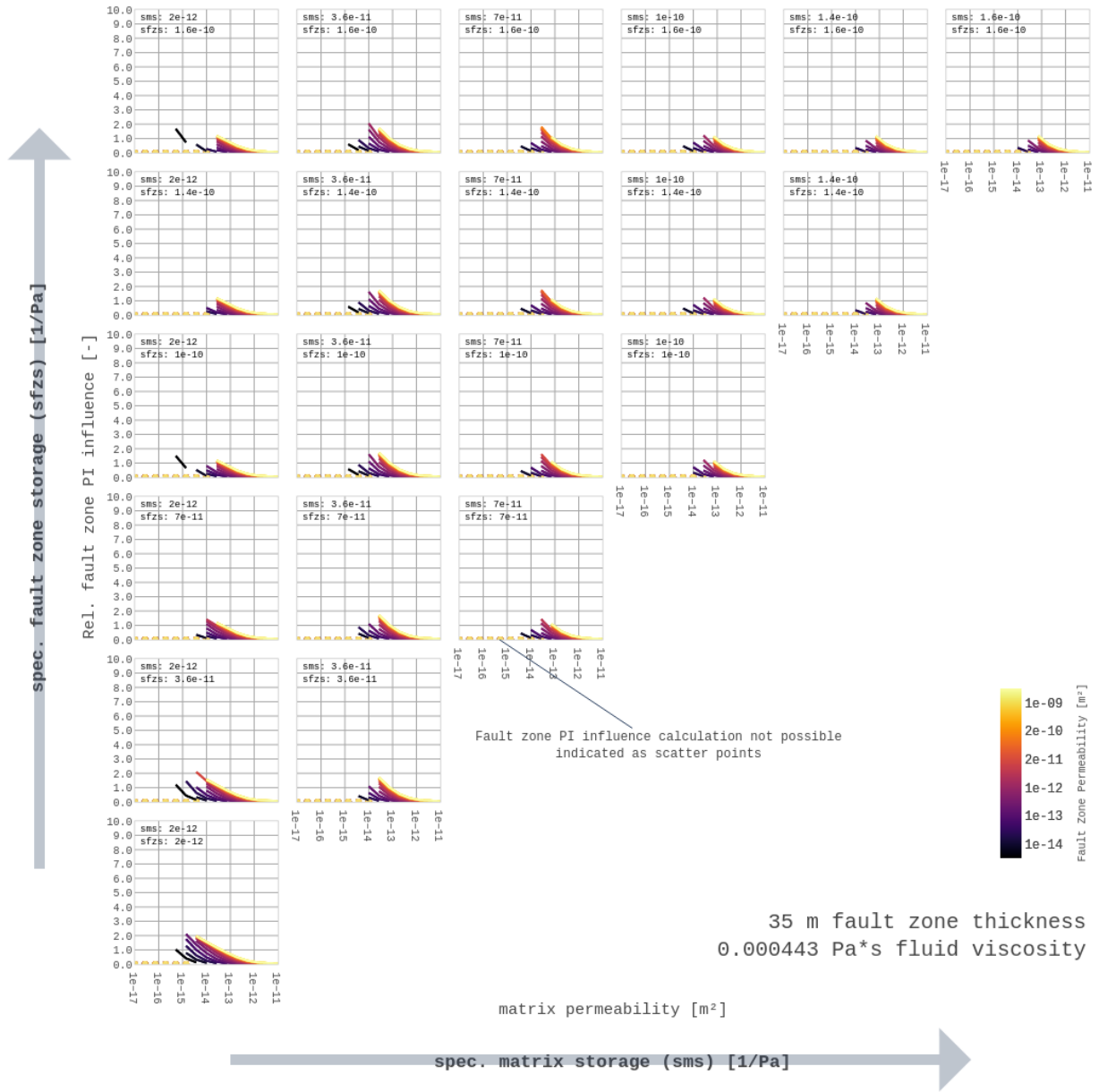
Fault Zone Permeability [m²]

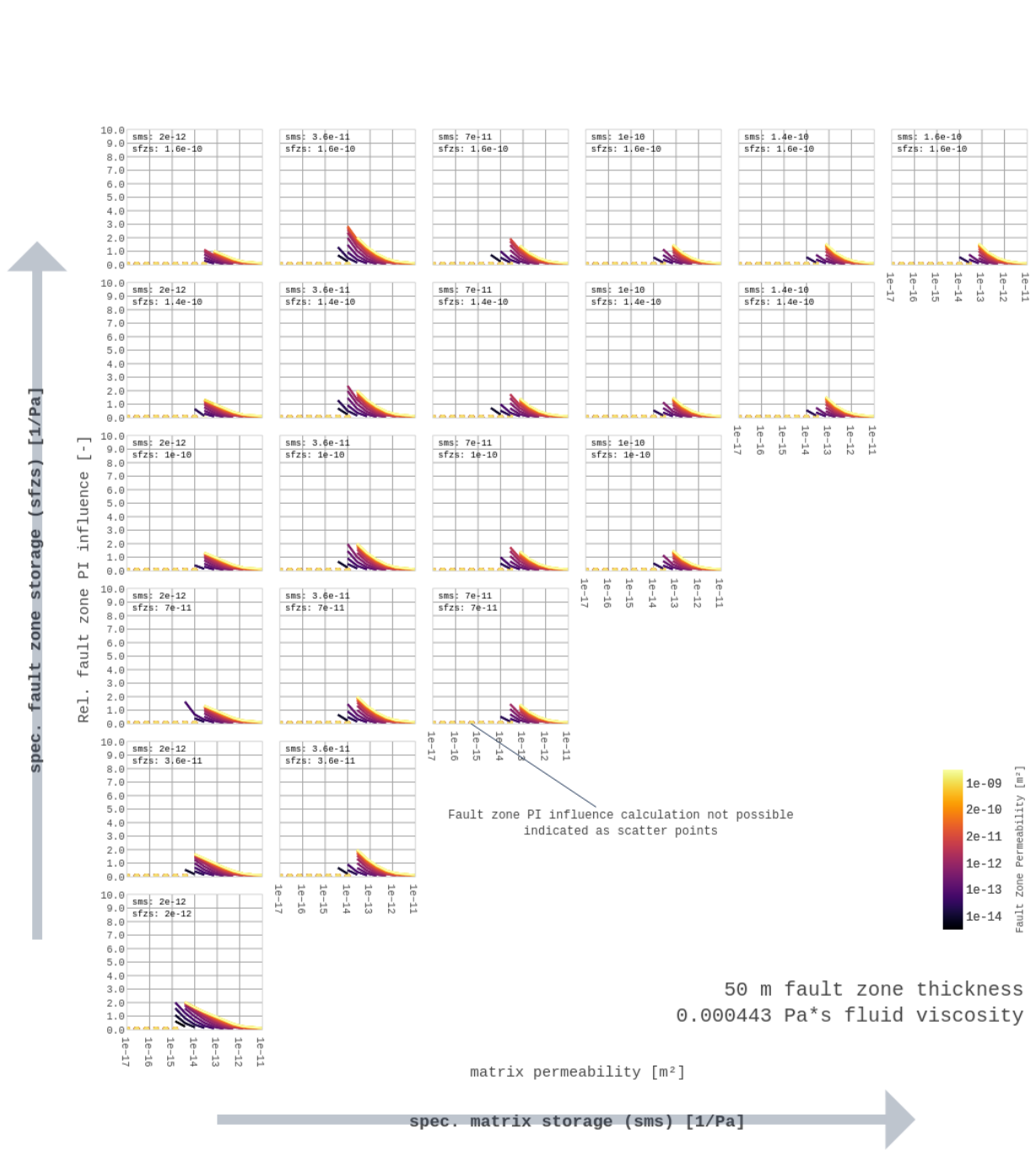


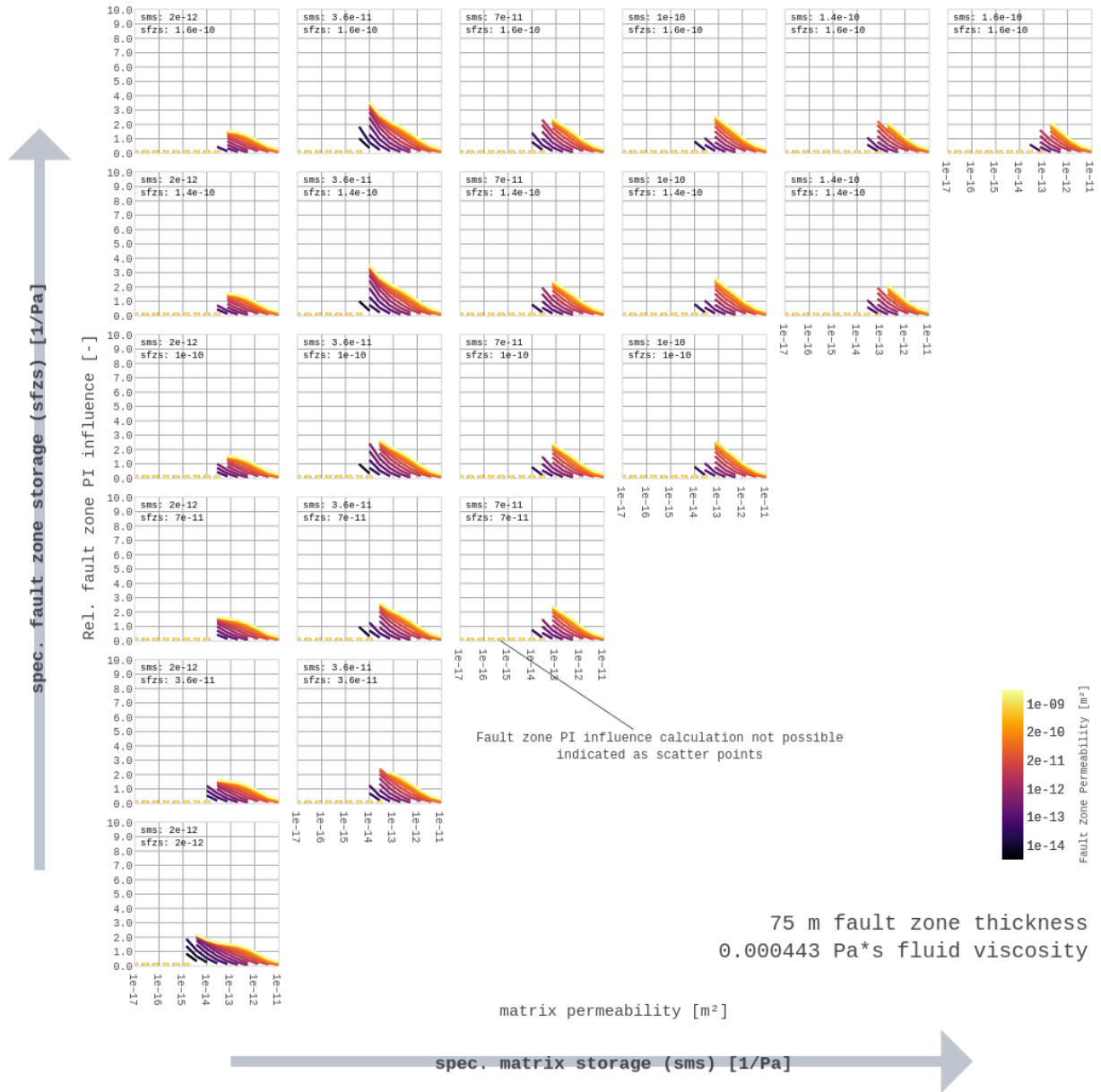


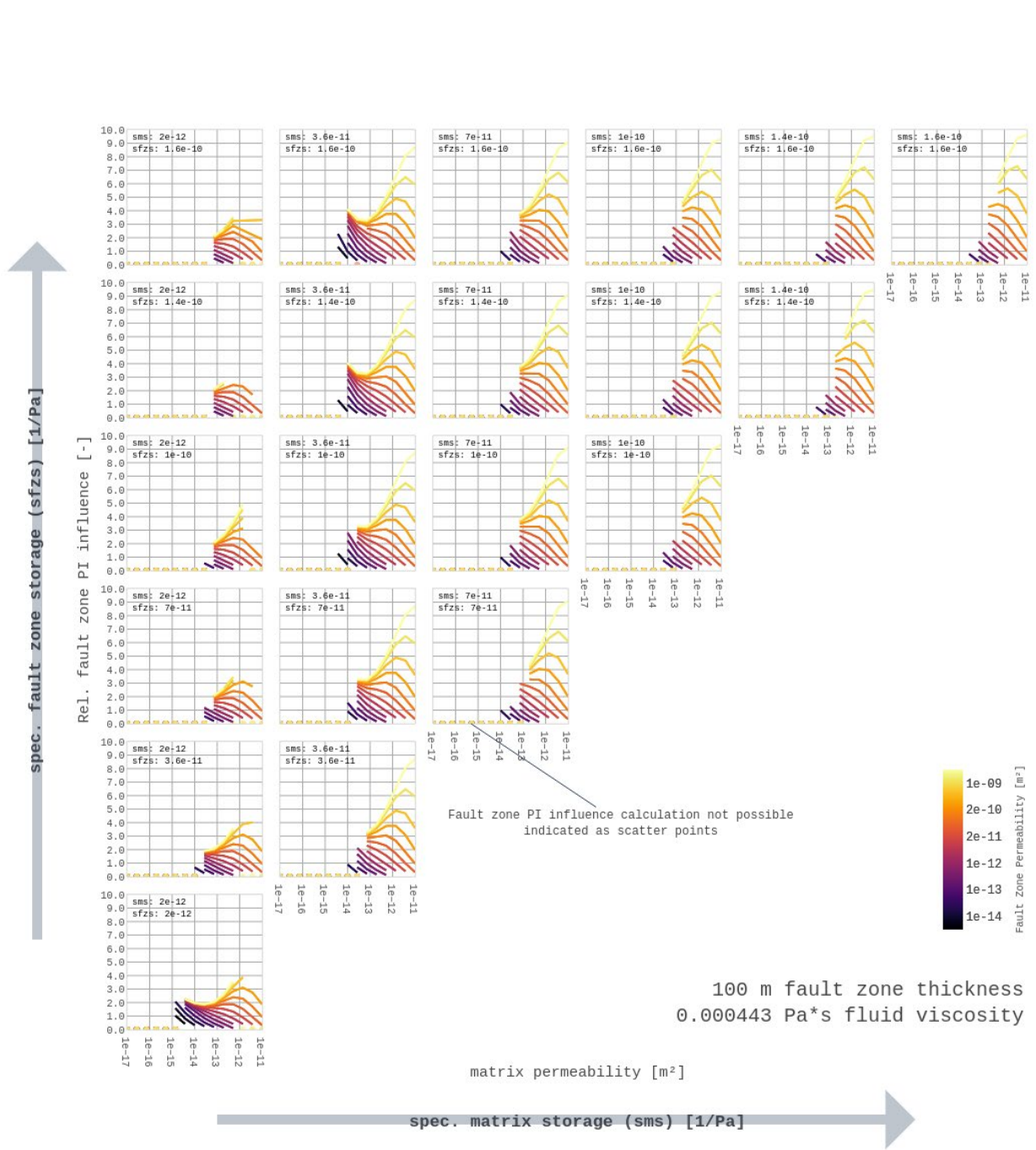


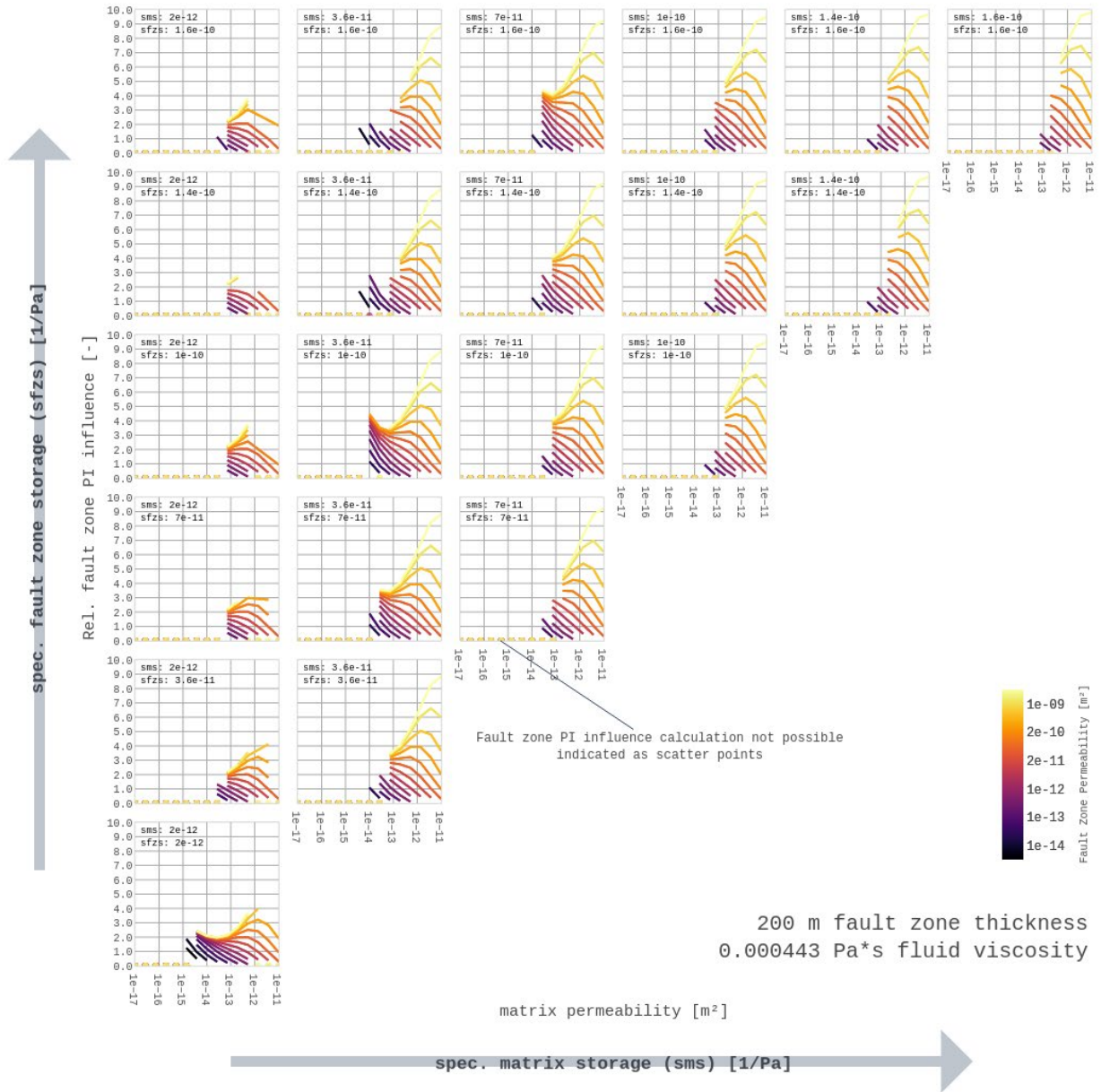


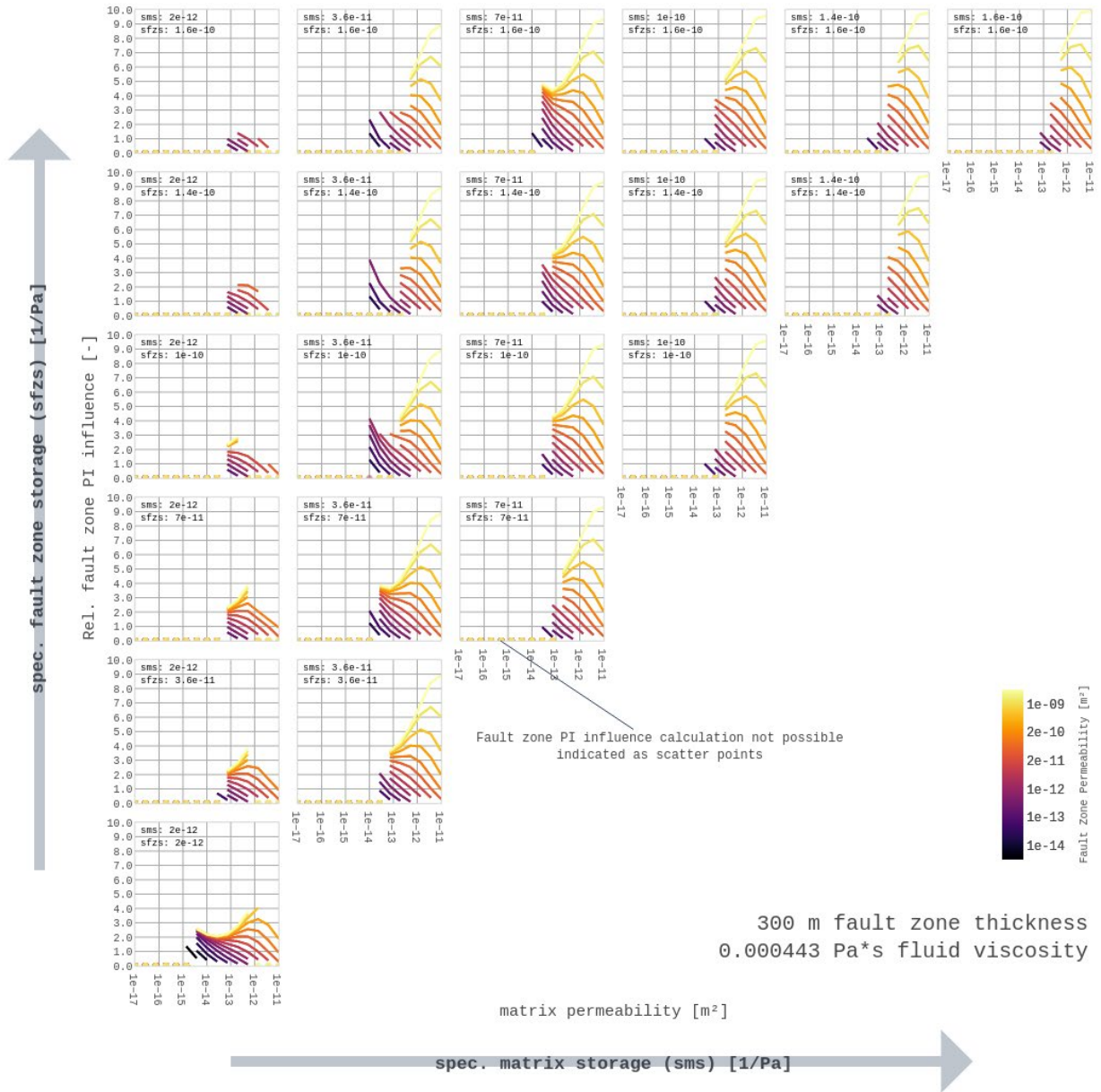












## 9.6 Statistics of the fault zones relative PI change in dependency of fault zone thickness and matrix permeability

Fault Zone Thickness [m]	Matrix Permeability [m <sup>2</sup> ]	1,00	2,68	7,20	1,93	5,18	1,39	3,73	1,00	2,68	7,20	1,93	5,18	1,39	3,73	1,00
		E-17	E-17	E-17	E-16	E-16	E-15	E-15	E-14	E-14	E-14	E-13	E-13	E-12	E-12	E-11
15	count	0	0	117	842	1485	4372	9683	15144	21473	21600	19800	18000	14400	12600	10800
	mean			4,45	3,47	1,97	0,84	0,76	0,87	0,79	0,45	0,21	0,09	0,06	0,04	0,03
	std			1,31	1,55	1,15	0,80	0,75	0,67	0,50	0,27	0,13	0,05	0,03	0,02	0,01
	min			2,11	0,96	0,42	0,16	0,05	0,03	0,02	0,01	0,01	0,01	0,01	0,01	0,01
	25%			3,52	2,13	0,66	0,23	0,17	0,24	0,21	0,17	0,07	0,04	0,03	0,02	0,03
	50%			4,38	3,45	2,17	0,46	0,39	0,83	0,91	0,53	0,25	0,10	0,06	0,04	0,03
	75%			5,53	4,64	2,96	1,36	1,43	1,44	1,24	0,70	0,33	0,15	0,08	0,06	0,04
	max			6,87	6,99	4,44	3,21	2,86	2,21	1,57	0,87	0,38	0,16	0,09	0,06	0,05
	count unsuccessful samples	27000	27000	26883	26158	25515	22628	17317	10056	1927	0	0	0	0	0	0
	unsuccessful fraction	1,00	1,00	1,00	0,97	0,95	0,84	0,64	0,40	0,08	0,00	0,00	0,00	0,00	0,00	0,00
20	count	0	0	102	593	1141	3760	9246	14905	21382	21600	19800	18000	14400	12600	10800
	mean			4,91	3,56	2,18	1,00	0,88	0,95	0,85	0,50	0,24	0,11	0,06	0,04	0,03
	std			1,32	1,46	1,17	0,88	0,83	0,69	0,51	0,29	0,14	0,06	0,03	0,02	0,01
	min			2,43	1,18	0,54	0,21	0,06	0,04	0,03	0,02	0,01	0,01	0,02	0,01	0,01
	25%			4,09	2,45	0,96	0,30	0,22	0,29	0,28	0,22	0,09	0,05	0,04	0,02	0,02
	50%			4,97	3,37	2,27	0,60	0,50	0,96	0,97	0,59	0,29	0,12	0,07	0,05	0,03
	75%			5,56	4,34	3,09	1,75	1,55	1,56	1,30	0,75	0,36	0,17	0,09	0,06	0,04
	max			7,58	7,63	5,24	3,48	3,09	2,33	1,64	0,94	0,42	0,19	0,10	0,07	0,05
	count unsuccessful samples	27000	27000	26898	26407	25859	23240	17754	10295	2018	0	0	0	0	0	0
	unsuccessful fraction	1,00	1,00	1,00	0,98	0,96	0,86	0,66	0,41	0,09	0,00	0,00	0,00	0,00	0,00	0,00
35	count	0	0	48	315	761	2649	7844	13524	20550	21600	19800	18000	14400	12600	10800
	mean			5,52	4,27	2,81	1,61	1,14	1,13	1,01	0,66	0,35	0,17	0,10	0,06	0,03
	std			1,06	1,58	1,24	1,11	0,95	0,74	0,55	0,34	0,18	0,09	0,04	0,02	0,02
	min			3,52	1,65	0,84	0,36	0,12	0,08	0,06	0,03	0,02	0,01	0,02	0,01	0,00
	25%			4,44	3,13	1,78	0,55	0,36	0,33	0,47	0,35	0,17	0,09	0,07	0,03	0,02
	50%			6,22	4,11	2,77	1,15	0,80	1,13	1,13	0,77	0,42	0,20	0,11	0,06	0,03
	75%			6,44	4,96	3,55	2,47	1,93	1,82	1,48	0,95	0,51	0,25	0,13	0,08	0,05
	max			6,63	9,20	6,57	4,48	3,37	2,56	1,90	1,21	0,61	0,28	0,14	0,08	0,05

	<b>count unsuccessful samples</b>	27000	27000	26952	26685	26239	24351	19156	11676	2850	0	0	0	0	0	0
	<b>unsuccessful fraction</b>	1,00	1,00	1,00	0,99	0,97	0,90	0,71	0,46	0,12	0,00	0,00	0,00	0,00	0,00	0,00
50	<b>count</b>	0	0	42	231	586	2142	6714	12214	19652	21600	19800	18000	14400	12600	10800
	<b>mean</b>			6,36	4,45	3,05	2,07	1,37	1,30	1,19	0,87	0,54	0,31	0,19	0,12	0,09
	<b>std</b>			1,43	1,36	1,11	1,15	1,02	0,78	0,60	0,42	0,26	0,15	0,06	0,04	0,02
	<b>min</b>			3,50	2,07	1,10	0,53	0,20	0,15	0,11	0,07	0,05	0,03	0,07	0,03	0,02
	<b>25%</b>			5,45	3,45	2,28	0,88	0,35	0,50	0,66	0,49	0,29	0,19	0,15	0,09	0,07
	<b>50%</b>			5,94	4,10	2,98	1,97	1,09	1,34	1,30	0,98	0,63	0,35	0,21	0,14	0,09
	<b>75%</b>			8,17	5,23	3,67	2,92	2,30	2,02	1,70	1,22	0,77	0,44	0,25	0,15	0,11
	<b>max</b>			8,95	8,53	6,77	5,23	3,80	2,92	2,24	1,61	0,92	0,50	0,26	0,16	0,12
	<b>count unsuccessful samples</b>	27000	27000	26958	26769	26414	24858	20286	12986	3748	0	0	0	0	0	0
	<b>unsuccessful fraction</b>	1,00	1,00	1,00	0,99	0,98	0,92	0,75	0,52	0,16	0,00	0,00	0,00	0,00	0,00	0,00
75	<b>count</b>	0	0	28	152	383	1618	5701	10490	17499	21218	19800	18000	14400	12594	10800
	<b>mean</b>			5,43	5,41	3,86	2,60	1,68	1,55	1,48	1,37	1,13	0,84	0,60	0,34	0,20
	<b>std</b>			0,82	1,65	1,30	1,27	1,16	0,91	0,76	0,69	0,60	0,47	0,26	0,14	0,08
	<b>min</b>			4,40	2,47	1,37	0,71	0,29	0,22	0,16	0,11	0,07	0,03	0,14	0,04	0,03
	<b>25%</b>			4,72	4,29	2,87	1,33	0,47	0,70	0,88	0,75	0,55	0,42	0,40	0,21	0,14
	<b>50%</b>			4,73	4,92	3,60	2,33	1,44	1,54	1,55	1,48	1,27	0,93	0,66	0,39	0,20
	<b>75%</b>			6,33	6,65	4,80	3,67	2,73	2,36	2,13	1,94	1,65	1,27	0,83	0,47	0,27
	<b>max</b>			6,34	8,90	7,35	6,04	4,74	3,70	3,04	2,65	2,18	1,55	0,94	0,51	0,57
	<b>count unsuccessful samples</b>	27000	27000	26972	26848	26617	25382	21299	14710	5901	382	0	0	0	6	0
	<b>unsuccessful fraction</b>	1,00	1,00	1,00	0,99	0,99	0,94	0,79	0,58	0,25	0,02	0,00	0,00	0,00	0,00	0,00
100	<b>count</b>	0	0	15	86	269	1199	4822	9089	15294	19855	19714	17644	13619	11701	9793
	<b>mean</b>			6,95	5,07	4,12	2,76	1,93	1,78	1,72	1,88	2,16	2,51	3,22	3,46	3,35
	<b>std</b>			0,82	1,14	1,41	1,19	1,26	1,03	0,91	1,00	1,28	1,70	2,13	2,65	2,89
	<b>min</b>			4,54	2,77	1,55	0,85	0,37	0,29	0,23	0,17	0,14	0,10	0,40	0,16	0,14
	<b>25%</b>			7,21	4,05	2,98	1,66	0,62	0,87	0,94	1,00	0,93	0,92	1,00	0,98	0,95
	<b>50%</b>			7,28	4,99	3,98	2,53	1,72	1,70	1,74	1,96	2,25	2,41	2,78	3,00	2,00
	<b>75%</b>			7,29	6,20	4,80	3,77	3,02	2,68	2,50	2,70	3,22	4,00	5,11	5,93	5,82
	<b>max</b>			7,30	8,16	8,28	6,19	5,56	4,30	3,84	4,02	5,00	6,49	8,09	9,46	9,70

	<b>count unsuccessful samples</b>	27000	27000	26985	26914	26731	25801	22178	16111	8106	1745	86	356	781	899	1007
	<b>unsuccessful fraction</b>	1,00	1,00	1,00	1,00	0,99	0,96	0,82	0,64	0,35	0,08	0,00	0,02	0,05	0,07	0,09
200	<b>count</b>	0	0	0	29	114	774	3672	7269	12622	18409	19436	17353	13415	11489	9531
	<b>mean</b>				6,64	4,70	3,41	2,30	2,08	1,89	1,99	2,30	2,65	3,37	3,56	3,38
	<b>std</b>				1,76	1,59	1,57	1,51	1,23	1,04	1,06	1,33	1,77	2,19	2,71	2,92
	<b>min</b>				3,87	1,81	1,02	0,44	0,34	0,26	0,20	0,15	0,10	0,43	0,16	0,13
	<b>25%</b>				5,14	3,54	2,05	0,77	1,00	0,90	1,13	1,08	1,04	1,09	1,03	0,97
	<b>50%</b>				5,29	4,82	3,08	1,99	1,98	1,87	2,03	2,41	2,59	2,95	3,11	2,04
	<b>75%</b>				8,63	5,70	4,56	3,52	3,12	2,76	2,85	3,38	4,20	5,31	6,06	5,89
	<b>max</b>				8,67	7,88	7,56	6,76	5,21	4,39	4,49	5,32	6,81	8,39	9,72	9,86
	<b>count unsuccessful samples</b>	27000	27000	27000	26971	26886	26226	23328	17931	10778	3191	364	647	985	1111	1269
	<b>unsuccessful fraction</b>	1,00	1,00	1,00	1,00	1,00	0,97	0,86	0,71	0,46	0,15	0,02	0,04	0,07	0,09	0,12
300	<b>count</b>	0	0	0	14	56	469	2921	6257	11147	16927	18752	17177	13275	11320	9375
	<b>mean</b>				5,51	4,47	3,30	2,43	2,21	2,02	2,04	2,35	2,73	3,44	3,61	3,37
	<b>std</b>				0,45	1,30	1,45	1,63	1,37	1,16	1,13	1,38	1,84	2,25	2,76	2,95
	<b>min</b>				4,03	1,95	1,09	0,47	0,36	0,28	0,21	0,15	0,10	0,43	0,16	0,13
	<b>25%</b>				5,57	3,50	2,13	0,83	0,98	0,95	1,14	1,11	1,06	1,11	1,03	0,95
	<b>50%</b>				5,58	4,48	2,69	2,00	2,06	1,95	2,05	2,44	2,65	2,99	3,12	2,03
	<b>75%</b>				5,58	4,99	4,40	3,76	3,36	2,98	2,96	3,48	4,33	5,43	6,15	5,91
	<b>max</b>				6,01	8,36	7,33	8,28	6,02	5,05	4,82	5,61	7,10	8,65	9,92	9,97
	<b>count unsuccessful samples</b>	27000	27000	27000	26986	26944	26531	24079	18943	12253	4673	1048	823	1125	1280	1425
	<b>unsuccessful fraction</b>	1,00	1,00	1,00	1,00	1,00	0,98	0,89	0,75	0,52	0,22	0,05	0,05	0,08	0,10	0,13

## 9.7 Statistics of the fault zones relative PI change for hydraulically hidden fault zones in dependency of fault zone thickness and matrix permeability

Fault Zone Thickness [m]	Matrix Permeability [m2]	1,00E-14	2,68E-14	7,20E-14	1,93E-13	5,18E-13	1,39E-12	3,73E-12	1,00E-11
		<b>count</b>	9424	17232	21250	19800	18000	14400	12600
<b>mean</b>	0,43	0,66	0,45	0,21	0,09	0,06	0,04	0,03	
<b>std</b>	0,38	0,47	0,27	0,13	0,05	0,03	0,02	0,01	
<b>min</b>	0,03	0,02	0,01	0,01	0,01	0,01	0,01	0,01	
<b>25%</b>	0,12	0,19	0,13	0,07	0,04	0,03	0,02	0,03	
<b>50%</b>	0,28	0,66	0,53	0,25	0,10	0,06	0,04	0,03	
<b>75%</b>	0,61	1,12	0,70	0,33	0,15	0,08	0,06	0,04	
<b>max</b>	1,53	1,43	0,87	0,38	0,16	0,09	0,06	0,05	
<b>count unsuccessful samples</b>	1980	615	0	0	0	0	0	0	
<b>unsuccessful fration</b>	0,17	0,03	0,00	0,00	0,00	0,00	0,00	0,00	
15	<b>count</b>	8871	16916	20999	19737	18000	14400	12600	10800
	<b>mean</b>	0,48	0,72	0,50	0,24	0,11	0,06	0,04	0,03
	<b>std</b>	0,41	0,49	0,29	0,14	0,06	0,03	0,02	0,01
	<b>min</b>	0,04	0,03	0,02	0,01	0,01	0,02	0,01	0,01
	<b>25%</b>	0,16	0,25	0,17	0,09	0,05	0,04	0,02	0,02
	<b>50%</b>	0,36	0,76	0,59	0,29	0,12	0,07	0,05	0,03
	<b>75%</b>	0,72	1,19	0,75	0,36	0,17	0,09	0,06	0,04
	<b>max</b>	1,65	1,52	0,94	0,42	0,19	0,10	0,07	0,05
	<b>count unsuccessful samples</b>	1543	569	0	0	0	0	0	0
	<b>unsuccessful fration</b>	0,15	0,03	0,00	0,00	0,00	0,00	0,00	0,00
20	<b>count</b>	7160	13940	19901	19355	18000	14400	12600	10800
	<b>mean</b>	0,54	0,80	0,65	0,35	0,17	0,10	0,06	0,03
	<b>std</b>	0,41	0,52	0,35	0,19	0,09	0,04	0,02	0,02
	<b>min</b>	0,08	0,06	0,03	0,02	0,01	0,02	0,01	0,00
	<b>25%</b>	0,15	0,23	0,30	0,17	0,09	0,07	0,03	0,02
	<b>50%</b>	0,34	0,79	0,75	0,42	0,20	0,11	0,06	0,03
	<b>75%</b>	0,72	1,29	0,95	0,52	0,25	0,13	0,08	0,05
	<b>max</b>	1,66	1,76	1,21	0,61	0,28	0,14	0,08	0,05
	<b>count unsuccessful samples</b>								
	<b>unsuccessful fration</b>								
35	<b>count</b>								
	<b>mean</b>								
	<b>std</b>								
	<b>min</b>								
	<b>25%</b>								
	<b>50%</b>								
	<b>75%</b>								
	<b>max</b>								
	<b>count unsuccessful samples</b>								
	<b>unsuccessful fration</b>								

	<b>count</b>								
	<b>unsuccessful samples</b>	1343	586	0	0	0	0	0	0
	<b>unsuccessful fraction</b>	0,16	0,04	0,00	0,00	0,00	0,00	0,00	0,00
50	<b>count</b>	5724	9557	17872	18695	17908	14400	12600	10800
	<b>mean</b>	0,59	0,72	0,81	0,53	0,31	0,19	0,12	0,09
	<b>std</b>	0,36	0,46	0,43	0,27	0,15	0,06	0,04	0,02
	<b>min</b>	0,15	0,11	0,07	0,05	0,03	0,07	0,03	0,02
	<b>25%</b>	0,22	0,33	0,43	0,29	0,18	0,15	0,09	0,07
	<b>50%</b>	0,49	0,65	0,90	0,61	0,35	0,21	0,14	0,09
	<b>75%</b>	0,86	1,08	1,19	0,77	0,44	0,25	0,15	0,11
	<b>max</b>	1,53	1,77	1,57	0,92	0,50	0,26	0,16	0,12
	<b>count</b>								
	<b>unsuccessful samples</b>	995	175	0	0	0	0	0	0
	<b>unsuccessful fraction</b>	0,15	0,02	0,00	0,00	0,00	0,00	0,00	0,00
75	<b>count</b>	3877	7469	11320	16766	17571	14400	12594	10800
	<b>mean</b>	0,59	0,84	0,91	1,04	0,84	0,60	0,34	0,20
	<b>std</b>	0,31	0,55	0,57	0,61	0,47	0,26	0,14	0,08
	<b>min</b>	0,22	0,16	0,11	0,07	0,03	0,14	0,04	0,03
	<b>25%</b>	0,31	0,40	0,39	0,52	0,42	0,40	0,21	0,14
	<b>50%</b>	0,59	0,76	0,88	1,12	0,92	0,66	0,39	0,20
	<b>75%</b>	0,75	1,29	1,38	1,60	1,27	0,83	0,47	0,27
	<b>max</b>	1,62	2,58	2,27	2,14	1,55	0,94	0,51	0,57
	<b>count</b>								
	<b>unsuccessful samples</b>	927	641	31	0	0	0	6	0
	<b>unsuccessful fraction</b>	0,19	0,08	0,00	0,00	0,00	0,00	0,00	0,00

## 9.8 Statistics of the flow type distribution in dependency of fault zone thickness and matrix permeability

Fault Zone Thickness [m]	Matrix Permeability [m <sup>2</sup> ]	1,00	2,68	7,20	1,93	5,18	1,39	3,73	1,00	2,68	7,20	1,93	5,18	1,39	3,73	1,00
		E-17	E-17	E-17	E-16	E-16	E-15	E-15	E-14	E-14	E-14	E-13	E-13	E-12	E-12	E-11
15	<b>samples count</b>	27000	27000	27000	27000	27000	27000	27000	25200	23400	21600	19800	18000	14400	12600	10800
	<b>steep</b>	21417	13404	7131	4645	2263	1514	3943	693	1025	350	0	0	0	0	0
	<b>linear</b>	3609	9801	14363	15337	15954	13610	1043	117	0	0	0	0	0	0	0
	<b>bilinear</b>	1974	3770	5277	6210	6964	7976	9141	11404	17847	21250	19800	18000	14400	12600	10800
	<b>radial</b>	0	25	219	808	1819	3900	12873	12784	157	0	0	0	0	0	0
	<b>unspecific</b>	0	0	10	0	0	0	0	202	4371	0	0	0	0	0	0
20	<b>samples count</b>	27000	27000	27000	27000	27000	27000	27000	25200	23400	21600	19800	18000	14400	12600	10800
	<b>steep</b>	23807	17674	9539	6118	2896	1761	6256	620	1428	601	63	0	0	0	0
	<b>linear</b>	1746	6194	12752	14817	16126	14591	2357	514	0	0	0	0	0	0	0
	<b>radial</b>	1447	3118	4533	5420	6079	6987	8894	10414	17485	20999	19737	18000	14400	12600	10800
	<b>bilinear</b>	0	14	176	645	1899	3661	9493	13645	294	0	0	0	0	0	0
	<b>unspecific</b>	0	0	0	0	0	0	0	7	4193	0	0	0	0	0	0
35	<b>samples count</b>	27000	27000	27000	27000	27000	27000	27000	25200	23400	21600	19800	18000	14400	12600	10800
	<b>steep</b>	26697	24583	19115	10729	5414	2520	4315	395	2904	1565	445	0	0	0	0
	<b>radial</b>	269	1194	4995	11882	15362	15993	10228	1261	0	0	0	0	0	0	0
	<b>linear</b>	34	569	786	446	43	5	110	5	4570	134	0	0	0	0	0
	<b>bilinear</b>	0	654	1744	2908	4111	5239	6988	8503	14526	19901	19355	18000	14400	12600	10800
	<b>unspecific</b>	0	0	360	1035	2070	3243	5359	15036	1400	0	0	0	0	0	0
50	<b>samples count</b>	2,70E+04	2,52E+04	2,34E+04	2,16E+04	1,98E+04	1,80E+04	1,44E+04	1,26E+04	1,08E+04						
	<b>steep</b>	26898	26229	23058	17430	8959	3842	3199	367	3485	2996	1105	92	0	0	0
	<b>linear</b>	102	377	2085	6074	12929	15776	13296	2450	0	0	0	0	0	0	0
	<b>radial</b>	0	0	1187	2163	2355	3383	5269	6719	9732	17872	18695	17908	14400	12600	10800
	<b>bilinear</b>	0	394	581	1242	2672	3860	5014	15501	8277	0	0	0	0	0	0
	<b>unspecific</b>	0	0	89	91	85	139	222	163	1906	732	0	0	0	0	0
75	<b>samples count</b>	2,70E+04	2,52E+04	2,34E+04	2,16E+04	1,98E+04	1,80E+04	1,44E+04	1,26E+04	1,08E+04						
	<b>steep</b>	26977	26895	25371	21673	17017	9647	4540	541	1020	5552	3034	429	0	0	0
	<b>linear</b>	23	105	832	2994	6103	11237	13546	12085	29	0	0	0	0	0	0
	<b>radial</b>	0	0	0	0	868	2901	3992	4804	8110	11351	16766	17571	14400	12600	10800
	<b>bilinear</b>	0	0	797	2333	3009	3121	4149	6679	12683	4357	0	0	0	0	0
	<b>unspecific</b>	0	0	0	0	3	94	773	1091	1558	340	0	0	0	0	0

100	<b>samples count</b>	27000	27000	27000	27000	27000	27000	27000	25200	23400	21600	19800	18000	14400	12600	10800
	<b>steep</b>	26999	26912	26372	23784	19432	15843	12649	5994	5433	4932	3938	1000	30	0	0
	<b>radial</b>	1	88	424	1553	4206	6123	6389	7775	1454	2866	2691	1874	306	5	0
	<b>bilinear</b>	0	0	0	0	4	1440	3148	4576	8032	9747	10209	11809	10996	12131	10794
	<b>linear</b>	0	0	204	1663	3358	3592	4322	4678	5096	3900	2962	3317	3068	464	0
	<b>unspecific</b>	0	0	0	0	0	2	492	2177	3385	155	0	0	0	0	6

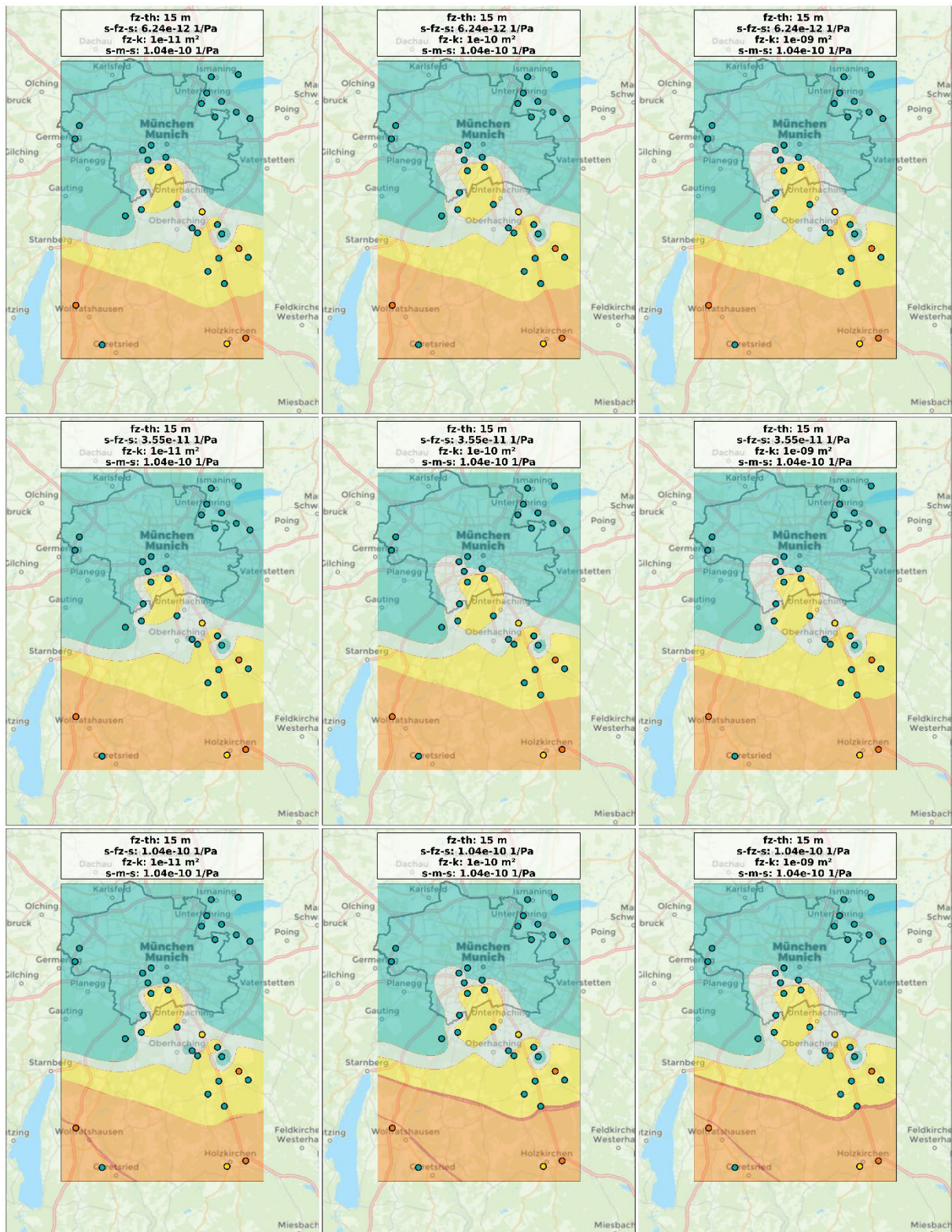
200	<b>samples count</b>	27000	27000	27000	27000	27000	27000	27000	25200	23400	21600	19800	18000	14400	12600	10800
	<b>steep</b>	27000	26982	26921	26383	23400	19097	15406	4853	4358	4875	6377	4760	675	0	0
	<b>radial</b>	0	0	0	202	1584	2695	3662	5847	9849	11024	9703	9951	10446	11738	10797
	<b>bilinear</b>	0	0	0	0	176	1039	2345	4115	5335	4495	2379	2178	2931	821	0
	<b>linear</b>	0	18	79	415	1840	4169	5587	7788	213	548	1339	1111	348	41	0
	<b>unspecific</b>	0	0	0	0	0	0	0	2597	3645	658	2	0	0	0	3

300	<b>samples count</b>	2,70E+04	2,52E+04	2,34E+04	2,16E+04	1,98E+04	1,80E+04	1,44E+04	1,26E+04	1,08E+04						
	<b>steep</b>	27000	27000	26953	26811	25204	21745	16941	4654	3416	3793	5894	7129	2341	116	0
	<b>radial</b>	0	0	0	0	831	2333	3826	5676	11573	12062	10573	8852	9373	11424	10798
	<b>bilinear</b>	0	0	0	0	47	323	1304	4539	4880	4717	2745	1398	2397	1008	0
	<b>linear</b>	0	0	47	189	918	2599	4929	7395	105	118	580	621	289	52	0
	<b>unspecific</b>	0	0	0	0	0	0	0	2936	3426	910	8	0	0	0	2

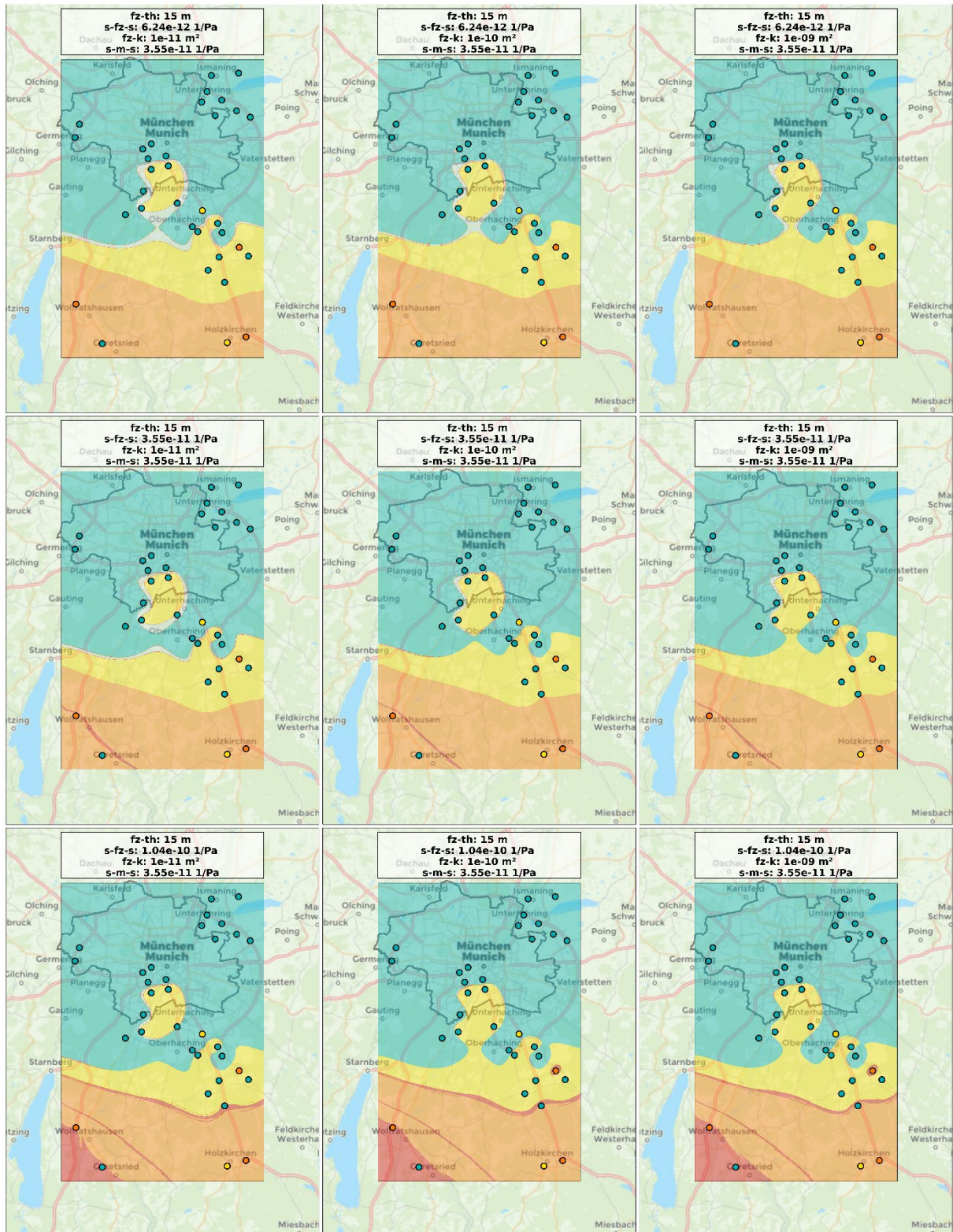
## **9.9 Spatial flow regime distributions for different fault zone types and specific matrix storage**

Colorized points in the following maps represent data points colored by their corresponding field observation in terms of flow regime. See also „List of abbreviations“ for the noted parameters above each map.

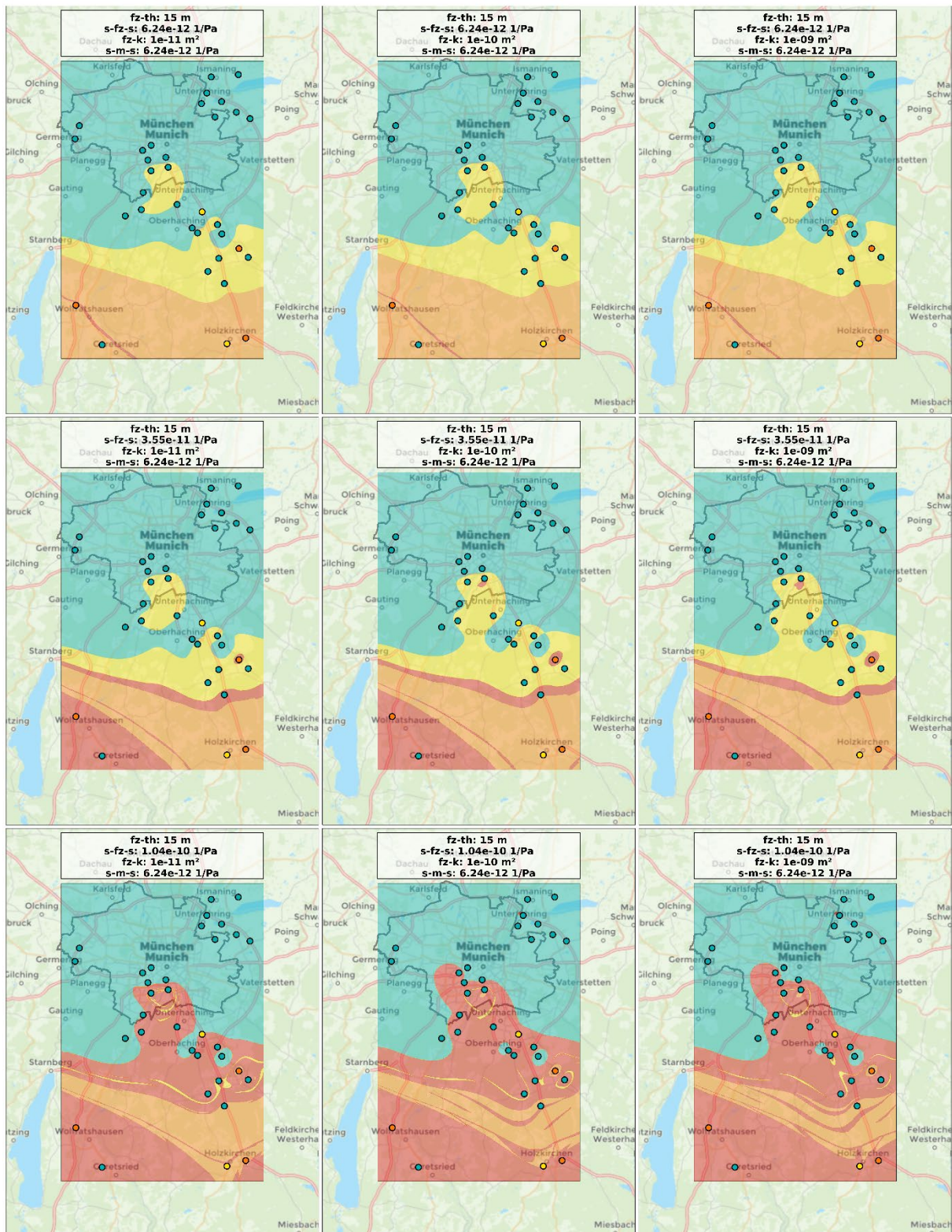
- 15 m fault zone thickness and  $1.04 \times 10^{-10}$  1/Pa spec. matrix storage:



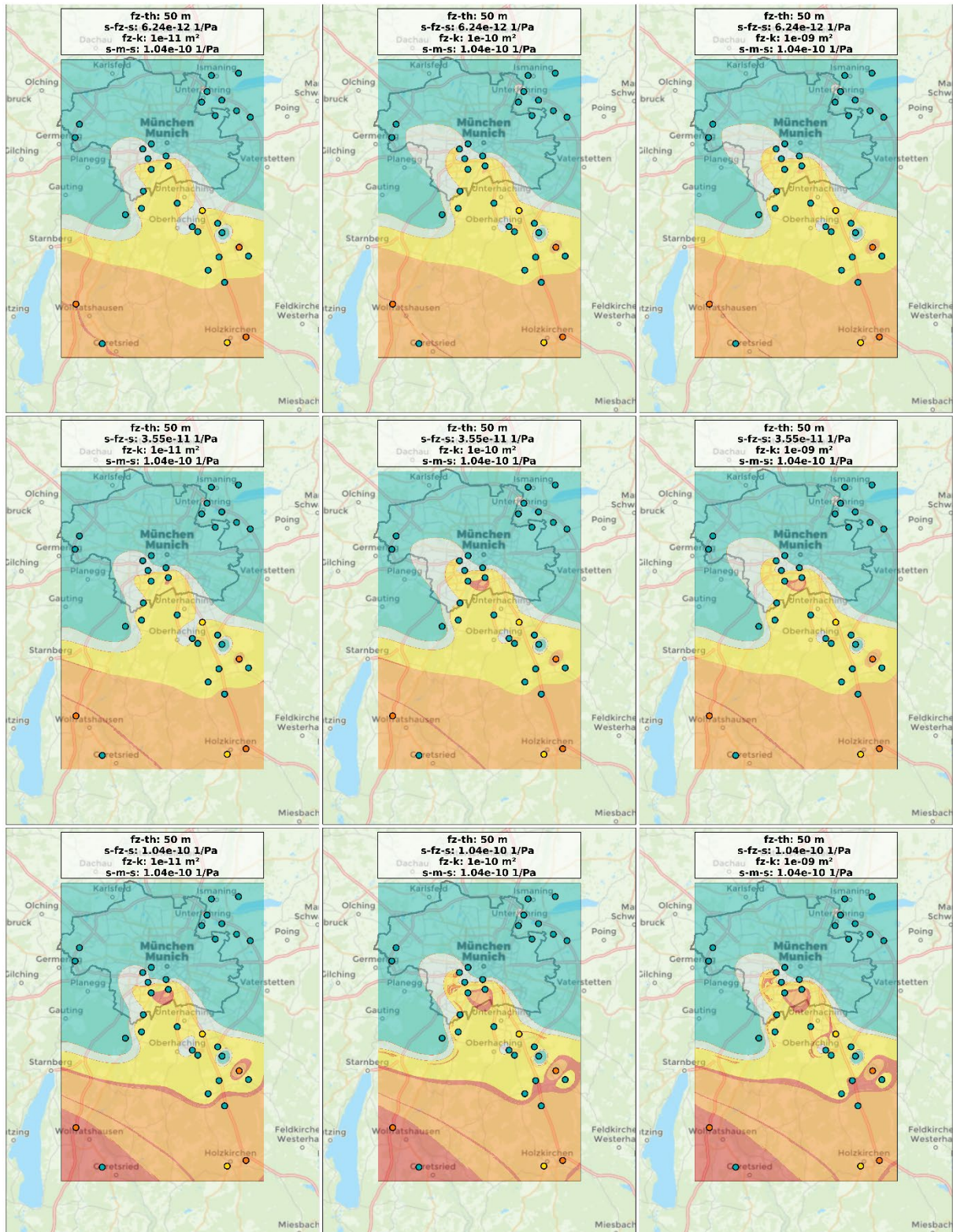
- 15 m fault zone thickness and  $3.55 \times 10^{-11}$  1/Pa spec. matrix storage:



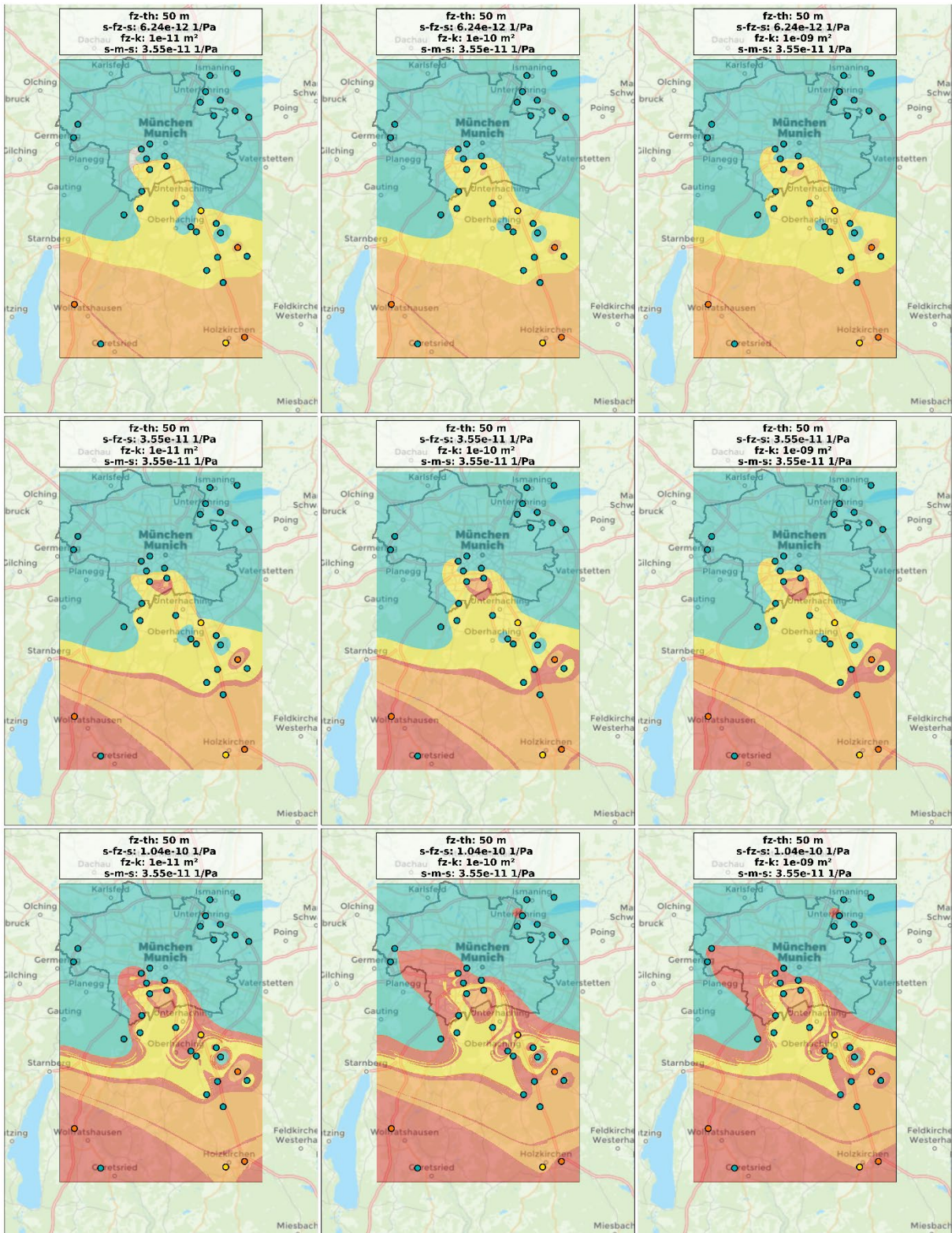
- 15 m fault zone thickness and  $6.24 \times 10^{-12}$  1/Pa spec. matrix storage:



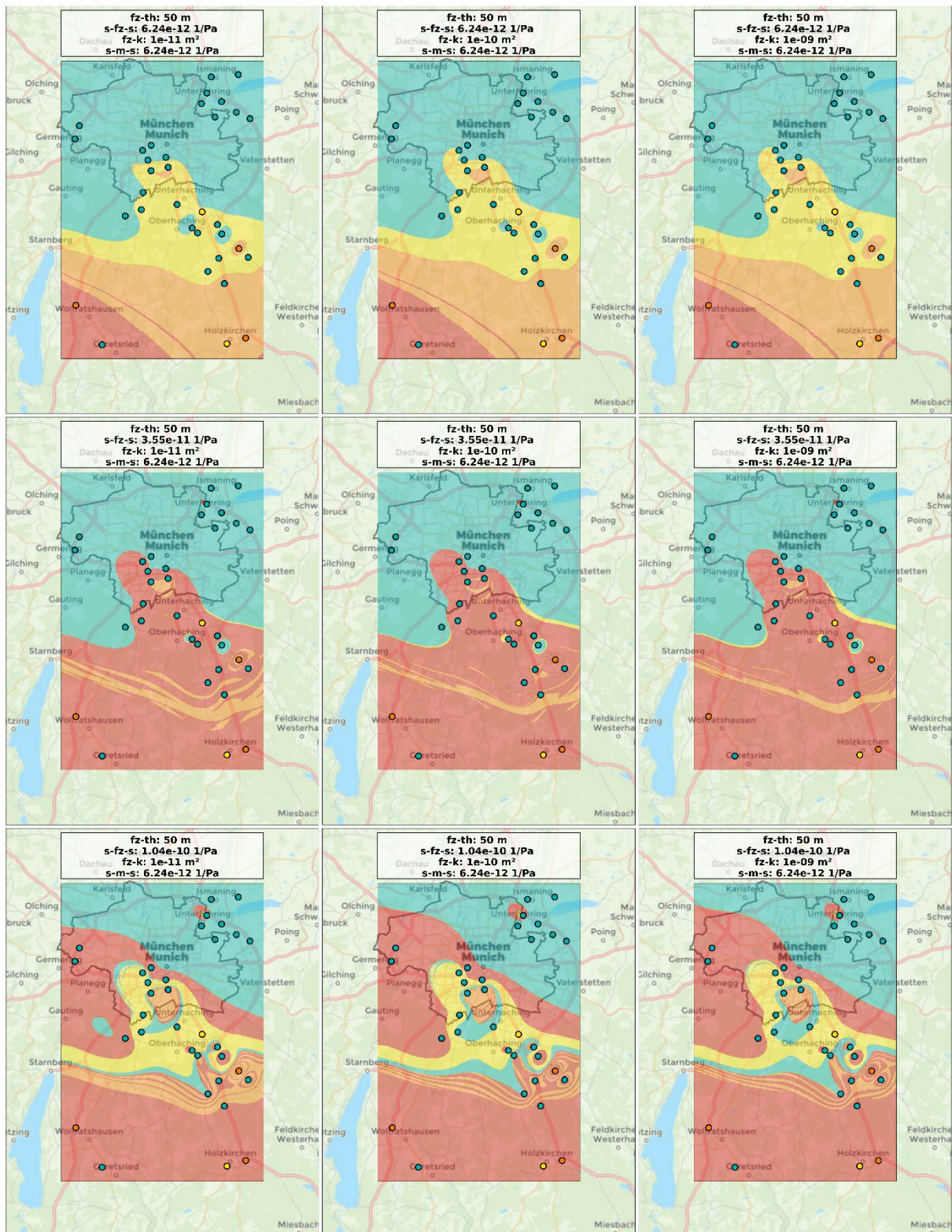
- 50 m fault zone thickness and  $1.04 \times 10^{-10}$  1/Pa spec. matrix storage:



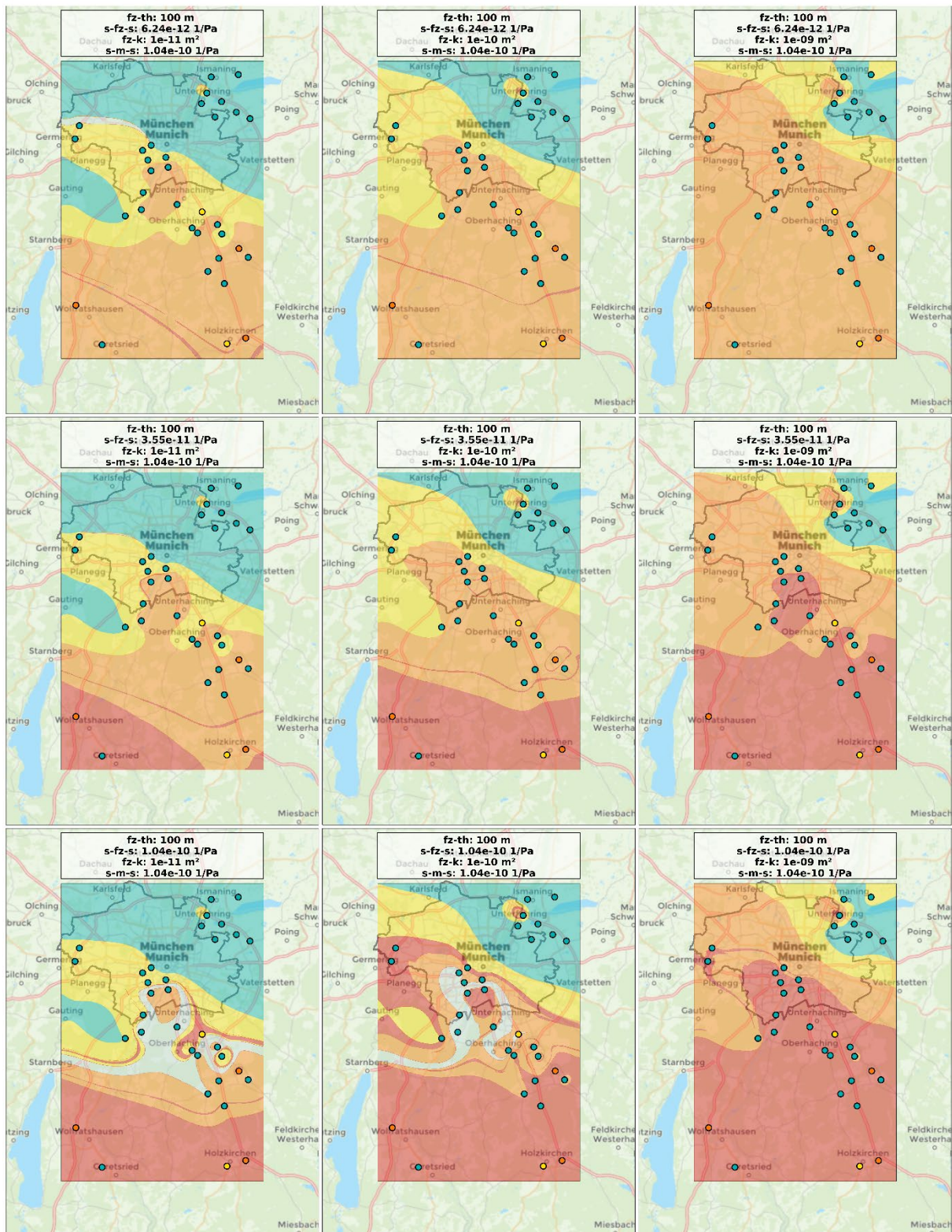
- 50 m fault zone thickness and  $3.55 \times 10^{-11}$  1/Pa spec. matrix storage:



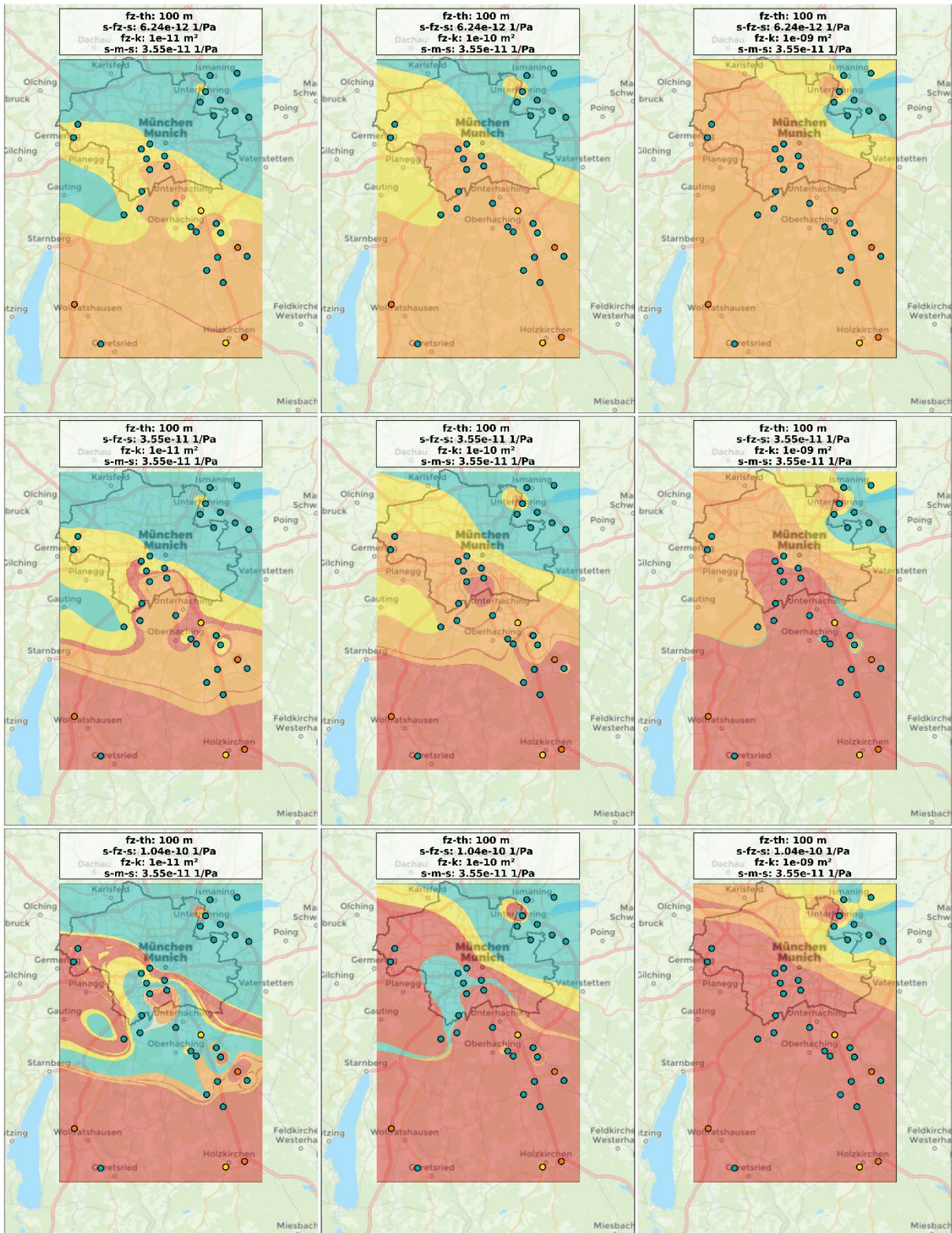
- 50 m fault zone thickness and  $6.24 \times 10^{-12}$  1/Pa spec. matrix storage:



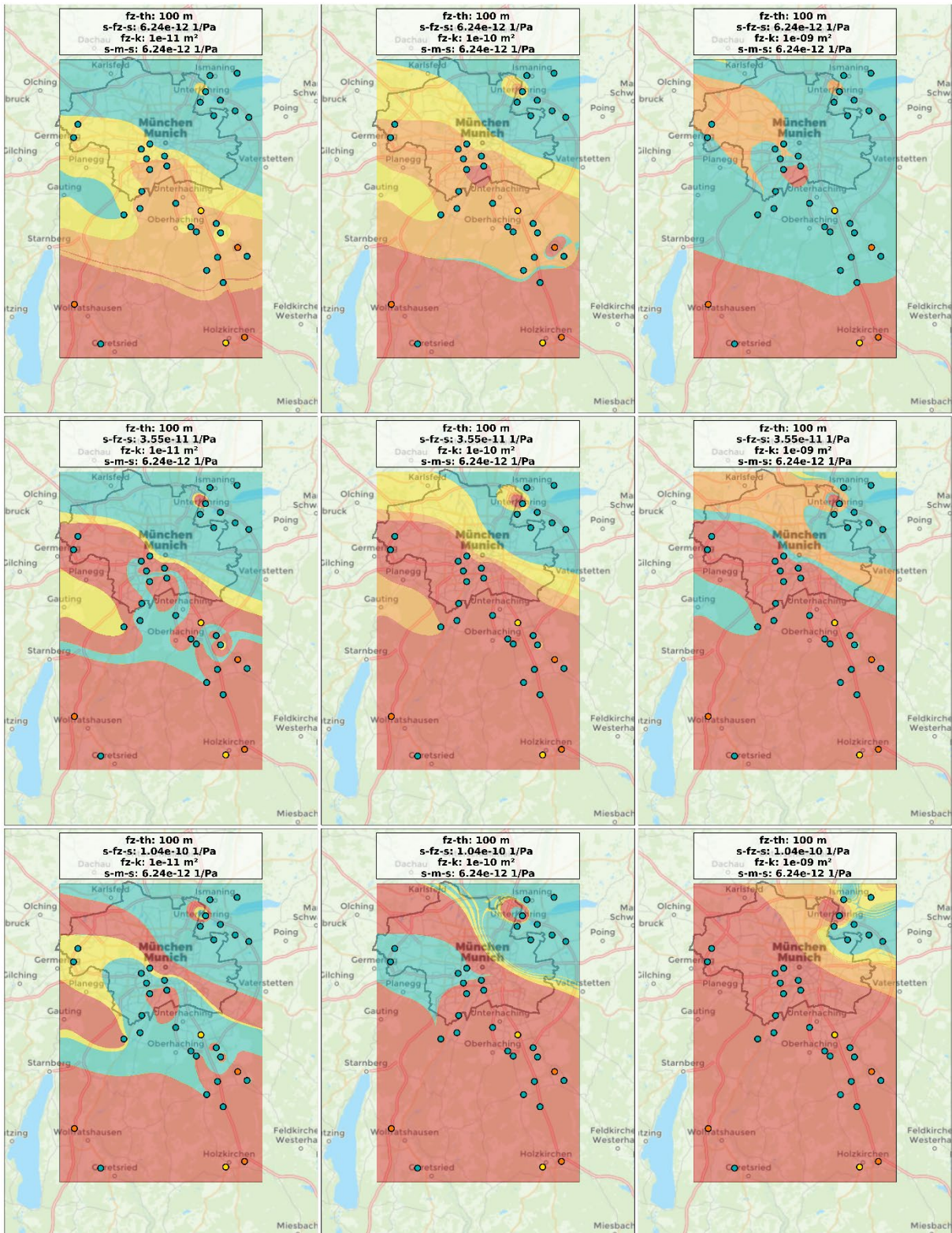
- 100 m fault zone thickness and  $1.04 \times 10^{-10}$  1/Pa spec. matrix storage:



- 100 m fault zone thickness and  $3.55 \times 10^{-11}$  1/Pa spec. matrix storage:

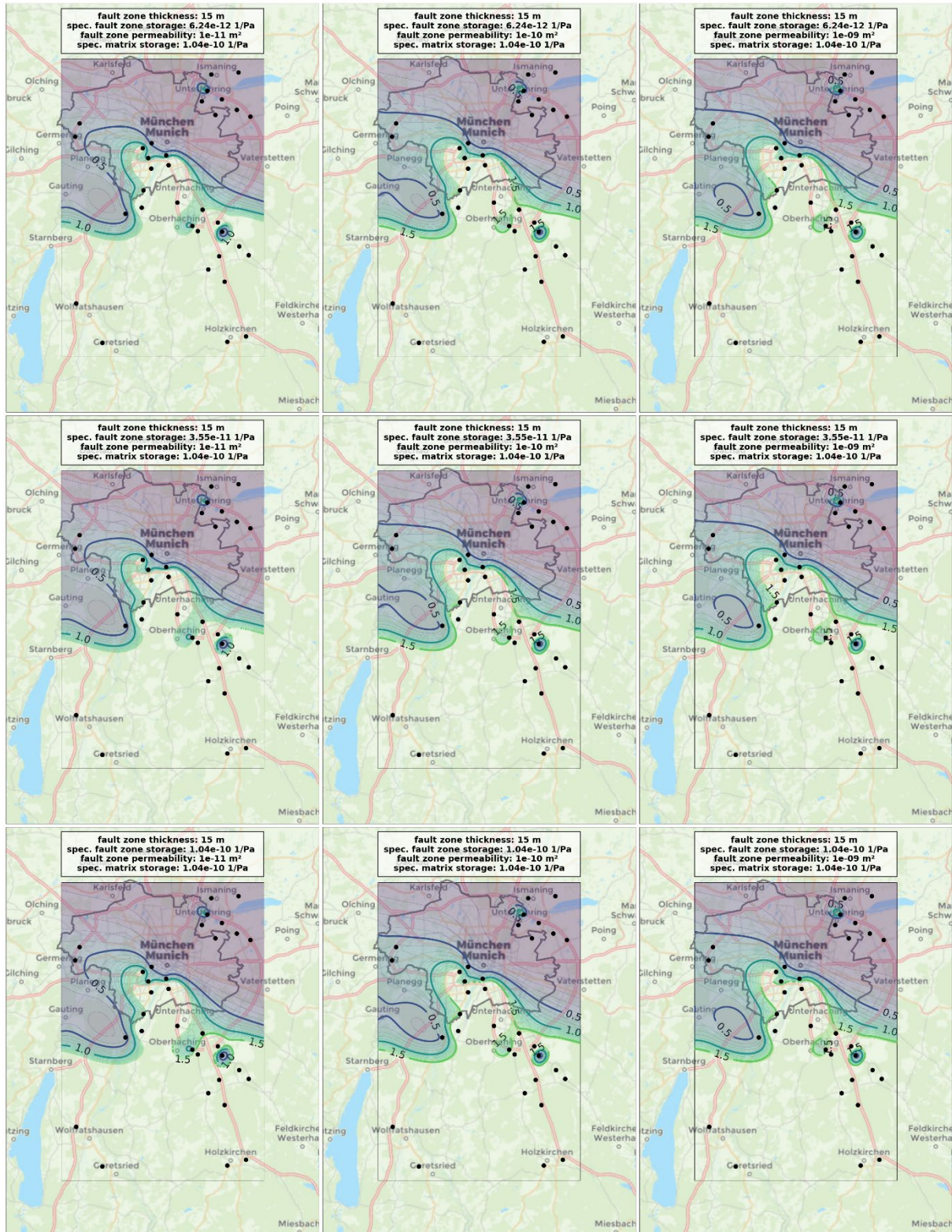


- 100 m fault zone thickness and  $6.24 \times 10^{-12}$  1/Pa spec. matrix storage:

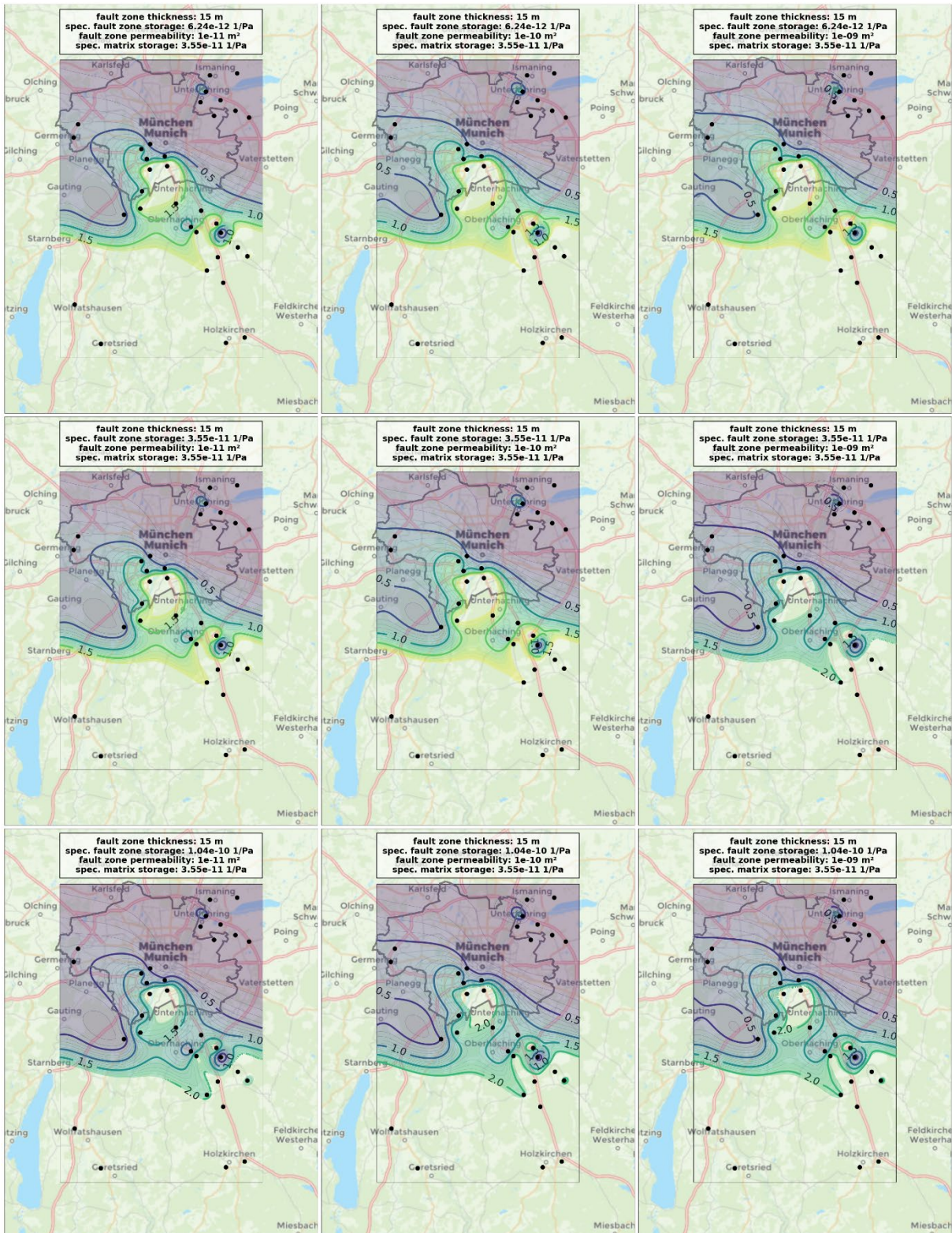


## 9.10 Spatial relative PI improvement for different fault zone types and specific matrix storage

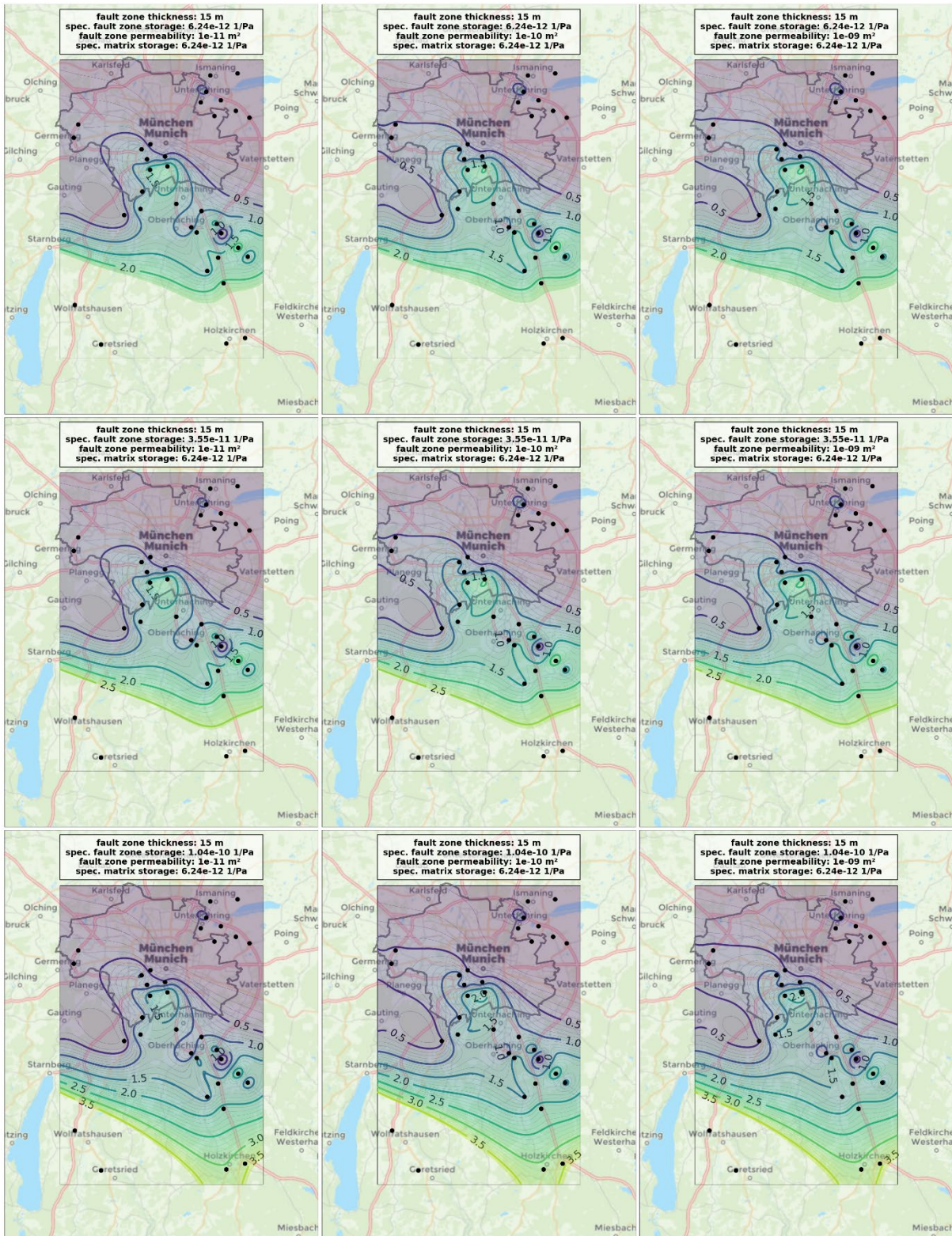
- 15 m fault zone thickness and  $1.04 \times 10^{-10}$  1/Pa spec. matrix storage:



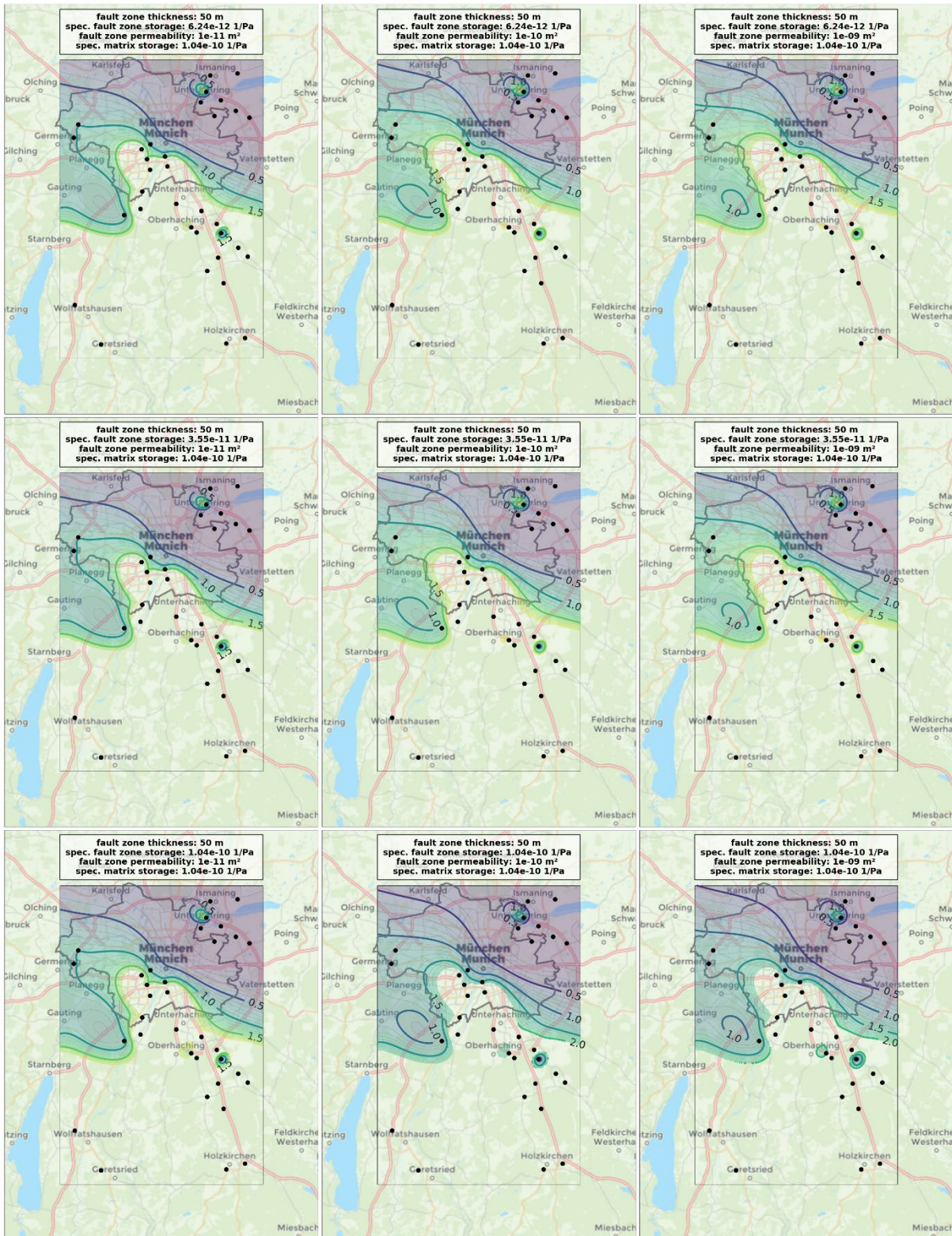
- 15 m fault zone thickness and  $3.55 \times 10^{-11}$  1/Pa spec. matrix storage:



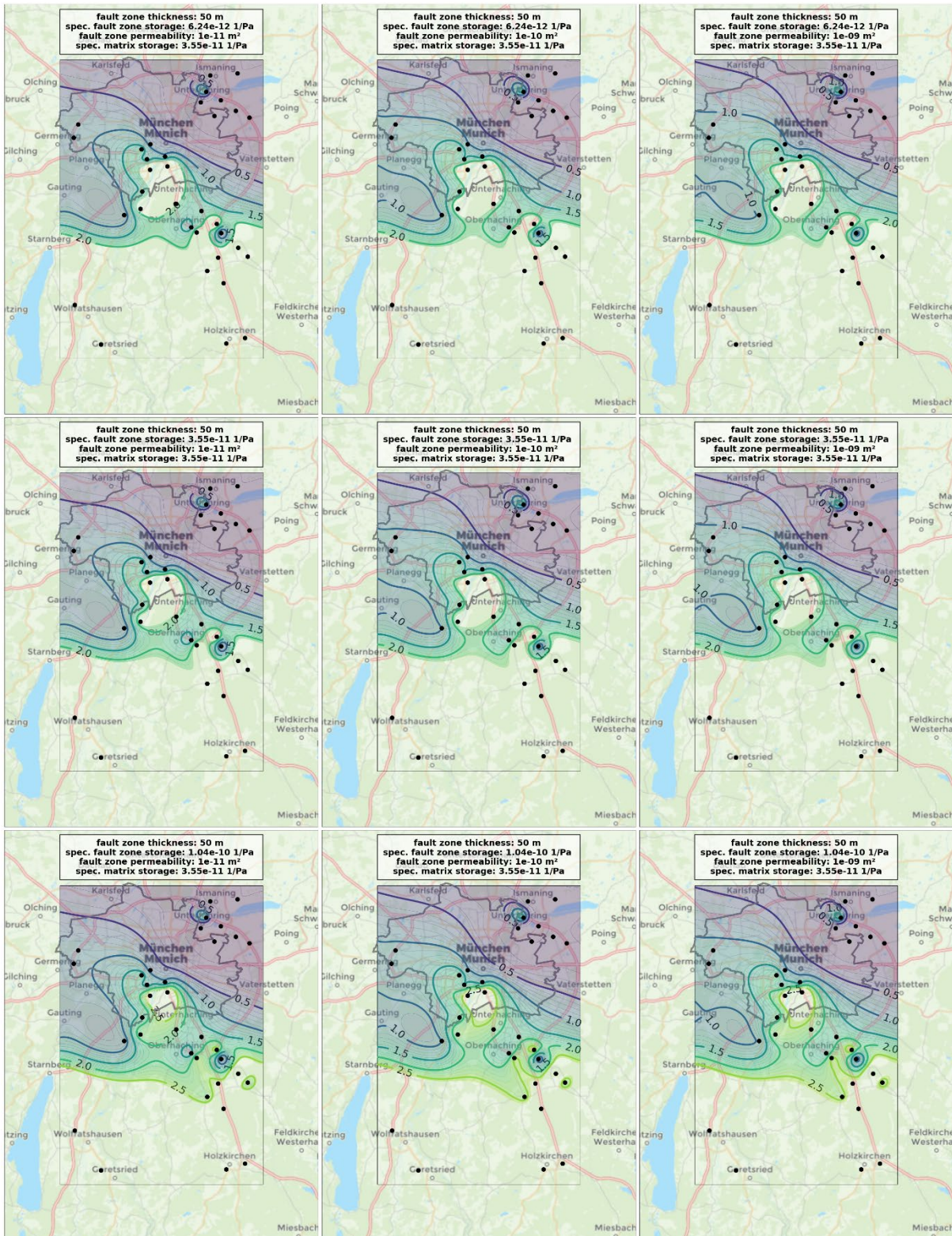
- 15 m fault zone thickness and  $6.24 \times 10^{-12}$  1/Pa spec. matrix storage:



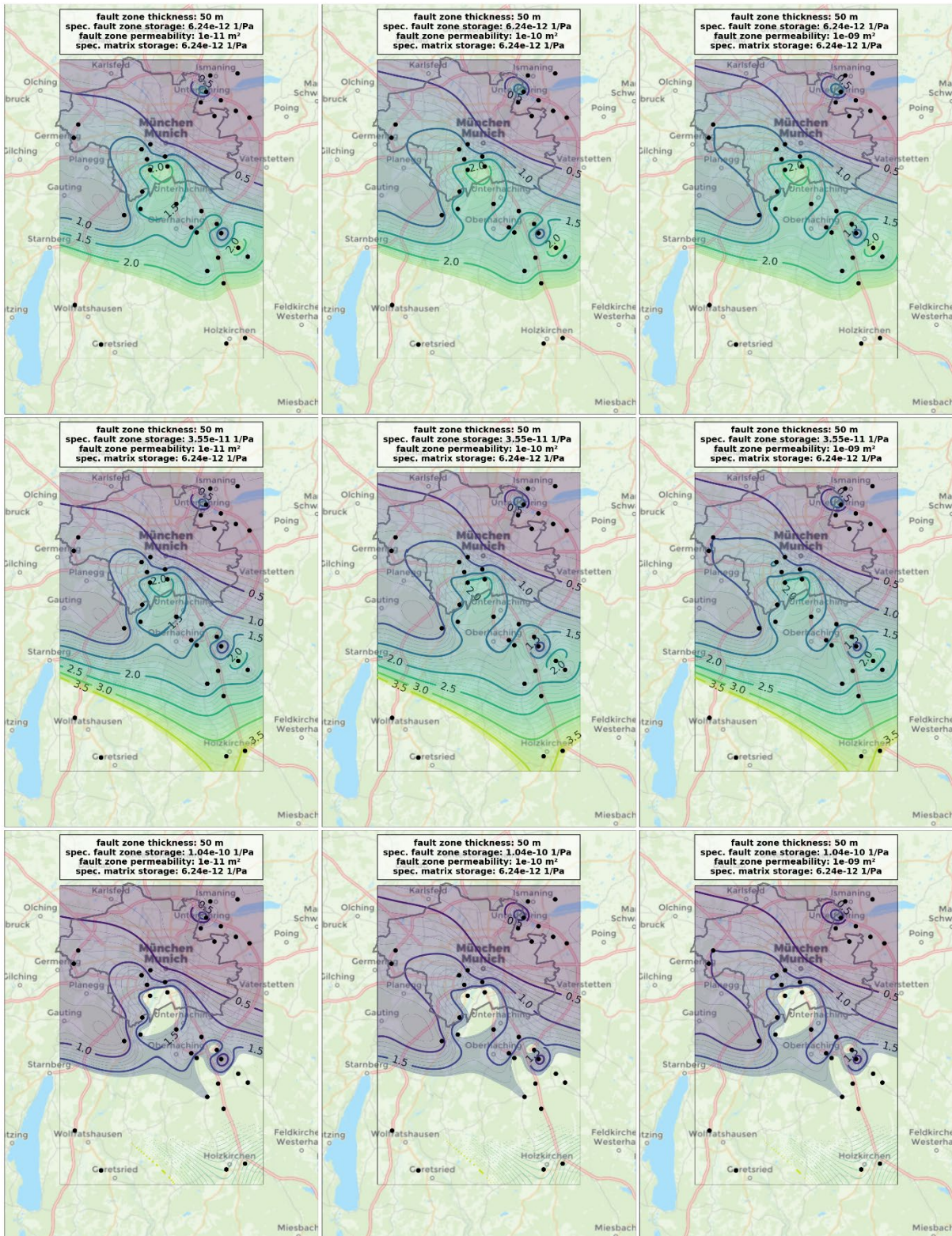
- 50 m fault zone thickness and  $1.04 \times 10^{-10}$  1/Pa spec. matrix storage:



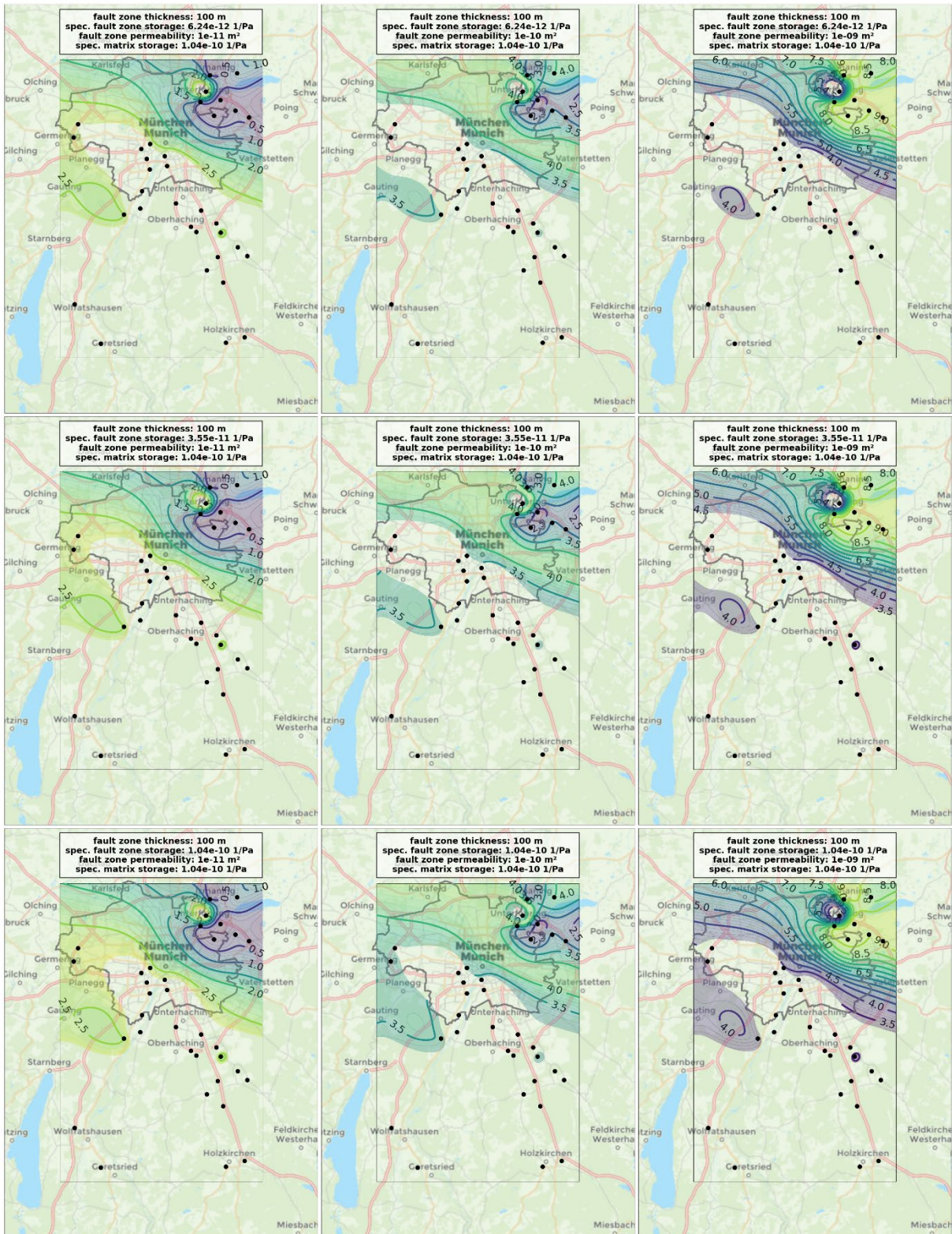
- 50 m fault zone thickness and  $3.55 \times 10^{-11}$  1/Pa spec. matrix storage:



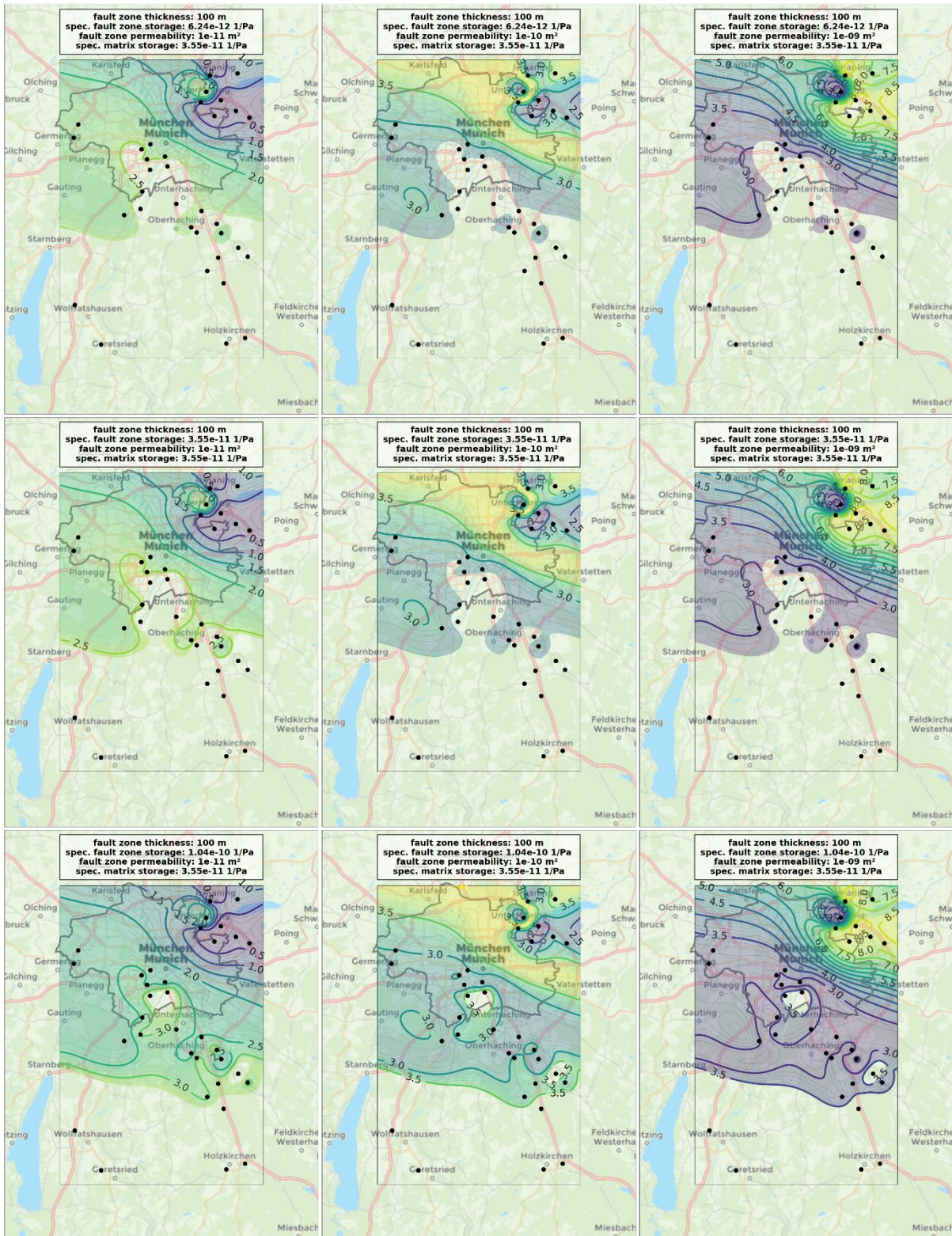
- 50 m fault zone thickness and  $6.24 \times 10^{-12}$  1/Pa spec. matrix storage:



- 100 m fault zone thickness and  $1.04 \times 10^{-10}$  1/Pa spec. matrix storage:



- 100 m fault zone thickness and  $3.55 \times 10^{-11}$  1/Pa spec. matrix storage:



- 100 m fault zone thickness and  $6.24 \times 10^{-12}$  1/Pa spec. matrix storage:

